Physical principles of size and density regulation in the cell and the cell nucleus

Romain Rollin

PSL UNIVERSITÉ PARIS

THÈSE DE DOCTORAT
DE L'UNIVERSITÉ PSL

Préparée à l'Institut Curie

Physical principles of size and density regulation in the cell and the cell nucleus

Principes physiques de la régulation de la taille et de la densité dans la cellule et le noyau cellulaire

Soutenue par
Romain Rollin
Le 8 Décembre 2022

École doctorale n°564
Physique en Île-de-France

Spécialité
Physique

Préparée au
Laboratoire Physico-Chimie Curie
UMR 168

Composition du jury :

Guillaume **Salbreux** Prof., Université de Genève	*Président du jury*
Helmut **Schiessel** Prof., Technische Universität Dresden	*Rapporteur*
Ariel **Amir** Prof., Weizmann Institute of Science	*Rapporteur*
Angela **Taddei** Dr., Institut Curie	*Examinateur*
Lydia **Robert** AgroParisTech	*Examinateur*
Pierre **Sens** Dr., Institut Curie	*Directeur de thèse*
Jean-François **Joanny** Prof., Collège de France	*Directeur de thèse*

institutCurie | PSL

Acknowledgments

Now that the final point of this Ph.D. has been written down and the defense passed it is time for introspections. The citation of Horace, "Non sum Qualis Eram" [I am not as I was] probably best embodies how I am feeling just after graduating. I am deeply grateful to my two supervisors Pierre Sens and Jean-François Joanny for guiding me through this tortuous but incredibly exciting and constructive journey in the unknown. I am particularly thankful to them for letting me free to explore, learn and form my own path while constantly being here at times where I could have drawn. Their quick-wittedness, their scientific culture and their curiosity made every single of our discussions enriching and worth a lesson. The goal of a theoretician is to predict. Well, it has been a great pleasure not being able to predict where our exchanges could go. It is to me the proof of how exciting and constructive our dialogues were, and I am sure that the diversity of our discussions will be reflected in the following manuscript. While research is about science, it is also about human skills. I feel that I have learnt from them as much on the science side than on the human side. Being humble, not being afraid of not-knowing, listening without a priori are among the many lessons that were implicitly assumed and promoted in our discussions. John Marko once told me that at each stage of an academic career, it is essential to choose the best people to work with. I cannot imagine having done a better choice for my Ph.D.

This Ph.D. uses physics to understand fundamental biological processes. It would not have been possible without the amazing environments provided by Institut Curie and College de France that promotes discussions and collaborations between fields. At College de France first, I would like to thank Thomas Lecuit for his remarkable and extensive courses at the interface between physics and biology and in particular one given in 2020: "Volume cellulaire determinants Physico-chimiques et regulation" which introduced me to the cell size scaling laws. I was far from imagining when I sat down half-awake in the comfortable lecture hall of the Collège de France, one winter morning, that the lecture I was about to listen to, would inspire me more than a year later, for what I consider to be the most original and biologically fundamental contribution of my thesis, i.e. the role of amino acids, mostly glutamate, in cell volume, nucleus volume and density regulation. At Institut Curie, I have really enjoyed and learnt a lot from the numerous collaborations that we initiated during this Ph.D. In particular, Alice Williart, Damien Cuvelier, Guillherme Nader and Nishit Srivastava in the team of Matthieu Piel for the several projects related to the consequences of the uniaxial confinement of nuclei and Simon Gemble in the team of Renata Basto for the project on the consequences of polyploidy induction. A special thanks to Matthieu Piel with whom I discussed regularly during these 3 years. His deep knowledge in biology but also his enthusiasm and his passion were a complementary source of inspiration for me that really pushed me to identify the pressing issues in the field of cell size and growth.

I would also like to thank my jury for whom I have great scientific respect and who all had an important impact on my work. The president of the jury, Guillaume Salbreux, whose thesis was one of the first scientific texts I read in depth as a newly born PhD candidate; a reading that was undeniably formative. The rapporteurs, Ariel Amir and Helmut Schiessle, whose article "Lin & Amir, Nat. Comm 2018" for the former and the book "A journey through the cell nucleus" for the latter inspired the models I propose to explain senescent cell dilution and mitotic swelling. The examiners, Angela Taddei and Lydia Robert for their expertise in biology and whose comments and questions will be helpful to strengthen the models' biological predictions. And finally, Lev Truskinovsky for your wise advice during my thesis advisory committees which have really changed my way to conduct my research. Thank you all for your time, for evaluating my work and for your pertinent and precious comments.

A Ph.D. is about success but also about failures. While failures are integrative part of the process of learning and understanding, they are necessarily accompanied by frustration, questioning and disappoint-

ment. I feel fortunate to have been part of the Sens team and more generally of the UMR 168. Without any doubt this healthy, stimulating, and kind lab environment helped me to cope and take a step back from those daily feelings. Although this Ph.D. has been conducted in the middle of the covid outbreak, I felt integrated from the very first day - thanks to the dynamism of my friends and colleagues - up to the very last when you all helped me to rehearse my defense and organize a memorable “pot de these” which to me embodies well how lively this UMR is. Peta, Mirna, Ranjit, Laure, Pulkit, John, Achille, Joanna, Lucie, Amit, Anne-Marie, Sam, Ander, Jason, Darine, Thanh, Jean, Gabriel, Brice, Pauline, Kotryna, Theresa, Jery, Gwendal, Alicia, Nastasia, Mathilde, Brieuc, Camille, Matthieu, Tapas, Raj, Carles, Ram, Maria, Thomas, Michele, Jacques, Françoise, Nolan, Efe, Charlie and all the diverse and colorful names that build up this UMR : a huge thanks to all of you, it has been a great pleasure to do research by your side!

Research can be overwhelming. Time is often limiting and is shared between so many diverse activities - reading, writing, teaching, planning, solving problems etc. - that it is easy to forget that a life out of the lab exists. J’en profite donc pour passer en Français et remercier tous mes amis d’enfance, du sud, du collège, du lycée, de la prépa, de l’ENS, et des Mines qui, au-delà d’avoir participé à ma construction personnelle, m’ont permis au cours de ces trois années de garder une vie un tant soit peu équilibrée. Les séances de sport trihebdomadaires qu’il pleuve, qu’il vente ou qu’il neige dans le parc Jane-et-Paulette Nardal qui nous auras vu suer à grosses gouttes et rire à sanglot plus d’une fois. Mais aussi les midi rue Mouffetard, les typiques « bar trials » du mercredi soir, les « quaranti-skype » et repas dominicaux du confinement, sans oublier les week-ends et vacances si ressourçants à Saint-Cyprien, Bordeaux, Praz-de-Lys ou Saint-Mandrier, sont autant de souvenirs qui resteront liés à ma vie de thésard. J’ai bien évidemment une pensée toute particulière pour Alice, Ulysse, Benjamin et Adrien qui ont toujours été là, peu importe l’épreuve que je traversais. Alors certes, la fin de la thèse est aussi la fin d’un cycle et le début d’un nouveau. Mais quel que soit le chemin à venir, sachez tous que vous faites partie de moi.

Si une thèse dure officiellement 3 ans, la préparation d’un docteur commence bien plus tôt. En ce sens, ma famille a été exemplaire : de mon éveil scientifique à la cité de la science ou au palais de la découverte, aux valeurs qui m’ont été inculquées comme la persévérance, la curiosité, la résilience ou encore l’ouverture d’esprit. Il m’est difficile de trouver les mots à la hauteur de ce que je vous dois. Alors, à l‘instar de ce que mes directeurs de thèse m’ont enseigné, l’élégance réside parfois dans la simplicité. Je vais donc m’en tenir à ce principe et conclure par un simple mais fort de sens : Merci pour tout.

Abstract

All living systems develop from individual cell growth and division. It is thus crucial for cells to actively regulate their size and densities. This exquisite control is embodied in the robust scaling laws relating cell size, protein content, and nuclear size. Despite accumulating experimental evidence, the origin of the regulation of these key cellular quantities are poorly understood. Therefore, in this thesis, we study how the interplay between physical constraints and biological processes both leads to the emergence of these scaling laws but also to their disruptions in diseases or under specific perturbations.

We first show that these laws and their breakdown can be explained quantitatively by three relatively simple, yet generic, physical constraints defining altogether the "Pump and Leak" model (PLM) (Chapter.1). Based on numerical estimates, we clearly mapped the PLM coarse-grained parameters with the dominant cellular events they stem from. We propose that the dry mass homeostasis arises from the scaling between proteins and small osmolytes, mainly amino-acids and ions. Our theory predicts this scaling to naturally fail, both at senescence when DNA and mRNAs are saturated by RNA polymerases and ribosomes, and at mitotic entry because of the Manning decondensation of chromatin counterions following histone tail modifications. Based on the same equations, we further show that nuclear scaling requires both osmotic balance at the nuclear envelope and a large pool of metabolites, allowing to dilute chromatin counterions which do not scale during growth. Altogether, our study points to the primary role of small osmolytes such as ions and metabolites in the regulation of the cellular size and density.

We next apply our theory to understand the consequences of "moderate" uniaxial confinement of nuclei (Chapter.2). The agreement between the theory and experiment is successful yet the model assumes an ad-hoc nonlinear elastic constitutive equation for the nuclear envelope. We thus extended our framework to understand how this non-linear elastic behavior arises from the presence of nuclear wrinkles and folds. We propose that wrinkles originate from the mechanical frustration induced by the competition between nuclear membrane formation after mitosis and chromosome decondensation. We use a Hookean non-linear elastic model to show that this frustration can indeed be the driving force towards a mechanical instability that results in the appearance of wrinkles. Together, the previous models provide a self-consistent framework to explain the nuclear envelope smoothening followed by the nuclear volume loss upon uniaxial compression on the timescale of minutes. On the timescale of seconds, we estimate that the dynamic of volume loss upon compression is likely driven by the permeation of nucleoplasm through the dense chromatin network (Chapter.3). We thus extend our model and derive a linear poro-elastic theory from entropy production and Onsager reciprocal relations. This theory makes two important predictions. It first shows that the relaxation of volume follows a diffusion equation, thus impeding volume variations on timescales faster than the diffusion timescale. The gel is then predicted to shrink, the magnitude of this deformation being driven by the Poisson's ratio of the gel. We conclude by providing preliminary experimental corroborations of this theory to polyacrylamide gels and then to nuclei.

An important consequence of the uniaxial confinement of nuclei is the stretching of the nuclear envelope. Under "strong" confinements, the tension becomes high enough to rupture the nuclear network of lamin and leads to the appearance of nuclear blebs. One salient observation is that nuclear blebs are highly unstable: they repeatedly grow, burst and repair. This has deleterious biological consequences such as genetic instabilities and increase of cancer invasiveness. We thus conclude this thesis by exploring and discussing the physical origins of the nuclear bleb instability (Chapter.4).

Keywords: Cell size scaling laws, Cell volume, Nucleus volume, Cell density regulation, Pump-leak model, Nuclear blebs

Résumé

Tout système vivant se développe grâce à la croissance et la division de ses cellules. Il est donc essentiel que ces cellules puissent réguler activement leur taille et leur densité. Ce contrôle précis s'incarne dans des lois d'échelle universelles qui relient linéairement la taille de la cellule à son contenu en protéines et à la taille de son noyau. Malgré l'accumulation de preuves expérimentales, l'origine de la régulation de ces quantités biologiques fondamentales est mal comprise. Dans cette thèse, nous étudions donc comment l'interaction entre les contraintes physiques et les processus biologiques conduisent à l'émergence de ces lois mais aussi à leurs dérèglements.

Dans un premier temps, nous montrons que ces lois et leurs ruptures peuvent être expliquées quantitativement par trois contraintes physiques relativement simples, mais génériques, définissant ensemble le modèle "Pump-and-Leak" (PLM) (Chapter.1). Sur la base d'estimations numériques, nous associons les paramètres mésoscopiques du PLM aux processus biologiques dont ils découlent. Nous proposons que l'homéostasie de la masse sèche cellulaire provienne de la proportionnalité entre protéines et petits osmolytes. Notre théorie prédit la perte spontanée de cette proportionnalité, pendant la senescence lorsque l'ADN et les mARNs sont saturés par les ARNs polymérases et les ribosomes, et en entrée de mitose à cause de la décondensation des contre-ions de la chromatine. A partir des mêmes équations, nous montrons que l'homéostasie du volume du noyau nécessite un équilibre osmotique au niveau de l'enveloppe nucléaire et une quantité importante de métabolites qui permettent de diluer les contre-ions de la chromatine. Dans son ensemble, notre étude met en évidence le rôle primordial des petits osmolytes tels que les ions et les métabolites dans la régulation de la taille et de la densité cellulaire.

Nous appliquons ensuite notre théorie à l'étude du confinement uniaxial des noyaux (Chapter.2). L'accord entre la théorie et l'expérience est satisfaisant. Le modèle suppose néanmoins une équation constitutive ad-hoc pour décrire le comportement élastique non-linéaire de l'enveloppe nucléaire. Nous justifions ce comportement par la présence de rides et de plis. Nous proposons que ces rides proviennent de la frustration mécanique induite par la compétition entre la formation de la membrane nucléaire en sortie de mitose et de la décondensation des chromosomes. Nous confirmons cet argument par l'utilisation d'un modèle élastique Hookéen non-linéaire qui prédit une instabilité mécanique et l'apparition de rides. Dans son ensemble, notre étude fournit un cadre auto-cohérent pour expliquer le lissage de l'enveloppe nucléaire suivi d'une perte de volume nucléaire à la suite d'une compression uniaxiale à l'échelle de quelques minutes. À l'échelle de quelques secondes, nous estimons que la perte de volume lors de la compression est due à la perméation du nucléoplasme à travers le réseau dense de chromatine (Chapter.3). Nous établissons donc une théorie linéaire poro-élastique à partir de la production d'entropie et des relations réciproques d'Onsager. Cette théorie fait deux prédictions importantes. Elle montre d'abord que la relaxation du volume suit une équation de diffusion, empêchant ainsi les variations de volume sur des échelles de temps plus rapides que l'échelle de temps de diffusion. Ensuite, elle prédit une rétractation du réseau. Ces prédictions sont alors vérifiées expérimentalement.

Une conséquence importante du confinement uniaxial des noyaux est l'étirement de l'enveloppe nucléaire. Dans le cas de confinements "forts", la tension devient suffisamment élevée pour rompre l'enveloppe et conduit alors à l'apparition de “blebs” nucléaires. Les blebs nucléaires sont très instables : ils grossissent, éclatent et se réparent de manière répétée. Ceci a des conséquences biologiques néfastes. Nous concluons donc cette thèse en explorant et en discutant les origines physiques de cette instabilité (Chapter.4).

Mots clés : Lois d'échelle cellulaire, Volume cellulaire, Volume nucléaire, Densité cellulaire, Pump-leak model, Blebs nucléaires

Résultats

Dans cette thèse, nous avons étudié les principes physiques à l'origine de la régulation de la taille et de la densité dans la cellule et son noyau. La pierre angulaire de notre travail est basée sur un modèle développé il y a 60 ans : le modèle "Pump-Leak" [Tosteson, 1960]. Bien que établi, ce modèle présente un nombre élevé de paramètres, ce qui a principalement empêché sa diffusion et son utilisation dans la communauté de biologistes.

La première partie de notre travail a donc consisté à concevoir la formulation minimale d'un tel modèle. En nous basant sur des estimations, nous faisons quatre approximations importantes. (1) Pour étudier les variations de taille cellulaire sur des échelles de temps de l'ordre de la minute, on peut supposer un état quasi-stationnaire pour les flux d'eau et les flux d'ions. Cela implique que le modèle "Pump-Leak" se réduit à trois contraintes physiques simples : l'électroneutralité, l'équilibre osmotique à la membrane plasmique et l'équilibre des flux ioniques Eq.1.1, Eq.1.2, Eq.1.3. (2) L'expression de la pression osmotique pour des solutions non-idéales peut être hautement non-linéaire et complexe [Barrat, 1996]. Pourtant, l'estimation de la contribution stérique des gros osmolytes comme les protéines suggère que ces effets sont négligeables par rapport à la contribution de gaz parfait (voir Section.3.12). Cela provient du fait que les petits osmolytes tels que les ions et les métabolites sont généralement cent fois plus concentrés que les grosses protéines dans la cellule Fig.1.1. (3) La théorie est insensible au nombre d'espèces ioniques prises en compte. En effet, l'expression du volume prend la même forme fonctionnelle à condition que les espèces ioniques considérées soient monovalentes Eq.S.59. Cette dernière approximation est très robuste, les ions multivalents comme le calcium sont typiquement 5 ordres de grandeur moins concentrés que leurs homologues monovalents [Rob Philipps, 2015]. La complexité importante du transport ionique à la membrane plasmique peut donc être réduite à un seul paramètre effectif α_0 qui, dans le modèle à deux ions, caractérise l'efficacité du pompage des cations en comparant leurs exportations actives à leurs fuites passives à travers la membrane plasmique Eq.1.3. (4) Les estimations de ce paramètre pour les cellules de mammifères montrent qu'il est proche de 0, c'est-à-dire que les cellules sont dans un régime de pompage élevé tel que les seuls ions qui restent dans la cellule sont les contre-ions des molécules imperméables. Ces approximations simplifient considérablement le modèle et rendent les résultats beaucoup plus intuitifs. Le volume de la cellule peut être exprimé simplement comme la somme de deux contributions : un volume sec, résultant principalement des protéines et occupant 30% du volume de la cellule, et un volume d'eau Eq.1.4. Ce dernier volume, dans le régime décrit précédemment, est simplement proportionnel au nombre de macromolécules imperméables, dont on a montré qu'elles étaient principalement constituées de métabolites et en particulier d'acides aminés Fig.1.1.

Sur la base de cette nouvelle interprétation réductionniste du modèle "Pump-Leak", nous avons étudié l'origine des lois d'échelle cellulaire qui relient linéairement le volume cellulaire avec son contenu protéique et le volume de son noyau. Nous montrons que les deux lois d'échelle découlent de trois contraintes physiques, à savoir, l'électroneutralité, l'équilibre osmotique et l'équilibre des flux ioniques. Pour l'homéostasie de la densité, c'est-à-dire la proportionnalité entre le volume cellulaire et le nombre de protéines, sachant que le volume cellulaire est au premier ordre représenté par les acides aminés (principalement le glutamate), le problème se réduit à comprendre le lien entre le nombre de protéines et le nombre d'acides aminés. Nous avons donc complété le modèle "Pump-Leak" par un modèle de biosynthèse des acides aminés et des protéines (voir Section.2.3). Ce modèle fait deux prédictions importantes. (1) L'homéostasie de la densité est naturellement atteinte dans le régime de croissance exponentielle de la cellule grâce au contrôle enzymatique de la production d'acides aminés. (2) L'homéostasie de la densité se rompt cependant lorsque les cellules sortent de ce régime exponentiel. Le modèle prédit en outre que le changement de régime se produit naturellement lorsque les cellules ne peuvent se diviser. Dans ce

cas, l'ADN et les ARN messagers deviennent saturés par les ARN polymérases et les ribosomes. Cela provoque un changement radical de régime de croissance : le nombre de protéines sature alors que le nombre d'acides aminés augmente linéairement avec le temps, entraînant la dilution du contenu protéique. Ces prédictions ne sont pas sans rappeler la dilution intracellulaire à la sénescence récemment rapportée dans les fibroblastes et les cellules de levure [Neurohr, 2019]. Nous avons donc naturellement comparé nos prédictions avec ces données récentes et encore inexpliquées. L'accord entre la théorie et l'expérience est frappant puisque le modèle est capable, sans paramètres ajustables, de prédire avec une bonne précision à la fois l'évolution du nombre de protéines et de la densité de masse sèche au cours de la croissance d'une cellule de levure qui ne peut se diviser Fig.1.2. Nous soulignons que nos conclusions résolvent un paradoxe connu dans le domaine, à savoir la proportionnalité entre le volume cellulaire et le nombre de protéines bien que la concentration en protéines soit relativement faible dans la cellule. Par ailleurs, nous avons proposé une interprétation originale de la dilution qui se produit au début de la mitose comme résultant du modèle "Pump-Leak" et d'un mécanisme électrostatique subtil associé à la libération des contre-ions condensés des chromosomes Fig.1.3.

Pour la loi d'échelle du noyau cellulaire, nous avons généralisé le modèle Pump-Leak en le mettant en série. Similairement à des études récentes, notre modèle montre qu'une condition nécessaire pour l'établissement de cette loi d'échelle est l'équilibre osmotique au niveau de l'enveloppe nucléaire Eq.1.12. Cette condition n'est néanmoins pas suffisante. En effet, comment expliquer que le volume du noyau évolue proportionnellement avec le volume du cytoplasme alors que les contre-ions de la chromatine, qui ne sont pas négligeables par rapport au nombre de protéines nucléaires, eux restent constant pendant la croissance ? Ici encore, nous résolvons ce paradoxe apparent en considérant les métabolites et leurs contre-ions. De manière contre-intuitive, les métabolites, bien que perméables à l'enveloppe nucléaire, jouent un rôle essentiel dans le rapport nucléocytoplasmique. Nous montrons que leurs concentrations élevées dans les cellules, une caractéristique communes aux cellules de mammifères, de levures et de bactérie, diluent les contre-ions de la chromatine, permettant ainsi la mise à l'échelle de la taille du noyau avec la taille de la cellule (Fig.1.4). Cependant, pourquoi la pression osmotique serait-elle équilibrée au niveau de l'enveloppe nucléaire ? C'est d'autant plus surprenant que, à la différence de la membrane plasmique, le critère pour que l'enveloppe nucléaire joue un rôle dans la régulation du volume du noyau est que la pression de Laplace provenant de la tension dans l'enveloppe soit de l'ordre de la pression osmotique créée par les protéines nucléaires piégées Eq.1.16. L'ordre de grandeur de cette pression osmotique est estimée être de l'ordre du kPa, ce qui s'avère être facilement atteint pour de petites déformations élastiques de la lamine. Le paradoxe peut être résolu phénoménologiquement en supposant une réponse élastique non linéaire de l'enveloppe nucléaire : la tension dans l'enveloppe n'augmente que lorsque la surface du noyau dépasse une certaine surface seuil Eq.S.112. Cette réponse phénoménologique est étayée par des expériences déjà publiées de chocs hypo-osmotiques montrant que la réponse osmotique des noyaux est non linéaire [Finan, 2009]. Pour de faibles chocs osmotiques, le volume du noyau et le volume du cytoplasme sont inversement proportionnels à l'ampleur du choc, ce qui impose un rapport nucléocytoplasmique constant. Neanmoins, après une transition brutale, alors que le cytoplasme conserve son taux de croissance, le noyau commence à croître de façon sublinéaire, ce qui entraîne une diminution du rapport nucléocytoplasmique (Fig.1.4.D).

Bien que le modèle "Pump-Leak" en série fasse des prédictions intéressantes, il reste à ce stade essentiellement théorique et basé sur une équation phénoménologique pour décrire la réponse mécanique de l'enveloppe nucléaire. Nous proposons donc dans le chapitre.2 une confrontation quantitative de notre théorie aux données non-publiés de l'équipe de Matthieu Piel étudiant les conséquences d'un confinement uniaxial "modéré" des noyaux à l'échelle de la minute. Les principales observations expérimentales sont de deux ordres. (1) La réponse du noyau peut être divisée en deux régimes clairement distincts : un

premier régime "sûr", à faible confinement, pour lequel la surface du noyau augmente à volume constant; et un second régime, à confinement modéré, pour lequel la surface continue d'augmenter mais à volume nucléaire décroissant Fig.2.2. (2) L'enveloppe nucléaire se lisse lors du confinement et la transition entre les deux régimes de déformation se produit précisément à la hauteur de confinement pour laquelle les noyaux ont entièrement perdu leurs plis. Nous proposons une réponse théorique en deux étapes. Tout d'abord, nous complétons le modèle "Pump-Leak" en série par une équation qui décrit la forme des noyaux confinés Eq.2.3. Le modèle résultant décrit quantitativement les données. Fait important, il prédit que le noyau commence à perdre du volume à la hauteur pour laquelle la tension dans l'enveloppe commence à augmenter. Mais quelle est l'origine d'une transition aussi nette pour la tension de l'enveloppe nucléaire ? En ayant à l'esprit la deuxième observation expérimentale, à savoir la causalité entre la disparition des plis nucléaires et la brusque diminution de volume, nous proposons un modèle mécanique pour expliquer l'origine de ces plis. Notre réponse théorique est basée sur une instabilité mécanique bien connue : des substrats mous liés à de fines couches élastiques rigides se déforment quand ils sont comprimés. Des estimations utilisant des valeurs typiques pour les modules élastiques de la chromatine et de la lamine confirment qu'un tel scénario est pertinent pour le noyau. La lamine est en effet mille fois plus rigide que la chromatine. Cette disparité de rigidité implique que le plissement est énergétiquement favorable même pour des petites déformations Tableau.2.2. Fait important, le modèle mécanique décrit l'équation phénoménologique utilisée dans le modèle "Pump-Leak". En effet, il prédit que les plis fixent la tension dans l'enveloppe nucléaire à des valeurs faibles par rapport aux tensions osmotiques et que ces plis tendent à disparaître sous confinement uniaxial Fig.2.11. Le modèle mécanique repose néanmoins sur une hypothèse clé : le système doit être compressé pour que les plis apparaissent. Quelle est l'origine biologique d'une telle compression ? Nous expliquons cette compression par deux caractéristiques importantes de l'enveloppe nucléaire. (1) L'enveloppe nucléaire se forme sur les chromosomes condensé (voir Fig.2.12). Nous montrons que cela peut entraîner une frustration mécanique lors de la transition géométrique qui suit leurs décondensation. (2) La lamine, contrairement à l'actine corticale, s'avère avoir un taux de renouvellement faible de l'ordre de quelques heures ([Moir, 2000],[Guilluy, 2014]). Cette propriété explique selon nous la conservation de la contrainte mécanique sur de longues périodes. Collectivement, les modèles précédents fournissent un cadre autocohérent pour expliquer le lissage de l'enveloppe nucléaire suivi par la perte de volume du noyau lors d'une compression uniaxiale à l'échelle de quelques minutes. Il est important de noter que notre étude s'ajoute à un nombre croissant d'articles récents qui démontrent la contribution fondamentale des formes nucléaires et en particulier des rides et des plis nucléaires à l'homéostasie cellulaire ([Lomakin, 2020],[Venturini, 2020],[Cosgrove, 2021]). En particulier, dans cette thèse, nous démontrons le rôle fondamental de ces plis sur l'homéostasie du volume nucléaire et par extension sur la robustesse de la loi d'échelle nucléaire.

Jusqu'à présent, nous avons démontré qu'un modèle unique de régulation de la taille cellulaire, à savoir le modèle "Pump-Leak" en série, couplé à une cartographie appropriée entre les processus cellulaires et les paramètres mésoscopiques du modèle, peut prédire avec succès une grande variété de processus biologiques indépendants tels que l'homéostasie et la dilution de la densité cellulaire, le gonflement mitotique, la loi d'échelle nucléaire et sa rupture en cas de perturbation. La caractéristique commune de ces phénomènes biologiques est qu'ils se produisent sur une échelle de temps de quelques minutes à quelques heures. Mais comment étendre notre théorie pour englober des variations de taille plus rapides ? Cette question est motivée par les données de l'équipe de Matthieu Piel qui montrent que la réponse du volume de noyaux confinés à l'échelle de la seconde est non triviale : le noyau se déforme d'abord à volume constant suite à une compression de l'ordre de la milliseconde, puis se rétracte avec une dynamique régie par une échelle de temps d'environ 10s. Il est intéressant de noter que cette dynamique est 1000 fois plus lente que celle du cytoplasme et qu'elle se produit à des hauteurs de confinement où l'enveloppe nucléaire ne devrait pas être

étirée. Le défi majeur pour proposer un modèle dynamique pour le volume du noyau est la multiplicité des facteurs qui jouent un rôle dans sa régulation tels que les ions, les protéines, les métabolites et la lamine. Pour aller dans cette direction, nous avons décidé d'étudier la réponse au confinement d'un système modèle simplifié constitué de seulement 2 composants : un réseau de polyacrylamide neutre et un fluide. Ce système simplifié et le noyau présentent une réponse au confinement similaire, à savoir, une déformation à volume constant suivie d'un rétrécissement du réseau. Pour comprendre cette dynamique particulière, nous établissons une théorie linéaire poroélastique à partir de la production d'entropie et des relations réciproques d'Onsager. Nous montrons que la théorie obtenue est équivalente au modèle "stress-diffusion coupling" développé il y a 40 ans par Tanaka et al [Tanaka, 1979]. La démonstration proposée présente deux avantages. Premièrement, elle identifie clairement ce qu'est la "pression du fluide" qui apparaît dans la théorie de Tanaka. Cette dernière est proportionnelle à la différence entre la pression hydrostatique et la pression osmotique résultant des répulsions stériques du gel Eq.3.29. Deuxièmement, elle peut facilement être adaptée pour inclure d'autres espèces telles que les ions. Une prédiction frappante de cette théorie est que les éléments mésoscopiques de volume constituant le gel évoluent suivant une équation de diffusion Eq.3.47. Des variations significatives du volume sur des échelles de temps plus rapides que l'échelle de temps de diffusion sont interdites. Le gel se déforme donc d'abord à volume constant lors d'une déformation rapide, puis relaxe en se contractant vers son état d'équilibre en suivant l'échelle de temps de diffusion, l'ampleur de cette déformation étant déterminée par le coefficient de Poisson du gel. Motivés par ces conclusions qualitatives, nous appliquons ensuite quantitativement cette théorie à deux problèmes distincts : la compression osmotique et la compression uniaxiale des billes de polyacrylamide. Nos solutions analytiques démontrent que les deux expériences sont bien décrites par la théorie. Cela s'incarne dans la superposition des données expérimentales sur une courbe maîtresse décrivant le rétrécissement des billes de différentes tailles suite à une compression osmotique ou mécanique (Fig.3.10 et 3.15).

Une conséquence importante du confinement modéré des noyaux est l'augmentation de la tension dans l'enveloppe nucléaire. Nous avons expliqué que cette augmentation était à l'origine de la perte de volume des noyaux modérément confinés. Cependant, pour des confinements plus important, la tension devient suffisamment élevée pour rompre l'enveloppe nucléaire. Cela conduit alors à l'apparition de blebs nucléaires Fig.4.2. Il est intriguant de constater que les blebs nucléaires sont instables : ils grossissent, éclatent et se réparent de façon périodique. Cette instabilité de l'enveloppe nucléaire s'avère délétère puisqu'elle est associée à des instabilités génétiques et à une augmentation du potentiel métastatique dans le carcinome du sein. Pourquoi les blebs nucléaires sont-ils instables ? Là encore, le modèle "Pump-Leak" en série apporte des réponses. Le modèle montre que la croissance du bleb est nécessairement induite par le passage dans le bleb d'osmolytes nucléaires préalablement piégés par l'enveloppe nucléaire comme des grosses protéines. La croissance du bleb permet à son tour de relâcher la pression nucléaire, ici induite par l'étirement de l'enveloppe nucléaire suite au confinement, en réduisant le volume du noyau et donc la tension dans son enveloppe. Cependant, l'ampleur de cette diminution de pression est en moyenne négligeable en raison de l'effet combiné de deux facteurs. Tout d'abord, le modèle "Pump-Leak" en série prédit que la croissance du bleb est accompagnée par un influx d'eau à l'intérieur du noyau, ce qui entrave partiellement la libération de la pression. Deuxièmement, après l'éclatement du bleb, les grosses protéines, qui possèdent un signal de localisation nucléaire, sont réimportées dans le noyau, ce qui rétablit la pression nucléaire initiale. Ces effets, combinés au faible taux de renouvellement de la lamine, expliquent pourquoi la croissance des blebs est périodique sur plusieurs heures. Une autre caractéristique clé des blebs nucléaires est que leur dynamique de croissance est lente, de l'ordre de la dizaine de minutes. Nos estimations réfutent fortement l'hypothèse selon laquelle la dynamique de croissance soit dominée par la perméation de l'eau à travers le réseau de chromatine. Nous avons donc

proposé un modèle alternatif où la croissance est ralentie par la friction entre les lipides qui s'écoulent vers le bleb et les protéines intégrales de la membrane nucléaire qui sont encastrées dans la couche de lamine (voir Section.2.3). Nous montrons que ce modèle peut expliquer quantitativement la dynamique de croissance si le coefficient de friction associé ξ_m est élevé de l'ordre de $10^{11} - 10^{12}$Pa.s.m^{-1} impliquant une viscosité de la membrane nucléaire de l'ordre de $10^{-5} - 10^{-4}$Pa.s.m. Une valeur aussi élevée de la viscosité de la membrane nucléaire remet en question notre modèle dynamique. Nous proposons deux explications pour cette observation. (1) L'enveloppe nucléaire est une double bicouche lipidique. Les deux membranes sont continues l'une avec l'autre, et la jonction se produit à l'endroit de l'insertion du pore nucléaire. Il est important de noter que seule la membrane nucléaire externe est continue avec la membrane du réticulum endoplasmique qui, selon nous, fournit des lipides pendant la croissance du bleb. Cela implique qu'il doit également y avoir un flux de lipides de la membrane nucléaire externe vers la membrane nucléaire interne. Ce flux est susceptible de se produire avec une friction supplémentaire à la jonction du pore nucléaire. Nous supposons donc que ce processus pourrait ralentir la dynamique et, à son tour, augmenter la friction apparente estimée à partir de notre modèle. Une modélisation plus fine ainsi qu'une caractérisation expérimentale de la membrane nucléaire restent un domaine passionnant pour de futures études. (2) Un effet supplémentaire qui ralentirait la dynamique de croissance des blebs est la prise en compte explicite de la diffusion des grosses protéines à travers le réseau de chromatine. Le modèle "Pump-leak" en série stipule que la force motrice de la croissance est l'entrée d'osmolytes qui étaient auparavant piégés dans le noyau. Dans sa version actuelle, notre modèle suppose que les protéines piégées s'équilibrent rapidement et nous imposons que la concentration de ces grosses protéines soit égale à travers le trou du bleb Eq.4.7. L'étape suivante de notre recherche consiste à relâcher cette hypothèse. En effet, des études ont montré que la diffusion de gros objets dans le noyau peut être lente. Par exemple, le coefficient de diffusion des ARN messagers dans le noyau a été mesuré à 0.12 $\mu m^2/s$, ou encore, l'échelle de temps typique pour qu'un ARN messager sorte du noyau est de l'ordre de quelques minutes [Coulon, 2014].

Pour conclure, dans cette thèse, j'ai fourni une étude théorique générale du volume cellulaire, du volume du noyau et de la densité cellulaire. Une attention particulière a par ailleurs été accordée à la vérification expérimentale des prédictions de nos modèles. Bien que montrant un accord quantitatif satisfaisant avec les expériences, les modèles présentés dans cette thèse peuvent être étendus dans un certain nombre de directions. Dans le chapitre 1, nous avons complété le modèle "Pump-Leak" en série avec un modèle de biosynthèse d'acides aminés et de protéines pour évaluer comment la densité cellulaire évolue au cours de la croissance. L'extension naturelle de ce modèle de croissance est d'ajouter un mécanisme de division cellulaire. Il a été démontré que plusieurs facteurs pouvait jouer le rôle de signal à l'induction de la division cellulaire, comme la dilution de l'inhibiteur du cycle cellulaire Rb dans les cellules humaines [Zatulovskiy, 2020] ou la tension de la paroi cellulaire pour les bactéries [Harris, 2016]. Une autre voie intéressante consisterait à coupler le modèle "Pump-Leak" en série à un modèle de transport nucléocytoplasmique. Nous pensons que cela pourrait révéler un nouveau mécanisme prometteur pour la translocation des protéines dans le noyau lors d'une perturbation, indépendamment de la tension de l'enveloppe nucléaire. Dans le chapitre.2, nous avons proposé un modèle mécanique pour comprendre les plis à la base de la loi d'échelle nucléaire. Ce modèle est volontairement simplifié afin d'obtenir des lois d'échelles et de vérifier si ce modèle mécanique est pertinent pour le noyau. Une extension naturelle de ce modèle serait d'effectuer des simulations pour inclure des effets géométriques et résoudre le système d'équations sans approximations. Nous pouvons également évaluer d'autres instabilités mécaniques telles que le froissement [1]qui peut émerger dans cette classe de système mécanique [Ciarletta, 2019]. Dans le chapitre 3, nous avons établi une théorie poroélastique linéaire pour un gel neutre à deux composants. Comme extension logique, nous proposons d'incorporer : la membrane en utilisant des conditions aux

limites appropriées Eq.3.44, des effets non linéaires ([Geng, 2012],[Tatara, 1993]), ou des effets électrostatiques par la prise en compte des ions [Yamaue, 2005]. Enfin, dans le chapitre 4, nous avons commencé à résoudre un modèle qui couple à la fois l'écoulement du nucléosol et celui de la membrane nucléaire. Nous proposons de complexifier le flux de nucléosol en incorporant la diffusion de grosses protéines à travers le réseau de chromatine.

[1]Un froissement ou "crease" en anglais, est une région localisée, de contact et de grande déformation par rapport à l'état homogène. Il est intéressant de noter que le plissement est une instabilité particulière dans le sens où le système passe brusquement d'un état non déformé à un état fortement déformé, de sorte que l'élasticité linéaire ne peut le décrire.

Contents

Figure List

List of Tables

Preface

Dans un voyage ce n'est pas la destination qui compte mais toujours le chemin parcouru, et les détours surtout.

Philippe Pollet-Villard
Mondial Nomade
2011

Biological growth is one of the very characteristics that most living system share. This process has always fascinated humans. First because of the amazing diversity of sizes, motifs, and symmetries that biology is able to produce. But also because of the medical challenges it raises. Growth associated diseases are indeed multiple. Cancer, in which cells proliferate in an uncontrolled fashion to give rise to macroscopic tumors, is probably one of the most illustrative and common example.

The latter example highlights two essential features of growth. First, this is a multiscale process: it is driven by the replication, the division, and the growth of individual cells, which taken as a whole leads to the development of the tissue and of the organism. Second, the process must be highly controlled. An order of magnitude is particularly enlightening here to grasp how controlled the process must be. A standard human adult possesses about 10^{13} cells. Among those cells, about 10% are renewed each day [Sender, 2021]. Equivalently, this means that 4 million of cells are produced every second in our bodies. It is hence clear that a small change in the balance between turnover and production rates would lead to drastic changes in term of cell number.

What drives, controls and stops growth are thus fundamental questions at the heart of the development of living systems. Researchers have identified two cross-talking levels of regulation: the sub-cellular and the supra-cellular levels of control. The former is probably best embodied by the fact that most dividing cells grow twofold before dividing. Yet, sub-cellular monitoring alone does not explain the appearance of complex, macroscopic, dynamic, and highly symmetric biological patterns. It would indeed be hard to imagine that such complex patterns only emerge from cellular close-range cooperativity, cells being typically one million times smaller than the motifs they belong to. The positional and temporal information of the pattern to form is instead encoded externally on macroscopic scales. One genuine example of such supra-cellular control are morphogens [Wolpert, 1969]. A morphogen is a signaling molecule that acts directly on cells to influence their fate depending on its local concentration. The establishment of precise macroscopic concentration profiles thus allows to adapt the cellular response spatially and temporally on large length scales.

The tight control of biological development also echoes in the scaling laws that are observed throughout biology. On the macroscopic scale, we can for example quote the Kleiber law [Kleiber, 1947] which relates the metabolic rate to the mass to the power $\frac{3}{4}$ of mammals, many insects and more generally most of metazoans. Other scaling laws exist such as the ones relating the mass and the size of an organism. Sea mammals for example have an average body length proportional to their mass to the power $\frac{1}{3}$ [Economos, 1983]. Cells also exhibit exquisite scaling laws ([Chan, 2010] and Chapter.1). Cell size for example scales linearly with the nucleus size and with the cellular protein content both in mammals, yeasts and bacteria.

Importantly, the biological control of growth appears as being the resultant of both active and passive mechanisms. The establishment of complex and steady morphogen concentration profiles indeed requires active consumption of energy. Else, equilibrium laws would bound the profile to be homogeneous. On the other hand, most of the macroscopic scaling laws mentioned above were shown to be the signature of passive physical and geometrical constraints. Already in the fifteenth century, Galileo understood that the laws of elasticity imposed some constraint on growth: bones of similar composition but of different scales must thicken to exhibit similar mechanical resistance to stress [Galilei, 1638]. A corollary is that this imposes an upper bound on the maximal size of an organism on earth: animals too large would either buckle under their own weights or they would be too massive to be able to move [Haldane, 1985]. Similarly, in his pioneering book [Thompson, 1912], Darcy Thomson proposed an interpretation of the laws of growth as resulting from mathematical conformal transformations to explain the evolution of shapes across species of the same evolutionary family. More recently, the Kleiber law was successfully described by the West-Brown-Enquist theory [West, 1997] as originating from the constraint on efficient and democratic energy delivery to every cell in our body. An estimate is again enlightening here. An average human adult possesses 10^{13} cells and eats about 8000kJ/day to have a steady weight. Assuming

that half of this energy consumption is used for cell maintenance implies that an average cell consumes 10^7 ATP molecules per second [Rob Philipps, 2015]. The typical concentration of ATP in cells is about $1-10$mMol, which for a typical cell of $1000\mu m^3$ is equivalent to 10^8-10^9 ATP molecules per cell. Hence, in only few minutes and without energy supply, cells would run out of ATP and would subsequently die. Biology has thus designed a democratic food supply chain that provides energy to the equivalent of 1000 human societies with an acceptance error of less than a minute. With regard to this estimate, it is thus not surprising that the efficiency constraint of this chain incarnates into a very robust scaling law ubiquitous among metazoans.

Paradoxically, although cells are the simplest building blocks of a human body, the principles ruling their size, their growth and the associated scaling laws have not yet been fully resolved. Our understanding of cells has indeed evolved drastically since the first static observation of a plant cell by Robert Hooke in 1665 [Hooke, 1665]. Nowadays, the very principle of cell identity is even questioned since controlled cell fate reprogramming was achieved upon electrical and mechanical signals ([Levin, 2013],[Roy, 2018]). This evolution has largely been made possible thanks to the huge technical progress that has occurred over the past twenty years in particular in imaging [Betzig, 2006]. New methods to precisely measure cell and organelle volumes as well as cellular dry mass or cellular protein content have been developed ([Model, 2018],[Cadart, 2017], [Burg, 2007],[Park, 2018]). The resulting data show how complex the regulation of cell size is. In a human body, cell size vary on 5 order of magnitudes ranging from $30\mu m^3$ for sperm cell to $40 \cdot 10^5 \mu m^3$ for oocytes [Rob Philipps, 2015]. Yet, one cell type often shows small volumetric variance at a given stage of its cycle. This emphasizes the importance of size in monitoring cell function. Cells have a host of regulatory mechanisms to achieve a tight control on their size ([Lang, 1998], [Hoffmann, 2009]). For example, more than 100 biological factors, as diverse as ions, amino-acids and hormones, were reported to affect cell size (see Table.2 in [Lang, 1998]). Physical laws were again acknowledged to impose key constraints on cell size [Cadart, 2019]. This is not surprising, cell volume is intrinsically coupled to the physical concept of osmosis which characterizes the spontaneous movement of solvent molecules through a selectively-permeable membrane. Besides, these physical constraints have recently been used to unravel novel mechanism of size regulation. It has indeed been proposed that the mechanical tension at the plasma membrane alters the permeability of ion channels, resulting in a volume adaptation ([Venkova, 2022], [Adar, 2020],[Roffay, 2021]).

Following up on the recent progress brought by physics in the understanding of cellular growth, we devote this thesis to the physical study of cell size and more precisely its relationship with other biological quantities such as the protein content and the nucleus size. As emphasized throughout this preface, growth is the exquisite result of passive physical constraints and active biological processes. While both quantities are well documented separately, their interplay is still unclear. All proportions kept, this will be the cornerstone of our work.

Chapter 1

Physical basis of the cell size scaling laws

Le savant doit ordonner; on fait la Science avec des faits comme une maison avec des pierres; mais une accumulation de faits n'est pas plus une science qu'un tas de pierres n'est une maison.

Henri Poincaré
La science et l'hypothèse
1902

Plancton : aux origines du vivant, Christan Sardet

1 Introduction

1.1 Objectives

The dimensions and compositions of cells are tightly regulated by active processes. This exquisite control is also embodied in the robust scaling laws relating cell size, dry mass, and nuclear size. Despite accumulating experimental evidence, a unified theoretical framework is still lacking. Here, we show that these laws and their breakdown can be explained quantitatively by three simple, yet generic, physical constraints defining altogether the Pump-Leak model. Based on estimations, we clearly map the Pump-Leak model coarse-grained parameters with the dominant cellular events they stem from. We propose that dry mass density homeostasis arises from the scaling between proteins and small osmolytes, mainly amino-acids and ions. Our theory predicts this scaling to naturally fail, both at senescence when DNA and RNAs are saturated by RNA polymerases and ribosomes respectively, and at mitotic entry due to the counterion release following histone tail modifications. Based on the same equations, we further show that nuclear scaling results from osmotic balance at the nuclear envelope (NE) and a large pool of metabolites, which dilutes chromatin counterions that do not scale during growth.

1.2 Context

Although cell size varies dramatically between cell types, during the cell cycle and depends on various external stresses [Cadart, 2019], each cell type often shows small volumetric variance at a given stage of their cycle. This tight control reflects the importance of size in monitoring cell function. It is often associated to generic linear scaling relations between cell volume, cell dry mass and the volume of the nucleus ([Neurohr, 2020], [Cantwell, 2019], [Webster, 2009]). These scaling laws have fascinated biologists for more than a century [Wilson, 1925] [Conklin, 1912], because of the inherent biological complexity and their ubiquity both in yeasts, bacteria and mammals, hence raising the question of the underlying physical laws.

Although robust, these scaling relations do break down in a host of pathologies. The nuclear-to-cytoplasmic (NC) ratio (also called karyoplasmic ratio) has long been used by pathologists to diagnose and stage cancers ([Jevtić, 2014],[Slater, 2005],[Zink, 2004]). Similarly, senescent cells such as fibroblasts are known to be swollen and their dry mass diluted [Neurohr, 2019], a feature suspected to be of fundamental biological importance since it could represent a determinant of stem cell potential during ageing [Lengefeld, 2021].

Paradoxically, there is still no unified understanding of these scaling laws and of the reasons of their breakdown in diseases. This is in part due to the experimental difficulty to perform accurate volume and dry mass measurements ([Model, 2018],[Cadart, 2017],[Burg, 2007],[Park, 2018]). Many methods were developed in the past decades but they sometimes lead to contradictory observations highlighting the need of comparing and benchmarking each method ([Guo, 2017],[Venkova, 2022]).

Moreover, extensive experimental investigations have identified a plethora of biological features influencing these scalings but comparatively fewer theoretical studies have precisely addressed them, leaving many experimental data unrelated and unexplained. Several phenomenological theories have emerged to understand individual observations, but they are still debated among biologists. The “nucleoskeletal theory” emphasizes the role of the DNA content in controling the NC ratio, based on the idea that ploidy dictates cell and nuclear sizes since tetraploid cells tend to be larger than their diploid homologs [Webster, 2009]. Other experiments suggest that genome size is not the only determining factor: indeed it would not explain why cells from different tissues, having the same amount of DNA, have different sizes. Instead, it has been shown that nuclear size depends on cytoplasmic content, nucleo-cytoplasmic transport, transcription, RNA processing and mechanics of nuclear envelope structural elements such as

lamina [Cantwell, 2019].

In parallel, theoretical models, based on non-equilibrium thermodynamics, were developed ([Kedem, 1958],[Mori, 2012],[Marbach, 2019]), often based on the “Pump-and-Leak" principle ([Cadart, 2019],[Venkova, 2022],[Adar, 2020]). Charged impermeant molecules in cells create an imbalance of osmotic pressure at the origin of the so-called Donnan effect [Sten-Knudsen, 2002]. Cells have two main ways to counteract the osmotic imbalance. They can adapt to sustain a high hydrostatic pressure difference as plants do by building cellulose walls. Or, as done by mammalian cells, they can use ion pumps to actively decrease the number of ions inside the cells, thus decreasing the osmotic pressure difference across the cell membrane and therefore impeding water penetration. However, due to the large number of parameters of these models, we still have a poor understanding of the correspondence between biological factors and physical parameters of the model.

In this paper, we bridge the gap between phenomenological and physical approaches by building a minimal framework based on a nested Pump-Leak model to understand the cell size scaling laws as well as their breakdown. Performing order of magnitude estimates, we precisely map the coarse-grained parameter of a simplified version of the Pump-Leak model to the main microscopic biological events. We find that the dry mass of the cell is dominated by the contribution of the proteins, while the cell volume is mostly fixed by the contribution to the osmotic pressure of small osmolytes, such as amino-acids and ions. The maintenance of a homeostatic cell density during growth is then due to a linear scaling relation between protein and small osmolyte numbers. Combining simplified models of gene transcription and translation and of amino-acid biosynthesis to the Pump-Leak model, we show that the linear scaling relation between protein and small osmolyte numbers is obtained in the exponential growth regime of the cell by virtue of the enzymatic control of amino-acid production.

On the other hand, the absence of linear scaling relation between protein and small osmolyte numbers is at the root of the breakdown of density homeostasis. We show that this is the case both at senescence and at mitotic entry due to two distinct physical phenomena. At senescence, cells cannot divide properly. Our theory then predicts that DNA and RNAs become saturated by RNA polymerases (RNAPs) and ribosomes respectively, leading to a change of the growth regime: the protein number saturates while the amino-acid number increases linearly with time, resulting in the experimentally observed dry mass dilution. This prediction is quantitatively tested using published data of growing yeast cells prevented from dividing [Neurohr, 2019]. At mitotic entry, chromatin rearrangements, such as histone tail modifications, induce a counterion release inside the cell, resulting in an influx of water and dry mass dilution in order to maintain the osmotic balance at the cell membrane.

Finally, to further illustrate the generality of our model, we show that the linear scaling of nucleus size with cell size originates from the same physical effects. Using a nested Pump-Leak model for the cell and the nucleus, we show that nuclear scaling requires osmotic balance at the nuclear envelope. The osmotic balance is explained by the nonlinear osmotic response of mammalian nuclei, that we attribute to the presence of folds at the surface of many nuclei [Lomakin, 2020], which in turn buffer the NE tension and enforce scaling. Nonetheless, the condition on osmotic balance appears to be insufficient to explain the robustness of the NC ratio during growth. Counter-intuitively, metabolites, though permeable to the NE, are predicted to play an essential role in the NC ratio. Their high concentrations in cells, a conserved feature throughout living cells, is shown to dilute the chromatin counterions which do not scale during growth; thereby allowing the scaling of nuclear size with cell size both at the population level and during individual cell growth.

2 Results

2.1 Pump and leak model.

Our theoretical approach to understand the various scaling laws associated to cell size is based on the Pump-Leak model ([Tosteson, 1960] and Figure1.1.A). The Pump-Leak model is a coarse grained model emphasizing the role of mechanical and osmotic balance. The osmotic balance involves two types of osmolytes, impermeant molecules such as proteins and metabolites, which cannot diffuse through the cell membrane, and ions, which cross the cell membrane and for which at steady state, the incoming flux into the cell must equal the outgoing flux. For simplicity, we restrict ourselves to a two-ions Pump-Leak model where only cations are pumped outward of the cell. We justify in the Discussion why this minimal choice is appropriate for the purpose of this paper. Within this framework, three fundamental equations determine the cell volume. (1) Electroneutrality: the laws of electrostatics ensure that in any aqueous solution such as the cytoplasm, the solution is neutral at length scales larger than the Debye screening length i.e. the electrostatic charge of any volume larger than the screening length vanishes. In physiological conditions, the screening length is typically on the nanometric scale. Therefore, the mean charge density of the cell vanishes in our coarse-grained description (Eq.S.42) (2) Osmotic balance: balance of the chemical potential of water inside and outside the cell; the timescale to reach the equilibrium of water is of the order of tens to hundreds of milliseconds after a perturbation [Venkova, 2022],[Rob Philipps, 2015]. (3) Balance of ionic fluxes: the typical timescales of ion relaxation observed during a cell regulatory volume response after an osmotic shock are of the order of a few minutes [Venkova, 2022], [Hoffmann, 2009]. Together, this means that our quasi-static theory is designed to study cell size variations on timescales larger than a few minutes. Mathematically, the three equations read (see Appendix 1 for the full derivations of these equations) :

$$n^+ - n^- - z \cdot x = 0 \tag{1.1}$$

$$\Delta P = \Delta\Pi = kT \cdot \left(n^+ + n^- + x - 2n_0\right) \tag{1.2}$$

$$n^+ \cdot n^- = \alpha_0 \cdot n_0^2 \quad \text{with,} \quad \alpha_0 = e^{-\frac{p}{k_B T g^+}} \tag{1.3}$$

where, n^+, n^-, n_0 are respectively the cationic and anionic concentrations inside and outside the cell. The external ionic concentrations are assumed to be identical for cations and anions in order to enforce electroneutrality since the concentrations of non-permeant molecules in the external medium are typically much lower than their ionic counterparts [Rob Philipps, 2015]. The cell is modelled as a compartment of total volume V divided between an excluded volume occupied by the dry mass R and a wet volume. The cell contains ions and impermeant molecules such as proteins, RNA, free amino-acids and other metabolites. The number X, respectively the concentration $x = \frac{X}{V-R}$, of these impermeant molecules may vary with time due to several complex biochemical processes such as transcription, translation, plasma membrane transport, and degradation pathways. The average negative charge $-z$ of these trapped molecules induces a Donnan potential difference U_c across the cell membrane. The Donnan equilibrium contributes to the creation of a positive difference of osmotic pressure $\Delta\Pi$ that inflates the cell. Cells have two main ways to counteract this inward water flux. They can either build a cortex stiff enough to prevent the associated volume increase, as done by plant cells. This results in the appearance of a hydrostatic pressure difference ΔP between the cell and the external medium. Or they can pump ions outside the cell to decrease the internal osmotic pressure, a strategy used by mammalian cells. We introduce a pumping flux of cations p. Cations can also passively diffuse through the plasma membrane via ion channels

with a conductivity g^+. In Eq.1.3, the pumping efficiency is measured by the dimensionless number $\alpha_0 = e^{-\frac{p}{k_B T g^+}}$ where T is the temperature and k_B the Boltzmann constant. The pumping efficiency varies between 0 in the limit of "infinite pumping" and 1 when no pumping occurs (see Appendix 1 for an explanation on the origin of this parameter).

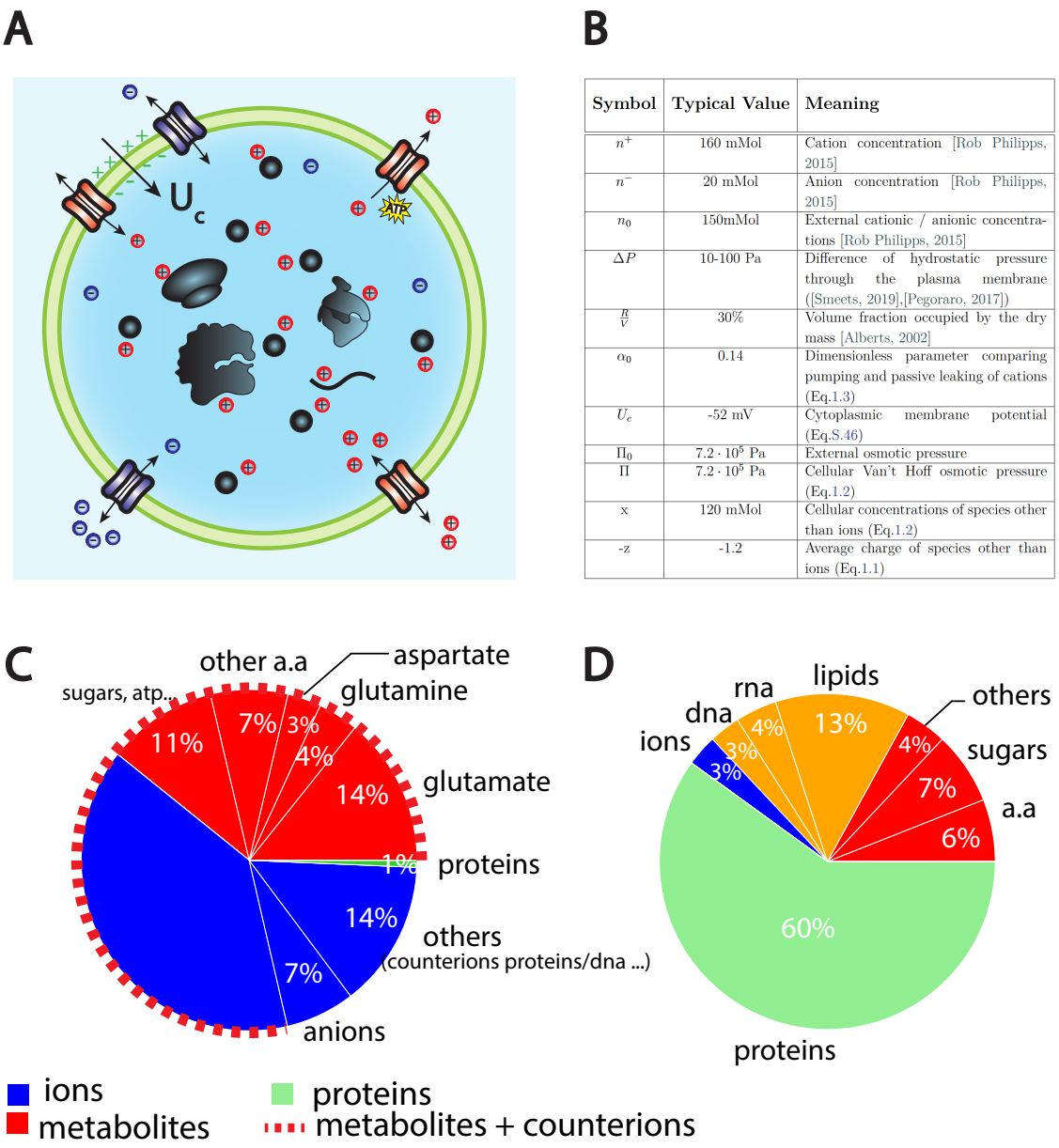

Symbol	Typical Value	Meaning
n^+	160 mMol	Cation concentration [Rob Philipps, 2015]
n^-	20 mMol	Anion concentration [Rob Philipps, 2015]
n_0	150mMol	External cationic / anionic concentrations [Rob Philipps, 2015]
ΔP	10-100 Pa	Difference of hydrostatic pressure through the plasma membrane ([Smeets, 2019],[Pegoraro, 2017])
$\frac{R}{V}$	30%	Volume fraction occupied by the dry mass [Alberts, 2002]
α_0	0.14	Dimensionless parameter comparing pumping and passive leaking of cations (Eq.1.3)
U_c	-52 mV	Cytoplasmic membrane potential (Eq.S.46)
Π_0	$7.2 \cdot 10^5$ Pa	External osmotic pressure
Π	$7.2 \cdot 10^5$ Pa	Cellular Van't Hoff osmotic pressure (Eq.1.2)
x	120 mMol	Cellular concentrations of species other than ions (Eq.1.2)
-z	-1.2	Average charge of species other than ions (Eq.1.1)

Figure 1.1: **The Pump-Leak model.** (A) Schematic of the Pump-Leak model. Species in black are impermeant molecules such as proteins, mRNAs and metabolites (black circles). In average, those molecules are negatively charged and thus carry positive counterions (red species) to ensure electroneutrality. Ions can freely cross the plasma membrane through channels. Their concentrations in the cell result from the balance of three fluxes: the electrical conduction, the entropic diffusion, and pumping. In the model, only cations are pumped out of the cell to model the Na/K pump but this assumption is not critical (see Discussion 3.3 and Appendix 2.3) (B) Estimation of the coarse grained Pump-Leak model parameters for a typical Mammalian cell. (C) Fraction of volume and (D) of the dry mass occupied by the constituents of a mammalian cell (see Appendix 3 and [Alberts, 2002]). Note that most of the number of impermeant molecules (X) are accounted for by metabolites (mainly amino-acids and glutamate).

2.2 Volume and dry mass scaling

Although proposed more than 60 years ago [Tosteson, 1960] and studied in depth by mathematicians [Mori, 2012], and physicists [Kay, 2017], little effort has been done to precisely map the coarse-grained parameters of the Pump-Leak model to microscopic parameters. We adopt here the complementary strategy and calculate orders of magnitude in order to simplify the model as much as possible, only keeping the leading order terms. We summarize in Figure.1.1.B the values of the Pump-Leak model parameters that we estimated for a "typical" mammalian cell. Three main conclusions can be drawn: (1) Pumping is important, as indicated by the low value of the pumping efficiency $\alpha_0 \sim 0.14$. Analytical solutions presented in the main text will thus be given in the "infinite pumping" limit, i.e., $\alpha_0 \sim 0$, corresponding to the scenario where the only ions present in the cell are the counterions of the impermeant molecules. Though not strictly correct, this approximation gives a reasonable error of the order 10% on the determination of the volume, due to the typical small concentration of free anions in cells Fig.1.1.B. This error is comparable to the typical volumetric measurement errors found in the literature. (2) Osmotic pressure is balanced at the plasma membrane of a mammalian cell, since hydrostatic and osmotic pressures differ by at least three orders of magnitude. This result implies that even though the pressure difference ΔP plays a significant role in shaping the cell, it plays a negligible role in fixing the volume (see Eq.S.53 for justification). (3) The cellular density of impermeant species is high, $x \sim 120$mMol, comparable with the external ionic density n_0.
In this limit, the volume of the cell hence reads (the complete expression is given in Appendix 2) :

$$V = R + \frac{(z+1)\cdot X}{2n_0} \tag{1.4}$$

The wet volume of the cell is thus slaved to the number of impermeant molecules that the cell contains. While this conclusion is widely acknowledged, the question is to precisely decipher which molecules are accounted for by the number X. We first estimate the relative contributions of the cellular free osmolytes to the volume of the cell and then, compute their relative contributions to the dry mass of the cell. We provide a graphical summary of our orders of magnitudes in Fig.1.1.C and D as well as the full detail of their derivations in Appendix.3. The conclusion is twofold. Metabolites and their counterions account for most of the wet volume of the cell, 78% of the wet volume against 1% for proteins. On the other hand, proteins account for most of the dry mass of mammalian cells, accounting for 60% of the cellular dry mass against 17% for metabolites.

We further note that metabolites are mainly amino-acids and in particular three of them, glutamate, glutamine and aspartate accounting for 73% of the metabolites [Park, 2016]. It is important to note that the relative proportion of free amino-acids in the cell does not follow their relative proportion in the composition of proteins. For instance, glutamate represents 50% of the free amino-acid pool while its relative appearance in proteins is only 6% [King, 1969]. This is evidence that some amino-acids have other roles than building up proteins. In particular, we demonstrate throughout this paper their crucial role on cell size and its related scaling laws.

These conclusions may appear surprising due to the broadly reported linear scaling between volume (metabolites) and dry mass (proteins), hence enforcing a constant dry mass density ρ during growth. Many theoretical papers have assumed a priori a linear phenomenological relation between volume and protein number in order to study cell size [Lin, 2018],[Wu, 2022],[Lemière, 2022]. Our results instead emphasize that the proportionality is indirect, only arising from the scaling between amino-acid and

protein numbers. The dry mass density reads (to lowest order):

$$\rho = \frac{M}{V} \approx \frac{\mathcal{M}_A \cdot l_p \cdot P_{tot}}{v_p \cdot P_{tot} + \frac{(z_{Af}+1)\cdot A^f}{2n_0}} \tag{1.5}$$

where, $\mathcal{M}_a$, z_{Af} and A^f are respectively the average mass, charge and number of amino-acids; l_p, v_p and P_{tot}, the average length, excluded volume and number of proteins. Note that density homeostasis is naturally achieved in the growth regime where A^f is proportional to P_{tot}.

2.3 Model of gene expression and translation

To further understand the link between amino-acid and protein numbers we build upon a recent model of stochastic gene expression and translation ([Lin, 2018] and Fig.1.2.A). The key feature of this model is that it considers different regimes of mRNA production rate $\dot{M}_j$ and protein production rate $\dot{P}_j$ according to the state of saturation of respectively the DNA by RNA polymerases (RNAPs) and mRNAs by ribosomes. For the sake of readability, we call enzymes both ribosomes and RNAPs, their substrates are respectively mRNAs and DNA and their products proteins and mRNAs. The scenario of the model is the following. Initially, the majority of enzymes are bound to their substrates and occupy a small fraction of all possible substrate sites. In this non saturated regime, i.e when the number of enzymes is smaller than a threshold value P_p^* and P_r^* Eq.S.75, the production rates of the products of type j read [Lin, 2018]:

$$\dot{M}_j = k_0 \cdot \phi_j \cdot P_p - \frac{M_j}{\tau_m}, \qquad if \quad P_p \leq P_p^* \tag{1.6}$$

$$\dot{P}_j = k_t \cdot \frac{M_j}{\sum M_j} \cdot P_r - \frac{P_j}{\tau_p}, \qquad if \quad P_r \leq P_r^* \tag{1.7}$$

Both production rates have two contributions. (1) a source term characterized by the rates k_0 and k_t at which the enzyme produces the product once it is bound to its substrate, times the average number of enzymes per substrate coding for the product of type j. This number is the fraction of substrates coding for product of type j - that can be identified as a probability of attachment ($\phi_j = \frac{g_j}{\sum g_j}$ and $\frac{M_j}{\sum M_j}$, where g_j, M_j accounts for the number of genes and mRNAs coding for the product of type j) - multiplied by the total number of enzymes (P_p and P_r). (2) A degradation term characterized by the average degradation times τ_m and τ_p of mRNAs and proteins. Note that we added a degradation term for proteins not present in [Lin, 2018], which turns out to be of fundamental importance below. Although these timescales vary significantly between species their ratio remains constant, τ_m being at least one order of magnitude smaller than τ_p in yeast, bacteria and mammalian cells [Rob Philipps, 2015]. This justifies a quasistatic approximation, $\dot{M}_j \sim 0$ during growth such that the number of mRNAs of type j adjusts instantaneously to the number of RNAPs, in the non saturated regime :

$$M_j = k_0 \cdot \tau_m \cdot \phi_j \cdot P_p \tag{1.8}$$

During interphase, the number of enzymes grows, increasingly more enzymes attach to the substrates up to the saturation value due to their finite size. In this regime, we use the same functional form for the production rates only replacing the average number of enzymes per substrate by their saturating values : $g_j \cdot \mathcal{N}_p^{max}$ for RNAPs and $M_j \cdot \mathcal{N}_r^{max}$ for ribosomes (see Appendix 4 and Eq.S.73,S.74); where, $\mathcal{N}_p^{max}$ and $\mathcal{N}_r^{max}$ are the average maximal number of RNAPs and ribosomes per mRNAs and genes. Note that the model predicts that the saturation of DNA precedes that of mRNAs, whose number initially increases with the number of RNAPs Eq.1.8 while the number of genes remains constant. We also highlight that

a more general gene expression model was recently proposed [Wang, 2021], in which the saturation of DNA by RNAPs is due to a high free RNAP concentration near the promoter. Yet, we do not expect the exact saturation mechanism to change our conclusions. Once DNA is saturated, the number of mRNAs plateaus, leading to their saturation by ribosomes (see Appendix 4 and Eq.S.79).

Our previous analysis has highlighted the fundamental importance of free amino-acids on cell volume regulation Fig.1.1.C. The production rate of free amino-acids can be related to the number of enzymes catalyzing their biosynthesis, using a linear process by assuming that the nutrients necessary for the synthesis are in excess:

$$\dot{A}^f = k_{cat} \cdot P_e - l_p \cdot \dot{P}_{tot} \tag{1.9}$$

where k_{cat} is the rate of catalysis and P_e the number of enzymes. The second term represent the consumption of amino-acids to form proteins, with $P_{tot} = \sum P_j$. Although Eq.1.9 is coarse-grained we highlight that, since glutamate and glutamine are the most abundant amino acids in the cell, it could in particular model the production of these specific amino-acids from the Krebs cycle [Alberts, 2002]. Note that we also ignored amino-acid transport through the plasma membrane. The rationale behind this choice is twofold. (1) We do not expect any qualitative change when adding this pathway to our model since amino-acid transport is also controlled by proteins. (2) We realized that the amino-acids that actually play a role in controlling the volume, mainly glutamate, glutamine and aspartate, are non-essential amino-acids, hence that can be produced by the cell.

2.4 Dry mass scaling and dilution during cell growth

We now combine the Pump-Leak model, the growth model and the amino-acid biosynthesis model to make predictions on the variation of the dry mass density during interphase. A crucial prediction of the growth model is that as long as mRNAs are not saturated, i.e., $P_r < P_r^*$, all the protein numbers scale with the number of ribosomes, $P_j \sim \frac{\phi_j}{\phi_r} \cdot P_r$. Moreover, the autocatalytic nature of ribosome formation makes their number grow exponentially Eq.1.7, i.e $P_r = P_{r,0} \cdot e^{k_r \cdot t}$; where, $k_r = k_t \cdot \phi_r - \frac{1}{\tau_p}$ is the effective rate of ribosome formation (and also the rate of volume growth in this regime Eq.S.77). The most important consequence of this exponential growth coupled to the equation modeling amino-acid biosynthesis Eq.1.9 is that it implies that both amino-acids and total protein content scale with the number of ribosomes ultimately leading to a homeostatic dry mass density independent of time (see Appendix 4):

$$\rho^H = \frac{\mathcal{M}_a}{\frac{v_p}{l_p} + \frac{(z_{Af}+1)}{2n_0} \cdot \left(\frac{\phi_e}{l_p} \cdot \frac{k_{cat}}{k_r} - 1 \right)} \tag{1.10}$$

We emphasize that Eq.1.10 only applies far from its singularity since it was obtained assuming that the volume of the cell is determined by free amino-acids, i.e, $\frac{\phi_e}{l_p} \cdot \frac{k_{cat}}{k_r} >> 1$.

Not only does our model explain the homeostasis of the dry mass, but it also makes the salient prediction that this homeostasis naturally breaks down if the time spent in the G1 phase is too long. Indeed, after a time $t^{**} = \frac{1}{kr} \cdot ln \left(\frac{\mathcal{N}_r^{max} \cdot \mathcal{N}_p^{max} \cdot k_0 \cdot \tau_m \cdot \sum g_j}{P_{r,0}} \right)$ (see Appendix4), mRNAs become saturated by ribosomes, drastically changing the growth of proteins from an exponential growth to a plateau regime where the number of proteins remains constant. After the time $t^{**} + \tau_p$, all protein numbers reach their stationary values $P_j^{stat} = k_t k_0 \tau_p \tau_m \mathcal{N}_R^{max} \mathcal{N}_p^{max} g_j$. In particular, the enzymes coding for amino-acids also plateau implying the loss of the scaling between free amino-acids and proteins as predicted by Eq.1.9. The number of amino-acids then increases linearly with time whereas the number of proteins saturates. In this regime, the volume thus grows linearly with time but the dry mass remains constant leading to its dilution and the decrease of the dry mass density (see Appendix 4 and Eq.S.83) :

$$\rho^{lin}(t) = \frac{\mathcal{M}_a}{\frac{v_p}{l_p} + \frac{(z_{Af}+1)}{2n_0} \cdot \left(\frac{\phi_e \cdot k_{cat}}{\phi_r \cdot k_r \cdot k_t \cdot l_p \cdot \tau_p} - 1 + \frac{k_{cat} \cdot \phi_e}{l_p} \cdot t \right)} \tag{1.11}$$

Finally, our model makes other important predictions related to the cell ploidy that we briefly enumerate. First, the cut-off P_r^* Eq.S.79 at which dilution is predicted to occur depends linearly on the genome copy number $\sum g_j$. Intuitively, mRNAs are saturated only if DNA has previously saturated. At saturation the RNA number is proportional to the genome size. As a consequence, the volume $V^* \propto P_r^*$ at which dilution occurs scales with the ploidy of the cell, a tetraploid cell is predicted to be diluted at twice the volume of its haploid homolog. On the other hand, by virtue of the exponential growth, the time t^{**} Eq.S.80 at which the saturation occurs only depends logarithmically on the number of gene copies making the ploidy dependence much less pronounced timewise. Second, the growth rate in the linear regime scales with the ploidy of the cell, as opposed to the growth rate in the exponential regime. Indeed, in the saturated regime, the growth rate scales as $k_{cat} \cdot P_e^{stat}$ (see Appendix 4 and Eq.S.81), where P_e^{stat} is the number of enzymes catalyzing the reaction of amino-acids biosynthesis after their numbers have reached their stationary values, while in the exponential regime, the growth rate $k_r = \phi_r \cdot k_t - \frac{1}{\tau_p}$ scales with the fraction of genes coding for ribosomes ϕ_r, which is independent of the ploidy.

2.5 Comparison to existing data

Our main prediction, namely that the cell is diluted after the end of the exponential growth, is reminiscent of the intracellular dilution at senescence recently reported in fibroblasts, yeast cells and more recently suspected in aged hematopoietic stem cells [Neurohr, 2019],[Lengefeld, 2021]. Here we quantitatively confront our theory to the data of [Neurohr, 2019], where the volume, the dry mass and the protein number were recorded during the growth of yeast cells that were prevented from both dividing and replicating their genome. Though our theory was originally designed for mammalian cells, it can easily be translated to cells with a cell wall provided that the hydrostatic pressure difference across the wall ΔP is maintained during growth by progressive incorporation of cell wall components (see Appendix 2). Indeed, our conclusions rely on the fact that the cell volume is primarily controlled by small osmolytes whose concentration in the cell dominates the osmotic pressure, a feature observed to be valid across cell types [Park, 2016].

We first check the qualitative agreement between our predictions and the experiments. Two clear and very distinct growth regimes are evident in non-dividing yeast cells; an initial exponential growth followed by a linear growth Fig.1.2.C. The occurrence of linear or exponential growth has been the object of intense debate. We think that the ambiguity comes from the fact that cells often divide too fast for the exponential regime to be properly identified. Our results suggest that the fact that cell division occurs in the exponential regime is essential to prevent cells from being diluted. Our theory also predicts that as long as protein number is constant the volume must grow linearly Eq.1.9,S.83. This is precisely what is observed in the experiments: cells treated with rapamycin exhibits both a constant protein content and a linear volume increase during the whole growth (see Fig.S6.F in [Neurohr, 2019]). Finally, our predictions on the relationship between ploidy and dilution are in very good agreement with experiments as well. Indeed, while the typical time to reach the linear growth regime - of the order of 3 hours - seems independent of the ploidy of the cell, the volume at which dilution occurs is doubled (see Fig.S7.A in [Neurohr, 2019]). Moreover, the growth rate during the linear regime scales with ploidy, as the haploid cells growth rate is of order 129 fL/h against 270 fL/h for their diploid counterparts [Neurohr, 2019].

Encouraged by these qualitative correlations, we further designed a scheme to test our theory more quantitatively. Although our theory has a number of adjustable parameters, many of them can be combined or determined self-consistently as shown in Appendix 4.4). We end up fitting four parameters,

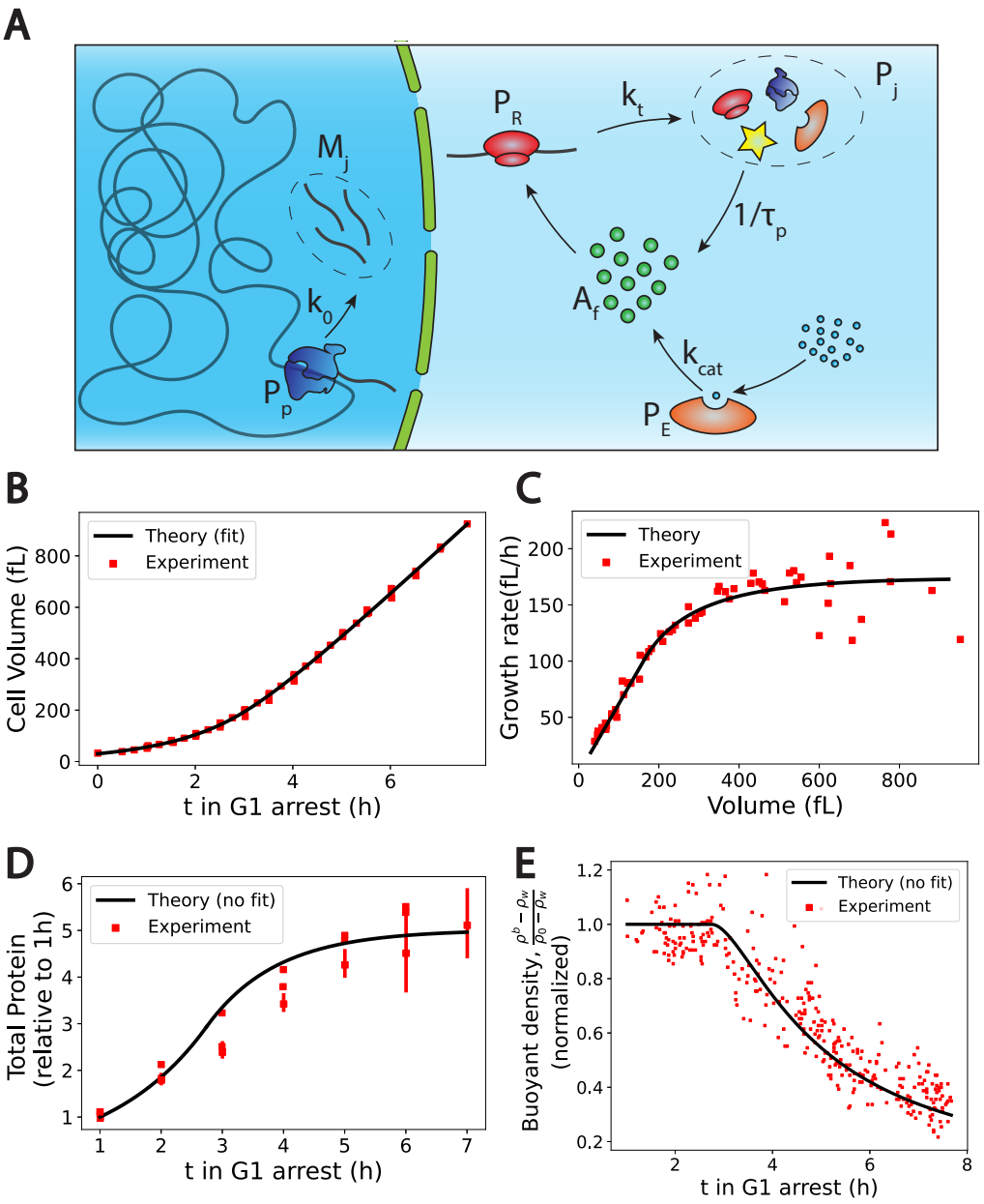

Figure 1.2: **The Pump-Leak model coupled to a growth model predicts quantitatively dry mass homeostasis and its subsequent dilution at senescence.** (A) Schematic of the growth model. RNAPs (P_p) transcribe DNA and form mRNAs (M_j) at an average rate k_0. mRNAs are then read by ribosomes (P_r) to produce proteins (P_j) at an average rate k_t. Proteins are degraded at an average rate $\frac{1}{\tau_p}$ into free amino-acids (A_f). Free amino-acids are also synthetized from nutrients (blue circles) at a rate k_{cat}. This reaction is catalyzed by enzymes (P_e). (B) to (E) Comparison between theory (black) and experiment (red). Data adapted from [Neurohr, 2019]. (D) and (E) model predictions without any fitting parameters. The buoyant mass ρ_b density is defined as the total mass of the cell (water and dry mass) over the total volume of the cell.

namely τ_p, t^{**}, k_r and the initial cell volume v_1, using the cell volume data Fig.1.2.B. We detail in the Appendix 4.5 the fitting procedure and the values of the optimal parameters. Interestingly, we find a protein degradation time $\tau_p = 1\text{h}9\text{min}$, corresponding to an average protein half-life time: $\tau_{1/2} \sim 48\text{min}$ which is very close to the value 43min, measured in [Belle, 2006].
Moreover, we obtain a saturation time $t^{**} = 2h44\text{min}$ which remarkably corresponds to the time at which the dry mass density starts to be diluted Fig.1.2.E, thus confirming the most critical prediction of our model. We can then test our predictions on the two other independent datasets at our disposal, i.e., the dry mass density, obtained from suspended microchannel resonator (SMR) experiments, and the normalized protein number, from fluorescent intensity measurements. We emphasize that the subsequent comparisons with experiments are done without any adjustable parameters. The agreement between theory and experiment is striking Fig.1.2.D,E, and gives credit to our model. We underline that the value of the density of water that we used is 4 % higher than the expected value, $\rho_w = 1.04\,\text{kg/L}$ to plot Fig.1.2.E. This slight difference originates from the fact that our simplified theory assumes that the dry mass is entirely due to proteins whereas proteins represent only 60% of the dry mass. This hypothesis is equivalent to renormalizing the density of water as shown in Appendix 4.4.

In summary, our theoretical framework combining the Pump-Leak model with a growth model and a model of amino-acid biosynthesis provides a consistent quantitative description of the dry mass density homeostasis and its subsequent dilution at senescence without invoking any genetic response of the cell; the dilution is due to the physical crowding of mRNAs by ribosomes. It also solves a seemingly apparent paradox stating that the volume is proportional to the number of proteins although their concentrations are low in the cell without invoking any non-linear term in the osmotic pressure (see Discussion and Appendix 3.12).

2.6 Mitotic swelling

Our previous results explain well the origin of the dilution of the cellular dry mass at senescence. But can the same framework be used to understand the systematic dry mass dilution experienced by mammalian cells at mitotic entry ? Although this so called mitotic swelling or mitotic overshoot is believed to play a key role in the change of the physio-chemical properties of mitotic cells, its origin remains unclear [Son, 2015],[Zlotek-Zlotkiewicz, 2015].

We first highlight five defining features of the mitotic overshoot. (1) It originates from an influx of water happening between prophase and metaphase, resulting in a typical 10% volume increase of the cells. (2) The swelling is reversible and cells shrink back to their initial volume between anaphase and telophase. (3) This phenomenon appears to be universal to mammalian cells, larger cells displaying larger swellings. (4) Cortical actin was shown not to be involved in the process, discarding a possible involvement of the mechanosensitivity of ion channels, contrary to the density increase observed during cell spreading [Venkova, 2022] (5) Nuclear envelope breakdown (NEB) alone cannot explain the mitotic overshoot since most of the swelling is observed before the prometaphase where NEB occurs [Son, 2015],[Zlotek-Zlotkiewicz, 2015].

The dry mass dilution at mitotic overshoot is thus different from the cases studied in the previous section. First, it happens during mitosis when the dry mass is constant [Zlotek-Zlotkiewicz, 2015]. Second, the 10% volume increase implies that we need to improve the simplified model used above, which considers only metabolites and proteins (and their counterions). Having in mind that ions play a key role in the determination of the cell volume Fig.1.1C, we show how every feature of the mitotic overshoot can be qualitatively explained by our theory, based on a well-known electrostatic property of charged polymer called counterion condensation first studied by Manning [Manning, 1969]. Many counterions are strongly bound to charged polymers (such as chromatin) because the electrostatic potential at their

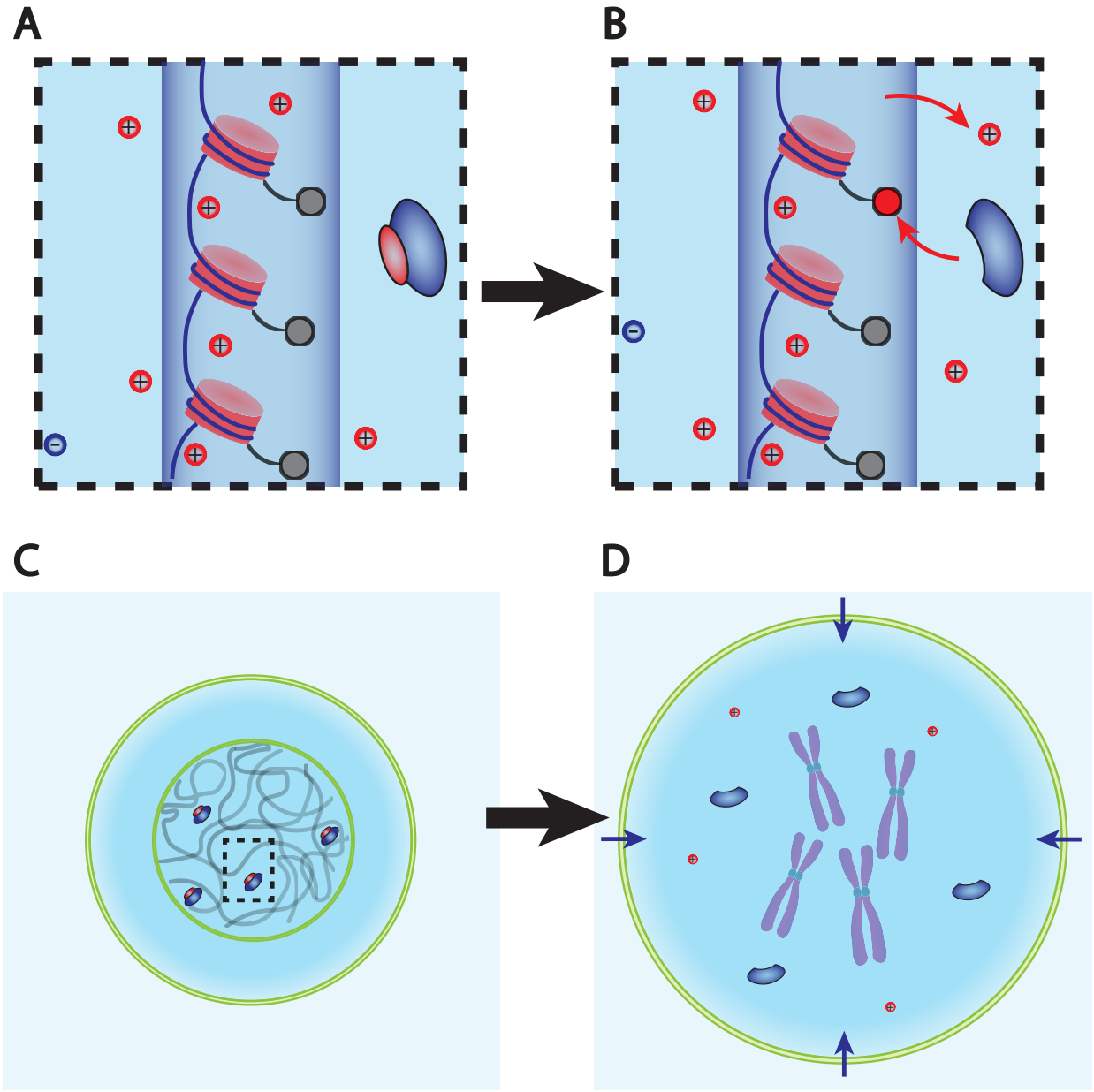

Figure 1.3: **Dry mass dilution at mitosis is explained with the Pump-Leak model by the decondensation of chromatin counterions following histone tail modifications.** (A) and (B) Microscopic working model. An enzyme gives its positive charge to a histone, resulting in the release of a condensed counterion. Ions depicted within the chromatin (dark blue cylinder) are condensed and those outside are freely diffusing and participate in the nuclear osmotic pressure. (C) and (D) The subsequent increase in the number of osmolytes lead to a water influx in order to sustain osmotic balance at the plasma membrane of mammalian cells. For readability, other osmolytes are not displayed.

surface creates an attractive energy for the counterions much larger than the thermal energy k_BT. The condensed counterions partially neutralize the charge of the object and reduce the electrostatic potential. Condensation occurs up to the point where the attractive energy for the free counterions is of the order k_BT.
The condensed counterions then do not contribute to the osmotic pressure given by Eq.1.2 which determines the cell volume. These condensed counterions act as an effective "internal" reservoir of osmolytes. A release of condensed counterions increases the number of free cellular osmolytes and thus the osmotic pressure inside the cell. Therefore, it would lead to an influx of water in order to restore osmotic balance at the plasma membrane Fig.1.3.

But how to explain such a counterion release at mitotic overshoot? For linear polymers such as DNA, the condensation only depends on a single Manning parameter $u = \frac{l_b}{A}$; where, l_b is the Bjerrum length Tab.S1 which measures the strength of the coulombic interaction and A the average distance between two charges along the polymer. The crucial feature of Manning condensation is the increase of the distance between charges A by condensing counterions and thus effectively decreasing u down to its critical value equal to 1 (see Appendix 5 for a more precise derivation). Hence, the number of elementary charges carried by a polymer of length L_{tot} is $Q_{tot} = \frac{L_{tot}}{A}$ before condensation. After condensation, the effective distance between charges increases to $A^{eff} = A \cdot u$ such that the effective number of charges on the polymer is reduced to $Q^{eff} = \frac{Q_{tot}}{u}$. The number of counterions condensed on the polymer is $Q^{cond} = Q_{tot} \cdot (1 - \frac{1}{u})$. The most important consequence of these equations is that they suggest that a structural modification of the chromatin could lead to a counterion release. Indeed, making the chromatin less negatively charged, i.e., increasing A, is predicted to decrease u and thus to lead to the decrease of Q^{cond}. Detailed numerical simulations of chromatin electrostatics show that this description is qualitatively correct [Materese, 2009].

Biologists have shown that chromatin undergoes large conformational changes at mitotic entry. One of them attracted our attention in light of the mechanism that we propose. It is widely accepted that the affinity between DNA and histones is enhanced during chromatin compaction by stronger electrostatic interactions thanks to specific covalent modifications of histone tails by enzymes. Some of these modifications such as the deacetylation of lysines add a positive charge to the histone tails, hence making the chromatin less negatively charged [Alberts, 2002]. Moreover, histone tails are massively deacetylated during chromatin compaction [Zhiteneva, 2017], potentially meaning that this specific reaction plays an important role in counterion release and thus on the observed mitotic swelling. However, we underline that the idea that we propose is much more general and that any reaction modifying chromatin electrostatics is expected to impact the swelling. The question whether deacetylation of lysines is the dominant effect is left open here.

Is the proposed mechanism sufficient to explain the observed 10% volume increase? We estimate the effective charge of chromatin for a diploid mammalian cell to be $Q^{eff} = 2 \cdot 10^9\,\mathrm{e}^-$ and the number of condensed monovalent counterions to be $Q^{cond} = 8 \cdot 10^9$ (see Appendix 3). The Pump-Leak model framework predicts the subsequent volume increase induced by the hypothetical release of all the condensed counterions of the chromatin. We find an increase of order $\Delta V \sim 100 - 150 \mu\mathrm{m}^3$ which typically represents 10% of a mammalian cell size (see Appendix 3 and Eq.S.67). Admittedly crude, this estimate suggest that chromatin counterion release can indeed explain the amplitude of mitotic swelling.

In summary, the combination of the Pump-Leak model framework with a well-known polymer physics phenomenon allows us to closely recapitulate the features displayed during mitotic swelling. In brief, the decondensation of the chromatin condensed counterions, hypothetically due to histone tail modifications, is sufficient to induce a 10% swelling. This implies that, all mammalian cells swell during prophase and shrink during chromatin decondensation after anaphase; again, consistent with the dynamics of the mitotic overshoot observed on many cell types. Another salient implication is that the amplitude of the swelling is positively correlated with the genome content of the cells: cells having more chromatin are also

expected to possess a larger "internal reservoir" of osmolytes, which can participate in decondensation. This provides a natural explanation for the observed larger swelling of larger cells. For instance, Hela cells were shown to swell on average by 20%, in agreement with the fact that many of them are tetraploid. Admittedly, many other parameters enter into account and may disrupt this correlation such as the degree of histone tail modifications or the initial state of chromatin; The existence of a larger osmolyte reservoir does not necessarily mean that more ions are released.

Finally, we point out that the ideas detailed in this section can be tested experimentally using existing in vivo or in vitro methods. For example, we propose to massively deacetylate lysines during interphase, by either inhibiting lysine acetyltransferases (KATs) or overexpressing lysine deacetylases (HDACS), in order to simulate the mitotic swelling outside mitosis. We also suggest to induce mitotic slippage or cytokinesis failure for several cell cycles, to increase the genome content, while recording the amplitude of swelling at each entry in mitosis [Gemble, 2022].

2.7 Nuclear scaling

Another widely documented scaling law related to cell volume states that the volume of cell organelles is proportional to cell volume ([Chan, 2010],[Cantwell, 2019]). As an example, we discuss here the nuclear volume. We develop a generalised "nested" Pump-Leak model that explicitly accounts for the nuclear and plasma membranes (see Fig.1.4.A). Instead of writing one set of equation (Eq.1.1,1.2,1.3) between the interior and the exterior of the cell, we write the same equations both inside the cytoplasm and inside the nucleus (see Eq.S.93). Before solving this nonlinear system of equations using combined numerical and analytical approaches, we draw general conclusions imposed by their structure. As a thought experiment, we first discuss the regime where the nuclear envelope is not under tension so that the pressure jump at the nuclear envelope ΔP_n is much smaller than the osmotic pressure inside the cell $\Delta P_n << \Pi_0$. The osmotic balance in each compartment implies that the two volumes have the same functional form as in the Pump-Leak model, with two contributions: an excluded volume due to dry mass and a wet volume equal to the total number of particles inside the compartment divided by the external ion concentration (see Eq.S.94). It is noteworthy that the total cell volume, the sum of the nuclear and cytoplasmic volumes, is still given by Eq.1.4 as derived in the simple Pump-Leak model. This result highlights the fact that the Pump-Leak model strictly applies in the specific condition where the nuclear envelope is under weak tension. In addition, a crucial consequence of the osmotic balance condition at the NE is that it leads to a linear scaling relation between the volumes of the two compartments:

$$V_n = \frac{N_n^{tot}}{N_c^{tot}} \cdot V_c + \left(R_n - \frac{N_n^{tot}}{N_c^{tot}} \cdot R_c \right) \tag{1.12}$$

where V_i, R_i and N_i^{tot} denote, respectively, the total volume, the dry volume and the total number of osmolytes of compartment i, the index $i = n, c$ denoting either the nucleus n, or the cytoplasm c. Importantly, this linear scaling between the nucleus and the cytoplasm was reported repeatedly over the last century and is known as nuclear scaling [Webster, 2009], [Cantwell, 2019]. While this conclusion is emphasized in some recent papers [Lemière, 2022], [Deviri, 2022], we point out that Eq.1.12 is only a partial explanation of the nuclear scaling. Indeed, we still need to understand what cellular and nuclear properties makes the ratio $\frac{N_n^{tot}}{N_c^{tot}}$ insensitive to external perturbations or to growth.

2.8 NC ratio in the low tension regime

We now examine the influence of the various cell osmolytes on the NC ratio. For the sake of readability, we assume that the volume fraction occupied by the dry mass is the same in the nucleus and the cytoplasm (see Appendix 6.1). The NC ratio is then the ratio between the wet volumes. Following the lines of our

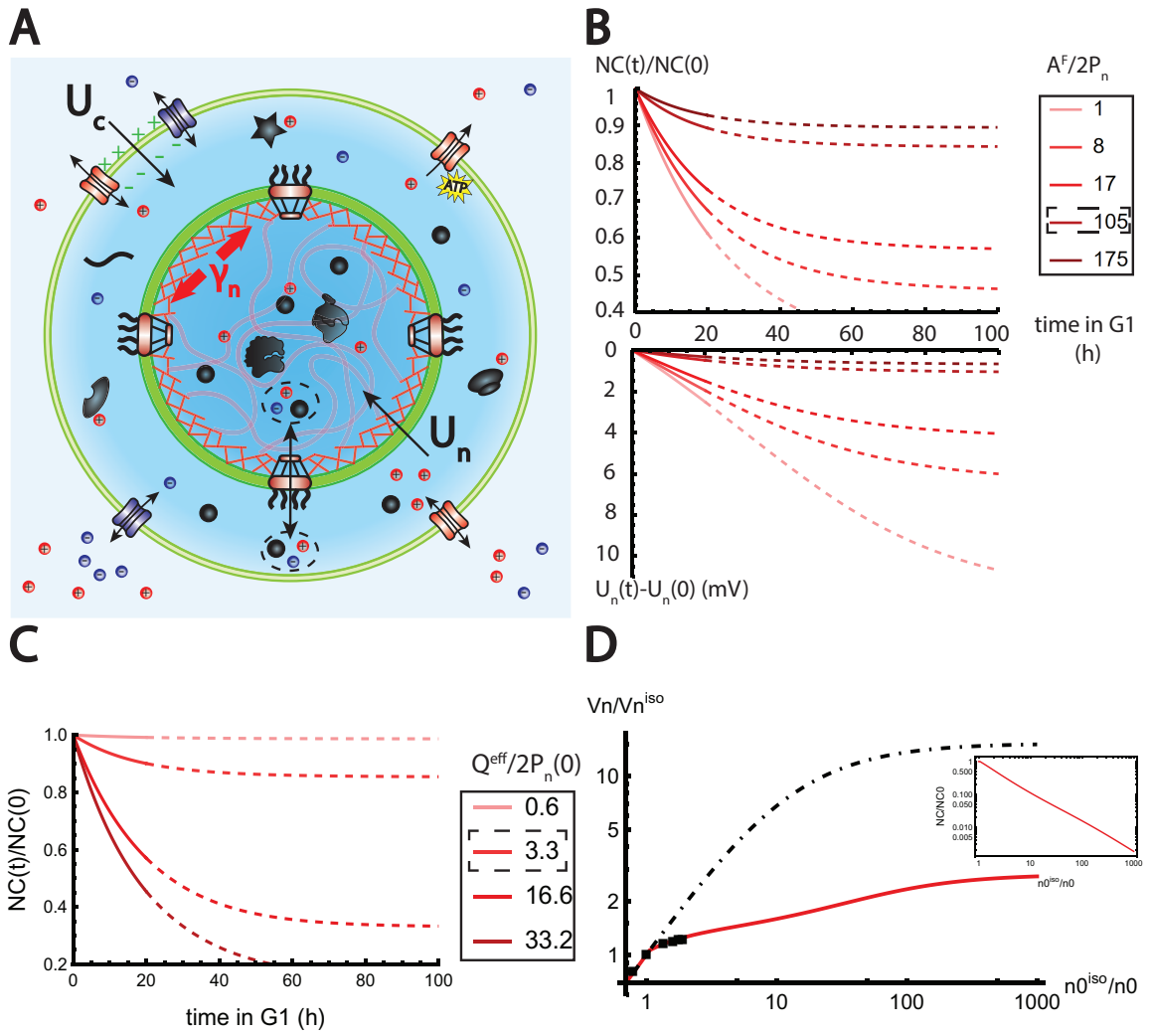

Figure 1.4: **The nested Pump-Leak model explains nuclear scaling.**(A) Schematic of the nested Pump-Leak model. Species in black are impermeant molecules (X) and are now partitioned between the cytoplasm and the nucleus. Among those, only metabolites (black circles) can cross the NE. The NE is composed of the membrane (green) and the lamina (red) can be stretched when the nuclear folds are flattened. (B) and (C) Simulations of the nested Pump-Leak model Eq.S.93 during growth when the osmotic pressure is balanced at the NE. The growth rate was adjusted to data in [Zlotek-Zlotkiewicz, 2015] (B) Though permeable to the NE, Metabolites play a role in the homeostasis of the NC ratio by diluting chromatin (free) counterions which do not scale during growth (top plot). Higher variations of the NC ratio correlate with higher variations of the NE potential (bottom plot). (C) Variations of the NC ratio during growth for different chromatin charges. (D) Normalized nuclear volume after a hypo-osmotic shock. Nuclear volume saturates because of the tension at the NE, leading to the decrease of the NC ratio (inset: log-log plot). The dash-dotted line represents the nuclear volume if the number of osmolytes in the nucleus were assumed constant throughout the shock. Thus, showing that Metabolites leave the nucleus during the shock which strongly decreases nucleus swelling. The value at the saturations are given by Eq.1.17. The square black dots are data extracted from [Finan, 2009]. We used K = 50mN/m [a] and $s = 4\%$ folds to fit the data. Additional results of the nested Pump-Leak model are plotted in the supplementary figure: Fig.S1

[a]The value of K used to fit the data [Finan, 2009] is twice the measured value in [Dahl, 2004]. The rationale is threefold. (1) Nuclei used in [Finan, 2009] are chondrocite nuclei originating from articular cartilage. They possess a high Lamina A to Lamina B ratio and are thus likely to be stiffer [Swift, 2013] (2) We could lower the value of the fitted K by increasing the pumping efficiency α_0. A more detailed caracterisation of the Pump-Leak model parameters for chondrocites would be required to precisely infer the elastic properties of the NE. (3) Considering the chromatin mechanical contribution would increase K by a factor $E_{DNA} \cdot R_{nucleus}$; with E_{DNA} the elastic modulus of the chromatin and $R_{nucleus}$ the radius of the nucleus.

previous discussion, four different components play a role in volume regulation: chromatin (indirectly through its non-condensed counterions), proteins (mainly contributing to the dry volume), metabolites and ions (mainly contributing to the wet volume). These components do not play symmetric roles in the determination of the NC ratio. This originates from the fact that metabolites are permeable to the nuclear membrane and that chromatin, considered here as a gel, does not contribute directly to the ideal gas osmotic pressure because its translational entropy is vanishingly small [Gennes, 1979]. The nested Pump-Leak model leads to highly nonlinear equations that cannot be solved analytically in the general case (see Eq.S.93). Nevertheless, in the particular regime of monovalent osmolytes and high pumping $z_a = 1$, $z_p = 1$ and $\alpha_0 = 0$ corresponding to the case where there is no free anions in the cell, the equations simplify and are amenable to analytical results. This regime is physically relevant since it corresponds to values of the parameters close to the ones that we estimated (Fig.1.1). For clarity, we first restrict our discussion to this particular limit. We will also discuss both qualitatively and numerically the influence of a change of the parameters later. In this scenario, the nested Pump-Leak model equations reduce to:

$$\begin{cases} p_c + a_c^f + n_c = 2n_0 \\ p_n + a_n^f + n_n = 2n_0 \\ n_c - a_c^f - p_c = 0 \\ n_n - a_n^f - p_n - q = 0 \\ n_c \cdot a_c^f = n_n \cdot a_n^f \end{cases} \tag{1.13}$$

where the first and second equations correspond to osmotic pressure balance in the two compartments; the third and fourth equation correspond to macroscopic electroneutrality in each compartment; and the fifth equation is the balance of the chemical potential of the cations and metabolites on each side of the NE. p_i, n_i, a_i respectively accounts for the concentrations of proteins, cations and metabolites either in the cytoplasm - subscript c - or in the nucleus, subscript n. q accounts for the effective chromatin charge density. From these equations, we express the concentrations of cations in each compartment as functions of the extracellular concentration n_0 and the chromatin charge density q (Eq.S.98), leading to the following expression of the NE potential:

$$U_n = -ln\left(1 + \frac{q}{2n_0}\right) = -ln\left(1 + \frac{Q^{eff}}{Q^{eff} + 2A_n^f + 2P_n}\right) \tag{1.14}$$

A salient observation from Eq.1.14 is that the NE potential difference U_n is a proxy of the chromatin charge density. At low q, $U_n = 0$, i.e., the respective concentrations of metabolites and cations are equal on each side of the membrane. Eq.1.13, also shows that the protein concentrations are equal in the two compartments. This implies that when the charge of chromatin is diluted, the volumes of the nucleus and of the cytoplasm adjust such that the NC ratio equals the ratio of protein numbers in the two compartments $NC_1 = \frac{P_n}{P_c}$. In the Pump-Leak model, which considers a single compartment, a membrane potential appears as soon as there exist trapped particles in the compartment (see Appendix 6.2 and Eq.S.96). In contrast, our extended nested Pump-Leak model predicts that in the case of two compartments, the system has enough degrees of freedom to adjust the volumes as long as q is small, thereby allowing the potential to be insensitive to the trapped charged proteins. At high values of the chromatin charge Q^{eff}, U_n saturates to the value $-ln(2)$ which in physical units is equivalent to -17mV at 300K. Note that this lower bound for the potential is sensitive to the average charge of the proteins z_p and can be lowered by decreasing this parameter. We also highlight that Eq.1.14 makes another testable prediction, namely, that the NE potential is independent of the external ion concentration. In the literature, NE potentials were recorded for several cell types [Mazzanti, 2001]. They can vary substantially between cell types ranging from ~ 0mV for Xenopus oocytes to -33mV for Hela Cells. This result is in line with our predictions. The Xenopus oocyte nucleus has a diameter roughly twenty times

larger than typical somatic nuclei, but its chromatin content is similar [Dahl, 2004], resulting in a very diluted chromatin and a vanishing NE potential. On the other hand, Hela cells are known to exhibit an abnormal polyploidy which may lead to a large chromatin charge density and a large nuclear membrane potential.

This last prediction allows to understand the influence of the metabolites on the NC ratio. An increase of the number of metabolites in the cell A^f_{tot}, induces growth of the total volume (Eq.S.94), leading to the dilution of the chromatin charge and a strong decrease of the nuclear membrane potential (Eq.1.14). In the limit where A^f_{tot} is dominant, we thus expect the NC ratio to be set to the value NC_1. On the other hand, at low A^f_{tot}, metabolites do not play any role on the NC ratio, which is then given by $NC_2 > NC_1$, with:

$$NC_1 = \frac{P_n}{P_c} \quad , \qquad NC_2 = \frac{P_n + Q^{eff}/2}{P_c} \tag{1.15}$$

(see Eq.S.97 for the general formula). The actual NC ratio is intermediate between the two limiting behaviors (see Fig.S1B and Eq.S.103).

During cell growth, the ratio NC_1 is constant, while the ratio NC_2 varies with time. Indeed, if nucleo-cytoplasmic transport is faster than growth, the protein numbers P_n and P_c are both proportional to the number of ribosomes in the exponential growth regime and the ratio NC_1 does not vary with time (see Appendix 6.5). On the other hand, the DNA charge Q^{eff} is constant during G1 phase while P_n grows with time, so NC_2 decreases with time. The fact that the NC ratio remains almost constant during growth ([Neumann, 2007], [Pennacchio, 2022]) suggest that cells are closer to the NC_1 regime, and point at the crucial role of metabolites in setting the NC ratio (Fig.1.4 and S1.B). Importantly, these conclusions are overlooked in a large part of the existing literature ([Wu, 2022],[Lemière, 2022],[Deviri, 2022]) which often assumes that metabolites do not play any role on the NC ratio due to their permeability at the NE. We end this qualitative discussion by predicting the effect of a variation of the parameters z_p, z_a and α_0 that were so far assumed to be fixed. Our main point is that, any parameter change that tends to dilute the chromatin charge, also tends to increase the (negative) NE potential and make the NC ratio closer to the regime NC_1 and further from the regime NC_2. Consequently, increasing both z_p and z_a, the number of counterions carried by each protein or metabolite increases, resulting in a global growth of the volume, hence to the dilution of the chromatin charge and to the increase of the NE potential. Any increase of the pumping parameter α_0 (decrease of pumping efficiency) has a similar effect. It increases the number of ions in the cell resulting again in the dilution of the chromatin charge. Note that in the absence of pumping, ($\alpha_0 = 1$), the Pump-Leak model predicts a diverging volume because this is the only way to enforce the balance of osmotic pressures at the plasma membrane (if there is no pressure difference at the membrane due to a cell wall).

Five crucial parameters have emerged from our analytical study: (1) $\frac{P_n}{P_c}$ (2) $\frac{A^f}{2P_n}$ (3) $\frac{Q^{eff}}{2P_n}$ (4) α_0 and (5) z_p/z_a. But what are the biological values of these parameters? We summarize our estimates in Appendix 3. Importantly, the ratio between chromatin (free) counterions and the number of nuclear trapped proteins (and their counterions) is estimated to be of order one (see Appendix 3 and Fig.1.4.C). As a key consequence, we find that the NC ratio would be four times larger in the absence of metabolites Fig.S1.B. This non intuitive conclusion sheds light on the indirect, yet fundamental, role of metabolites on the NC ratio, which have been overlooked in the literature.

We now turn to a numerical solution to obtain the normalized variations of the NC ratio during growth in the G1 phase for different parameters Fig.1.4. Interestingly, variations of the NC ratio and variations of the NE potential are strongly correlated, a feature that can be tested experimentally Fig.1.4.B. Moreover, we deduce from our numerical results that, in order to maintain a constant NC ratio during the cell cycle, cells must contain a large pool of metabolites, see Fig.1.4.C. Our estimates point out that this regime is

genuinely the biological regime, thus providing a natural explanation on the origin of the nuclear scaling, which is a robust feature throughout biology.

In summary, many of the predictions of our analysis can be tested experimentally. Experiments tailored to specifically modify the highlighted parameters are expected to change the NC ratio. For example, we predict that depleting the pool of metabolites, by modifying amino-acid biosynthesis pathways, i.e., lowering $\frac{A^f}{2P_n}$, would lead to an increase of the NC ratio. Importantly, good metabolic targets in these experiments could be glutamate or glutamine because they account for a large proportion of the metabolites in the cell [Park, 2016]. We also point out that cells with a smaller metabolic pool are expected to experience higher variations of the NC ratio during growth and thus larger fluctuations of this ratio at the population level Fig.1.4.B. These predictions could shed light on understanding the wide range of abnormal karyoplasmic ratio among cancer cells. Indeed, metabolic reprogramming is being recognized as a hallmark of cancer [Fujita, 2020]; some cancer cells increase their consumption of the pool of glutamate and glutamine to fuel the TCA cycle and enhance their proliferation and invasiveness [Altman, 2016].

Moreover, disruption of either nuclear export or import is expected to change $\frac{P_n}{P_c}$ and thus the NC ratio. Numerical solutions of the equations displayed in Fig.S1 show a natural decrease of the NC ratio due to the disruption of nuclear import. On the other hand, if nuclear export is disrupted, we expect an increase of the NC ratio. This is in agreement with experiments done very recently in yeast cells [Lemière, 2022]. The authors reported a transient decrease followed by an increase of the diffusivities in the nucleus. This is precisely what our theory predicts. The initial decay is due to the accumulation of proteins in the nucleus, resulting in an associated crowding. While, the following increase, is due to the impingement of ribosome synthesis. As this step requires nuclear export, it leads to the loss of the exponential growth and a decoupling between protein and amino acid numbers that drives the dilution of the nuclear content.

Finally, our framework also predicts that experiments that would maintain the 5 essential parameters unchanged, would preserve the nuclear scaling. We thus expect that, as long as the NE is not under strong tension, changing the external ion concentration does not influence the scaling directly. Experiments already published in the literature [Guo, 2017] shows precisely this feature.

2.9 Mechanical role of the Lamina on the NC ratio

So far we have assumed that the osmotic pressure is balanced at the NE, which is a key condition for the linear relationship between nuclear and cytoplasmic volume. But why should this regime be so overly observed in biology? We first address this question qualitatively. For simplicity in the present discussion, we assume that DNA is diluted so that the NE potential is negligible. This implies that metabolites are partitioned so that their concentrations are equal in the nucleoplasm and the cytoplasm, hence cancelling their contribution to the osmotic pressure difference at the NE Eq.1.13. In the limit $\alpha_0 \sim 0$, this allows to express the volume of the nucleus as:

$$V_n = \frac{kT \cdot (z_p + 1) \cdot P_n}{\Delta P_n + (z_p + 1) \cdot p_c} \tag{1.16}$$

While the previous expression does not represent the exact solution of the equations, it qualitatively allows to realise that the NE hydrostatic pressure difference plays a role in the volume of the nucleus if it is comparable to the osmotic pressure exerted by proteins and their counterions. This pressure is in the 1000Pa range since protein concentration are estimated to be in the millimolar range (Appendix3). We further estimated an upper bound for the nuclear pressure difference to be in the 10^4Pa range (Eq.S.71). Admittedly crude, these estimates allow us to draw a three-fold conclusion. (1) The nuclear pressure difference can be higher than the cytoplasmic pressure difference, in part due to the fact that Lamina has

very different properties compared to cortical actin: it is much stiffer and its turnover rate is lower. This points out the possible role of nuclear mechanics in the determination of the nuclear volume contrary to the cortical actin of mammalian cells that does not play any direct role for the cell volume, (2) The typical hydrostatic pressure difference at which mechanical effects become relevant is at least two orders of magnitude lower for the nucleus than for the cytoplasm, for which it is of order π_0, (3) Assuming linear elasticity, small NE extensions of 10% would be sufficient to impact nuclear volume. These conclusions stand in stark contrast to the observed robustness of the nuclear scaling, thus pointing out that the constitutive equation for the tension in the lamina is nonlinear. Biologically, we postulate that this non-linearity originates from the folds and wrinkles that many nuclei exhibit [Lomakin, 2020]. These folds could indeed play the effective role of membrane reservoirs, preventing the NE tension to grow with the nuclear volume, and setting the nuclear pressure difference to a small constant value, thereby maintaining cells in the scaling regime discussed in the previous sections. This conclusion is consistent with the results of Ref. [Finan, 2009], which observed that the nucleus exhibits non-linear osmotic properties.

To further confirm our conclusions quantitatively, we consider the thought experiment of non-adhered cells experiencing hypoosmotic shock. This experiment is well adapted to study the mechanical role of nuclear components on nuclear volume because it tends to dilute the protein content while increasing the hydrostatic pressure by putting the NE under tension. For simplicity, we ignore the mechanical contribution of chromatin that was shown to play a negligible role on nuclear mechanics for moderate extensions [Stephens, 2017]. To gain insight into the non-linear set of equations, we split the problem into two parts. First, we identify analytically the different limiting regimes of nuclear volume upon variation of the number of impermeant molecules X_n present in the nucleus and the NE tension γ_n. We summarize our results in a phase portrait (see Appendix 6.6 and Fig.S1). Two sets of regimes emerge: those, studied above, where nuclear and cytoplasmic osmotic pressures are balanced, and those where the nuclear hydrostatic pressure matters. In the latter situations, the nuclear volume does not depend on the external concentration and saturates to the value (see Appendix 6.7) :

$$\frac{V_n^{max}}{V_n^{iso}} = \frac{(1+s)^{3/2}}{2\sqrt{2}} \cdot \left(1 + \sqrt{1 + \frac{1}{(1+s)\cdot K^{eff}}}\right)^{3/2} \quad \text{with,} \quad K^{eff} = \frac{K}{kT \cdot \frac{N_n^{tot}}{V_n^{iso}} \cdot \left(\frac{6}{\pi} \cdot V_n^{iso}\right)^{1/3}} \tag{1.17}$$

where, s and V_n^{iso} are respectively the fraction of membrane stored in the folds and the volume of the nucleus at the isotonic external osmolarity $2 \cdot n_0^{iso}$. K^{eff} is an effective adimensional modulus comparing the stretching modulus of the nuclear envelope K with an osmotic tension that depends on the total number of free osmolytes contained by the nucleus N_n^{tot}. The saturation of the nuclear volume under strong hypoosmotic shock originating from the pressure build up in the nucleus after the unfolding of the folds, implies a significant decrease of the NC ratio and a loss of nuclear scaling Fig.1.4.D.

As a second step, we investigate the variations of $X_n = A_n^f + P_n$ after the shock. Our numerical solution again highlight the primary importance of considering the metabolites A_n^f for the modelling of nuclear volume. Indeed, disregarding their contribution would lead to an overestimation of the number of trapped proteins. Additionally, X_n would remain constant during the osmotic shock, resulting in the reduction of the effective modulus of the envelope Eq.1.17. We would thereby overestimate the nuclear volume (Fig.1.4.D dashed line). In reality, since free osmolytes are mainly accounted for by metabolites which are permeable to the NE, the number of free osmolytes in the nucleus decreases strongly during the shock. This decrease can easily be captured in the limit where metabolites are uncharged $z_a = 0$. The balance of concentrations of metabolites Eq.1.13 implies that the number of free metabolites in the nucleus, A_n^f, passively adjusts to the NC ratio:

$$A_n^f = \frac{1}{1+\frac{1}{NC}} \cdot A^f \tag{1.18}$$

As mentioned earlier, the tension of the envelope is responsible for the decrease of the NC ratio. This in turn decreases the number of metabolites inside the nucleus, reinforcing the effect and thus leading to a smaller nuclear volume at saturation Fig.1.4.D. We find the analytical value of the real saturation by using Eq.1.17 with $N_n^{tot} = (zp+1) \cdot P_n + Q^{eff}$, i.e., no metabolites remaining in the nucleus.

Our investigations on the influence of the hydrostatic pressure term in the nested Pump-Leak model, lead us to identify another key condition to the nuclear scaling, i.e., the presence of folds at the NE. Moreover, although not the purpose of the present article, using our model to analyse hypoosmotic shock experiments could allow a precise charaterisation of the nucleus mechanics.

3 Discussion

In this study, we have investigated the emergence of the cell size scaling laws, which are the linear relations between dry mass, nuclear size and cell size, and which seem ubiquitous in living systems. Using a combination of physical arguments ranging from thermodynamics, statistical physics, polymer physics, mechanics and electrostatics, we have provided evidence that the robustness of these scaling laws arises from three physical properties : electroneutrality, balance of water chemical potential, and balance of ionic fluxes. The set of associated equations defines a model developed 60 years ago named the Pump-Leak model. The major challenge in probing the origin of the scaling laws using the Pump-Leak model, which we have addressed in this study, is to link a wide range of cell constituents and microscopic biological factors, such as ion transport, translation, transcription, chromatin condensation, nuclear mechanics, to the mesoscopic parameters of the Pump-Leak model, Fig.1.1.B. A host of experimental papers has gathered evidence on these scaling laws and their breakdown over the past century [Neurohr, 2020],[Cantwell, 2019],[Webster, 2009], but no theoretical analyses have unified these observations within a single theoretical framework.

In order to go in this direction, we have simplified the Pump-Leak model to its utmost based on the determination of precise orders of magnitude of the relevant parameters. The use of a simplified model focusing on the leading order effects, such as the homeostasis between amino-acids and proteins, is a powerful way to isolate and better study the origin of the scaling laws. This is embodied in the accurate predictions, without any adjustable parameters, for the dry mass dilution and the protein dynamics of yeast cells, which are prevented from dividing. A phenomenon that was so far unexplained [Neurohr, 2019] despite the fact that it is believed to be of fundamental biological importance [Lengefeld, 2021] by establishing a functional relationship between cell size (and density) and cell senescence, potentially providing a novel mechanism driving this important aging process.

The key ingredient of our model is the consideration of small osmolytes and in particular metabolites and small ions. Their high number fractions among cell free osmolytes implies that they dominate the control of cell volume. We make three quantitative predictions from this finding (1) The homeostasis between amino-acids and proteins, originating from the enzymatic control of the amino-acid pool, explains the dry mass density homeostasis. The disruption of homeostasis, due to mRNA crowding by ribosomes or pharmacological treatment such as rapamycin, is predicted to lead to dry mass dilution upon cell growth, due to the saturation of the protein content while the number of amino-acids and thus the volume keeps increasing with time, (2) The dry mass dilution observed at mitotic entry for mammalian cells can naturally be explained by the release of counterions condensed on the chromatin, leading to the increase of the number of osmolytes inside the cell and to the subsequent influx of water to ensure osmotic pressure balance at the plasma membrane, (3) The robustness of the NC ratio to the predicted

value $\frac{P_n}{P_c}$ is due to the high pool of metabolites within cells, resulting in the dilution of the chromatin (free) counterions which do not scale during growth.

Interestingly, only few amino-acids represent most of the pool of the metabolites possessed by the cell, i.e., glutamate, glutamine and aspartate. Emphasizing their crucial role on cell size. Our investigations thus link two seemingly distinct hallmark of cancers : the disruption of the cell size scaling laws such as the abnormal karyoplasmic ratio, historically used to diagnose cancer, and metabolic reprogramming, some cancer cells showing an increased consumption of their pool of glutamate and glutamine to fuel the TCA cycle and enhance their proliferation and invasiveness [Altman, 2016]. This may thus represent possible avenues for future research related to the variability of nucleus size in cancer cells [Rizzotto, 2017]. Moreover, the large pool of metabolites is a robust feature throughout biology [Park, 2016], making it one of the main causes of the universality of the cell size scaling laws observed in yeasts, bacteria and mammalian cells. We believe that the more systematic consideration of such small osmolytes will allow to understand non-trivial observations. For instance, the recent observation of the increase of diffusivities in the nucleus after blocking nuclear export, is explained in our model by the decoupling between protein and amino-acid homeostasis after the impingement of ribosome synthesis, a step that requires nuclear export [Lemière, 2022].

3.1 The nucleoskeletal theory

To study the nuclear scaling law, we developed a model for nuclear volume, by generalizing the Pump-Leak model, that includes both nuclear mechanics, electrostatics and four different classes of osmolytes. The clear distinction between these classes of components is crucial according to our analysis and is new. (1) Chromatin, considered as a gel, does not play a direct role in the osmotic pressure balance because its translational entropy is vanishingly small. Yet, it plays an indirect role on nuclear volume through its counterions. This creates an asymmetry in our system of equations, leading to the unbalance of ionic concentrations across the NE and to the appearance of a NE potential related to the density of chromatin. (2) Proteins, are considered as trapped in the nucleus, their number being actively regulated by nucleo-cytoplasmic transport. (3) Metabolites, are considered as freely diffusable osmolytes through the NE but not through the plasma membrane. Note that only half of the proteins are trapped in the nucleus because about half of them have a mass smaller than the critical value 30-60kDa [Rob Philipps, 2015], which corresponds to the typical cut-off at which they cannot freely cross nuclear pore complexes. This represents more a semantic issue than a physical one, and permeant proteins are rigorously taken into account as metabolites in the model, but are negligible in practice due to the larger pool of metabolites. (4) Free ions, are able to diffuse through the plasma membrane and the NE.

As a consequence, we show that the nuclear scaling originates from two features. The first one is the balance of osmotic pressures at the NE, that we interpret as the result of the non-linear elastic properties of the nucleus likely due to the presence of folds in the nuclear membrane of mammalian cells. Interestingly, yeast cells do not possess lamina such that the presence of nuclear folds may not be required for the scaling. In this regard, our model adds to a recently growing body of evidence suggesting that the osmotic pressure is balanced at the NE in isotonic conditions [Deviri, 2022],[Lemière, 2022],[Finan, 2009]. The second feature is the presence of the large pool of metabolites accounting for most of the volume of the nucleus. This explains why nuclear scaling happens during growth while the number of chromatin counterions does not grow with cell size.

Interestingly, although not the direct purpose of this article, our model offers a natural theoretical framework to shed light on the debated nucleoskeletal theory [Webster, 2009], [Cantwell, 2019]. Our results indicate that the genome size directly impacts the nuclear volume only if the number of (free) counterions of chromatin dominates the number of trapped proteins and the number of metabolites inside

the nucleus. We estimate that this number is comparable to the number of trapped proteins while it is about 60 times smaller than the number of metabolites, in agreement with recent observations that genome content does not directly determine nuclear volume [Cantwell, 2019]. Although not directly, chromatin content still influences nuclear volume. Indeed, nuclear volume (Eq.S.99) is mainly accounted by the number of metabolites, which passively adjusts according to Eq.S.93(7). In the simple case, of diluted chromatin and no NE potential, metabolite concentration is balanced and $NC = \frac{P_n}{P_c}$, such that the metabolite number depends on two factors (Eq.1.18). The first one, is the partitioning of proteins $\frac{P_n}{P_c}$, that is biologically ruled by nucleo-cytoplasmic transport in agreement with experiments that suggest that the nucleo-cytoplasmic transport is essential to the homeostasis of the NC ratio [Cantwell, 2019]. The second one is the total number of metabolites, ruled by the metabolism Eq.1.9, which ultimately depends upon gene expression (Appendix 4), as shown by genetic screen experiments done on fission yeast mutants [Cantwell, 2019]. However, when the chromatin charge is not diluted, which is likely to occur for cells exhibiting high NE potential such as some cancer cells, our theory predicts that the number of metabolites in the nucleus also directly depends on the chromatin content due to electrostatic effects. This highlights the likely importance of chromatin charge in the nuclear scaling breakdown in cancer.

3.2 Role of NE breakdown in cell volume variations

The nested Pump-Leak model predicts that the cell swells upon NE breakdown if the NE is under tension. NE breakdown occurs at prometaphase, and does not explain most of the mitotic swelling observed in [Son, 2015; Zlotek-Zlotkiewicz, 2015], which occurs at prophase. Within our model based on counterion release, mitotic swelling is either associated with cytoplasm swelling if the released counterions leave the nucleus, or with nuclear swelling if they remain inside. In the latter case, swelling at prophase would be hindered by an increase of NE tension, and additional swelling would occur at NE breakdown. This prediction can be tested by artificially increasing the NE tension through strong uniaxal cell confinement [Le Berre, 2014], which would synchronise mitotic swelling with NE breakdown.

3.3 Physical grounds of the model

Physically, why can such a wide range of biological phenomena be explained such a simple theory? A first approximation is that we calculated the osmotic pressure considering that both the cytoplasm and the nucleus are ideal solutions. However, it is known that the cytoplasm and the nucleoplasm are crowded ([Feig, 2015],[McGuffee, 2010]). The qualitative answer again comes from the fact that small osmolytes constitute the major part of the free osmolytes in a cell so that steric and short range attractive interactions are only a small correction to the osmotic pressure. We confirm this point by estimating the second virial coefficient that gives a contribution to the osmotic pressure only of order 2kPa (see Appendix 3), typically 2 orders of magnitude smaller than the ideal solution terms Fig.1.1.B. However, note that we still effectively take into account excluded volume interactions in our theory through the dry volume R. Moreover, we show in appendix 7) that although we use an ideal gas law for the osmotic pressure, the Donnan equilibrium effectively accounts for the electrostatic interactions. Finally, our theory can be generalized to take into account any ions species and ion transport law while keeping the same functional form for the expressions of the volume Eq.S.59, as long as only monovalent ions are considered. This is a very robust approximation, because multivalent ions such as calcium are in the micromolar range. Together, these observations confirm that the minimal formulation of the Pump-Leak model that we purposely designed is well adapted to study cell size.

3.4 Future extensions of the theory

As a logical extension of our results, we suggest that our framework be used to explain the scaling of other membrane bound organelles such as vacuoles and mitochondria [Chan, 2010]. We show in appendix (Eq.S.121) that the incorporation of other organelles into our framework lead to the same equations as for the nucleus, thus pointing out that the origin of the scaling of other organelles may also arise from the balance of osmotic pressures. We also propose that our theory be used to explain the scaling of membraneless organelles such as nucleoids [Gray, 2019]. Indeed, the Donnan picture that we are using does not require membranes [Barrat, 1996]. However, we would have to add other physical effects in order to explain the partitioning of proteins between the nucleoid and the bacterioplasm.

Taken as a whole, our study demonstrates that cell size scaling laws can be understood and predicted quantitatively on the basis of a remarkably simple set of physical laws ruling cell size as well as a simple set of universal biological features. The multiple unexplained biological phenomena that our approach allows to understand indicates that this theoretical framework is fundamental to cell biology and will likely benefit the large community of biologists working on cell size and growth.

Chapter 2

Nuclei under uniaxial confinement

La Science remplace du visible compliqué par de l'invisible simple.

Jean Perrin
Les Atomes
1913

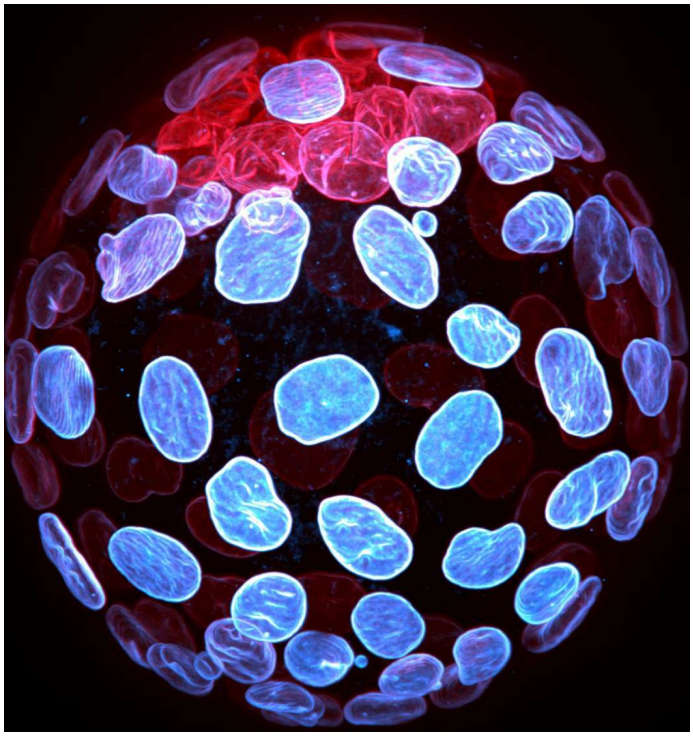

Nuclei of a mouse embryo, Jean-Leon Maitre

1 Introduction

1.1 Objectives

In Chapter 1, we developed a general framework based on the Pump-Leak model to study the emergence of the cell size scaling laws which linearly relates three fundamental biological quantities: cell volume, nucleus volume and cell dry mass. While the predictions on the cell density homeostasis were quantitatively tested based on already published data, the second set of predictions, namely the physical origins of the nuclear scaling law remained almost purely theoretical. We therefore propose in this chapter to apply and quantitatively confront our theory to the unpublished data of Matthieu Piel's team studying the consequences of "moderate" uniaxial confinement of nuclei on the timescale of minutes. The chapter is divided into two distinct parts. In Section.2, we adapt the nested Pump-Leak model to the problem of nuclear confinement. The model shows good quantitative agreement with the data but is based on a phenomenological equation for the elastic response of the nuclear envelope Eq.S.112. In Section.3, we justify this phenomenological equation with a Hookean non-linear elastic model.

1.2 Static 6-well confiner experiment

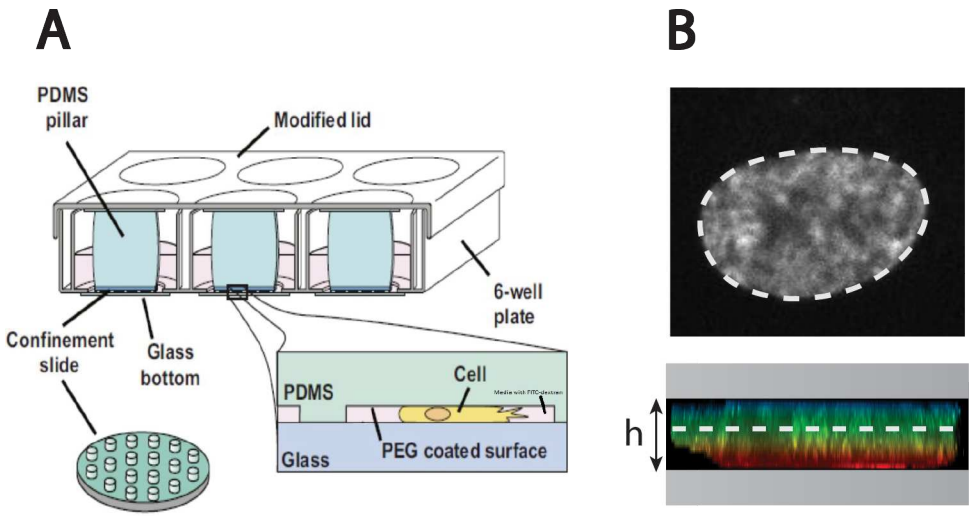

Figure 2.1: **Static 6-well confiner experiment.** (A) Schematic of the static confiner set-up [Le Berre, 2014]. Cells are deposited on the confinement slide glass plate. PDMS pillars are then added on top of the confinement slide to compress the cells. The confinement height h is fixed by the size of the PDMS pillars and is changed between experiments. (B) The set-up is placed 10 to 40 minutes after compression under a microscope to image the confined nuclei. The projected area S_n^{proj} of the nucleus (gray dashed line) is measured and the volume of the nucleus approximated by the formula $V_n = S_n^{proj} \cdot h$.

Cells are confined uniaxially following the experimental procedure described in [Le Berre, 2014] (see Fig.2.1.A). They are placed in wells and compressed by adding PDMS plates on top. Note that the plates were treated with Trypsin to minimize the adhesion of the cells. The key control parameter of the experiment is the confinement height h. This parameter is changed between experiments by crafting PDMS pillars of different heights. Cells are then placed under a microscope and their nuclei imaged using either the Hoechst labeling to image chromatin or by expressing Lap2b-GFP to image the nuclear envelope. Importantly, the time of initial observation is not precisely controlled in this experiment and range from 10 to 40 minutes after compression. The quasistatic theory developed in Chapter.1 is thus

adapted to study such experiments. The projected area of the nucleus S_n^{proj} was then measured using the ImageJ software and the nucleus volume was estimated from the formula (see Fig.2.1.B):

$$V_n = S_n^{proj} \cdot h \tag{2.1}$$

1.3 Experimental observations

The data presented in this chapter were mainly acquired by Alice Williart, PhD student in Matthieu Piel's team. They unambiguously show two distinct regimes of compression upon uniaxial confinement on the timescale of minutes. A first regime, at weak confinements, i.e., high h, where the nucleus deforms at constant volume. And a second regime, at moderate confinements, i.e. low h, where the nucleus loses volume (see Fig.2.2.A). Note that we also address in Chapter.4 a third regime, at strong confinement, for which the nuclear envelope ruptures. We emphasize that this loss of nuclear volume is substantial. For instance, Hela cells loose on average 50% of their homeostatic volume between the critical height at which the volume loss occur, $h_c \approx 5\mu$m for Hela Cells, and the height at which nuclear rupture occurs $h = 2\mu$m (see Chapter.4). Moreover, a salient observation is that the loss of volume coincides with the disappearance of nuclear folds at the nuclear envelope (see Fig.2.2.B). This is reminiscent of the prediction of the "nested" Pump-Leak model according to which there is a surface S^* above which the nuclear envelope becomes tensed and starts to play a role on the nucleus volume (see Fig.1.4.D).

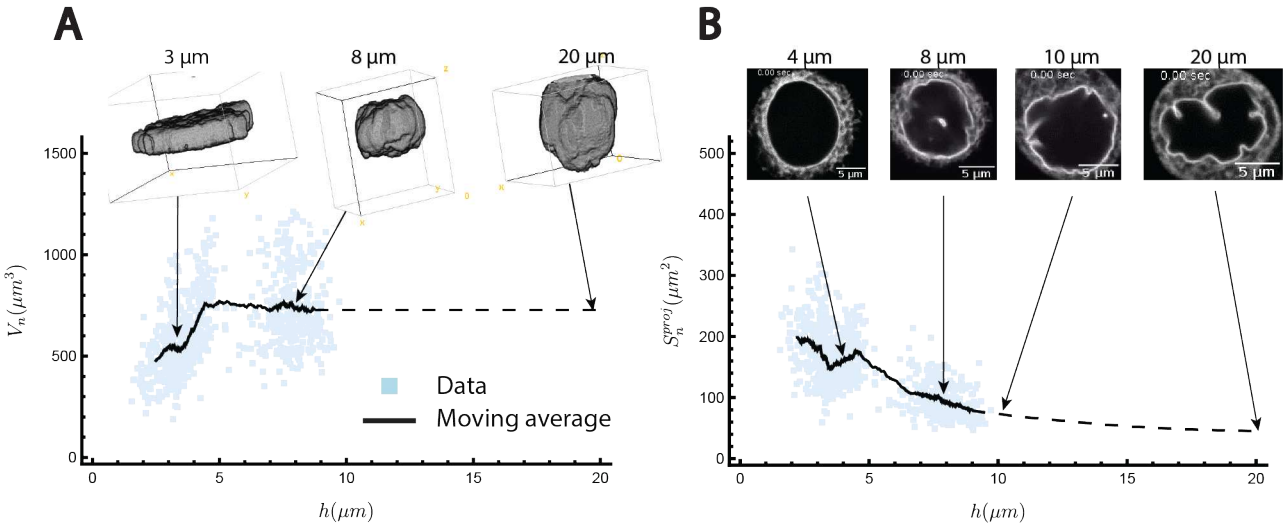

Figure 2.2: **Experimental observations.** (A) Volume of Hela Cell nuclei 10 to 40 minutes after confinement at a given height h. For illustration, 3D reconstruction of the nuclei at different height of confinement are shown. (B) Projected surface of Hela Cell nuclei 10 to 40 minutes after confinement at a given height h. For illustration, the top view images of representative Hela Cell nuclei are shown at different h. The nuclear envelope is labeled by Lap2b-GFP. Courtesy of Alice Williart.

1.4 Biological Relevance and Motivations

These experimental findings are of biological importance. They identify a first "safe" regime of nuclear deformations where the volume is constant, and the surface is not tensed. And a second regime, where the volume is decreased, and the surface is stretched. This latter regime is likely deleterious for the cell. First because the decrease of the nucleus volume implies a compaction of the chromatin which is known to dramatically affects the DNA machinery [Shah, 2021]. Second, because the tension in the envelope

can cause nuclear ruptures [Deviri, 2019] and the appearance of nuclear blebs which are known to be one of the main sources of nuclear and genetic instabilities (see Chapter.4).

Two fundamental questions thus arise: What are the physical origins of this volume loss? And what are the physical and biological origins of these folds that set the physiological range of "safe" deformation? Both of these questions will be respectively addressed in Section.2 and Section.3.

2 Nuclear volume loss upon uniaxial confinement

2.1 Qualitative understanding of the nuclear volume loss

Following the experimental observations, we hypothesize in this chapter that the driving force responsible for the nuclear volume loss at moderate confinements originates from the stretching of the nuclear envelope. For simplicity, we neglect the mechanical role of the chromatin. This is justified because it was shown that lamina dominates the mechanical response of the nucleus for substantial deformations [Stephens, 2017]. At weak confinements however, when the nuclear envelope is not stretched, the gel of chromatin becomes important in the volume response of the nucleus. The role of the gel of chromatin in the deformation response of weakly confined nuclei will be addressed in Chapter.3.

We first qualitatively discuss the predictions of the nested Pump-Leak model to the uniaxial confinement of nuclei. We remind that on the timescale of minutes the chemical potential of water must be balanced at the nuclear envelope:

$$\underbrace{\Delta P_n}_{\sim 2\cdot\gamma_n\cdot\mathcal{C}} = \underbrace{\Delta\Pi_n}_{\sim kT\cdot\frac{N_n^{tot}}{V_n}-2n_0} \tag{2.2}$$

In the nested Pump-Leak framework, as long as the envelope is not stretched, $\gamma_n \sim 0$ and the osmotic pressure in the nucleus equals the osmotic pressure in the cytoplasm which is itself fixed by the external osmotic pressure π_0 (see Chapter.1). As such, before tensing the NE, we predict that the nucleus deformations happen at constant volume. Moreover, during the deformation, nuclei deform from a spherical to a pancake shape. The sphere is the geometrical shape that minimizes the surface of any given 3D object of fixed volume. We thus predict that the surface of the nucleus increases during confinement. After reaching a threshold surface S^*, the nuclear envelope becomes tensed, and the tension starts to increase following the phenomenological constitutive equation Eq.S.112. From Laplace's law, we then predict that the nuclear pressure difference increases as h is decreased. The nucleus in turn looses volume to increase the nuclear osmotic pressure and thus to enforce the balance of pressures at the nuclear envelope Eq.2.2. While the effect qualitatively described here is the driving force of the observed nuclear volume loss, a more careful quantitative treatment of the nested Pump-Leak model must be done to assess how the total number of nuclear osmolytes N_n^{tot}, the tension γ_n and the curvature $\mathcal{C}$ evolves for different confinement heights.

2.2 The nested Pump-Leak model applied to nuclear uniaxial confinements

We remind that the nested Pump-Leak model is defined by the following system of equations (See Eq.S.93):

$$\begin{cases} n_c^+ - n_c^- - z_p \cdot p_c - z_a \cdot a_c = 0 \\ n_n^+ - n_n^- - z_p \cdot p_n - z_a \cdot a_n - q = 0 \\ \Pi_c \approx kT \cdot 2n_0 \\ \Pi_n = kT \cdot 2n_0 + \Delta P_n \\ n_c^+ \cdot n_c^- = \alpha_0 \cdot n_0^2 \\ n_n^+ \cdot n_n^- = \alpha_0 \cdot n_0^2 \\ (n_n^+)^{z_a} \cdot a_n = (n_c^+)^{z_a} \cdot a_c \end{cases} \tag{2.3}$$

Where we use the same notations as in Chapter.1 (see Eq.1.13). We remind that p_i, n_i, a_i respectively account for the concentrations of proteins of average charge z_p, ions, either cations n^+ or anions n^-, and metabolites of average charge z_a either in the cytoplasm, subscript c, or in the nucleus, subscript n. q accounts for the effective chromatin charge density, n_0 for the osmolarity of the external medium and α_0 for the pumping efficiency parameter Eq.1.3. This system is non-linear and cannot be solved in its full generality analytically. We thus propose in this section a numerical resolution of this system for the problem of nuclear confinement at stake. Multiple methods exist to solve the problem. However, of the three methods tested, the one that we choose to present in this thesis appeared to be the most robust numerically. We first transform the system following the line of thought presented in the supplementary information (see Appendix.2). We combine the electroneutrality and balance of ionic fluxes constraints to obtain:

$$\begin{cases} N_n^+ = \frac{1}{2} \cdot \left(z_n^{eff} \cdot (A_n + P_n) + \sqrt{\left(z_n^{eff} \cdot (A_n + P_n) \right)^2 + 4\alpha_0 n_0^2 \cdot (V_n - R_n)} \right) \\ N_n^- = \frac{1}{2} \cdot \left(-z_n^{eff} \cdot (A_n + P_n) + \sqrt{\left(z_n^{eff} \cdot (A_n + P_n) \right)^2 + 4\alpha_0 n_0^2 \cdot (V_n - R_n)} \right) \end{cases} \quad With,\ z_n^{eff} = \frac{z_a \cdot A_n + z_p \cdot P_n + Q}{A_n + P_n} \tag{2.4}$$

Similarly,

$$\begin{cases} N_c^+ = \frac{1}{2} \cdot \left(z_c^{eff} \cdot (A_c + P_c) + \sqrt{\left(z_c^{eff} \cdot (A_c + P_c) \right)^2 + 4\alpha_0 n_0^2 \cdot (V_c - R_c)} \right) \\ N_c^- = \frac{1}{2} \cdot \left(-z_c^{eff} \cdot (A_c + P_c) + \sqrt{\left(z_c^{eff} \cdot (A_c + P_c) \right)^2 + 4\alpha_0 n_0^2 \cdot (V_c - R_c)} \right) \end{cases} \quad With,\ z_c^{eff} = \frac{z_a \cdot A_c + z_p \cdot P_c}{A_c + P_c} \tag{2.5}$$

We further use the constraint on the balance of pressures Eq.1.2 to show that:

$$\begin{cases} V_n^{(1)} = R_n + \frac{A_n + P_n}{2n_0 + \frac{\Delta P_n}{kT}} \cdot \frac{\left(z_n^{eff}\right)^2 - 1}{-1 + \sqrt{1 + \left(\left(z_n^{eff}\right)^2 - 1\right) \cdot \left(1 - \frac{\alpha_0}{1 + \frac{\Delta P_n}{kT \cdot 2n_0}}\right)}} \\ V_c = R_c + \frac{A_c + P_c}{2n_0} \cdot \frac{\left(z_c^{eff}\right)^2 - 1}{-1 + \sqrt{1 + \left(\left(z_c^{eff}\right)^2 - 1\right) \cdot (1 - \alpha_0)}} \end{cases} \tag{2.6}$$

Where we add the superscript (1) on the nuclear volume V_n because we will derive an additional expression in the next section. Finally, the balance of metabolite fluxes leads to one of the two equation that we will solve for A_n:

$$N_n^{+^{z_a}} \cdot A_n = N_c^{+^{z_a}} \cdot A_c \cdot \left(\frac{V_n - R_n}{V_c - R_c} \right)^{z_a + 1} \quad With, \quad A_c = A_{tot} - A_n \tag{2.7}$$

The system is not closed yet. We must add equations that model how the nuclear pressure difference ΔP_n evolves with h. This is the object of the next section.

2.3 The shape equation

2.3.1 Force balance

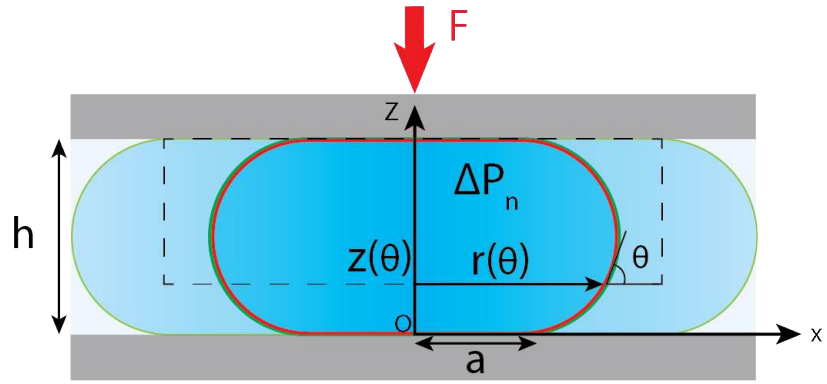

Figure 2.3: **Parametrization of the static nuclear confinement problem.**

We assume that the geometry of the nucleus is axisymmetric upon compression, i.e., there is an invariance by rotation around the z axis. We can thus fully describe a point located on the surface of the nucleus by two coordinates: (r(θ),z(θ)). We call θ the angle between the tangent to the nucleus surface in the plane (Oxz) and the horizontal axis (see Fig.2.3). The force balance at the contact point of coordinate (x=a, z=0), projected on the x-axis, leads to the Young-Dupre relation:

$$cos(\theta_c) = \frac{\gamma_n + \gamma_{adh}}{\gamma_n} \tag{2.8}$$

With, θ_c, the contact angle between the nuclear surface and the PDMS plate. γ_n, the elastic tension of the nuclear envelope and γ_{adh} a tension related to the interaction between the nuclear surface and the PDMS plates. While the nucleus is not in direct contact with the plates, it is known that there are specific protein complexes that link both surfaces such as the LINC complex for the nucleus and integrins for the plasma membrane. However, here, the PDMS plates are treated with Trypsin to avoid adhesion and we thus neglect γ_{adh}. Hence, $\theta_c \sim 0$ and θ varies between [0,π].

We next write the force balance on the dashed rectangle displayed in Fig.2.3 to obtain a constraint on the shape of the nucleus surface. For simplicity, we neglect the influence of the cytoplasm in the force balance.

$$F + 2\pi \cdot r(\theta) \cdot \gamma_n \cdot sin(\theta) - \Delta P_n \cdot \pi r^2(\theta) = 0 \tag{2.9}$$

With, F the part of the force applied by the PDMS plate cancelled by the nucleus and ΔP_n the difference of hydrostatic pressures between the nucleus and the cytoplasm. The latter two quantities are not independent. Taking $\theta = 0$ in Eq.2.9 leads to the relation:

$$F = \Delta P_n \cdot \pi a^2 \tag{2.10}$$

Substituting Eq.2.10 in the force balance equation Eq.2.9 leads to a second order polynomial for r:

$$r^2 - \frac{2\gamma_n \cdot sin(\theta)}{\Delta P_n} \cdot r - a^2 = 0 \tag{2.11}$$

Which implies that:

$$r(\theta) = a \cdot \left(B \cdot sin(\theta) + \sqrt{1 + B^2 \cdot sin^2(\theta)} \right) \quad With, \quad B = \frac{1}{2 \cdot a \cdot \mathcal{C}} \tag{2.12}$$

Where, $\mathcal{C} = \frac{\Delta P_n}{2\gamma_n}$ is the average curvature at the edge of the nucleus. We introduce an important nondimensional parameter B that naturally arises in the problem. It compares the average radius of curvature $\frac{1}{\mathcal{C}}$ at the edge of the nucleus with the radius of contact a (see Fig.2.3). $z(\theta)$ can then be deduced from $r(\theta)$ from the following geometrical constraint:

$$\frac{\mathrm{d}z}{\mathrm{d}r} = tan(\theta) \implies \frac{\mathrm{d}z}{\mathrm{d}\theta} = tan(\theta) \cdot \frac{\mathrm{d}r}{\mathrm{d}\theta} \tag{2.13}$$

By enforcing that $z(\theta = 0) = 0$, we further integrate Eq.2.13 between 0 and θ and obtain:

$$z(\theta) = a \cdot \left[B \cdot [1 - cos(\theta)] + E_1(\theta, -B^2) - E_2(\theta, -B^2) \right] \quad \text{With,} \quad \begin{cases} E_1 = \int_0^\theta \sqrt{1 + B^2 \cdot sin^2(\theta')}\, \mathrm{d}\theta' \\ E_2 = \int_0^\theta \frac{1}{\sqrt{1 + B^2 \cdot sin^2(\theta')}}\, \mathrm{d}\theta' \end{cases} \tag{2.14}$$

Eq.2.14 is written according to two Euler incomplete elliptic integrals of the first and second kind. For clarity in the following, we simply denote by E_1 and E_2 the values of these integrals for $\theta = \frac{\pi}{2}$. We obtain an important constraint by taking $\theta = \frac{\pi}{2}$ in Eq.2.14:

$$\frac{h}{2} = a \cdot [B + E_1 - E_2] \tag{2.15}$$

We further use Eq.2.14 and Eq.2.12 to express the surface of the nucleus as a function of a and B. We decompose the area in two terms: the contact area with the two PDMS plates $2\pi a^2$, and the contact area with the cytoplasm S_n^{eff}. We express the latter area as:

$$\frac{S_n^{eff}}{2} = \int_0^{\frac{\pi}{2}} 2\pi r \, \mathrm{d}s = 2\pi \cdot (aB)^2 \left[2 + \frac{2}{B} \cdot E_1 - \frac{1}{B} \cdot E_2 \right] \tag{2.16}$$

Such that the total surface of the nucleus S_n reads:

$$S_n = S_n^{eff} + 2\pi a^2 = 4\pi (aB)^2 \left[2 + \frac{2}{B} \cdot E_1 - \frac{1}{B} \cdot E_2 \right] + 2\pi a^2 \tag{2.17}$$

As a side note, it is straightforward to show that the projected surface of the nucleus is simply given in this framework by:

$$S_n^{proj} = \pi \cdot r^2(\theta = \frac{\pi}{2}) = \pi \cdot a^2 \cdot \left(B + \sqrt{1 + B^2} \right)^2 \tag{2.18}$$

Finally, following the same reasoning, the nucleus volume can be expressed as:

$$V_n^{(2)} = \int_0^{\frac{\pi}{2}} \pi r^2 \, \mathrm{d}z = \frac{2\pi}{3} \cdot (aB)^3 \cdot \left[\left(\frac{3}{B^2} + 8 \right) + \frac{1}{B} \cdot \left(8 + \frac{1}{B^2} \right) \cdot E_1 - \frac{1}{B} \cdot \left(4 + \frac{1}{B^2} \right) \cdot E_2 \right] \tag{2.19}$$

2.3.2 Sanity checks

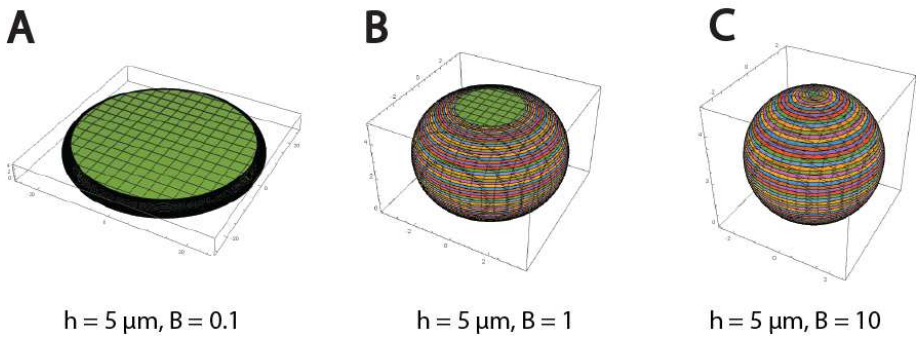

Figure 2.4: **Range of nuclear shapes described by our model.** Shapes obtained from Eq.2.12, Eq.2.14 and Eq.2.15 for different values of the parameter B at a given h.

We first test the consistence of the previous set of equations in two important limiting regimes. In the strong confinement limit, $B << 1$, we check that the equations describe a Pancake shape and Eq.2.19 simply reduces to $V_n \sim \frac{S_n}{2} \cdot h$, which is consistent. On the other hand, for weak confinements, $B >> 1$, we verify that the equations describe a sphere and Eq.2.17 and Eq.2.19 simply reduces to: $S_n = 4\pi R_0^2$ and $V_n = \frac{4\pi}{3} \cdot R_0^3$, with R_0 the radius of the nucleus before compression. For illustration we display the shapes obtained for different values of the parameter B in Fig.2.4.

Moreover, we also check that the parametrization of the surface $(r(\theta), z(\theta))$ that we derived respects the Laplace law. We compute the first and second Gauss fundamental forms of the nucleus surface. The first fundamental form is also commonly called in physics the metric and is described by a matrix $\mathcal{I}_{\vec{M}}$ of term $g_{ij} = \vec{t_i} \cdot \vec{t_j}$, with $\vec{t_i}$ a basis of the tangent plane of S_n^{eff}. A point $\vec{M}$ on the surface can be parametrized as:

$$\vec{M} = (r(\theta)cos(\phi), r(\theta)sin(\phi), z(\theta)) \tag{2.20}$$

With, ϕ the angle of rotation around the z axis. The tangent vectors can then simply be expressed as:

$$\begin{cases} \vec{t_\theta} = \frac{\partial \vec{M}}{\partial \theta} = ((\partial_\theta r(\theta) \cdot cos(\phi), \partial_\theta r(\theta) \cdot sin(\phi), tan(\theta)) \\ \vec{t_\phi} = \frac{\partial \vec{M}}{\partial \phi} = (-rsin(\phi), rcos(\phi), 0) \end{cases} \tag{2.21}$$

Such that the first Gauss fundamental form reads:

$$\mathcal{I}_{\vec{M}} = \begin{pmatrix} \frac{(\partial_\theta r)^2}{cos^2(\theta)} & 0 \\ 0 & r^2 \end{pmatrix} \tag{2.22}$$

The second fundamental form can be described by the following matrix:

$$\mathcal{II}_{\vec{M}} = \left(\vec{n} \cdot \partial_j \vec{t_i}\right)_{i,j} \tag{2.23}$$

With, $\vec{n} = \frac{\vec{t_\theta} \times \vec{t_\phi}}{||\vec{t_\theta} \times \vec{t_\phi}||}$, the unit normal vector to the tangent plane at $\vec{M}$. After straightforward algebra, we show that the Laplace law is indeed verified:

$$\boxed{2 \cdot \mathcal{C} = Tr(\mathcal{I}_{\vec{M}}^{-1} \cdot \mathcal{II}_{\vec{M}}) = \left[\frac{d\theta}{ds} + \frac{sin(\theta)}{r}\right] = \frac{\Delta P}{\gamma}} \tag{2.24}$$

Where, $s = \sqrt{dr^2 + dz^2}$ denotes the curvilinear abscissa of the surface in the plane (Oxz).

2.4 Numerical resolution

2.4.1 Normalization

The nested Pump-Leak model is now closed, and we can proceed with its numerical resolution. For clarity and numerical stability, we normalize the physical quantities appearing in our equations:

- Volumes are normalized by the volume $V_n^0 \approx \frac{4}{3}\pi R_0^3$, with R_0 the radius of the nucleus assumed to be a sphere before being confined.
- Surface are normalized by the homeostatic nuclear surface $S_n^0 \approx 4\pi R_0^2$.
- Tensions are normalized by the osmotic tension $kT \cdot 2n_0 \cdot R_0$.
- a is normalized by R_0 and h by $2R_0$.

Following the experimental procedure, we impose h and want to know how all the other quantities evolve. The two coupled equations that we solve numerically in A_n and B are:

$$\begin{cases} \overline{V_n}^{(1)} = \overline{V_n}^{(2)} \\ \overline{N_n}^{+^{z_a}} \cdot \overline{A_n} = \overline{N_c}^{+^{z_a}} \cdot \overline{A_c} \cdot \left(\frac{\overline{V_n}-\overline{R_n}}{\overline{V_c}-\overline{R_c}}\right)^{z_a+1} \end{cases} \tag{2.25}$$

With, $\overline{V_n}^{(1)}$ and $\overline{V_n}^{(2)}$ are respectively given by Eq.2.6 and Eq.2.19.

2.4.2 Numerical values of the parameters

Parameters	Value	Meaning
V_n^0	$740\mu\text{m}^3$	Homeostatic volume of Hela Cell nuclei (Fig.2.2.A)
V_{tot}^0	$2160\mu\text{m}^3$	Homeostatic volume of a Hela Cell [Venkova, 2022]
V_c^0	$V_{tot}^0 - V_n^0 = 1420\mu\text{m}^3$	Homeostatic volume of Hela Cell cytoplasm
S^*	$1.2 \cdot S_n^0 = 476\mu m^2$	Surface at which the NE becomes tensed (Fig.2.2.B)
R_n	$0.3 \cdot V_n^0 = 223\mu\text{m}^3$	Nuclear dry volume
R_c	$0.3 \cdot V_c^0 = 426\mu\text{m}^3$	Cytoplasmic dry volume
P_{tot}	$p_{tot} \cdot (V_{tot}^0 - (R_n + R_c)) = 2 \cdot 10^9$	Total protein number
Q^{eff}	$2 \cdot 10^9$	Effective chromatin charge
z_a	1	Metabolite charge
z_p	0.8	Protein charge
α_0	0.14	Ion pump parameter
kT	4.1pN.nm	Thermal energy at $T = 300$K
n_0	150mMol	External osmolarity
K	25mN/m	Area stretching modulus of lamina [Dahl, 2004]

Table 2.1: **Summary of the nested Pump-Leak parameters used in the confinement problem.**

For consistency, we decided to use the same parameters as the one estimated in Chapter 1 (see Fig.1.1 and Appendix.3). We summarize the value of these parameters in Table.2.1. For full completeness however, the values of the nuclear protein number P_n, the nuclear metabolites number before compression A_n^0 and the total metabolites number A_{tot} are determined by enforcing the three equations Eq.2.6 and Eq.2.7 and assuming that before confinement $\Delta P_n^0 = 0$. For the values of the parameters used in Table.2.1, we find:

$$P_n = 6 \cdot 10^8, \quad A_n^0 = 4 \cdot 10^{10}, \quad A_{tot} = 1.1 \cdot 10^{11} \tag{2.26}$$

We emphasize that we find $A^{tot} \sim 60 \cdot P_{tot}$ which is consistent with Chapter.1 (see Appendix.3). Nevertheless, we emphasize that the values of these parameters change if we vary the values of some of the parameters present in Table.2.1 such as α_0, z_a, or z_p.

2.5 Results

2.5.1 Regimes of deformation

We explained qualitatively that the volume of the nucleus must decrease following the stretching of the envelope to ensure the pressure balance Eq.2.2. Our numerical solution shows two different regimes of compression depending on the critical parameter $\overline{K} = \frac{K}{kT \cdot 2n_0 \cdot R_0}$. At $\overline{K} << 1$, the volume loss happens after a subsequent extension of the envelope and most of the deformation is at constant volume. On the other hand, at $\overline{K} >> 1$, the volume loss is visible just after the stretching of the envelope. We illustrate these different regimes in Fig.2.5.

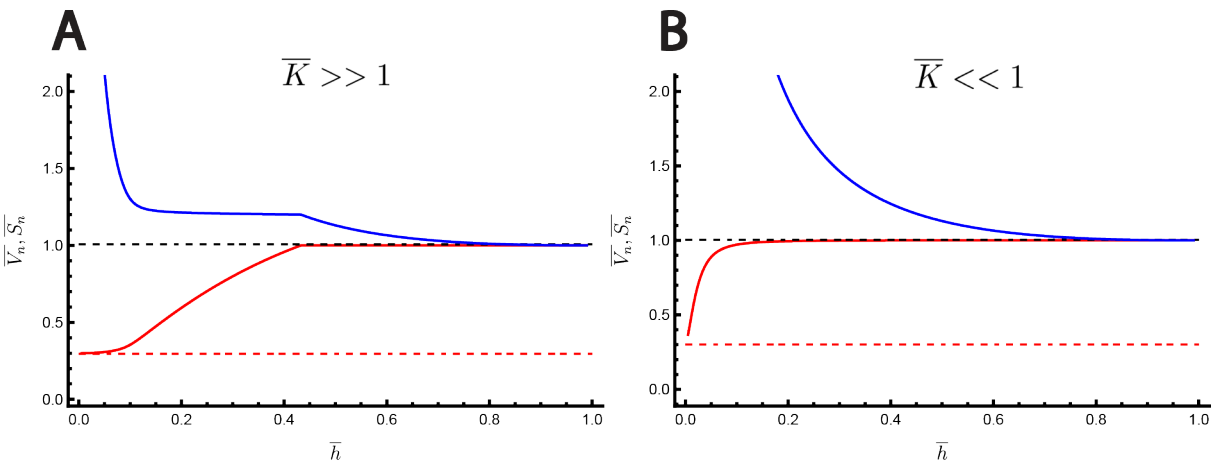

Figure 2.5: **Two limiting regimes of deformation upon confinement.** Normalized volume (red) and surface (Blue) of the nucleus at different confinement heights as described by the nested Pump-Leak model Eq.2.3. The dashed red lines account for the normalized dry volume of the nucleus $\frac{R_n}{V_n^0}$. Two limiting regimes are shown depending on the value of the normalized envelope stretching modulus $\overline{K} = \frac{K}{kT \cdot 2n_0 \cdot R_0}$: (A) Inextensible nuclear envelope ($\overline{K} = 0.24$ corresponding to $K = 1$N/m). The non-derivability of the solutions originates from the phenomological constitutive equation used to model the nuclear envelope elastic behavior Eq.S.112. (B) Highly extensible nuclear envelope ($\overline{K} = 2.4 \cdot 10^{-5}$ corresponding to $K = 0.1$mN/m). The other parameters used are listed in Table.2.1.

2.5.2 Comparison with experiments

We next quantitatively confront the nested Pump-Leak model to the data acquired by Alice Williart. The model displays a high number of fitting parameters. To reduce overfitting, we decided to use the parameters estimated independently in Chapter.1 (see Table.2.1). Note that the surface at which the nuclear envelope becomes tensed S^* (see Eq.S.112) was estimated from the 2D images of the nuclei (see Fig.2.2.B). The subsequent comparisons with experiments are thus done without any adjustable parameters. We first check that the shapes predicted by the theory qualitatively match the observed 3D images of the confined nuclei Fig.2.6.A. Encouraged by these early correlations, we further compared the nucleus volume and projected surface data to our model predictions Fig.2.6.B and C.

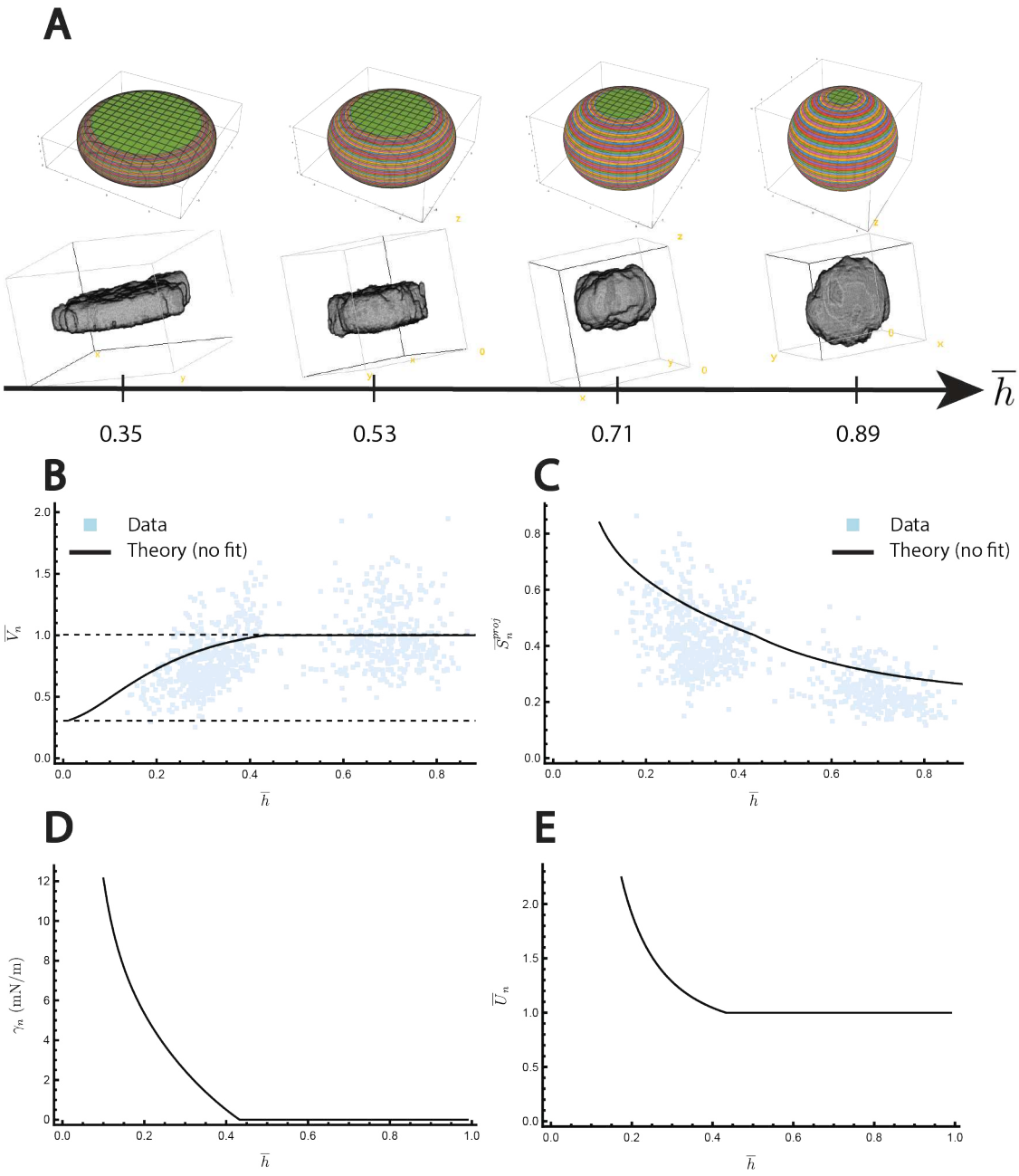

Figure 2.6: **The nested Pump-Leak model explains quantitatively the nuclear volume loss observed upon moderate uniaxial confinements.** (A) Qualitative agreement between the shapes solutions of the nested Pump-Leak model (see Eq.2.12,Eq.2.14,Eq.2.15) and the 3D reconstruction images of Hela Cell nuclei at different confinements. (B)&(C) Comparison between theory (Black) and Experiment (Light blue). The black lines are the solution of Eq.2.3 with no fitting parameters. The parameters used are listed in Table.2.1. (D)&(E) Further predictions of the nested Pump-Leak model for the tension γ_n (in real unit) at the nuclear envelope and the normalized nuclear potential difference $\overline{U}_n$. The normalization is done with respect to the potential before confinement.

Although the data exhibits important variations, the theory and the experiments are in good agreement (see Fig.2.6). Moreover, the nested Pump-Leak model makes additional predictions that can be tested experimentally. It predicts that both the NE tension γ_n and the normalized nuclear membrane potential difference $\overline{U}_n$ rise sharply at the threshold confinement height for which the nucleus volume

starts to decrease. Methods have been developed to measure both quantities. Mechanosensitive flipper probes can be used to report quantitatively membrane tension changes in fluorescence lifetime imaging microscopy (FLIM) images of living cells [Dal Molin, 2015]. Nuclear membrane potential difference can be measured through the use of intranuclear microelectrodes [Mazzanti, 2001].

2.6 Discussion

Our theory shows good quantitative agreement with the experiments while the values of the parameters are not precisely known. This raises the question of the origin of the robustness of our predictions? To answer the question, we decided to assess the sensitivity of the nested Pump-Leak solutions $\overline{V}_n$ and $\overline{S}_n$ to the parameters featured in the model. Our analysis shows that only two parameters are critical: $\overline{K} = \frac{K}{kT \cdot 2n_0 \cdot R_0}$ and $\overline{S}^* = \frac{S^*}{S_n^0}$ (see Fig.2.7.A to C). This is not surprising since we normalize the nucleus volume after confinement by its homeostatic value which has the effect to cancel the dependence of the parameters that are not related to the nuclear envelope stretching. We thus emphasize that these graphs are particularly well adapted to characterize the mechanical properties of the nuclear envelope.

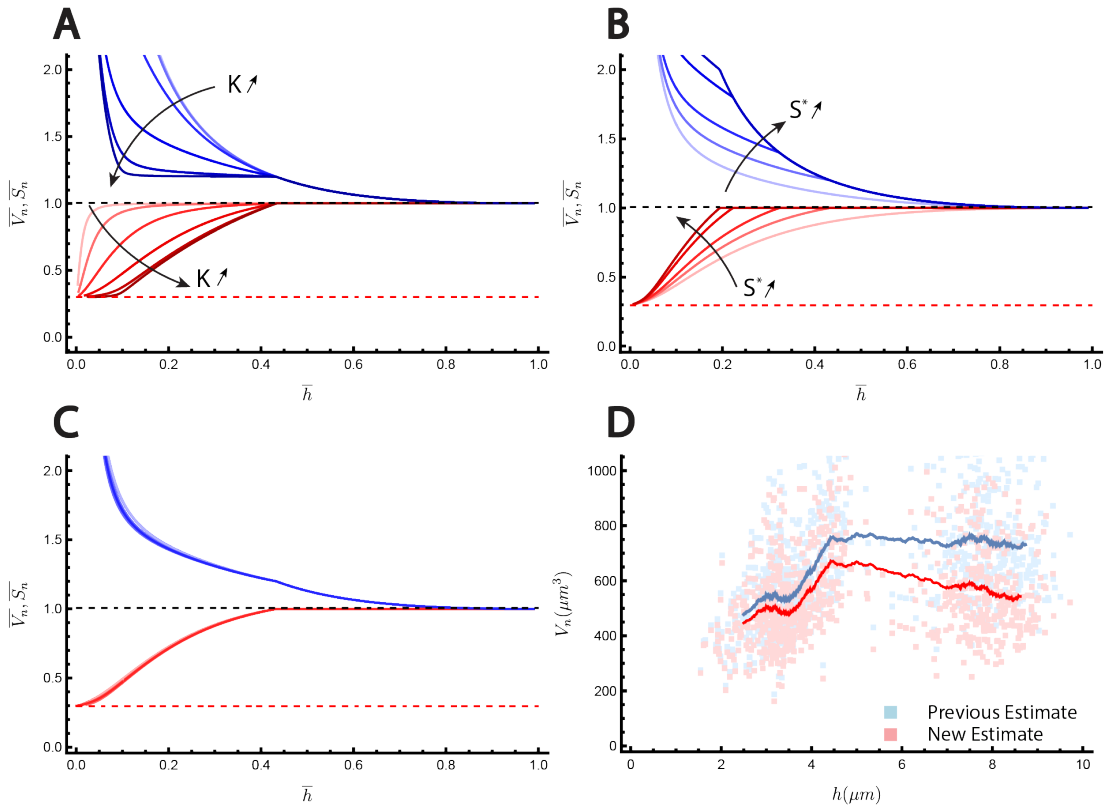

Figure 2.7: **Test of the robustness of the nested Pump-Leak solutions and of the nuclear volume estimate.** (A) to (C) Evolution of the normalized nuclear volume (red) and surface (blue) varying one of the nested Pump-leak parameters listed in Table.2.1. (A) K is varied. From light to dark, K $= 25 \cdot \{10^{-3}, 10^{-2}, 10^{-1}, 1, 10^1, 10^2\}$mN/m. (B) S^* is varied. From light to dark, $S^* = \{1, 1.2, 1.4, 1.8, 2\} \cdot S_n^0$. (C) Superposition of the solutions obtained for different values of the parameters: $Q^{eff} = 2 \cdot \{10^5, 10^7, 10^9\}$, $\alpha_0 = \{0, 0.14, 0.5, 0.9\}$, $z_p = \{0, 0.8, 3\}$, and $z_a = \{0, 1, 2\}$. (D) Comparison of nuclear volume estimates of confined Hela Cells. The estimates are obtained from the measurement of the projected surface S_n^{proj} of the nucleus (see Fig.2.1.B) combined with either Eq.2.1 (previous estimate), or Eq.2.19 (new estimate).

However, with the current data in our possession, the characterization is limited by the important variations of the nucleus volume at the population level. At the time of redaction of the thesis, experiments are being optimized to reduce these variations. The idea behind this noise reduction is to synchronize the cells at the same stage of their cell cycle. Different methods exist, cells can be reversibly blocked at a specific stage of their cycle, or they can be sorted using dies that shine at a certain stage of the cycle. Another source of data improvement is the formula that was used to estimate the volume (see Eq.2.1 and Fig.2.1.B). While the formula is of high accuracy at strong confinements, its quality deteriorates at weak confinement (see Fig.2.6.A). Nevertheless, for the current project at stake, namely, to understand the loss of volume at strong confinement, we show that the formula is a good approximation. To do so, we use Eq.2.18 to infer B from the projected surface area measured. Nuclear volume is then estimated in a new way using Eq.2.19. Fig.2.7.D shows good agreement between both estimates in the regime of volume loss which is of interest here. Interestingly, this new inference shows a first slight nuclear volume increase as h is decreased. This increase can be understood as follows: Eq.2.1 systematically overestimates the real volume of the nuclei. Moreover, the quality of the estimation deteriorates as h increases. Therefore, having a constant nuclear volume with this estimate (see Fig.2.2.A) implies that the actual nuclear volume must decrease as h is increased in the low confinement regime. But is this effect significative? Our new estimate shows that the nucleus volume increases in average by 25% between $h = 8.5\mu$m where $V_n = 534\mu\text{m}^3$ and $h = 4.4\mu$m where $V_n = 670\mu\text{m}^3$. We however qualify the magnitude of this prediction because our theory seems to slightly overestimate the curvature of the nucleus edge, maybe due to steric crowding of the cytoplasm, which would in turn lead to an overestimation of the effect described (see Fig.2.6.A). This prediction would thus need to be verified by a direct measurement to be validated. Such a verification could be done by fluorescence exclusion measurement of nuclear volume using the recent protocol proposed in [Pennacchio, 2022]. Nevertheless, we point out that this nuclear volume increase upon confinement is reminiscent of recent studies that correlate the mechanical state of the envelope to the increase of nuclear protein import [Elosegui-Artola, 2017], [Andreu, 2022] and [Pennacchio, 2022]. We emphasize that this effect, if prealably validated experimentally, could be incorporated easily in our model, at the expense of adding more phenomenological parameters.

Moreover, in the current version of the model, we predict that the cell volume remains constant for all confinement heights and thus that the volume of the cytoplasm increases in the regime of nuclear volume loss. This increase originates from the assumption that the total number of osmolytes in the cell remains constant for all the confinement heights h and that the subsequent loss of metabolites during the nuclear shrinkage leads to an increase of the cytoplasmic osmolytes number which in turn results in its swelling. This prediction goes against previously published experiments that shows that Hela cells could lose up to 20% of their volume 100 ms after confinements [Venkova, 2022]. Due to lack of experimental evidence on the origin of this volume loss, we did not include this effect in our model. Yet, we propose two interpretations of this cellular volume loss which was shown to occur at constant dry mass. First, it may originate in the formation of transient small pores upon confinement which would lead to the loss of metabolites and small osmolytes. Metabolites were shown to play a second order role in the dry mass (see Chapter 1) which would thus allow to understand the loss of volume at constant dry mass observed. Experiments were conducted to test this hypothesis by adding in the external medium propidium iodide dies which are impermeant to the plasma membrane and assess if they enter the cell during the compression. The entry of these dies would allow to demonstrate that the plasma membrane is damaged and that transient pores form. However, no cellular propidium iodide could be observed after confinements of the cells. We emphasize that this does not invalidate entirely the hypothesis since propidium iodide is still much bigger than an amino-acid. We nevertheless looked for another theoretical interpretation of the cell volume loss upon confinement at constant dry mass and constant metabolite number. Our proposition relies on four fundamental observations. (1) Potassium concentration, about

140mMol inside the cell, is higher than in the external medium where it is about 5mMol [Rob Philipps, 2015]. (2) Ions channels are mechanosensitive and their threshold mechanosensitivity differs. Besides, potassium channels were shown to have a low threshold mechanosensitivity [Schmidt, 2012]. (3) Potassium channels can be reversibly activated or inactivated following a change of conformation [Kuang, 2015]. (4) Potassium ions are conducted very efficiently at near diffusion-limited rates (10^7ion channel$^{-1} \cdot s^{-1}$) if the channel is activated [Sansom, 2002]. Based on these observations we propose the following working model: during the compression, potassium channels are preferentially activated over sodium channels. There is thus a diffusion-driven outflux of potassium during the compression (and associated counterions) which would in turn lead to: an outflux of water, a decrease of membrane tension and a subsequent inactivation of the channels. One critical prediction that would allow to test the validity of this theoretical proposition is that the volume loss of cells upon confinement should be reversible following the inactivation of the potassium channels. The cell volume should thus recover its homeostatic value in the tenth of minutes range after the compression.

To conclude, our results collectively demonstrate that the nested Pump-Leak model provides a consistent quantitative description of the nuclear volume loss upon moderate confinements. However, the model assumes a phenomenological non-linear elastic constitutive equation for the nuclear envelope. We therefore propose in the next section to investigate the origin of this non-linearity having in mind that it was shown to be highly correlated with the disappearance of nuclear folds and wrinkles at moderate confinements.

3 Nuclear folds

3.1 Introduction

3.1.1 Physiological importance of nuclear folds

Interphase nuclei are often depicted as smooth spherical bags containing the genetic code Fig.2.8.A. This conception is largely idealized: nuclei adopt a wide variety of shapes throughout biology Fig.2.8. Interestingly, this zoology of nuclear shapes can either be physiological or associated to diseases. Physiologically, specific nuclear shapes can serve cell function. In migration for example, the nucleus, which is the stiffest organelle of the cell, acts as a ruler: cells confronted to paths of various width choose the path of minimum nuclear deformations [Renkawitz, 2019]. To cope with this feature, neutrophils, which are immune cells and thus need to migrate and deform a lot, have adapted the mechanical and geometrical properties of their nuclei in order to enhance their migration ability Fig.2.8.E. Not only nuclear shapes influence migration but they also correlate with cell fate decision. In mouse embryo, nuclei which are at the periphery of the embryo (blue nuclei in Fig.2.8.B) are less wrinkled and more compressed than their homolog (red nuclei in Fig.2.8.B). Those two categories of cells are known to later have very different fates. The origin of the link between cell fate and nuclear shape is still unclear at the time of redaction of the thesis. However, recent studies have shown that mechanical forces applied to the nucleus regulates nucleocytoplasmic transport [Andreu, 2022]. For example, the YAP transcription factor was shown to translocate into the nucleus after stretching of the envelope which in turn triggers the genetic activation of multiple signaling pathways. On the other hand, abnormal nuclear shapes are likely deleterious for cell function as they are associated to many diseases such as cancer (Fig.2.8.C and G) and laminopathies (Fig.2.8.I) sadly known for the progeria syndrome.

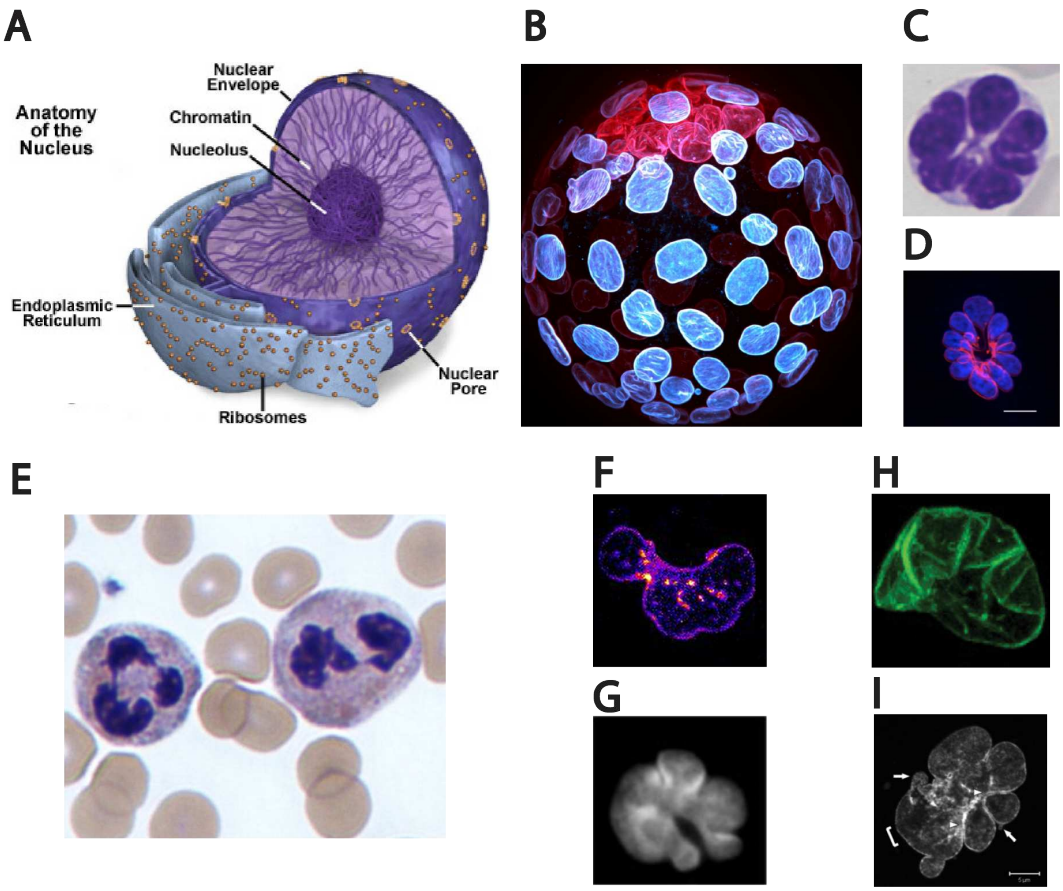

Figure 2.8: **Zoology of nuclear shapes.** (A) Typical textbook representation of a nucleus[a]. (B) In vitro mouse embryo. Nuclei are labeled in blue for mural trophectoderm cells or red for polar trophectoderm cells. Courtesy of Jean-Leon Maitre. (C)&(D) Flower-like nuclei observed in leukemic cells (top) [Matsuoka, 2005] and cells where SUN2 is overexpressed (bottom) [Donahue, 2016]. Chromatin is stained in blue and SUN2 in red. (E) Typical multilobulated Neutrophil nuclei. Extracted from Wikipedia[b]. (F) A tetraploid RPE-1 nucleus. Courtesy of Simon Gemble. (G) A leukemic cell nucleus [Fukuda, 2005]. (H) Nucleus of a mouse embryonic fibroblasts prealably detached from the collagen-coated glass-bottomed dish using trypsin [Kim, 2015]. (I) Nucleus of a progeria cell [Taimen, 2009].

[a]Extracted from: https://micro.magnet.fsu.edu/cells/nucleus/nucleus.html
[b]Extracted from: https://en.wikipedia.org/wiki/Neutrophil

All these examples highlight the tight relationship between nuclear shapes and cell function. It is thus of paramount importance to understand the origins of those shapes. However, both the wide variety of shapes and the multiplicity of nuclear mechanical components make it unlikely to describe these forms with one unified model. For instance, we initiated a disjoint collaboration with Simon Gemble in the team of Renata Basto to understand the influence of ploidy on nuclear shapes. While the model that we present in this chapter focuses on the role of chromatin and lamina, our preliminary results in the ploidy project instead point to the role of microtubules and of chromatin decondensation on the multilobulated nuclei that are observed in polyploid cells (see Fig.2.8.F). Here, we focus on one particular shape: the teardrop like folds observed in Hela Cell lines Fig.2.9.B. Although specific, these folds are of tremendous importance as they were shown to be at the root of the mechanotransduction of external mechanical signals and ultimately in the cellular proprioception ([Lomakin, 2020],[Venturini, 2020], [Cosgrove, 2021]). When the mechanical signal is a uniaxial confinement, the resulting nuclear envelop smoothening described previously was shown to successively trigger: the activation of the cPLA2-AA pathway, the myosin II

recruitment at the cortex, the enhancement of cell contractility, and finally the migration. Understanding the origin of these wrinkles as well as their unfolding following stretching might thus be an interesting lead towards understanding compression induced cell migration and possibly metastasis.

3.1.2 Motivations

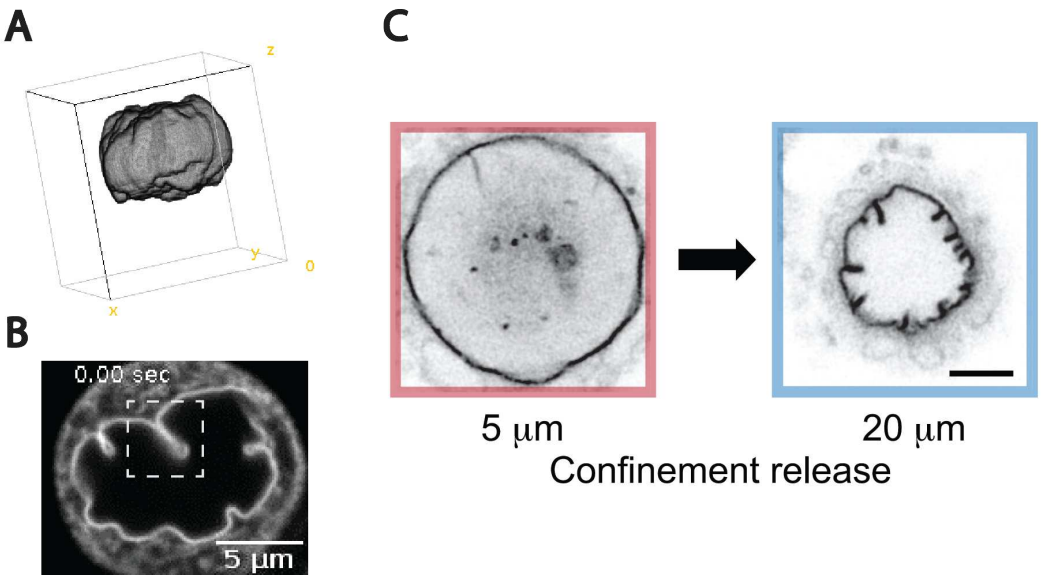

Figure 2.9: **Properties of nuclear folds.** (A) 3D reconstruction of a Hela cell nucleus confined at $h = 8\mu$m. (B) Top projected view of a non-confined Hela cell nucleus. Inset: teardrop. (C) Nuclear envelope of the same Hela cell line confined to $h = 5\mu$m and subsequently unconfined to $h = 20\mu$m. Extracted from [Lomakin, 2020].

In 2D, the nuclear folds under study adopt teardrops like shapes (see Fig.2.9.B). However, 3D images of nuclei instead show that the folds are closer to trench shapes with curved edges (see Fig.2.9.A). Films of the folds clearly demonstrate that they form well defined structures that are stable for long period of time. Besides, natural thermal fluctuations of the nuclear envelope are not strong enough to modify the shape of these folds. We enumerate three important properties of the folds. (1) As explained earlier, they disappear with increasing uniaxial confinement (Fig.2.2.B). (2) The process is reversible: removing the confinement makes the folds appear again (Fig.2.2.C). (3) They are systematically oriented inward. These properties are reminiscent of an elastic mechanical instability such as buckling. Buckling have already been proposed, in the literature, to be at the root of some nuclear shapes. In [Kim, 2015], the authors describe the nucleus as an elastic shell, compressed by the external cytoskeleton, to explain the crumpling of the nuclear envelope upon cell detachment. This is not the hypothesis that we develop in this chapter because the shapes produced by such a model do not match the forms of the folds that we observe (Fig.2.8.H). Instead, we propose an instability originating from the difference of mechanical properties of the chromatin and of the lamina. For clarity, we ignore the cytoskeleton, but we discuss in Section.4 how to include it in our framework.

3.2 Results

3.2.1 Modelling

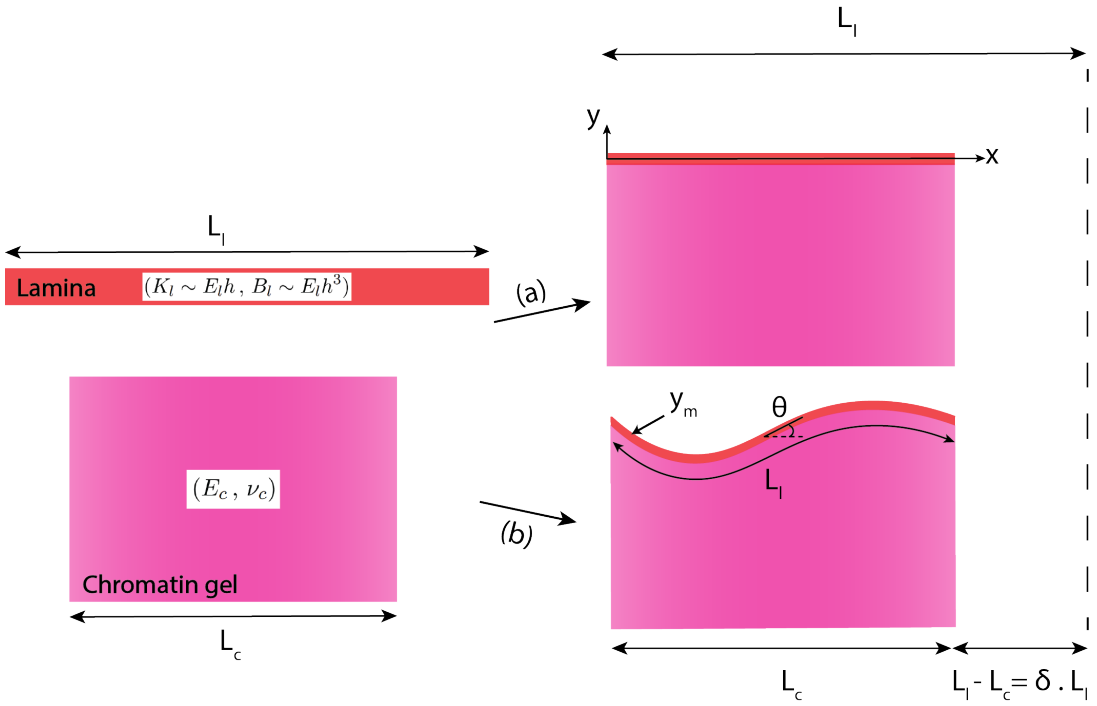

Figure 2.10: **Schematic representation of the mechanical system modelling the nucleus.** A semi-infinite soft substrate filled with chromatin is perfectly bound to a thin stiff lamina layer. Two limiting regimes are considered: (a) Lamina is purely compressed. (b) Lamina is purely bent.

We model the nucleus as being composed by a soft chromatin elastic substrate enclosed by a thin stiff elastic nuclear envelope. Both materials have distinct mechanical properties as well as different resting surfaces. Lamina and chromatin are known to interact strongly through a host of inner nuclear membrane proteins such as emerin, sun complex, lamin-associated proteins (Lap2b) and lamin B receptors (LBR). We thus assume that both materials are perfectly attached in our model. Based on [Brau, 2011] and appropriate order of magnitude estimates, we show that this disparity of properties creates a mechanical frustration strong enough to buckle the nuclear envelope. For simplicity, we consider an infinite, negative half plane filled with chromatin which is covered by a thin layer of lamina. Both materials are assumed to have homogeneous mechanical properties. Based on the thin shell theory, we characterize the lamina by two moduli: the bending modulus $B \sim E_l \cdot h^3$ and the stretching modulus $K \sim E_l \cdot h$, with h and E_l the typical width and young modulus of the lamina. The chromatin is similarly characterized by two moduli that we choose to be the young modulus E_c and the Poisson's ratio ν_c. Importantly, both materials do not have the same resting lengths. We respectively call L_c and L_l such respective lengths for which the elastic stresses of each material vanish. We also assume that $L_l > L_c$. This hypothesis will be justified in Section.3.3. We finally build a dimensionless control parameter δ which represents the relative compression ratio of the lamina:

$$\delta = \frac{L_l - L_c}{L_l} \tag{2.27}$$

3.2.2 Weak mechanical frustration

We first assess what is the equilibrium conformation of the mechanical system depicted in Fig.2.10 in the regime of weak deformations, i.e. $\delta << 1$. To answer the question, we make the following thought experiment. We start from the two materials taken separately and bind them with each other. Among the ensemble of resulting equilibrium configurations we consider two limiting states (Fig.2.10). (a) A flat state where the lamina is homogeneously compressed. (2) A bent state where the lamina is purely bent (Fig.2.10). Note that these states are not chosen randomly. When there is no frustration, the flat state is the equilibrium configuration. On the other hand, at higher δ the purely bent state is favorable. Indeed, in a thin shell theory, i.e., $h \longrightarrow 0$, bending deformations are energetically more favorable because of the cubic scaling of the bending modulus with h compared to compression deformations for which the stretching modulus scales linearly with h. The question becomes to determine what is the threshold value δ^* for which the geometrical transition occurs. We solve the problem in two steps. We first derive the free energy of each state depending on the mechanical parameters of the problem. We then compare the resulting free energies to assess their relative stabilities depending on the control parameter δ.

Purely compressed state We first consider the energetic cost of the flat state (Fig.2.10). The free energy per unit transversal length (along the z-axis in Fig.2.10) of the whole system reads:

$$\mathcal{F}_a \sim \frac{E_c}{2} \cdot L_c L_y \cdot (\frac{L - L_c}{L_c})^2 + \frac{K}{2} \cdot L_l \cdot (\frac{L - L_l}{L_l})^2 \tag{2.28}$$

Where, L is the horizontal length of the system and L_y the vertical length occupied by the chromatin. Note that this free energy is valid up to a factor unity because we discarded the Poisson's ratio for clarity. Note that Eq.2.28 only considers states where chromatin has a constant horizontal length over its entire width. This is justified because the nucleus is in reality spherical which translates into periodic boundaries in our simplified model. Based on the observation that thermal fluctuations do not change the shape of the folds, we assume that the system chooses L by minimizing its free energy. The resulting equilibrium horizontal length L^{eq} adopted by the system reads:

$$L^{eq} = \frac{E_c \cdot L_y + K}{E_c \cdot \frac{L_y}{L_c} + \frac{K}{L_l}} \tag{2.29}$$

Note that, when $E_c \cdot \frac{L_y}{L_c} >> \frac{K}{L_l}$, the equilibrium length chosen by the system is simply the resting length of the chromatin L_c. Using that $K \approx E_1 \cdot h$, we get the criterion:

$$\frac{L_l}{L_c} \cdot \frac{L_y}{h} >> \frac{E_l}{E_c} \tag{2.30}$$

In our simple scaling model, and for sake of simplicity, we assume that $L_y \longrightarrow \infty$ and $h \longrightarrow 0$. Under these assumptions, the criterion is always verified, and the system adopts the resting length of the chromatin $L^{eq} = L_c$. This is intuitive, it is energetically infinitely costly to deform an infinite system. However, for the nucleus, we highlight that the state chosen by the system is likely an intermediate state where the lamina is compressed, and the chromatin is stretched. Indeed, we estimate that $\frac{E_l}{E_c} \approx 10^2 - 10^3$ and $\frac{L_y}{h} \approx 10^2$ (see Tab.2.2). Nevertheless, following our simplified hypothesis, the free energy of the flat state reads:

$$\mathcal{F}_a \approx \frac{K}{2} \cdot \delta^2 \tag{2.31}$$

Purely bent state We now suppose that the membrane has buckled. We closely follow the approach proposed in [Brau, 2011] to derive the free energy of such a state. We remind that we approximate the

thin membrane to be inextensible because the bending modulus scales as $B \sim E_l \cdot h^3$ and the stretching modulus scales as $K \sim E_l \cdot h$. Assuming that $h \longrightarrow 0$ thus makes bending energetically more favorable. For clarity, we first derive the normal force balance equation of an inextensible free planar sheet under compression. We will then add the contribution of the chromatin in the next paragraph. The normal force balance can be derived by minimizing the bending energy (per unit of transverse length L_z) of the lamina layer $U_b = \int_0^{L_l} \left[\frac{B}{2} \cdot \dot{\theta}^2\right] \cdot ds$ subjected to three constraints:

$$\delta = \frac{1}{L_l} \int_0^{L_l} [1 - Cos[\theta]] \cdot ds \approx \frac{1}{L_l} \int_0^{L_l} \left[\frac{\theta^2}{2}\right] \cdot ds \tag{2.32}$$

$$\dot{x}_m = Cos[\theta] \approx 1 \tag{2.33}$$

$$\dot{y}_m = Sin[\theta] \approx \theta \tag{2.34}$$

Where, Eq.2.32 is a global constraint that enforces the inextensibility of the lamina layer and Eq.2.33 and Eq.2.34 are two local geometrical constraints. We emphasize that we consider here small deformations, i.e., $\theta << 1$. As such, we linearized all the previous constraints to the smallest order in θ. We introduce two Lagrange multipliers in order to enforce the constraints on δ and $\dot{y}$ that we call P and Q. Note that Q can in principle depends on x because the associated constraint is local.

$$\mathcal{S} = \int_0^{L_l} \underbrace{\left[\frac{B}{2} \cdot \dot{\theta}^2 - Q \cdot (\dot{y}_m - \theta) - P \cdot (\frac{\theta^2}{2} - \delta)\right]}_{\equiv \mathcal{L}(\theta, \dot{\theta}, \dot{y}_m)} \cdot dx \quad \text{With,} \quad P \sim \frac{\partial \mathcal{S}}{\partial(\delta \cdot L_l)} \tag{2.35}$$

We highlight that P represents the pressure, or minus the tension inside the sheet. Indeed, when the volume decreases, P increases Eq.2.35. Extremizing $\mathcal{S}$ leads to the famous Euler-Lagrange equations: $\frac{\partial \mathcal{L}}{\partial q_i} - \frac{d}{dx} \cdot \left(\frac{\partial \mathcal{L}}{\partial \dot{q}_i}\right) = 0$, with $\mathcal{L}$ the Lagrangian of the system. Applied to the problem at stake, the Euler equations become:

$$\begin{cases} Q = cste \\ Q - P \cdot \theta - B \cdot \ddot{\theta} = 0 \end{cases} \tag{2.36}$$

Differentiating the latter equation finally leads to the famous Foppl-Von-Karman equation of an inextensible free planar sheet resting initially at $y = 0$ and invariant along one direction:

$$B \cdot y_m^{(4)} + P \cdot y_m^{(2)} = 0 \tag{2.37}$$

With, y_m representing the vertical elevation of the membrane (Fig.2.10). This equation is equivalent to the normal force balance on an infinitesimal portion of surface of the lamina layer. Note that the tangential force balance was already considered since the pressure P is homogeneous in the lamina layer.

For completeness, we next add to Eq.2.37 the normal force exerted by the chromatin substrate $\sigma^c_{yy}(x, y = 0)$. We remind that in the limit of small deformations, $\sigma^c_{yy}(x(s), y_m(s)) \approx \sigma^c_{yy}(x, y = 0)$. We further add the subscript "$_m$" to emphasize that y_m represents the vertical elevation of the membrane to be distinguished with y which represents the vertical coordinate. Inside the chromatin, i.e $(y < 0)$, the force balance reads:

$$\overline{\nabla} \cdot \overline{\overline{\sigma}}^c = 0 \tag{2.38}$$

We then use Hooke's law as a linear constitutive equation relating the elastic stress tensor of the chromatin,

$\overline{\overline{\sigma}}^c$, and the strain tensor $\overline{\overline{\epsilon}}^c$. In vectorial notations the Hooke's equation reads:

$$\overline{\overline{\sigma}}^c = \frac{E_c}{1+\nu_c} \cdot \left[\overline{\overline{\epsilon}}^c + \frac{\nu_c}{1-2\nu_c} \cdot \mathrm{Tr}(\overline{\overline{\epsilon}}^c) \cdot \mathbb{1} \right] \tag{2.39}$$

It is straightforward to show that:

$$\overline{\nabla} \cdot \overline{\overline{\epsilon}} = \frac{1}{2} \cdot \left(\overline{\nabla} \cdot (\overline{\overline{\nabla}}(\overline{u})) + \overline{\nabla} \cdot (\overline{\overline{\nabla}}(\overline{u}))^T \right) = \frac{1}{2} \cdot \left(\Delta \overline{u} + \overline{\nabla}(\overline{\nabla} \cdot \overline{u}) \right) \tag{2.40}$$

Where, $\overline{u}$ is the displacement field inside the chromatin. We next combine equations 2.38,2.39 and 2.40 with the appropriate boundary conditions to obtain the close problem to solve:

$$(1-2\nu_c) \cdot \Delta \overline{u} + \overline{\nabla}(\overline{\nabla} \cdot \overline{u}) = 0 \quad \text{With,} \quad \begin{cases} u_x(x, y=0) = 0\,,\ u_x(x, y=-\infty) = 0 \\ u_y(x, y=0) = y_m(x)\,,\ u_x(x, y=-\infty) = 0 \end{cases} \tag{2.41}$$

Note that we set $u_x(x, y=0) = 0$ because it is an order 2. Indeed, $\dot{x} = cos(\theta) \approx 1 - \frac{\theta^2}{2}$. Hence, $u_x(x, y=0) \sim \theta^2 \cdot L$. Projected on each coordinates the PDE equation reads:

$$\begin{cases} 2 \cdot (1-\nu_c) \cdot \partial_x^2 u_x + (1-2\nu_c) \cdot \partial_y^2 u_x + \partial_x \partial_y u_y = 0 \\ 2 \cdot (1-\nu_c) \cdot \partial_y^2 u_y + (1-2\nu_c) \cdot \partial_x^2 u_y + \partial_x \partial_y u_x = 0 \end{cases} \tag{2.42}$$

We solve Eq.2.42 by going into Fourier space for the x coordinate. Eq.2.42 becomes:

$$\begin{cases} -2 \cdot (1-\nu_c) \cdot k^2 \tilde{u}_x + (1-2\nu_c) \cdot \partial_y^2 \tilde{u}_x - ik \cdot \partial_y \tilde{u}_y = 0 \\ 2 \cdot (1-\nu_c) \cdot \partial_y^2 \tilde{u}_y - (1-2\nu_c) \cdot k^2 \tilde{u}_y - ik \cdot \partial_y \tilde{u}_x = 0 \end{cases} \tag{2.43}$$

Where we have made use of the following convention:

$$\tilde{u}_i(k, y) = \int_{-\infty}^{\infty} u_i(x, y) \cdot e^{ikx} dk \tag{2.44}$$

Eq.2.43 is then uncoupled by expressing $ik \cdot \partial_y \tilde{u}_y$ with the first equation and injecting it in the second equation prealably multiplied by ik. We obtain:

$$\begin{cases} ik \cdot \partial_y \tilde{u}_y = -2 \cdot (1-\nu_c) \cdot k^2 \tilde{u}_x + (1-2\nu_c) \cdot \partial_y^2 \tilde{u}_x \\ \partial_y^4 \tilde{u}_x - 2k^2 \partial_y^2 \tilde{u}_x + k^4 \tilde{u}_x = 0 \end{cases} \tag{2.45}$$

The solutions for $\tilde{u}_x$ and $\tilde{u}_y$ that fulfils the boundary condition thus read:

$$\begin{cases} \tilde{u}_x = ik \frac{\tilde{y}_m}{3-4\nu_c} \cdot y \cdot e^{|k|y} \\ \tilde{u}_y = \frac{\tilde{y}_m}{4\nu_c - 3} \cdot ((4\nu_c - 3) + y \cdot |k|) \cdot e^{|k|y} \end{cases} \tag{2.46}$$

As a side note, it is interesting to go back in real space in the regime where $y_m(x)$ is a pure harmonic deformation. Assuming, $y_m(x) = \xi_0 \cdot cos(qx)$, we show that the chromatin displacement field is screened over a length of order q^{-1}:

$$\overline{u}(x, y) = \begin{pmatrix} \frac{qy}{3-4\nu_c} \cdot sin(qx) \\ (1 + \frac{qy}{4\nu_c - 3}) \cdot cos(qx) \\ 0 \end{pmatrix} \cdot \xi_0 \cdot e^{qy} \tag{2.47}$$

We next use Eq.2.46 to compute the Fourier transform of the normal stress:

$$\tilde{\sigma}_{yy}(y=0) = E_c^{eff} \cdot i \cdot sign(k) \cdot -i \cdot k\tilde{y_m}(k) = E_c^{eff} \cdot TF(\frac{1}{\pi x}) \cdot TF(\partial_x y_m) \tag{2.48}$$

Such that in real space we have:

$$\sigma_{yy}(y=0) = E_c^{eff} \cdot \mathcal{H}(\partial_x y_m) \quad \text{With,} \quad E_c^{eff} = \frac{2E_c(1-\nu_c)}{(1+\nu_c)(3-4\nu_c)} \tag{2.49}$$

Where, $\mathcal{H}$ is the Hilbert operator defined as $\mathcal{H} = \frac{1}{\pi x} \star \partial_x y_m$ with "$\star$" representing the product of convolution. We highlight two interesting properties of the Hilbert operator: $\mathcal{H}(cos(qx)) = sin(qx)$ and $\mathcal{H}(sin(qx)) = cos(qx)$. We finally inject Eq.2.49 into Eq.2.37 to obtain the equation describing the equilibrium configuration of the lamina:

$$B \cdot y_m^{(4)} + P \cdot y_m^{(2)} + E_c^{eff} \cdot \mathcal{H}(\partial_x y_m) = 0 \tag{2.50}$$

An harmonic deformation of the form $y_m = \xi_0 \cdot cos(qx)$ is solution provided that:

$$P = B \cdot q^2 + \frac{E_c^{eff}}{q} \tag{2.51}$$

The envelope chooses the wave vector that minimizes its internal pressure P and as such its energy Eq.2.35 because it is incompressible and the chromatin is at its resting length (see Sec.3.2.2). Hence, the q selected is:

$$q_0 = \left(\frac{E_c^{eff}}{2B}\right)^{1/3} \tag{2.52}$$

The latter frequency can be understood as being the resultant of two opposite physical contributions. First, the bending of the lamina which intuitively tends to penalize large frequencies. Second, the deformation of the chromatin substrate which tends to penalize small frequencies. Indeed, harmonic lamina deformations of frequency q_0 propagate in the chromatin medium over a characteristic vertical distance of order q_0^{-1} Eq.2.47. Moreover, we see that Eq.2.51 introduces a cut-off pressure below which wrinkling is inadmissible:

$$P^* = P(q_0) = 3 \cdot B^{1/3} \cdot \left(E_c^{eff}\right)^{2/3} \tag{2.53}$$

We finally determine the amplitude of the wrinkle deformation -ξ_0 - through the inextensibility condition Eq.2.32:

$$\xi_0 = \frac{\lambda_0}{\pi} \cdot \delta^{1/2} \tag{2.54}$$

Having found the shape that minimizes the wrinkled state we compute the free energy associated to it. The energy associated to the deformation of the substrate reads:

$$\mathcal{F}_s = E_c^{eff} \cdot q_0 \cdot \int_0^L y^2 dx \tag{2.55}$$

and the energy of the full system {lamina + chromatin} finally reads:

$$\mathcal{F}_b = \delta \cdot \left(E_c^{eff}\right)^{2/3} \cdot B^{1/3} \tag{2.56}$$

Relative stability of each state By virtue of the different power law dependence of the free energies of each state with δ Eq.2.31,2.56, the theory predicts a transition from a state of pure compression to a

state of pure bending. This transition occurs at a cut-off compression δ_1^* that can be expressed as:

$$\delta > \delta_1^* \sim \left(\frac{E_c}{E_l}\right)^{2/3} \tag{2.57}$$

Note that this transition is reminiscent of a first order transition because there is a discontinuity in the pressure P which is defined as a first order derivative of the energy. We highlight that this might be an artefact resulting from only considering two limiting states.

Estimations We finally summarize in Table.2.2 the estimates of the important physical parameters that arise in our scaling theory. The dependence of these parameters with ν_c is weak and we take it to be $\frac{1}{2}$ for simplicity.

Parameters	Value	Meaning
K	25mN/m	Stretching modulus of the lamina [Dahl, 2004]
e	14nm	Thickness of the lamina [Turgay, 2017]
$E_l \sim \frac{K}{e}$	$2 \cdot 10^6$Pa	Young modulus of the lamina
E_c	$10^3 - 10^4$Pa	Young modulus of the chromatin [Hampoelz, 2011], [Nava, 2020]
P^*	$4 \cdot 10^{-4}$N/m	Equilibrium pressure in the lamina layer Eq.2.53
δ_1^*	$7 \cdot 10^{-3}$	Cut-off above which the wrinkling transition occurs Eq.2.57
$\lambda_0 = \frac{1}{q_0}$	3μm	Wavelength of the wrinkle Eq.2.52

Table 2.2: **Estimation of the nuclear wrinkling transition parameters.**

The salient conclusion of these scaling estimates is that the threshold δ_1^* to reach the wrinkling transition is very low. Only one percent mismatch between the two resting lengths of the chromatin and of the lamina is indeed sufficient for the nucleus to wrinkle. Such a fine tuning is likely not achieved in biology and may explain why many nuclei are wrinkled. We discuss in Section.3.3 the biological origin of the mismatch. Moreover, the wrinkling wavelength λ_0 is of order the radius of the nucleus. As stated above, this again shows that the consideration of an infinite chromatin medium to model the nuclear folds, though simple and enlightening, is not perfectly rigorous. Nevertheless, λ_0 is a natural length scale of the problem that should remain even in a more complicated model. When compared to the typical perimeter of the nucleus $2\pi R \sim 18\mu m$, we would expect few wrinkles which is somewhat in line with experimental observations Fig.2.9. Another consequence of the low value of the wrinkling threshold δ_1^* is that it is likely that the actual biological strains δ are much larger. Hence, the linear elastic theory presented here is likely not enough to describe accurately the folds. This is reassuring. First because the folds are localized deformations while the wrinkles are not. Second, because Eq.2.50 cannot explain why the folds are oriented inward since it is symmetric with respect to the plan $y = 0$.

3.2.3 Larger mechanical frustration

What if, in the framework presented above, we increase δ? It is clear that deformations will become larger and eventually linear elasticity will break down. The study of large deformations of solid materials is well known to be difficult due to the combined complexity of geometric non-linearities and material non-linearities. Our goal in our scaling framework is to build the simplest model that corroborate the main observations. Namely that wrinkles are oriented towards the interior of the nucleus. And that there is a strain focusing effect, i.e., that the deformation is focused inside the folds Fig.2.9.C. The study of moderately large deflection of planar sheet was described successfully by the non-linear Foppl-Van-Karman equations [Landau, 1959]. However, it is characterized by an upside-down symmetry which

means that the associated non-linearities cannot explain why the folds orientation is biased towards the interior of the nucleus. This implies that the substrate non-linearities are at the root of the symmetry breaking. In a quest for simplicity, we only account for the geometric non-linearities present in the Lagrange deformation tensor of the substrate. We again follow closely the approach developed in [Brau, 2011]. The chromatin strain tensor now reads (see Eq.2.40 for comparison):

$$\overline{\overline{\epsilon}} = \frac{1}{2} \cdot \left(\overline{\overline{\nabla}}_X(\overline{u}) + \overline{\overline{\nabla}}_X(\overline{u})^T + \overline{\overline{\nabla}}_X(\overline{u})^T \cdot \overline{\overline{\nabla}}_X(\overline{u}) \right) \tag{2.58}$$

Note that X should in principle accounts for the material coordinates, i.e. the coordinates before deformation of the substrate. Yet, in this simple model since we do not take the geometric non-linearities of the plate into account we still assume that $x \approx X$. Moreover, we still assume that the strain is still small enough that we can use Hooke's law Eq.2.39 but with the strain tensor now defined by Eq.2.58. Note that this model is a simplified version of the Saint-Venant Kirchoff model [Holzapfel, 2000]. The equation on the displacement now reads:

$$(1-2\nu_c) \cdot \Delta u_i + \nabla_i(\vec{\nabla} \cdot \overline{u}) + \partial_i \partial_l u_k \cdot \partial_l u_k + (1-2\nu_c) \cdot \partial_j^2 u_k \cdot \partial_i u_k \tag{2.59}$$

We refer the reader to [Brau, 2011] for a more detailed derivation of the solution of this problem. We instead propose here a simple scaling justification for the non-linearity that appears in the normal force balance due to the substrate. For a harmonic deformation of the substrate, we had:

$$B \cdot y_m^{(4)} + P \cdot y_m^{(2)} + E_c^{eff} \cdot q \cdot y_m = 0 \tag{2.60}$$

We see from the strain that the non-linearity is quadratic in the displacement Eq.2.58. The non-linearity in the normal force applied to the envelope should thus scale as $\sim y_m^2$ and since there is no length scale associated to the substrate (which is supposed to be infinite) this term must be multiplied by q^2 in order to have a pressure. The equation now reads:

$$B \cdot y_m^{(4)} + P \cdot y_m^{(2)} + E_c^{eff} \cdot q \cdot y_m + E_c^{eff'} \cdot q^2 \cdot y_m^2 = 0 \quad \text{With,} \quad \begin{cases} E_c^{eff} = \frac{2E_c(1-\nu_c)}{(1+\nu_c)(3-4\nu_c)} \\ E_c^{eff'} = \frac{E_c}{2} \cdot \frac{(1-2\nu_c)(13-16\nu_c)}{(1+\nu_c)(3-4\nu_c)^2} \end{cases} \tag{2.61}$$

Where, $E_c^{eff'}$ is an effective modulus built from E_c and ν_c that arises in the calculation [Brau, 2011]. Interestingly, when $\nu_c = 1/2$, $E_c^{eff'} \longrightarrow 0$, the non-linearity disappears. This is consistent. Eq.2.61 is no longer invariant by the change of variable $y_m \longleftrightarrow -y_m$ due to the quadratic non-linearity. Hence, the shapes described by Eq.2.61 do not conserve the volume of the chromatin. A corollary is that if the chromatin is incompressible, i.e. $\nu_c = 1/2$, such quadratic non-linearity cannot develop, and $E_c^{eff'}$ must vanish. We next generalize Eq.2.61 to multi-modal deformations. Similarly to Eq.2.50, this can be done by using the Hilbert operator:

$$B \cdot y_m^{(4)} + P \cdot y_m^{(2)} + E_c^{eff} \cdot \mathcal{H}(\partial_x y_m) + E_c^{eff'} \cdot \left(\mathcal{H}(\partial_x y_m)^2 - < \mathcal{H}(\partial_x y_m) >^2 \right) = 0 \tag{2.62}$$

Where, "<>" represents the average over spatial coordinates. We next look for a periodic solution of period $2q_0^{-1}$, with q_0 the frequency selected by the wrinkled state Eq.2.52. Indeed, a natural way to have a strain focusing effect from a sinusoid is to make one of its minimum grow at the expense of the next minimum. This effect was observed when a thick PDMS substrate bound to a soft thin PDMS film was mechanically compressed [Brau, 2011]. The solution of Eq.2.62 must be smooth and as such can be decomposed into a Fourier series. Solving the problem boils down to determining the Fourier coefficients c_j:

$$y_m = \sum_j c_j \cdot cos(\frac{q_0}{2} \cdot j \cdot s) \tag{2.63}$$

Note that we choose without loss of generality an even profile because we consider the envelope as infinite and as such the choice of the origin of the coordinates is arbitrary. We determine the Fourier coefficients perturbatively. Considering an expansion containing two modes is already sufficient to understand the physics behind the strain focusing effect. We restrict our discussion to this order in this chapter, but the solution obtained can be easily generalized to higher modes [Brau, 2011]. We normalize all the quantities as follow: $\overline{P} = \frac{P}{Bq_0^2}$, $\overline{E}_c^{eff} = \frac{E_c^{eff}}{Bq_0^3} = 2$, $\overline{E}_c^{eff'} = \frac{E_c^{eff'}}{Bq_0^3}$, $\overline{c_i} = c_i \cdot q_0$. Injecting Eq.2.63 into Eq.2.62, and discarding all the terms that are higher than the mode q_0 leads to:

$$\begin{cases} \frac{\overline{c_1}}{16} \cdot \left(17 - 4\overline{P} + 4 \cdot \overline{E}_c^{eff'} \cdot \overline{c_2}\right) = 0 \\ \overline{c_1}^2 = 2 \cdot \overline{c_2} \cdot \left(\frac{5}{\overline{E}_c^{eff'}} + 8 \cdot \overline{c_2}\right) \end{cases} \tag{2.64}$$

Where, $\overline{c_2}$ is determined from the incompressibility constraint (Eq.2.32) to lowest order:

$$\delta = \frac{\overline{c_1}^2}{8} + \frac{\overline{c_2}^2}{2} \tag{2.65}$$

Importantly, the system Eq.2.64 has two distinct solutions:

$$\begin{cases} \overline{c_1} = 0 \\ \overline{c_2} = \pm 2 \cdot \delta^{1/2} \\ \overline{P} = 3 \end{cases} \quad \text{Or,} \quad \begin{cases} \overline{c_1} = \pm \left(2 \cdot \overline{c_2} \cdot \left(\frac{5}{\overline{E}_c^{eff'}} + 8\overline{c_2}\right)\right)^{1/2} \\ \overline{c_2} = -\frac{1}{4\overline{E}_c^{eff'}} - \frac{1}{2} \cdot \left(\frac{1}{4\left(\overline{E}_c^{eff'}\right)^2} + \frac{16}{5} \cdot \delta\right)^{1/2} \\ \overline{P} = \frac{17}{4} + 2 \cdot \overline{E}_c^{eff'} \cdot \overline{c_2} \end{cases} \tag{2.66}$$

The first solution (left system) corresponds to the linear solution found in the previous section Eq.2.53. The second solution (right system) is the (weakly) non-linear solution that develops for larger δ. Importantly, there is a clear upside-down symmetry breaking in this non-linear solution. Indeed, $\overline{P}$ and thus the energy of the system (Eq.2.35) is no longer invariant to a change of sign of the amplitude c_2. Note that we choose the sign of c_2 to be negative because, to develop, the energy associated to the subharmonic solution must be lower than the purely harmonic solution, i.e., $\overline{P} < 3$. We thus obtain a criterion for the stability of the subharmonic mode:

$$\begin{cases} \overline{c_2} < \frac{-5}{8\overline{E}_c^{eff'}} \\ \delta > \delta^*_{2,approx} \end{cases} \quad \text{With,} \quad \delta^*_{2,approx} = \left(\frac{5}{32} \cdot \frac{E_c^{eff}}{E_c^{eff'}}\right)^2 = \left(\frac{5}{8} \cdot \frac{(1-\nu_c)\cdot(3-4\nu_c)}{(1-2\nu_c)\cdot(13-16\nu_c)}\right)^2 \tag{2.67}$$

The analytical value for δ_2^* is an approximation since we only used two modes to deduce the solution. It was shown however than considering 4 modes was sufficient for δ_2^* to converge. Its real value was numerically estimated in [Brau, 2011] and the value found was:

$$\delta_2^* \approx \left(0.105 \cdot \frac{E_c^{eff}}{E_c^{eff'}}\right)^2 \tag{2.68}$$

In principle we could design materials where $\delta_1^* \geq \delta_2^*$ (see Eq.2.57 and Eq.2.67) such that the transition between the flat to folded state could be achieved. Here, we estimate that $\delta_1^* \sim \delta_2^*$ for many values of ν_c

such that the sinusoid regime stability may be very shallow Fig.2.11.

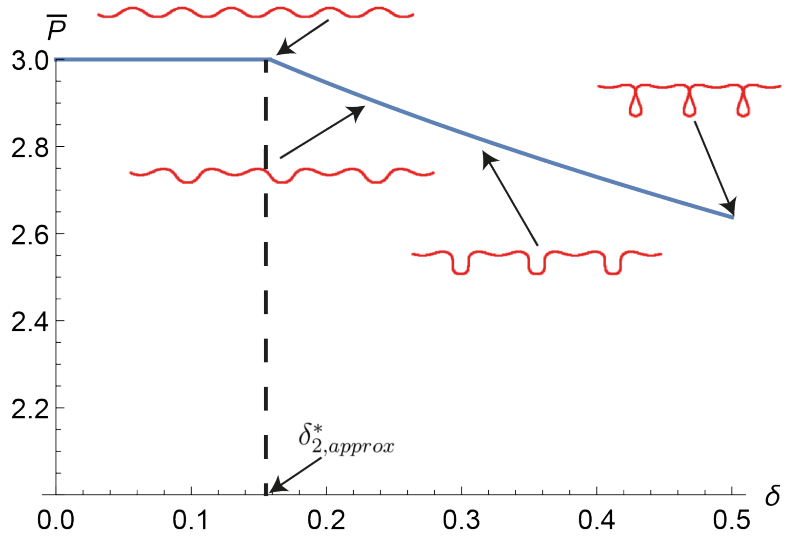

Figure 2.11: **Theoretical prediction of the non-linear scaling theory.** Evolution of the rescaled pressure in the lamina layer as a function of the relative mismatch between the resting lengths δ. For illustration, we display the representative envelope profiles as predicted by Eq.2.63 with two modes for $\nu_c = 0.40$. Note that these profiles are only rigorously justified close to the threshold $\delta^*_{2,approx}$.

3.3 Discussion

So far, the mechanical model that we have presented, although being particularly simplistic when compared to the complexity of the nucleus, have made important predictions that are qualitatively in line with experimental observations. First, the model proposes a natural explanation of why so many nuclei are not smooth. Indeed, we estimate that a disparity of less than 1% between the resting surfaces of the chromatin and of the lamina would be enough to reach the first wrinkling threshold Tab.2.2. Second, the model predicts that the nuclear envelope smoothens when δ is decreased 2.11. This is consistent with the observation that the nuclear envelope looses its folds upon confinement Fig.2.2.B. Indeed, confining the nucleus is equivalent to effectively increase the resting length of the chromatin and thus decrease δ Eq.2.27. Third, we estimate that the folds set the tension in the lamina, which likely dominates the mechanical response of the nuclear envelope, to small values of order ~ -0.1mN/m. This value is two orders of magnitudes smaller than the typical value of the stretching modulus of the lamina K [Dahl, 2004]. A key consequence is that this provides a natural explanation of the success of the phenomenological constitutive non-linear elastic equation that we used in the nested Pump-Leak model. Indeed, when the nuclear envelope is wrinkled, the tension is small enough to be discarded when compared to the osmotic tensions. It is only at the threshold for which the lamina becomes stretched that the mechanical tensions become large enough to influence the nuclear volume. Note that the threshold is also predicted to be sharp from our theory. Finally, the model naturally accounts for the inward orientation of the folds as resulting from the geometric non-linearities of the substrate. Collectively, these results provide an important understanding of the origin of the osmotic balance at the nuclear envelope which we remind is at the root of the nuclear scaling law (see Chapter.1). Yet, our results are based on a fundamental assumption, namely that the mechanical frustration at the root of the mechanical instability originates from the mismatch between the resting surfaces of the chromatin and of the lamina.

What is the biological origin of such a mismatch? We propose in this paragraph an explanation based on the history of the nuclear envelope formation. Mammalian cells undergo open mitosis. The nuclear envelope is disassembled at the prometaphase and assembled again after chromosome segregation at the end of mitosis. Importantly, the nuclear envelope forms on chromosomes that are condensed. This step is physiologically essential. While compacted chromosomes where shown to be isolated from cytosolic proteins through surfactants such as KI-67, chromosomes undergoing decompaction are free of these surfactants and the membrane is thus essential to avoid mixing between chromatin and cytoplasmic proteins such as nucleases whose role are to cleave nucleotides ([Cuylen-Haering, 2020], [Dey, 2021]). Based on this key observation we make the following thought experiment. Let us first assume for the sake of reasoning that the volume occupied by the chromosomes remains constant during decondensation. Chromatin transitions from a cylindrical-like shape at telophase to a spherical-like shape at interphase (see Fig.2.12.D). The sphere is the geometrical shape that minimizes the surface of any given 3D objects of given volume. This mathematical theorem implies that under the current hypothesis of constant volume, the external surface of the chromatin decreases during the geometric transition that happens following its decondensation. We thus interpret this geometrical transition as the driving force at the root of the mechanical instability and of the folds. Yet, our reasoning must be refined because it is clear that the volume occupied by the chromatin increases during the decondensation. The numerical value of δ at interphase is thus be the result of two opposite phenomena. (1) The surface decrease associated to the geometrical transition following decondensation (2) And, the growth associated to chromosome decondensation. The only way to convincingly validate this hypothesis is through direct experimental measurements which are not yet done at the time of the redaction of the thesis.

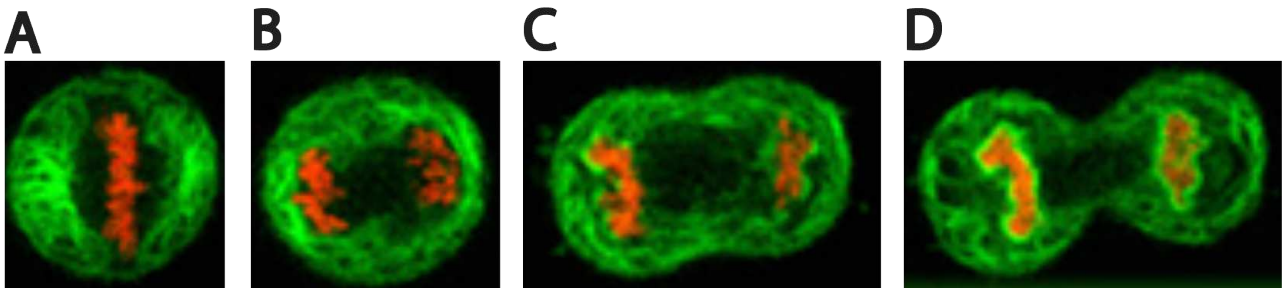

Figure 2.12: **Biological origin of the folds.** Xenopus oocyte undergoing mitosis expressing a marker for chromosomes in red and a marker for the endoplasmic reticulum in green. Image courtesy of Daniel J.Anderson [Anderson, 2007] [a]. (A) Cell at metaphase. Nuclear envelope has broken down and the nuclear membrane belongs to the ER. Chromosome have condensed and aligned along the equatorial plane of the cell. (B) Anaphase. (C) Telophase. Nuclear envelope starts to assemble. Membrane from the ER starts to bind to the condensed chromosome cluster. (D) Cytokinesis. Note that the nulear membrane is formed before the full decompaction of chromatin. We propose that this creates an excess of membrane during the geometrical transition following chromatin's decompaction that is at the origin of the nuclear folds observed at interphase (Fig.2.9).

[a] https://www.salk.edu/news-release/salk-scientists-solve-mystery-behind-how-nuclear-membrane-forms-during-mitosis/

4 General discussion and perspectives

In this chapter we have investigated the distinctive response of nuclei under uniaxial confinement on the minute timescale. The response of the nucleus can be divided into two clearly distinct regimes of deformation. (1) A first "safe" regime, at low confinements, for which the surface of the nucleus increases at constant volume. (2) And a second regime, at moderate confinements, for which the surface keeps increases but at decreasing nuclear volume. Interestingly, the height of confinement for which the transition occurs $h_c \sim 4\mu$m for Hela Cells, is physiological. Indeed, important nuclear confinements are commonly observed in biology [Weigelin, 2012]. This highlights the importance of understanding the origin of such a transition and identifying the underlying key physical parameters that rule the transition. We have first adapted the nested Pump-Leak model that was developed in Chapter.1 and have applied it to the nuclear confinement problem. The model shows good quantitative agreements with experiments for the nuclear volume confined at different heights (see Fig.2.6.B). Importantly, the model reproduces the two deformation regimes that are observed in experiments. In the model, the transition between the two regimes originates from the non-linear elastic response of the lamina to stretch Eq.S.112. At low confinements, the model assumes that the nuclear surface is lower than the surface at which the envelope becomes tensed, and the nuclear envelope tension hence stays constant equal to 0. The model then predicts that confinement does not influence the pressure balance at the nuclear envelope Eq.2.2 and that there is no volume loss in this regime. On the other hand, when the nuclear envelope becomes tensed, tension increases and the nuclear volume must decrease to enforce the pressure balance. These predictions are in line with experiments not shown in the chapter that track the fluctuations of the nuclear envelope for different confinement heights. They show that there is a sharp transition in the fluctuations at h_c which is consistent with our modelling.

Although satisfying, the success of our model only relied on a phenomenological equation that was designed to reproduce the nucleus volume response to hypo-osmotic shocks. We thus decided to further study the origin of the constitutive equation of the lamina. We propose an interpretation of this non-linear behavior of the lamina based on a well-known mechanical instability: thin stiff elastic layers bound to soft substrates buckle upon compression. Estimates using typical values of the chromatin and lamina elastic moduli indeed show that such a scenario is likely relevant for the nucleus. Lamina is indeed a thousand time stiffer than the chromatin such that wrinkling is energetically favorable even for low compressive strains. Additionally, the model makes a non-intuitive prediction: localized folds can emerge from two purely homogeneous materials. We think this prediction is important to highlight because a large part of the literature focuses on localize forces to explain nuclear shapes ([Biedzinski, 2020],[Lionetti, 2020]). But what is the biological origin of such compression in the nucleus? We propose that it originates from two essential features of the nuclear envelope. (1) The nuclear envelope forms on the condensed chromosome cluster (see Fig.2.12). This can lead to frustrations during the geometric transition following chromosome decondensation. (2) The lamina, contrary to cortical actin, was shown to have a low turnover rate of the order of few hours ([Moir, 2000],[Guilluy, 2014]) which we propose explains the conservation of stress over long period of time.

Our results can be further extended in two important directions. First, we propose to refine the coarse-grained mechanical model that we used. This can be achieved by conducting numerical simulations to include geometrical effects and solve the full system of equations without approximations. We can also consider other mechanical instabilities such as creasing[1]that can emerge in these mechanical system [Ciarletta, 2019]. We also propose to add the contribution of the external cytoskeleton by the consideration of an additional elastic medium on top of the lamina layer. Second, due to lack of experimental data, we did not consider the cellular volume loss upon confinement. Yet, we think that the nested Pump-Leak model is particularly suited to describe this effect. We proposed two interpretations of this volume loss

in Sec.2.6. Importantly, we highlight that the different volume responses of the nucleus and of the cell at low confinements could impact the nucleocytoplasmic transport. Indeed, at low confinements, nuclear volume is constant (or slightly increases) while the cytoplasmic volume decreases. This in turn is likely to impact the RAN-GTP gradient and thus the nucleocytoplasmic transport. We thus think that coupling the nested Pump-Leak model to the nucleocytoplasmic transport is an exciting avenue for future research.

To conclude, our study adds up to a growing number of recent papers that demonstrate the fundamental contribution of nuclear shapes and in particular of nuclear wrinkles and folds to the cell homeostasis ([Lomakin, 2020],[Venturini, 2020],[Cosgrove, 2021]). We demonstrated the fundamental role of these folds on the nuclear volume homeostasis and by extension on the robustness of the nuclear scaling law.

[1] A crease is a localized, sharped tip, self-contact region of large strain relative to the homogeneous state. Interestingly, creasing is one peculiar instability in the sense that the system sharply transition from an underformed to a highly deformed state such that linear elasticity cannot describe it.

Chapter 3

Poroelasticity of confined gels

On ne progresse guère si on n'accepte pas de se mettre en position vulnérable.

Cedric Villani
Théorème vivant
2012

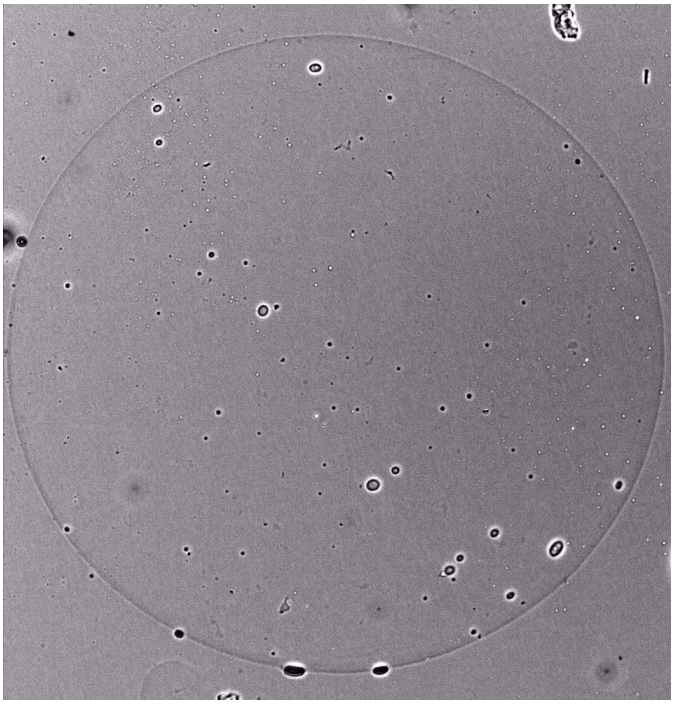

Confined polyacrylamide bead, Damien Cuvelier

1 Introduction

1.1 Objectives

In Chapter 2, we applied the "nested" Pump-Leak model to understand the smoothening of the envelope followed by the loss of volume of nuclei upon uniaxial confinements on the timescale of tenth of minutes. The latter quasistatic theory is not adapted to study variations on timescales faster than the minute. We have thus started to extend our framework to shorter timescales to study the non-trivial volume response of nuclei on the timescale of seconds. To go in this direction, we propose in this chapter a linear poroelastic theory that we apply to the compression of polyacrylamide beads.

1.2 Dynamic confiner experiment

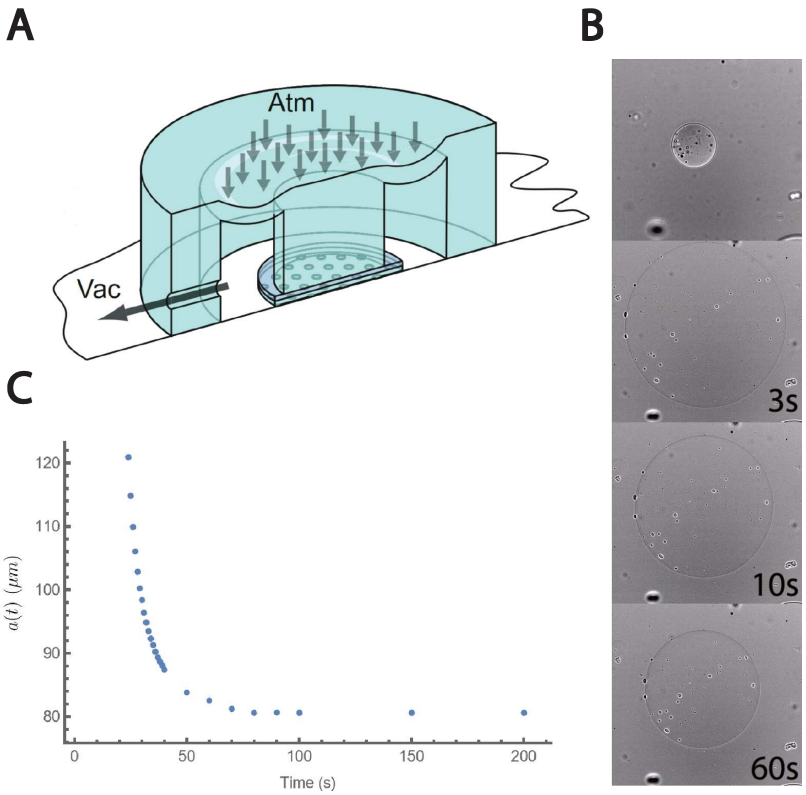

Figure 3.1: **Dynamic confiner experiment**. (A) Schematic of the dynamic confiner set-up [Le Berre, 2014]. The cell confiner acts as a suction cup. A vacuum (Vac) is created in the confiner chamber. The atmospheric pressure (Atm) will thus push on a central piston which will in turn maintain the two confinement plates at a controlled distance between each other. (B) Example of a sequence of images recorded during the confinement of a polyacrylamide bead. The top image represents the gel before its confinement. The time indicated on each frame is indexed on the time of confinement. (C) Evolution of the radius of the gel. Here, the time is indexed on the beginning of the recording.

The static 6-well confiner described in Chapter 2 and [Le Berre, 2014] cannot be used to record deformations of nuclei at timescales shorter than tenth of minutes. Instead, Damien Cuvelier and three intern students : Shuang Li, Aditya S.Kulkarni, and Laetitia Fournier, used a dynamic confiner to study the confinement-induced deformations at timescales of the order of seconds. The experimental procedure is described in [Le Berre, 2014] and Fig.3.1.A. The confiner experiment lies above a microscope which records the deformations at a frequency of 1 frame per second. The compression part of the deformation

$\sim ms$ is much faster than that of volume change such that the compression can be considered as instantaneous. While this experiment allows for a better time resolution it has the disadvantage to require more work force since only one-well can be compressed at a time.

1.3 Motivations

1.3.1 Observations

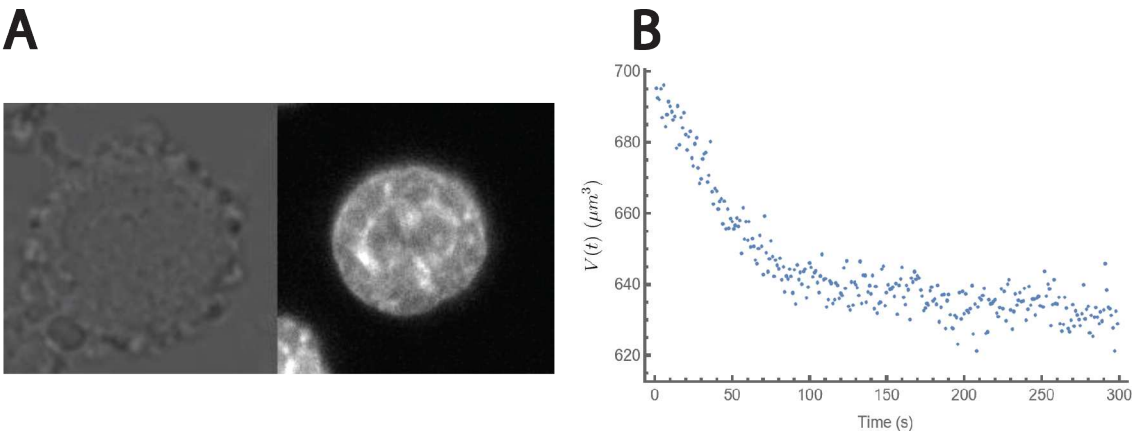

Figure 3.2: **Short timescale dynamic of nuclear volume loss upon uniaxial confinement.** (A) Snapshot of a confined Hela cell (left) and of its nucleus (right) at $h = 7.6\mu$m (B) Evolution of the nuclear volume after a fast ($\sim ms$) uniaxial confinement of a Hela cell confined at $h = 6\mu$m.

The dynamic of volume loss of nuclei upon uniaxial confinement is non-trivial and attracted our attention. We list below a couple of significant observations made on the preliminary experiments that we were given for analysis :

- The nucleus first deforms at constant volume during the millisecond compression.
- The nucleus then shrinks with a dynamic governed by a timescale of about 30s (see Fig.3.2.B).
- The dynamic of volume loss of nuclei is about 1000 times slower than that of the cytoplasm [Venkova, 2022].

1.3.2 Estimations

In chapter 2, we have highlighted the role of the envelope in the volume loss of the nucleus. Here, the origin of the nuclear volume loss and its associated dynamic is likely to be of different origin. First, the nuclei should in principle possess folds in the regime of compression where the dynamic experiments are conducted (see Fig.2.2.B and Fig.3.2.B). Second, the large nuclear pores are constituted by two main pathways. An internal viscous channel acting as the pathway for passive diffusion of various small molecules. The radius of this channel varies according to the size of the small molecules, but for water molecules it is at least $r \sim 20nm$ wide [Ma, 2012]. Its height H is about 100nm. Bigger molecules take a distinct transport pathway at the periphery of the passive channel, which is occluded by a meshwork of phenylalanine-glycine filaments [Ma, 2012]. We estimate the permeation of a viscous fluid through a channel from Poiseuille flow to scale as $l_p \sim \frac{\pi r^4}{8\eta H} \sim 10^{-4}\mu m^3 \cdot Pa^{-1} \cdot s^{-1}$, with $\eta \sim 5 \cdot 10^{-3} Pa.s$ the viscosity in the pore. There are $N \sim 1000$ pores in mammalian nuclei. Hence, the total water permeation of the nuclear envelope should roughly be 1000 times higher than the permeation of one pore l_p. Thus, from this permeation estimate we can compute the average time Δt for a nucleus to lose $\Delta V \sim 100\mu m^3$

knowing that the difference of pressure induced by a hypothetical 10% stretch of the lamina is about $\Delta P \sim 10^3 Pa$:

$$\Delta t = \frac{\Delta V}{l_p \cdot \Delta P} \sim 1s \tag{3.1}$$

This is more than one order of magnitude slower than the observed dynamics. We acknowledge that the previous order of magnitude is particularly sensitive to the pore size. We nevertheless decided to focus in this chapter on the nuclear bulk dynamic. As highlighted in chapter 1, the cell and its nucleus are complex systems, and a host of factors influence their volume. In front of such a complexity, Damien Cuvelier decided to use a simpler model system of polyacrylamide beads. The goal was twofold. First, understand the dynamic of volume change of such a simple system upon uniaxial confinement. Second, compare this dynamic with the one displayed by nuclei in order to confirm or disprove our hypothesis that the dynamic observed originates from the permeation of the fluid through the chromatin network and not through the nuclear envelope.

2 Derivation of a linear poroelastic theory

2.1 Preamble

In this section, we derive the dynamical equations that we use extensively in the next two chapters of this thesis. We consider an abstract system of volume Ω_t which is able to move and deform. The system is composed by two components: a fluid - upper script f - and an elastic gel network - upper script s. We divide the system between mesoscopic elements of volume. There are chosen to be small in front of the macroscopic size of the system but big compared to λ^3 where λ is the typical mesh size of the network. Each volume element is characterized by a density of fluid n^f and a density of gel n^s. We denote by m^i and w^i the molecular mass and volume of the component $i = \{f, s\}$. For the network, these molecular quantities are somewhat arbitrary and depends on the definition of the subunits composing the network. Several natural choices can be made such as the unit repeat of the polymer constituting the gel. However, what is physical and does not depend on this choice are the mass and volume density $m^s \cdot n^s$ and $w^s \cdot n^s$ of the gel in the small element of volume $d\Omega_t$. Our final results must thus only depend on these quantities. The total mass density ρ in the small element of volume can easily be expressed according to the previous quantities as:

$$\rho = m^f \cdot n^f + m^s \cdot n^s \tag{3.2}$$

During the deformation of the system, each volume element moves and deforms. We follow their deformation in the frame of the center of mass and denote by $\vec{v}$ its velocity. $\vec{v}$ can be expressed according to the velocities of the network $\dot{\vec{u}}$ and $\vec{v}^f$ as :

$$\rho \cdot \vec{v} = m^f \cdot n^f \cdot \vec{v}^f + m^s \cdot n^s \cdot \dot{\vec{u}} \tag{3.3}$$

We follow closely the approach developed in [Groot, 1984] and later extended to active matter (see [Jülicher, 2018] for a review). The core of the approach is to first identify the fluxes and the forces that the system exhibits when it is perturbed out of equilibrium and then linearly relate them following Onsager reciprocal relations. The obtained relations are called constitutive equations and they rule the dynamic of the system. The fluxes and forces naturally appear in the entropy production of the system. One central assumption of such an approach is to assume that each mesoscopic volume elements defined earlier is in a state of local thermodynamic equilibrium. We thus associate to them a free energy density

f, an energy density e, and an entropy density s. The first principle of thermodynamic states that the energy is conserved. If we call $\vec{j_e}$ the energy flux, the energy conservation at this mesoscopic scale must take the following form:

$$\frac{\partial e}{\partial t} + \vec{\nabla} \cdot \vec{j_e} = 0 \tag{3.4}$$

The second principle of thermodynamic states that entropy is created during a non-quasistatic transformation. If we call $\vec{j_s}$ the entropy flux and $\dot{\theta}$ the local entropy density production rate, the continuity equation for the entropy density must take the following form:

$$\frac{\partial s}{\partial t} + \vec{\nabla} \cdot \vec{j_s} = \dot{\theta} \tag{3.5}$$

For the purpose of this thesis we assume that the temperature T is fixed. Following Eq.3.4 and 3.5, the continuity equation for the free energy density thus reads:

$$\frac{\partial f}{\partial t} + \vec{\nabla} \cdot \left(\vec{j_e} - T\vec{j_s} \right) = -T\dot{\theta} \tag{3.6}$$

Using the Reynolds transport theorem and Eq.3.6, we can write the rate of change of the free energy as:

$$\frac{dF}{dt} = \iiint \left[\frac{\partial f}{\partial t} + \vec{\nabla} \cdot (f \cdot \vec{v}) \right] \cdot d\Omega_t \sim -T \iiint \dot{\theta}\, d\Omega_t + \text{surface terms} \tag{3.7}$$

Thus, the entropy production rate can be derived from the rate of change of the free energy of the system.

2.2 Useful equations

2.2.1 Incompressibility of the network

We first establish a constraint from the incompressibility of each individual component that relates the divergence of the network displacement $\vec{u}$ with its local density n^s. To do so, we follow a volume element $d\tau$ mapped on the deformations of the network. Since the network, taken separately, is considered as incompressible, the volume that the network occupies in $d\tau$ remains constant during the deformation, i.e., the only variations of the volume $d\tau$ are due to the permeation of water in or out of this element. We thus have:

$$n^s \cdot w^s \cdot d\tau = n_0^s \cdot w^s \cdot d\tau_0 \tag{3.8}$$

Where, the subscript 0 refers to the reference state. The laws of kinematics allow to relate the volumes $d\tau_0$ and $d\tau$ through the Jacobian matrix of the deformation [Holzapfel, 2000]:

$$d\tau = J \cdot d\tau_0 \quad \text{with,} \quad J = det\left(\overline{\overline{\mathbb{1}}} + \overline{\overline{\nabla}}_X (\vec{u}) \right) \tag{3.9}$$

For small deformations, Eulerian and Lagrangian coordinates are equivalent and the leading terms in J are simply the ones appearing in the diagonal of the 3*3 matrix $\overline{\overline{\mathbb{1}}} + \overline{\overline{\nabla}}_X (\vec{u})$. We obtain:

$$J \approx 1 + \vec{\nabla} \cdot \vec{u} \tag{3.10}$$

Combining Eq.3.8, 3.9, 3.10 finally allows to write, at linear order, the constraint sought:

$$\vec{\nabla} \cdot \vec{u} = \frac{n_0^s - n^s}{n_0^s} \tag{3.11}$$

2.2.2 Conservation equations

For a two-components system, there are three conservation equations:

Conservation of particle densities:

$$\begin{cases} \frac{\partial n^f}{\partial t} + \vec{\nabla} \cdot (n^f \vec{v}^f) = 0 \\ \frac{\partial n^s}{\partial t} + \vec{\nabla} \cdot (n^s \dot{\vec{u}}) = 0 \end{cases} \tag{3.12}$$

Furthermore, by definition of the Gibbs free energy we have:

$$w^f n^f + w^s n^s = 1 \tag{3.13}$$

We assume that the molecular volumes w^s and w^f are constant because of the incompressibility of each individual component. Combining the density continuity equations (see Eq.3.12) naturally leads to the cancellation of the divergence of the total volume flux:

$$\vec{\nabla} \cdot \left((w^f n^f) \cdot \vec{v}^f + (w^s n^s) \cdot \dot{\vec{u}} \right) = 0 \tag{3.14}$$

Similarly, by multiplying Eq.3.12 by the molecular masses m^i, we naturally obtain a conservation equation for the total mass density ρ:

$$\frac{\partial \rho}{\partial t} + \vec{\nabla} \cdot (\rho \vec{v}) = 0 \tag{3.15}$$

Momentum balance:

$$\rho \frac{d\vec{v}}{dt} = \vec{\nabla} \cdot \overline{\overline{\sigma}} \tag{3.16}$$

Where, $\overline{\overline{\sigma}}$ is the total stress tensor. As a side note we can write slightly differently Eq.3.16:

$$\frac{\partial (\rho \vec{v})}{\partial t} = \vec{\nabla} \cdot \left(\overline{\overline{\sigma}} - \overline{\overline{\mathcal{R}}} \right) \tag{3.17}$$

Where, $\overline{\overline{\mathcal{R}}}_{\alpha\beta} = \rho v_\alpha v_\beta$ is the Reynolds tensor which is used extensively in high Reynolds number hydrodynamic. We stress that many papers in active matter define their total stress tensor as $\overline{\overline{\sigma}} - \overline{\overline{\mathcal{R}}}$ which slightly differs from our choice [Jülicher, 2018]. However, in practice there are no difference because we apply the theory to low Reynolds number problems, and we will thus discard the Reynolds tensor.

2.2.3 Gibbs-Duhem equation for a 2-components poroelastic material

We will make use of the Gibbs-Duhem equation to write the entropy production. In classical thermodynamics, the Gibbs-Duhem relation constrain the variations of intensive variables. In the case of a two-components isothermal fluid, the free energy density reads:

$$f = \frac{1}{2} \cdot \rho \cdot \vec{v}^2 + f_0(n_1, n_2) \tag{3.18}$$

Where, n_1, n_2 are the particle densities. The Gibbs-Duhem relation in such a system reads:

$$dP^e = n^1 d\mu^1 + n^2 d\mu^2 \tag{3.19}$$

Where, $P^e = -\frac{\partial F_0}{\partial d\Omega_t}$ is the equilibrium pressure, with $F_0 = f_0 \cdot d\Omega_t$ the free energy in the reference frame of the center of mass and $\mu^i = \frac{\partial f_0}{\partial n^i}$ the chemical potentials of each specie. In the system under study the

Gibbs-Duhem relation must be modified due to the elasticity of the network. We must include another state variable which is the strain of the network $u_{\alpha,\beta}$:

$$u_{\alpha,\beta} = \frac{1}{2} \cdot (\partial_\beta u_\alpha + \partial_\alpha u_\beta) \tag{3.20}$$

Throughout this thesis we will make use of the Einstein summation convention. Following the same line of thought as the two-components fluid, we define a free energy density for the poroelastic system as:

$$f = \frac{1}{2} \cdot \rho \cdot \vec{v}^2 + f_0(n^f, u_{\alpha,\beta}) \tag{3.21}$$

Importantly, Eq.3.14 constrain the variations of $u_{\alpha,\beta}$ and n^s. We thus chose to discard n^s as a state variable in Eq.3.21 because it is already encompassed in $u_{\alpha,\beta}$. On the other hand, note that Eq.3.13 is not considered as a constraint to impose because it is already encompassed in the very definition of the free energy. To further demonstrate the Gibbs-Duhem relation, we make the following thought experiment: let us imagine that we translate the whole system by an infinitesimal translation with constant translation vector δx_γ. The variations of the free energy between these two resting states can be written from the Reynolds theorem as:

$$\delta F = \iiint \delta f \cdot d\Omega_t + \oiint f \delta x_\gamma dS_\gamma \tag{3.22}$$

Using the chain rule $\delta f = \mu^f \cdot \delta n^f + \sigma^{el}_{\alpha,\beta} \cdot \delta u_{\alpha,\beta}$. The variations of the state variables between the two resting states a and b can simply be related with each other as: $n^f_b(x_\gamma) = n^f_a(x_\gamma - \delta x_\gamma)$. The same reasoning also applies to $u_{\alpha,\beta}$. For small translations we thus obtain:

$$\begin{cases} \delta n^f = -\partial_\gamma n^f \cdot \delta x_\gamma \\ \delta u_{\alpha,\beta} = -\partial_\gamma u_{\alpha,\beta} \cdot \delta x_\gamma \end{cases} \tag{3.23}$$

After simple algebra the free energy change can be written as:

$$\delta F = \iiint \left(n^f \cdot \partial_\gamma \mu^f - \sigma^{el}_{\alpha,\beta} \cdot \partial_\gamma u_{\alpha,\beta}\right) \cdot \delta x_\gamma \cdot d\Omega_t + \oiint \left(f - n^f \mu^f\right) \cdot \delta x_\gamma \cdot dS_\gamma \tag{3.24}$$

Similar to classical thermodynamics, we define the fluid pressure as $P^f = n^f \mu^f - f$. We discuss in the next subsection the physical meaning of such a pressure. By integrating by part again we finally obtain:

$$\delta F = \iiint \left(n^f \cdot \partial_\gamma \mu^f - \sigma^{el}_{\alpha,\beta} \cdot \partial_\gamma u_{\alpha,\beta} - \partial_\gamma P^f\right) \cdot \delta x_\gamma \cdot d\Omega_t \tag{3.25}$$

By virtue of the translational invariance of the laws of non-relativistic physics, δF must vanish. Our reasoning works for any given volume and any given translations. As such the term in the integral must vanish which leads to the Gibbs-Duhem relation:

$$\partial_\gamma P^f = n^f \cdot \partial_\gamma \mu^f - \sigma^{el}_{\alpha,\beta} \cdot \partial_\gamma u_{\alpha,\beta} \tag{3.26}$$

The second term in the right hand side of Eq.3.26 is a second order term in the strain. It can be discarded in a linear theory such that the Gibbs-Duhem relation simply becomes:

$$\partial_\gamma P^f = n^f \cdot \partial_\gamma \mu^f \tag{3.27}$$

2.3 Interpretation of the fluid pressure

In our linear theory, the fluid pressure has a simple physical interpretation. This will be of fundamental importance later on to fix the right boundary conditions. Using the definition of the osmotic pressure Π we have:

$$\partial_\gamma \mu^f = w^f \cdot \partial_\gamma \left(P - \Pi\right) \tag{3.28}$$

Where P is the hydrostatic pressure. In a linear theory we thus have:

$$P^f \sim n_0^f w^f \cdot (P - \Pi) \tag{3.29}$$

Moreover, the fluid pressure can be related to the total equilibrium pressure P^e. We define the equilibrium pressure as $P^e = n^f \mu^f + n^s \mu^s - f$. Using Eq.3.14, the chain rule, and the fact that all the diagonal terms of the elastic tensor are equal, we can express the chemical potential of the network as $\mu^s = -\frac{1}{3 \cdot n_0^s} \cdot \sigma^{el}_{\gamma,\gamma}$ which leads to, at linear order :

$$P^e = P^f - \frac{1}{3} \cdot \sigma^{el}_{\gamma,\gamma} \tag{3.30}$$

2.4 Entropy production

We now have all the ingredients to write the entropy production resulting from a non-quasistatic transformation of the two-components system under study. For clarity, we will denote by $\frac{dg}{dt} = \frac{\partial g}{\partial t} + (\vec{v} \cdot \vec{\nabla})\, g$ the material derivative of a quantity g associated to the movement of the center of mass. To identify the entropy production we need to express $\frac{df}{dt} + f \vec{\nabla} \vec{v}$ (see Eq.3.7). We use the chain rule to first express this term as:

$$\frac{df}{dt} + f \cdot \vec{\nabla} \vec{v} = \frac{1}{2} \vec{v}^2 \cdot \frac{d\rho}{dt} + \rho v_\alpha \cdot \frac{dv_\alpha}{dt} + \mu^f \cdot \frac{dn^f}{dt} + \sigma^{el}_{\alpha,\beta} \cdot \frac{du_{\alpha,\beta}}{dt} + f \cdot \partial_\alpha v_\alpha \tag{3.31}$$

We then use the conservation laws Eq.3.15, Eq.3.17,Eq.3.12, that we express in term of particle derivatives to transform the previous equation into :

$$\begin{aligned} \frac{df}{dt} + f \cdot \vec{\nabla} \vec{v} = &- \left[\sigma_{\alpha,\beta} - \sigma^{el}_{\alpha,\beta} + P^f \cdot \delta_{\alpha,\beta}\right] \cdot \partial_\beta v_\alpha + \sigma^{el}_{\alpha,\beta} \cdot \left(\frac{du_{\alpha,\beta}}{dt} - \partial_\beta v_\alpha\right) + \partial_\alpha P^f \cdot \left(v^f_\alpha - v_\alpha\right) \,(...) \\ &(...) + \partial_\beta \left(v_\alpha \sigma_{\alpha,\beta} - n^f \mu^f \cdot \left(v^f_\beta - v_\beta\right)\right) \end{aligned} \tag{3.32}$$

Where, we have also made use of the Gibbs-Duhem relation Eq.3.27. In our linear theory, $\frac{du_{\alpha,\beta}}{dt} \approx \frac{\partial u_{\alpha,\beta}}{\partial t}$. By further using Eq.3.20 and the symmetry of the elastic stress tensor we show that : $\sigma^{el}_{\alpha,\beta} \cdot \frac{du_{\alpha,\beta}}{dt} = \sigma^{el}_{\alpha,\beta} \cdot \partial_\beta \dot{u}_\alpha$. Moreover, $v^f_\alpha - v_\alpha = -\frac{n^s m^s}{n^f m^f} \cdot (\dot{u}_\alpha - v_\alpha)$ such that, by integrating by part we finally obtain :

$$\begin{aligned} \frac{df}{dt} + f \cdot \vec{\nabla} \vec{v} = &- \left[\sigma_{\alpha,\beta} - \sigma^{el}_{\alpha,\beta} + P^f \cdot \delta_{\alpha,\beta}\right] \cdot \partial_\beta v_\alpha - (\dot{u}_\alpha - v_\alpha) \cdot \left[\frac{n^s m^s}{n^f m^f} \cdot \partial_\alpha P^f + \partial_\beta \sigma^{el}_{\alpha,\beta}\right] \,(...) \\ &(...) + \underbrace{\partial_\beta \left(v_\alpha \sigma_{\alpha,\beta} - n^f \mu^f \cdot \left(v^f_\beta - v_\beta\right) + \sigma^{el}_{\alpha,\beta} \cdot (\dot{u}_\alpha - v_\alpha)\right)}_{\text{Surface terms}} \end{aligned} \tag{3.33}$$

By using Eq.3.7 we identify the entropy production to be:

$$T\dot{\theta} = \left[\sigma_{\alpha,\beta} - \sigma^{el}_{\alpha,\beta} + P^f \cdot \delta_{\alpha,\beta}\right] \cdot \partial_\beta v_\alpha + (\dot{u}_\alpha - v_\alpha) \cdot \left[\frac{n^s m^s}{n^f m^f} \cdot \partial_\alpha P^f + \partial_\beta \sigma^{el}_{\alpha,\beta}\right] \tag{3.34}$$

Note that even if the identification may seem somewhat arbitrary, it is unique. Indeed, the entropy source term must satisfy a number of requirements. It must vanish at the thermodynamic equilibrium and remains invariant under a Galilean transformation since the notion of irreversibility should be independent of the definition of the referential.

2.5 Constitutive equations

2.5.1 General form

We first identify the fluxes and forces from the entropy production. We define the dissipative stress tensor as: $\overline{\overline{\sigma}}^d = \overline{\overline{\sigma}} - \overline{\overline{\sigma}}^{el} + P^f \cdot \mathbb{1}$. We call $\overset{\sim}{\overline{\overline{\sigma}}}^d$ its traceless part. We summarize them in Table.3.1.

Force	Flux	Time reversal signature	Type
$\overset{\sim}{\overline{\overline{\sigma}}}^d$	$\left(\overline{\overline{\nabla}}\vec{v}\right) + \left(\overline{\overline{\nabla}}\vec{v}\right)^T - \frac{2}{3} \cdot \vec{\nabla} \cdot \vec{v} \cdot \mathbb{1}$	-1	Traceless Tensor
$\sigma^d_{\gamma,\gamma}$	$\partial_\gamma v_\gamma$	-1	Scalar
$\frac{n^s m^s}{n^f m^f} \cdot \vec{\nabla} P^f + \vec{\nabla} \cdot \sigma^{el}_{\alpha,\beta}$	$\dot{\vec{u}} - \vec{v}$	+1	Vector

Table 3.1: **Pairs of thermodynamic fluxes and forces in the two-components linear poroelastic material under study.** The signature under time reversal of the force and its mathematical type is specified.

Following Onsager reciprocal relations, we derive the constitutive equations ruling the dynamic of the 2-component linear poroelastic material under study:

$$\begin{cases} \overline{\overline{\sigma}}^d = \bar{\eta} \cdot \vec{\nabla}\vec{v} + \eta \cdot \left[\left(\overline{\overline{\nabla}}\vec{v}\right) + \left(\overline{\overline{\nabla}}\vec{v}\right)^T - \frac{2}{3} \cdot \vec{\nabla} \cdot \vec{v} \cdot \mathbb{1}\right] \\ \frac{n^s m^s}{n^f m^f} \cdot \vec{\nabla} P^f + \vec{\nabla} \cdot \overline{\overline{\sigma}}^{el} = \xi \cdot \left(\dot{\vec{u}} - \vec{v}\right) \end{cases} \tag{3.35}$$

Where, we introduced three dissipation coefficients η, $\bar{\eta}$ and ξ corresponding respectively to a shear viscosity, a bulk viscosity and a friction coefficient. Note that these coefficients are independent of the flow considered. In particular, we can imagine a flow where the network is fixed. By identification with the viscous stress tensor of the fluid, we relate, at linear order, the previously defined viscosities with the solvent viscosities as: $\eta = n^f_0 m^f \cdot \eta^f$ and $\bar{\eta} = n^f_0 m^f \cdot \bar{\eta}^f$. Similarly, we identify the phenomenological coefficient ξ with the friction between the fluid and the network ξ^f by using the definition of the center of mass velocity $\vec{v}$ Eq.3.3. We obtain, $\xi^f = \frac{n^f m^f}{\rho} \cdot \xi$. If we further assume that $\frac{m^s}{w^s} \sim \frac{m^f}{w^f}$, the previous expression simplifies as :

$$\xi = \frac{1}{n^f w^f} \cdot \xi^f \tag{3.36}$$

In practice this is a good approximation. For example, the mass density of DNA is close to 1g/mL.

2.5.2 Simplifications

The effective coefficient ξ^f arise in our mesoscopic approach because of the friction between the network and the fluid. It can be related through the viscosity of the fluid η^f and the network mesh-size λ by scaling arguments. We now consider a microscopic volume element only containing the fluid. Without loss of generality, we assume that the network is immobile. The fluid velocity must vanish at the network position. Hence, the Laplacian of the fluid velocity must be of order $\sim \frac{v^f}{\lambda^2}$ and the associated viscous

dissipation of order $\sim \frac{\eta^f}{\lambda^2} \cdot (v^f)^2$. On the other hand, in the mesoscopic approach, the dissipation due to the friction between the fluid and the network should scale as $\sim \xi^f \cdot (v^f)^2$. Thus, by identification ξ^f and subsequently ξ must scale as:

$$\xi \sim \frac{1}{n^f w^f} \cdot \frac{\eta^f}{\lambda^2} \tag{3.37}$$

Moreover, we identified other dissipation coefficients η and $\bar{\eta}$ and we related them to the viscous dissipation of the fluid at mesoscopic scale. The associated viscous dissipation should scale as $\sim \frac{\eta}{l^2} \cdot (v^f)^2$, with l a macroscopic length associated to the system size. The natural criterion to neglect one dissipation in front of the other is thus given by the comparison between l^2 and λ^2. In practice, in the problems we will apply our theory to, $\lambda^2 << l^2$, such that we will neglect the macroscopic viscous dissipation $\overline{\overline{\sigma}}^d \sim 0$. Under this assumption, the total stress tensor becomes $\overline{\overline{\sigma}} = \overline{\overline{\sigma}}^{el} - P^f \cdot \mathbb{1}$. At low Reynolds number, we neglect the inertial term in the momentum balance equation Eq.3.16 such that the momentum balance reduces to a force balance:

$$\vec{\nabla} \cdot \overline{\overline{\sigma}}^{el} = \vec{\nabla} P^f \tag{3.38}$$

Injecting the latter force balance in the second constitutive equation Eq.3.35 and using Eq.3.3 leads to:

$$\vec{\nabla} P^f = \xi \cdot \left(n^f w^f\right)^2 \cdot \left(\dot{\vec{u}} - \vec{v}^f\right) \tag{3.39}$$

Where we have again assumed that $\frac{m^s}{w^s} \sim \frac{m^f}{w^f}$.

2.5.3 Interpretations

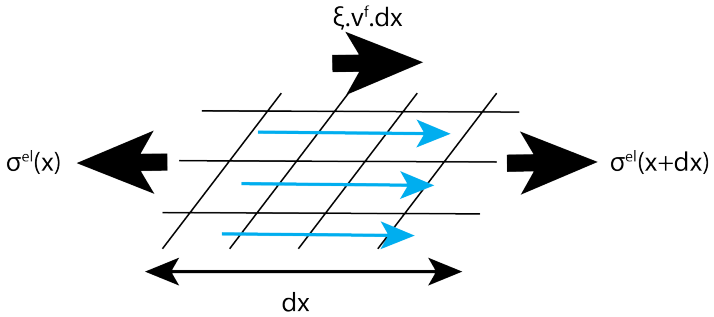

Figure 3.3: **Schematic of the force balance on a fixed elastic network.** The blue arrows represent the direction of the flow of the fluid. The black arrows represent the forces on the network per unit of transversal surface applied on the element of size dx.

Using the interpretation of P^f Eq.3.29, it becomes natural to interprete the constitutive equation Eq.3.39 as a generalization of the Darcy law to poroelastic materials:

$$\vec{\nabla} \left(P - \Pi\right) = \xi \cdot \left(n^f w^f\right) \cdot \left(\dot{\vec{u}} - \vec{v}^f\right) \tag{3.40}$$

Note that if there is only the fluid, i.e., $\Pi = 0$, we find back the usual Darcy law. The fluid flows toward the high to low pressure direction. On the other hand, let us assume that the hydrostatic pressure is homogeneous and that there is a gradient of osmotic pressure, the equation predicts that the fluid flows in the direction of the osmotic pressure gradient to dilute and thus homogenize the osmotic pressure. This is again what we would expect. Note that we can also interpret Eq.3.40 as a force balance on the fluid. Moreover, combining Eq.3.39 and Eq.3.38 leads to:

$$\vec{\nabla} \cdot \overline{\overline{\sigma}}^{el} = \xi \cdot \left(n^f w^f\right)^2 \cdot \left(\dot{\vec{u}} - \vec{v}^f\right) \tag{3.41}$$

Which can be interpreted as the force balance on the network. We can interpret the sign of the right hand side of Eq.3.41 easily by considering the 1D permeation of a fluid through an elastic network (see Fig.3.3). In order enforce the force balance, it is clear that $\sigma^{el}(x) > \sigma^{el}(x+dx)$ which justifies the minus sign in front of $\vec{v}^f$ in Eq.3.41.

2.6 Full closed problem

2.6.1 Summary of the equations

We summarize in this section the closed set of equations ruling the dynamic of a two-components linear poroelastic material:

$$\left\{\begin{array}{l} \xi \cdot (1-\phi_0)^2 \cdot \left(\dot{\vec{u}} - \vec{v}^f\right) = \vec{\nabla} P^f \\ \vec{\nabla} \cdot \overline{\overline{\sigma}}^{el} = \vec{\nabla} P^f \\ \vec{\nabla} \cdot \left(\phi_0 \cdot \dot{\vec{u}} + (1-\phi_0) \cdot \vec{v}^f\right) = 0 \end{array}\right. \quad \text{With,} \quad \left\{\begin{array}{l} \overline{\overline{\sigma}}^{el} = \left(K\, \vec{\nabla} \cdot \vec{u}\right) \cdot \overline{\overline{\mathbb{1}}} + 2G \cdot \left(\overline{\overline{u}} - \left(\frac{1}{3}\, \vec{\nabla} \cdot \vec{u}\right) \cdot \overline{\overline{\mathbb{1}}}\right) \\ \overline{\overline{u}} = \frac{1}{2} \cdot \left[\left(\overline{\overline{\nabla}} \vec{u}\right) + \cdot \left(\overline{\overline{\nabla}} \vec{u}\right)^T\right] \end{array}\right. \tag{3.42}$$

Where, for clarity, we call $\phi_0 = n^s w^s$ the volume fraction of the network in the mesoscopic elements of volume $d\Omega_t$. At linear order, ϕ is assumed constant during the deformation. K and G are the osmotic bulk and shear moduli of the gel network. Finally, we emphasize that this set of equations is equivalent to the stress diffusion coupling model of Tanaka and Fillmore [Tanaka, 1979] later improved by Doi [Doi, 2009].

2.6.2 Boundary conditions

To fully solve our problems, we will need to impose boundary conditions. There exist two kinds of boundary conditions:

Mechanical condition Our previous analysis lead us to identify the total stress tensor as the sum of two contributions : $\overline{\overline{\sigma}} = \overline{\overline{\sigma}}^{el} - P^f \cdot \mathbb{1}$. Then the force balance at the boundary gives the following condition:

$$\left(\overline{\overline{\sigma}}^{el} - P^f \cdot \mathbb{1}\right) \cdot \vec{n} = \vec{f}_{ext} \tag{3.43}$$

Where, f_{ext} accounts for the force acting on the boundary surface of the gel and $\vec{n}$ the outward unit normal vector to the gel surface.

Permeation condition If the fluid permeates freely through the gel surface, the fluid pressure must be continuous with the external fluid pressure P^f_{ext}. If the fluid cannot permeate through the gel surface, the normal velocity of the network and of the fluid must be identical and from Darcy's law Eq.3.39 we obtain that the fluid pressure gradient normal to the boundary must cancel. We can consider intermediate regimes by adding a surface friction ξ_s to describe the dynamic of flow through the boundary surface of the gel. All the regimes can be expressed mathematically as follows:

$$\left\{\begin{array}{l} P^f = P^f_{ext} \quad \text{Permeable boundary} \\ \vec{\nabla} P^f \cdot \vec{n} = 0 \quad \text{Impermeable boundary} \\ P^f - P^f_{ext} = \xi_s \cdot \left(\vec{v}^f - \dot{\vec{u}}\right) \cdot \vec{n} \quad \text{Intermediate permeable boundary} \end{array}\right. \tag{3.44}$$

2.7 Qualitative agreements with experiments

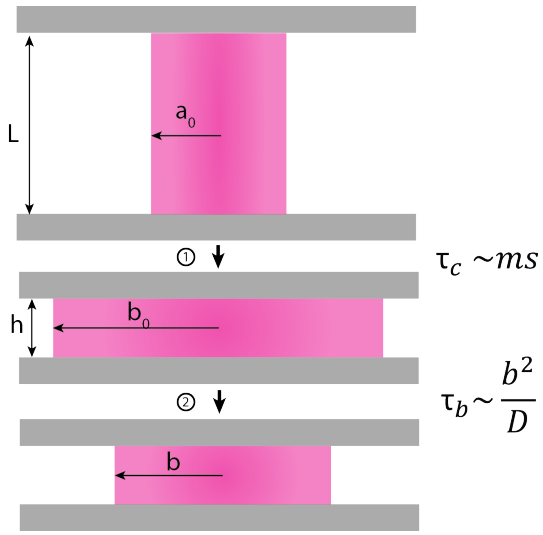

Figure 3.4: **Schematic of the different stages of deformation of a cylindrical gel upon fast compression as depicted by Eq.3.47.** Two stages and their associated timescales are depicted. (1) Compression of the gel at constant volume. (2) Shrinking of the gel.

We first make a number of qualitative comments that motivate the use of such a theory to the uniaxial confinement of nuclei. By using the property that the divergence of a curl is zero, we show from Eq.3.42 that:

$$\vec{\nabla}\cdot\left(\vec{\nabla}\cdot\overline{\overline{\sigma}}^{el}\right)=\left(K+\frac{4}{3}\cdot G\right)\cdot\Delta\left(\vec{\nabla}\cdot\vec{u}\right) \tag{3.45}$$

We then use Darcy's law Eq.3.39, the force balance Eq.3.38 and the non-divergence of the volume flux velocity Eq.3.14 to derive a diffusion equation for the divergence of the network displacement:

$$\frac{\partial\left(\vec{\nabla}\cdot\vec{u}\right)}{\partial t}=D\cdot\Delta\left(\vec{\nabla}\cdot\vec{u}\right)\quad\text{With,}\quad D=\frac{K+\frac{4}{3}G}{\xi\cdot(1-\phi_0)} \tag{3.46}$$

In Section.2.2.1, we linked $\vec{\nabla}\cdot\vec{u}$ to the variations of the mesoscopic elements of volume $d\tau$ mapped on the deformations of the network. The previous diffusion equation can be interpreted as a diffusion equation for these volume elements:

$$\frac{\partial\left(d\tau\right)}{\partial t}=D\cdot\Delta\left(d\tau\right)\quad\text{With,}\quad D=\frac{K+\frac{4}{3}G}{\xi\cdot(1-\phi_0)} \tag{3.47}$$

This allows to draw several important remarks for the volume loss of a gel.

Timescales ruling volume change. Some timescales are predicted to naturally appear in the volume variations of the gel. They scale as $\tau\sim\frac{l^2}{D}$, with l a macroscopic length scale associated to the gel geometry. If the gel exhibits different length scales the dynamic will be ruled by several timescales.

Deformations at constant volume for fast deformation. Eq.3.47 predicts that the volume loss is negligible if the timescale of the imposed deformation τ_c is smaller than the diffusion timescale τ. Indeed, the diffusive process implies that the typical length scale l_c over which the volume has relaxed after a

timescale τ_c scales as $l_c \sim \sqrt{D \cdot \tau_c}$. Taking a typical $D \approx 10\mu\text{m}^2/\text{s}$ and $\tau_c \approx 1ms$ we obtain $l_c \approx 0.1\mu\text{m}$ which is much smaller than the size of the nuclei and of the gels.

Shrinking happens even if the nuclear envelope is not stretched. Eq.3.47 also provides a natural explanation of why the nucleus shrinks after a fast compression even if the envelope should not be stretched at such confinements (see Fig.2.2.B and Fig.3.2). To understand why, we make the thought experiment depicted in Fig.3.4. Let us consider a cylindrical gel of initial radius a_0 and initial height L. We then compress infinitely fast the gel uniaxially and impose its height to be h. Eq.3.47 predicts that the deformation must be without volume change. As such, at linear order, the radius of the cylinder just after the compression must be:

$$b_0 = a_0 \cdot \left(1 + \frac{r}{2}\right) \quad \text{With,} \quad r = \frac{L-h}{L} \tag{3.48}$$

The gel will then relax toward its equilibrium position. The equilibrium radius of an elastic network after an uniaxial compression is classically determined by its Poisson's ratio as:

$$b = a_0 \cdot (1 + \nu \cdot r) \quad \text{With,} \quad \nu = \frac{K - \frac{2}{3}G}{2 \cdot \left(K + \frac{1}{3}G\right)} \leq \frac{1}{2} \tag{3.49}$$

The gel will thus relax toward equilibrium by shrinking since $b \leq b_0$ (see Fig.3.4).

2.8 Non-rotational problems

We derived Eq.3.47 for a qualitative understanding of the dynamic described by the full system of equations Eq.3.42. However, in practice, it is not convenient to work directly on Eq.3.47. It is indeed hard to write down the right boundary conditions for this equation. However, one important simplification of the full system of equation Eq.3.42 is obtained for non-rotative flows. In that case, $\vec{\nabla} \wedge \vec{u} = \vec{0}$ and $\vec{\nabla} \wedge \vec{v}^f = \vec{0}$. This implies that, at linear order, the volume flux velocity $\vec{q} = (1-\phi_0) \cdot \vec{v}^f + \phi_0 \cdot \dot{\vec{u}}$ vanishes since it has neither a divergence (see Eq.3.14) nor a curl. The velocities of the network and fluid are thus related as:

$$\vec{v}^f = -\frac{\phi_0}{1-\phi_0} \cdot \dot{\vec{u}} \tag{3.50}$$

In such a regime, Eq.3.42 simplifies and leads to the diffusion equation for the displacement of the network:

$$\frac{\partial \vec{u}}{\partial t} = D \cdot \Delta \vec{u} \quad \text{With,} \quad D = \frac{K + \frac{4}{3}G}{\xi \cdot (1-\phi_0)} \tag{3.51}$$

3 Osmotic compression of polyacrylamide beads

3.1 Parametrization of the problem

We first apply the previously derived theory Eq.3.42 to the osmotic compression of polyacrylamide beads. The goal is two-fold. First, characterize the gels at our disposal. Second, get familiarized with the theory and test its main predictions (see Sec.2.7) on a simpler problem.

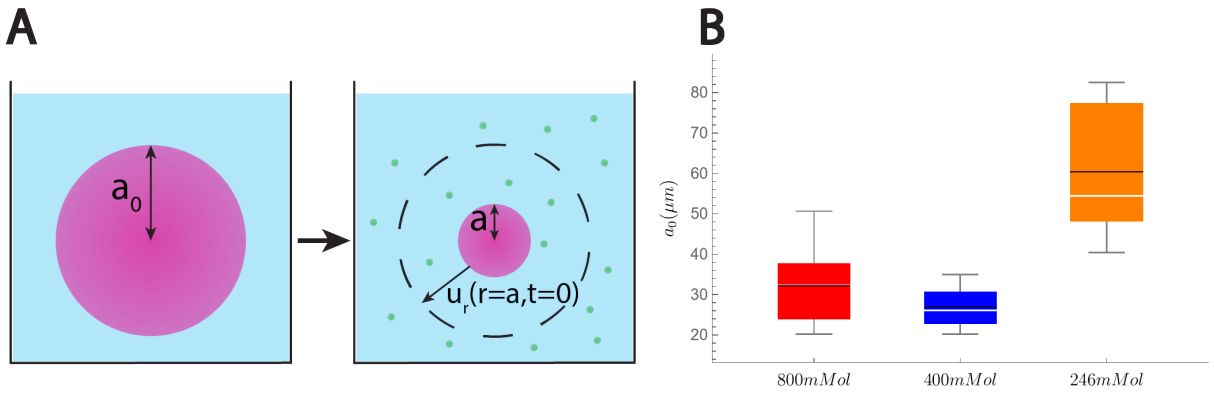

Figure 3.5: **Parametrization of the hyper-osmotic shock problem.** (A) Definition of the notations. We take the reference of the displacements to be the equilibrium configuration of the gel. We call by $\pi_0 = \pi^{in} - \pi^f < 0$ the magnitude of the hyper-osmotic shock. π^{in} and π^f are thus the absolute osmotic pressures of the external medium respectively before and after the shock. (B) Distributions of the initial radii of the beads for three sets of experiment where $|\pi_0| = \{246\text{mMol}, 400\text{mMol}, 800\text{mMol}\}$ is varied.

Hyper-osmotic shocks were performed on polyacrylamide beads by addition of a PEG solution to the medium. Three different sets of osmotic-shock experiments were performed and the dynamic of shrinking recorded. We index these experiments by the magnitude of the osmotic shock applied $\pi_0 = \pi^{in} - \pi^f$. Depending on the concentration of the PEG solution added, the magnitude of the shock varies. For simplicity, we neglect the gravity and the adhesion of the beads with the substrate such that we assume that the beads are spherical with an initial radius a_0. Upon addition of the PEG solution, the gel shrinks toward an equilibrium radius a. For each set of experiments we plot in Fig.3.5.B the experimental distribution of the initial radii of the beads.

We finally highlight that we define the stress tensor $\overline{\overline{\sigma}}^{el}$ with respect to its final equilibrium state. The displacements are thus defined compared to the final state and we choose as the reference of pressure the outer final fluid pressure $P^f_{out} = P - \pi^f$, with P the hydrostatic pressure which remains constant during the shock. This choice is a convention. Yet, we think that this convention makes our linear theory more robust to the data. Indeed, the elastic moduli are defined with respect to the final state which is particularly adapted to describe the long term response of the exponential shrinkage.

3.2 Boundary conditions

We first adapt the boundary conditions (see Sec.2.6.2) to the osmotic shock problem under study. As there is no membrane around the gel, we use the permeable boundary condition Eq.3.44:

$$P^f(r = a, t) = 0 \tag{3.52}$$

We remind that we take for reference pressure $P^f_{out} = P - \pi^f$. There is no external force applied to the gel $\vec{f}_{ext} = \vec{0}$. Thus, from Eq.3.43 we obtain :

$$\sigma^{el}_{rr}(r = a, t) = 0 \tag{3.53}$$

We must add an initial condition to close the problem. At $t < 0$, we assume that the beads are at equilibrium. Hence, from Eq.3.51 applied to spherical problem with radial symmetry, it is clear that:

$$u_r(r, t = 0) = \frac{a_0 - a}{a} \cdot r \tag{3.54}$$

Moreover, from the definition of the elastic stress tensor Eq.3.42, it is straightforward to show that:

$$\sigma_{rr}^{el}(r, t=0) = \sigma_{\theta\theta}^{el}(r, t=0) = \sigma_{\phi\phi}^{el}(r, t=0) = 3K \cdot \frac{a_0 - a}{a} \tag{3.55}$$

At equilibrium there are no flows. Hence, there are no gradients of fluid pressure in the gel. The force balance Eq.3.38 thus implies that $\sigma_{rr}^{el}(r, t=0)$ is constant throughout the gel. Finally, we again use the mechanical boundary condition Eq.3.43 at $t < 0$ to show that:

$$\sigma_{rr}^{el}(r, t=0) = -\pi_0 \tag{3.56}$$

Where we remind that $\pi_0 = \pi^{in} - \pi^f$. We thus obtain the useful relation:

$$-\pi_0 = 3K \cdot \frac{a_0 - a}{a} \tag{3.57}$$

3.3 Resolution

Hyper-osmotic shock experiments on polyacrylamide beads are thus fully described by three equations. The diffusion equation ruling the displacement of the gel Eq.3.51 complemented by the boundary condition of no elastic stress at the boundary Eq.3.53 and the initial condition of uniform stress before the shock Eq.3.54:

$$\partial_t u_r = D \cdot \left(\partial_r^2 u_r + \frac{2}{r} \cdot \partial_r u_r - \frac{2}{r^2} \cdot u_r \right) \tag{3.58}$$

$$\left[(K + \frac{4}{3}G) \cdot \partial_r u_r + 2 \cdot (K - \frac{2}{3}G) \cdot \frac{u_r}{r} \right] \Big|_{r=a} = 0 \tag{3.59}$$

$$u_r(r, t=0) = (a_0 - a) \cdot \frac{r}{a} \tag{3.60}$$

We first solve Eq.3.58 by separating the space and time variables and look for a solution for u_r of the form:

$$u_r(r, t) = f(t) \cdot g(r) \tag{3.61}$$

Injecting Eq.3.61 in Eq.3.58 we obtain:

$$\frac{1}{D} \cdot \frac{\dot{f}(t)}{f(t)} = \frac{1}{g(r)} \cdot \left(g''(r) + \frac{2}{r} \cdot g'(r) - \frac{2}{r^2} \cdot g(r) \right) = -\mu^2 \tag{3.62}$$

Where, μ is a constant independent of time nor of the position. Hence, f is of the form:

$$f(t) \propto \cdot e^{-D\mu^2 t} \tag{3.63}$$

And g is ruled by a Helmotz equation in spherical coordinates:

$$g''(r) + \frac{2}{r} \cdot g'(r) - \left(\mu^2 - \frac{2}{r^2} \right) \cdot g(r) = 0 \tag{3.64}$$

The solution of Eq.3.64 are the spherical Bessel function of the first and second kind of order one. We respectively call these function j_1 and y_1. We impose that the displacement remains finite for $r = 0$. As such, the constant before y_1 must vanish and u_r hence simply reads:

$$u_r(r, t) = A \cdot e^{-D\mu^2 t} \cdot j_1(\mu r) \tag{3.65}$$

With, A a constant. We then inject this solution into the boundary condition Eq.3.59. This leads to constrain the range of admissible μ:

$$tan(X_n) = -\frac{\alpha \cdot X_n}{X_n^2 - \alpha} \quad \text{With,} \quad \begin{cases} \alpha = \frac{4G}{K+\frac{4}{3}G} \\ X_n = a \cdot \mu_n \end{cases} \tag{3.66}$$

The range of physically accepted α lies between 0, when there is no shear modulus, to 3, when the shear modulus is dominant. Note that for $\alpha > 2$, the associated Poisson's ratio is negative, and the gel is auxetic (see Eq.3.78). We index the solutions of Eq.3.66 by an integer number n. An important limit is obtained when $G << K$. In this case, $X_n = n\pi$. Fig 3.6.(A) shows the curves $Y_1(X) = tan(X)$ and $Y_2(X, \alpha) = -\frac{\alpha \cdot X_n}{X_n^2 - \alpha}$ for $\alpha = 2$. The solutions of Eq.3.66 $X_n(\alpha)$ are the abscissa of the intercepts of Y_1 and Y_2. In practice, $n\pi - X_n$ decreases and tends to zero when n increases (see Fig.3.6.C). Moreover, X_1 decreases from π for $\alpha = 0$ to 0 for $\alpha = 3$ Fig.3.6.B. We do not expect a priori the beads to have auxetic properties such that $\alpha \leq 2$. Importantly, natural timescales arise to describe the dynamic of relaxation of the volume: $\tau_n = \frac{a^2}{DX_n^2}$. The slowest timescale is the one that rules the "long term" dynamic and reads:

$$\tau_1 = \frac{a^2}{DX_1^2} \tag{3.67}$$

We will thus choose to adimensionalize the time by this timescale. Eq.3.66 has a singularity when $\alpha_{lim} = X^2$. This is only achieved for n = 1 when $X_1 = \frac{\pi}{2}$. This remark will have its importance later.

$$\begin{cases} \text{If } \alpha \leq \alpha_{lim} : X_1 \in [\frac{\pi}{2}, \frac{3\pi}{2}] \\ \text{If } \alpha \geq \alpha_{lim} : X_1 \in [0, \frac{\pi}{2}] \end{cases} \quad \text{With,} \quad \alpha_{lim} = \frac{\pi^2}{4} \tag{3.68}$$

In practice, we solve numerically Eq.3.66 for n>1. For n=1, it is much more stable numerically to solve the equivalent equation $\alpha - X_1^2 \cdot \frac{tan(X_1)}{tan(X_1) - X_1} = 0$ to find $X_1(\alpha)$.

It is not possible to find a solution of the form Eq.3.65 that fulfils the initial condition Eq.3.60. However, by virtue of the linearity of our problem we look for a solution of the form:

$$\frac{u_r(r,t)}{a_0 - a} = \sum_{n=1}^{\infty} A_n \cdot j_1\left(X_n \cdot \frac{r}{a}\right) \cdot e^{-\left(\frac{X_n}{X_1}\right)^2 \cdot \frac{t}{\tau_1}} \tag{3.69}$$

It is clear by linearity that Eq.3.69 is solution of the diffusion equation Eq.3.58 and of the boundary condition Eq.3.59. We then use the following orthogonality relations to find the constant A_n:

$$\begin{cases} \text{If } k \neq n : \int_0^1 j_1(X_k y) \cdot j_1(X_n y) \cdot y^2 dy = 0 \\ \int_0^1 j_1(X_k y)^2 \cdot y^2 dy = \frac{-1 + X_k^2 + cos(2X_k) + \frac{X_k}{2} \cdot sin(2X_k)}{2X_k^4} \\ \int_0^1 j_1(X_k y) \cdot y^3 dy = -\frac{3X_k cos(X_k) + (-3 + X_k^2) \cdot sin(X_k)}{X_k^4} \end{cases} \tag{3.70}$$

By using Eq.3.66, classical trigonometric relations and the properties of the modes X_k (see Fig.3.6 and Eq.3.68), it is straightforward to show that:

$$\begin{cases} \text{if } \alpha \leq \frac{\pi^2}{4}, \quad A_1 = 2 \cdot \sqrt{1 + \left(\frac{\alpha \cdot X_1}{X_1^2 - \alpha}\right)^2} \cdot \frac{(3-\alpha) \cdot (X_1^2 - \alpha)}{X_1 \cdot \left(X_1^2 - (3-\alpha) \cdot \alpha\right)} \\ \text{if } \alpha \geq \frac{\pi^2}{4}, \quad A_1 = -2 \cdot \sqrt{1 + \left(\frac{\alpha \cdot X_1}{X_1^2 - \alpha}\right)^2} \cdot \frac{(3-\alpha) \cdot (X_1^2 - \alpha)}{X_1 \cdot \left(X_1^2 - (3-\alpha) \cdot \alpha\right)} \\ \text{for } n \geq 2, \quad A_n = 2 \cdot (-1)^{n+1} \cdot \sqrt{1 + \left(\frac{\alpha \cdot X_n}{X_n^2 - \alpha}\right)^2} \cdot \frac{(3-\alpha) \cdot (X_n^2 - \alpha)}{X_n \cdot (X_n^2 - (3-\alpha) \cdot \alpha)} \end{cases} \tag{3.71}$$

We finally end this resolution by computing analytically the radial stress in the network:

$$\frac{\sigma_{rr}^{el}(r,t)}{-\pi_0} = \frac{1}{3-\alpha} \cdot \sum_{n=1}^{\infty} A_n \cdot X_n \cdot \left(j_0\left(X_n \cdot \frac{r}{a}\right) - \alpha \cdot \frac{j_1\left(X_n \cdot \frac{r}{a}\right)}{X_n \cdot \frac{r}{a}} \right) \cdot e^{-\left(\frac{X_n}{X_1}\right)^2 \cdot \frac{t}{\tau_1}} \tag{3.72}$$

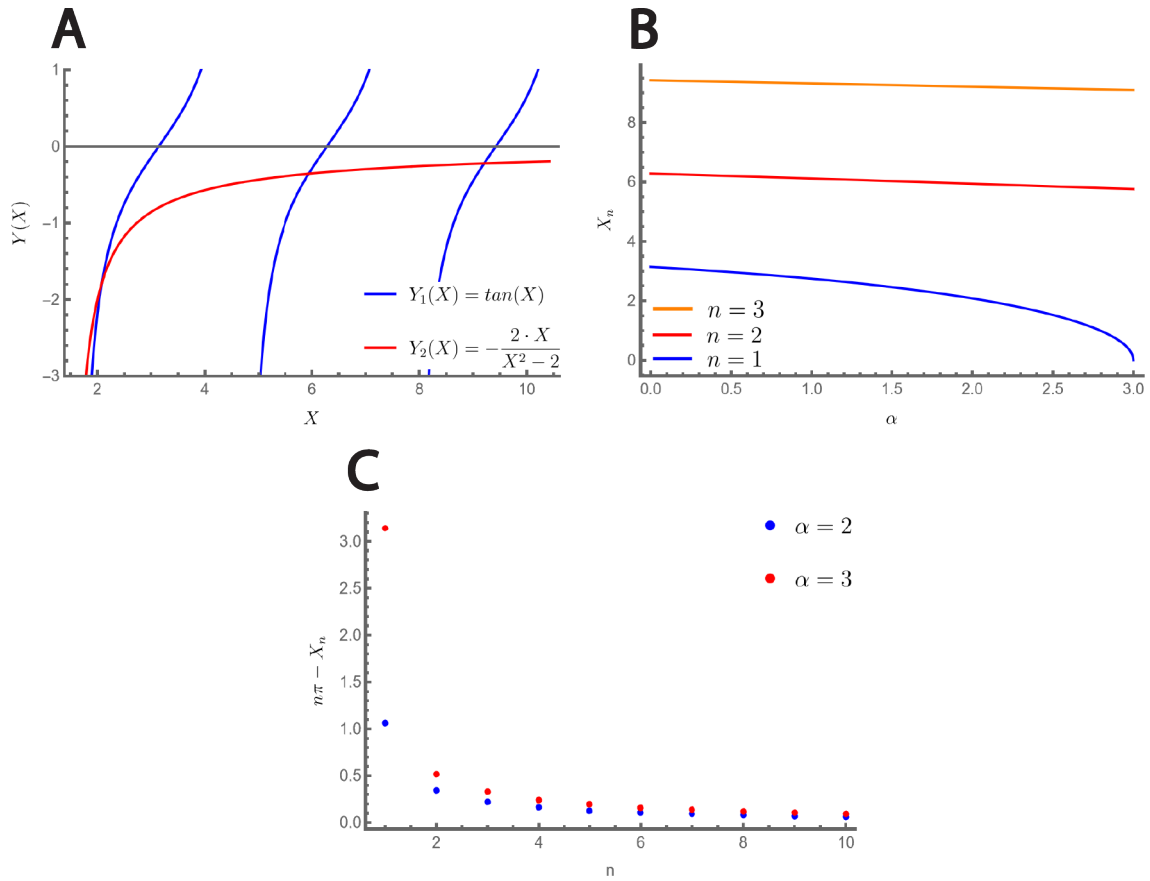

Figure 3.6: **Properties of the relaxation modes X_k.** (A) The mode X_k lies at the abscissa of the intercepts between the blue curve Y1 and the red curve Y2 (see Eq.3.66). The three first modes are shown for $\alpha = 2$. (B) Dependence of the three first modes with α. In practice, only the first mode has a strong dependence with α. (C) Evolution of $n\pi - X_n$ with n for different fixed α.

3.4 Theoretical results

One essential result is that the shrinking pattern of any given spherical gel will be identical as long as the parameter α (see Eq.3.66) of the gel is fixed. Indeed, from Eq.3.69, the radius of the gel during shrinking reads:

$$\frac{a(t)-a}{a_0-a} = \sum_{n=1}^{\infty} A_n \cdot j_1\left(X_n\right) \cdot e^{-\left(\frac{X_n}{X_1}\right)^2 \cdot \frac{t}{\tau_1}} \tag{3.73}$$

Where τ_1, A_n, X_n are respectively given by Eq.3.67, Eq.3.71 and Eq.3.66. Thus, assuming that the beads were made in a reproducible manner such that α is constant, we predict that the curve $\frac{a(t)-a}{a_0-a}$ plotted with respect to the normalized timescale $\frac{t}{\tau_1}$ is a master curve independent of the initial radius of the gel ball as well as how it was osmotically compressed.

Another salient prediction is that the shrinking of the radius of the gel upon osmotic compression will be dominated by only one mode in the "long-term" dynamic. Indeed, the function $\left(\frac{X_n}{X_1}\right)^2$ is an increasing

function of the mode number n. After a "transition time" that depends on α, all the modes will have relaxed except the first one such that the normalized radius will behave as (see Fig.3.7.D) :

$$log\left(\frac{a(t)-a}{a_0-a}\right) \approx log\left(A_1 \cdot j_1(X_1)\right) - \frac{t}{\tau_1} \tag{3.74}$$

This was qualitatively predicted in Sec.2.7 and arise only because the displacement is ruled by a diffusion equation Eq.3.58. τ_1 is the diffusion timescale ruling the "long-term" dynamic of shrinking and is expected to scale with the square of the equilibrium radius of gel a^2 Fig.3.7.B. The diffusive process of the dynamic implies that both the displacement and the stress in the gel will relax to their equilibrium values from the edge to the center of the gel, the time to relax toward equilibrium being given by τ_1 Fig.3.7.A and C.

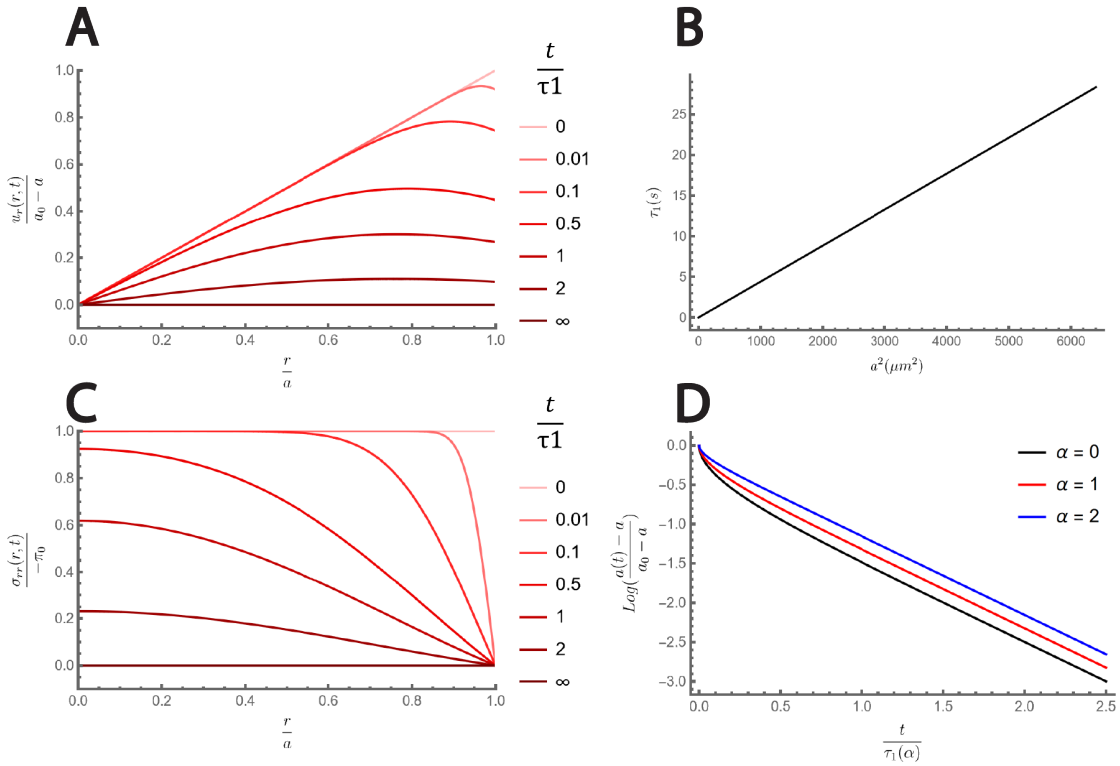

Figure 3.7: **Theoretical solutions of the osmotic compression of spherical gels.** (A) Radial component of the gel displacement u_r in a spherical gel during a hyper-osmotic shock. (B) Characteristic relaxation time τ_1 Eq.3.67 of shrinking as a function of the square of the equilibrium radius a of the beads. We choose for illustrative purposes $\alpha = 1$, $D = 30\mu m^2/s$, $a \in [0\mu m, 80\mu m]$. (C) Radial component of the elastic stress σ_{rr}^{el} in a spherical gel during a hyper-osmotic shock. (D) Logarithm of the normalized radius change of a spherical gel during a hyper-osmotic shock as a function of the normalized time $\frac{t}{\tau_1}$ for different values of the elastic modulus α (see Eq.3.66 for a definition).

3.5 Comparison with the literature

3.5.1 Comparison with [Tanaka, 1979]

The osmotic compression of spherical gels has been studied in detail in the literature. In particular, [Tanaka, 1979] provided an analytical solution of Eq.3.42 in the limit regime where $G << K$. We check that our solution Eq.3.69 and Eq.3.71 are equivalent in this limit. We obtain for $\alpha = 0$:

$$\frac{u_r(r,t)}{a_0-a} = \frac{6}{\pi} \cdot \sum_{n=1}^{\infty} (-1)^{n+1} \cdot \frac{1}{n} \cdot j_1(n\pi \cdot \frac{r}{a}) \cdot e^{-n^2 \cdot \frac{t}{\tau_1(\alpha=0)}} \tag{3.75}$$

With, $\tau_1(\alpha = 0) = \frac{a^2}{D\pi^2}$. This indeed corresponds to the solution proposed in [Tanaka, 1979] since $j_1(x) = \frac{sin(x)}{x^2} - \frac{cos(x)}{x^2}$

3.5.2 Comparison with [Peters, 1986]

A generalisation was proposed by [Peters, 1986] to arbitrary shear moduli G. However, their solution was obtained using a weaker initial condition:

$$u_r(r = a, t = 0) = (a_0 - a) \tag{3.76}$$

Their solution does not fulfil the linear radial displacement condition that we established for $t \leq 0$ and $r \in [0, a]$ (see Eq.3.60). Both solutions are thus not equivalent Fig.3.8. The difference with our solution increases with α. However, note that α was estimated to be ~ 1.2 for the beads used in [Peters, 1986]. For such a value of α we checked that the difference between our two solutions is below the measurement errors. This is why we think that they were able to find a diffusion coefficient in good agreement with that measured by quasi-elastic light scattering.

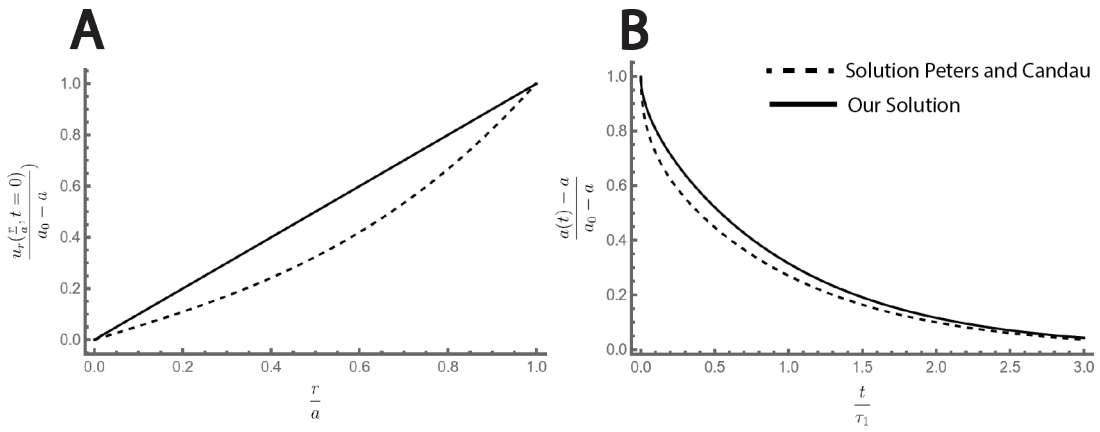

Figure 3.8: **Comparison with the solution provided by Peters and Candau for $\alpha = 2$ [Peters, 1986]**. (A) Radial displacement in the gel at the initial time. The continuous line is the solution derived in the previous section (see Eq.3.69). The dashed line is the solution proposed in [Peters, 1986]. (B) Evolution of the radius of the gel with respect to the normalized time for both solutions.

3.6 Application to experimental data

Damien Cuvelier gave us the evolutions of the radii of the beads for the three sets of experiments (see Fig.3.5). The radii were measured visually for each individual beads and for each frame using the software ImageJ. We show in this section the results of our analysis on respectively 8, 9, and 11 beads for different hyper-osmotic shocks $|\pi_0| = \{246, 400, 800\}$kPa.

3.6.1 Static characterization of the polyacrylamide beads

We first characterize the bulk moduli of the beads from the relative radius change at steady state upon osmotic compression $\frac{a_0 - a}{a}$. Eq.3.57 predicts a linear relationship between this radius change and the magnitude of the osmotic compression π_0. We estimate the resulting bulk modulus K for each individual gel ball from the resulting relation:

$$K = \frac{1}{3} \cdot \left(\frac{a}{a_0 - a} \right) \cdot (-\pi_0) \tag{3.77}$$

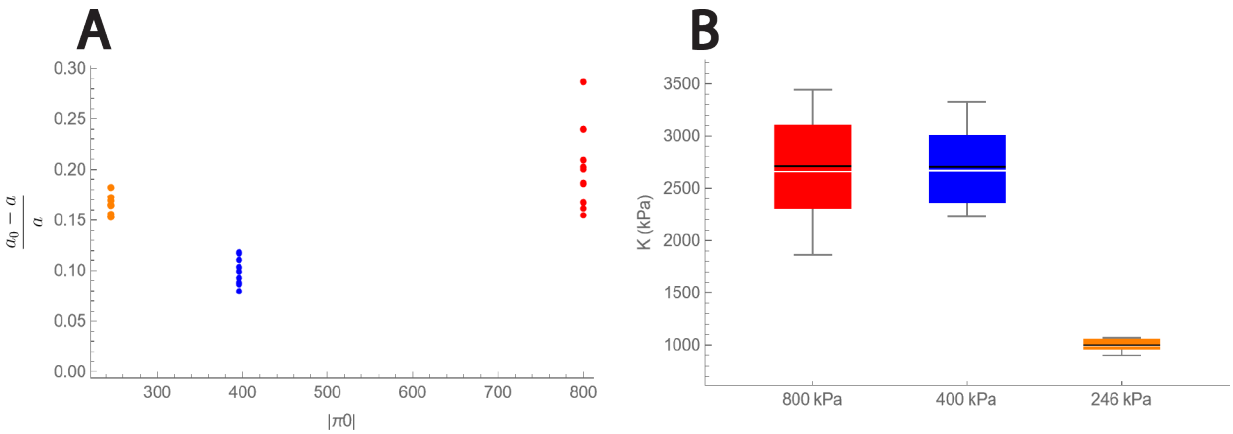

Figure 3.9: **Static caracterization of the polyacrylamide beads.** (A) Normalized radius change between the initial and the equilibrium states for each sets of experiments (B) Distribution of the estimated bulk moduli for each sets of experiments $\pi_0 = [800\text{kPa}, 400\text{kPa}, 246\text{kPa}]$.

Interestingly, in the three sets of experiments under study Fig.3.5, the beads belonging to the experiment $|\pi_0| = 246\text{mMol}$ display a significantly smaller bulk modulus of average value $K = 999\text{kPa}$ compared to $K \approx 2710\text{kPa}$ for the two other sets of experiments Fig.3.9. We thus expect the odd beads to exhibit distinct dynamical properties as the diffusion coefficient depends on the elastic properties of the beads Eq.3.51. The beads were supposed to be prepared following the tables provided in [Tse, 2010] and the concentration of reactants was adjusted to obtain a young modulus of 35kPa for each bead. Even though we do not expect this value to be precise, we can nevertheless estimate an order of magnitude of the shear modulus, the Poisson's ratio and the coefficient α from the following relationships:

$$\begin{cases} \nu = \frac{3K-E}{6K} \\ G = \frac{3KE}{9K-E} \\ \alpha = \frac{4G}{K+\frac{4}{3}G} \end{cases} \tag{3.78}$$

We summarize the resulting moduli in Table.3.2 assuming that the young modulus of the polyacrylamide beads is the same for all beads and is equal to 35kPa. Note that α is predicted to be small.

Experiments	$\|\pi_0\| = 246\text{kPa}$	$\|\pi_0\| = \{400, 800\}\,\text{kPa}$
K (kPa)	999	2710
G (kPa)	12	12
ν	0.494	0.498
α	0.05	0.01

Table 3.2: **Estimates of the elastic moduli of the polyacrylamide beads.**

3.6.2 Dynamic characterization of the polyacrylamide beads

We further use our dynamical theory to characterize the beads. One of the main predictions is that the long term dynamic of the shrinking is ruled by only one mode characterized by the timescale τ_1. This behavior is indeed observed (see Fig.3.10).B. Note that the last points are not representative due to the exponential nature of the shrinking at constant error measurement of the radius. Moreover, the relaxation timescale τ_1 is expected to scale with the square of the equilibrium radius a. We verify this prediction in Fig.3.10.C. Remarkably, the 800kPa and 400 kPa experiments display identical fits as expected from their similar elastic properties Fig.3.9.B.

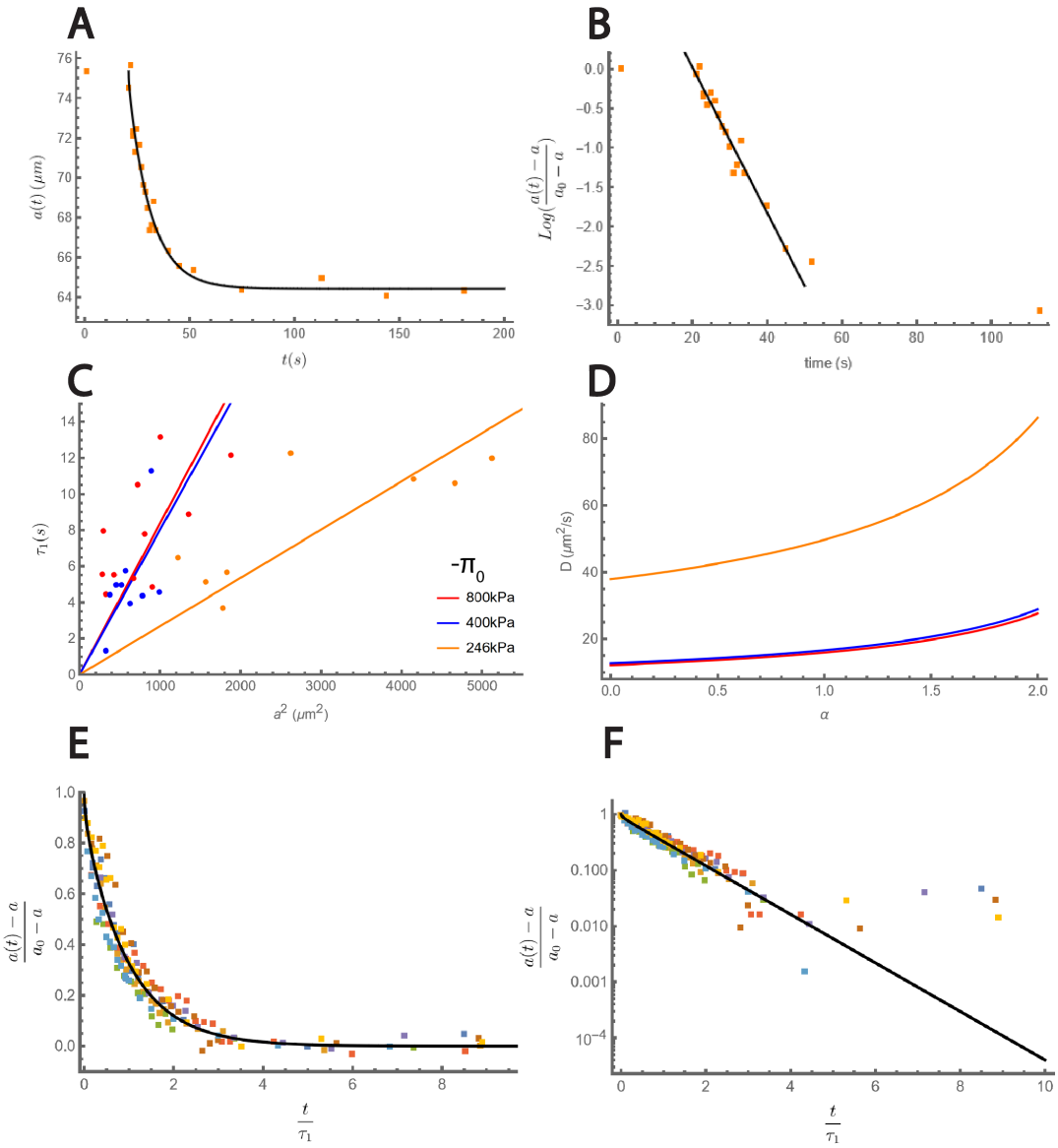

Figure 3.10: **Dynamic characterization of the polyacrylamide beads.** (A) Evolution of the radius of one gel ball during a 246kPa hyper-osmotic shock. The black line is the theoretical solution Eq.3.73 with 100 modes, $\tau_1 = 10.9s$, $\alpha = 2.6$ and $t_0 = 18s$. (B) Logarithmic evolution of the normalized radius changes of the same gel ball. The orange dots are the experimental points and the black line the least mean square fit to a straight line with slope $\frac{1}{\tau_1}$ (see Eq.3.74). We discard the last four points due to the noise at long time that arise from the exponential nature of the shrinking at constant error measurement on the radius. The error thus increases with time in logarithmic scale. (C) Characteristic diffusion time τ_1 as a function of the square of the equilibrium radius a. Each colored dots account for a bead osmotically compressed with a magnitude $-\pi_0$. The continuous lines account for the least mean square regression fits to a straight line. The R^2 of the regression are respectively from the low to high hyper osmotic shock experiment : $R^2 = [0.65, 0.31, 0.42]$ (D) Range of plausible diffusion constants of the beads according to the unknown elastic modulus α Eq.3.66 as obtained from the slope of the straight lines $\frac{1}{D \cdot X_1(\alpha)}$ measured in (C) combined with Eq.3.66. (E) and (F) Master curves as predicted by Eq.3.73 in real and logarithmic space. The colored squares are the experimental traces of the radius change in the re-scaled time $\frac{t}{\tau_1}$ of the beads osmotically compressed at $|\pi_0| = 246$kPa. The average elastic modulus $< \alpha >$ of each bead used to plot the black theoretical line is 2.19. We discuss in Sec.3.6.3 the reasons of such a high value.

On the other hand, the beads used in the 246kPa experiment exhibit a significantly higher diffusion coefficient Fig.3.10. Although we predicted that their dynamic should be different because the beads used in this set of experiments displayed distinct elastic properties Fig.3.10.B, we could not predict with a simple reasoning the increase of the diffusion coefficient. Indeed, D should decrease with K at constant friction Eq.3.51. We thus conclude that not only the elastic properties of these beads are different but their friction coefficients ξ too. Nevertheless, it is noteworthy that the quality of the fit is higher for the 246 kPa experiment which is in line with the smaller dispersion of the elastic moduli of these beads Fig.3.9.B.

We then used the trace of the radii (see Fig.3.10.A) to determine the elastic modulus α of each bead. We designed two ways to determine α. We either used the value of the coefficient $Log\,(A_1 \cdot j_1(X_1))$ of Eq.3.74 extracted from the long-term dynamic fit (see Fig.3.10.B). Or we performed a least mean square minimization to Eq.3.73 using the value of τ_1 determined before. The precise value of the initial time of osmotic compression t_0 was not known due to the experimental limitation that the image blurs for several seconds when the PEG solution is injected in the set-up. Hence, the second method with two fitting parameters (α and t_0) was more adapted here. For all the beads, the extracted α was close to 2 which is far from the expected value $\alpha \sim 0$ (see Tab.3.2). We discuss in section 3.6.3 the reasons of this overestimation. Finally, we verify our last prediction that the shrinking pattern of any given spherical beads must collapse on the same master curve as long as α is identical (see Eq.3.73). Fig.3.10.E and F show such master curves for the 8 beads osmotically compressed at $|\pi_0| = 246$kPa. Altogether, the derived linear poroelastic theory provides a consistent quantitative description of the shrinking of spherical polyacrylamide gel beads upon osmotic compression.

3.6.3 Discussion

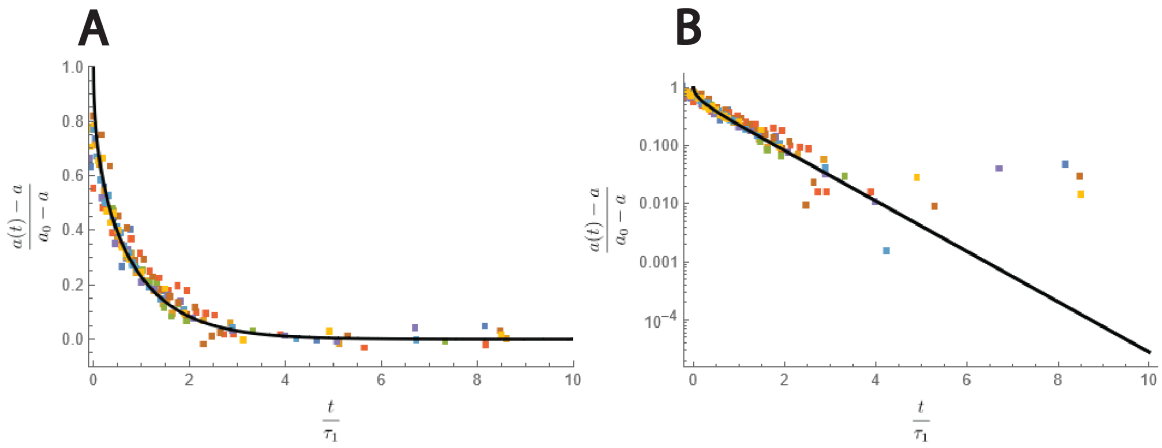

Figure 3.11: **Impossibility of determining α.** (A) and (B) Master curves as predicted by Eq.3.73 in real and logarithmic space. The colored squares are the experimental traces of the radius change in the rescaled time $\frac{t}{\tau_1}$ of the beads osmotically compressed at $|\pi_0| = 246$kPa. We used the value $\alpha = 0.05$ as estimated in Tab.3.2 to plot the black theoretical line. The values of τ_1 used are identical to those of Fig.3.10. We determined by least mean-square minimization the value of the initial time of osmotic compression imposing $\alpha = 0.05$. The average value was 19.8s against 17.6s for Fig.3.10.

While the determination of τ_1 was robust, a precise extraction of α would require a better measurement of the radii combined with a better time resolution. Indeed, the main effect of α is to decrease the transient rescaled time after which the slowest mode becomes dominant Fig.3.7.D. For $\alpha \in [0, 2]$, the typical value of the transient time is about $0.1 \cdot \frac{t}{\tau_1}$ (see Fig.3.7.D). Here, $\tau_1 \sim 10s$ which means that we should only be able to observe this transient dynamic on timescales which coincides with the time resolution of the

experiment. This also implies that an error of the order of the second on the initial time of compression will lead to drastic changes in the value of α. As a matter of illustration, we show in Fig.3.11 that we can obtain a good agreement between the theory and the experiment by imposing $\alpha = 0.05$ and by changing in average the initial time of osmotic compression by 2 seconds.

4 Uniaxial confinement experiments

4.1 Theory

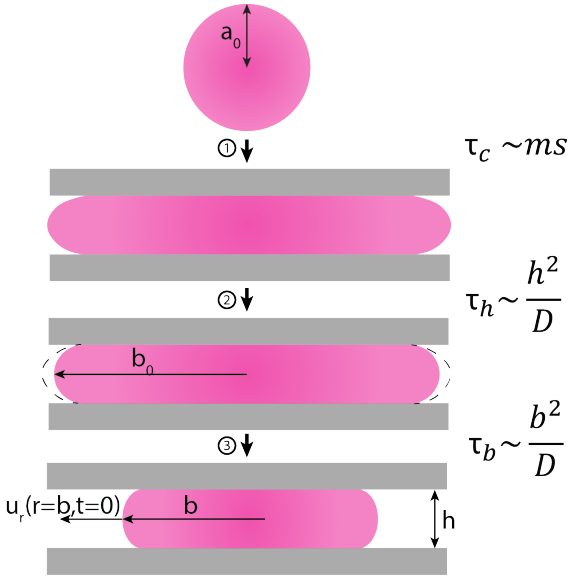

Figure 3.12: **Schematics of the different modes of deformation of a spherical gel upon uniaxial confinement.** Three stages and their associated timescales are depicted. (1) Compression of the gel (2) Deformation of the edges of the gel (3) Shrinking of the gel.

We now apply our theory to the uniaxial confinement experiments for a thickness h. The problem displays two length-scales and thus two important timescales $\tau_b \sim \frac{b^2}{D}$ and $\tau_h \sim \frac{h^2}{D}$. The former timescale is associated to the dynamic of shrinking while the latter is associated to the deformation of the edges of the gel (see Fig.3.12). While the problem displays rotationals on timescales of order τ_h - i.e., $\vec{\nabla} \wedge \vec{u} \neq 0$, $\vec{\nabla} \wedge \vec{v}^f \neq 0$ -, we expect them to vanish on timescales of order τ_b. In practice, $\frac{\tau_h}{\tau_b} << 1$ (see Fig.3.14.A). This separation of timescales hence justifies the use of Eq.3.51 to describe the deformations on timescales of order τ_b. In line with the previous section we thus solve the following problem:

$$\partial_t u_r = D \cdot \left(\partial_r^2 u_r + \frac{1}{r} \cdot \partial_r u_r - \frac{1}{r^2} \cdot u_r \right) \tag{3.79}$$

$$\left[(K + \frac{4}{3}G) \cdot \partial_r u_r + (K - \frac{2}{3}G) \cdot \frac{u_r}{r} \right] \Big|_{r=b} = 0 \tag{3.80}$$

$$u_r(r, t = 0) = (b_0 - b) \cdot \frac{r}{b} \tag{3.81}$$

For simplicity, we chose the initial condition to be that of uniform stress in the gel and did not consider the friction with the walls. We discuss in Section.4.3 the consequence of adding such an effect in our theory. Using the same mathematical procedure as in the previous section, we show that the solutions

read:

$$\frac{u_r(r,t)}{b_0-b} = \sum_{n=1}^{\infty} B_n \cdot J_1\left(x_n \cdot \frac{r}{b}\right) \cdot e^{-\left(\frac{x_n}{x_1}\right)^2 \cdot \frac{t}{\tau_1}} \tag{3.82}$$

And,

$$\frac{\sigma_{rr}(r,t)}{(2K+\frac{2}{3}G)\cdot\frac{b_0-b}{b}} = 8 \cdot \sum_{n=1}^{\infty} \frac{x_n}{J_1(x_n)\cdot(\alpha^2-4\alpha+4x_n^2)} \cdot \left(J_0\left(x_n\cdot\frac{r}{b}\right) - \frac{\alpha}{2}\cdot\frac{J_1\left(x_n\cdot\frac{r}{b}\right)}{x_n\cdot\frac{r}{b}}\right)\cdot e^{-\left(\frac{x_n}{x_1}\right)^2\cdot\frac{t}{\tau_1}} \tag{3.83}$$

With,

$$\begin{cases} B_n = 16\cdot\frac{(1-\alpha/4)}{J_1(x_n)\cdot(\alpha^2-4\alpha+4x_n^2)} \\ \tau_1 = \frac{b^2}{D\cdot x_1^2} \end{cases} \tag{3.84}$$

Where, following Eq.3.80, x_n are the n^{th} solution of the equation:

$$x\cdot J_0(x) = \frac{\alpha}{2}\cdot J_1(x) \tag{3.85}$$

With, J_0 and J_1 the zeroth and first order Bessel function of the first kind. Note that we have made use of the following Bessel integrals to obtain the previous results:

$$\begin{cases} \text{If } k\neq m: \int_0^1 J_1(x_k y)\cdot J_1(x_n y)\cdot y\,\mathrm{dy} = 0 \\ \int_0^1 J_1(x_k y)^2\cdot y\,\mathrm{dy} = \frac{J_1(x_k y)^2}{2} \\ \int_0^1 J_1(x_k y)\cdot y^2\,\mathrm{dy} = \frac{J_2(x_k)}{x_k} \end{cases} \tag{3.86}$$

The only difference with the last section is geometrical. The behavior of the solutions is thus qualitatively the same (see Fig.3.13). In particular, the long term dynamic of the shrinking of the radius of the bead is again ruled by the slowest timescale τ_1 Eq.3.84:

$$Log\left(\frac{b(t)-b}{b_0-b}\right) \approx Log\left(B_1\cdot J_1(x_1)\right) - \frac{t}{\tau_1} \tag{3.87}$$

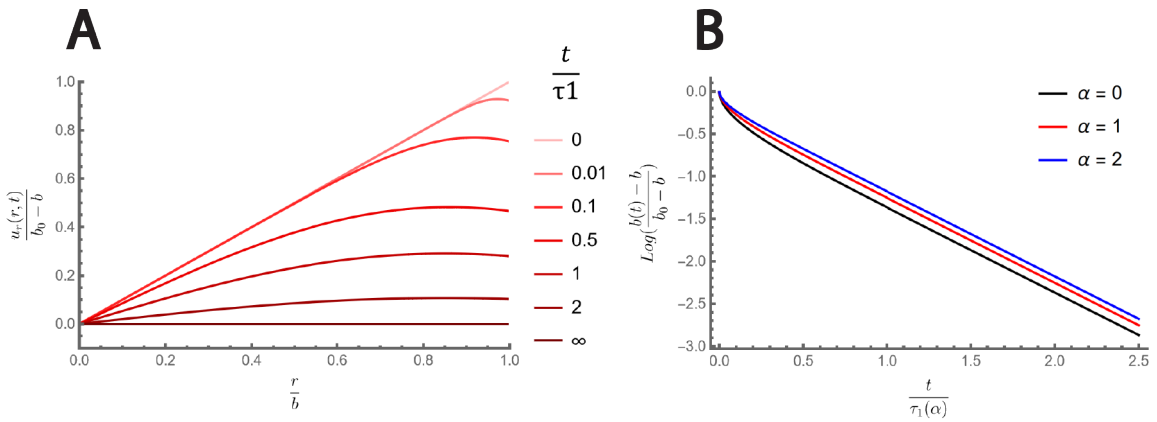

Figure 3.13: **Theoretical solutions of the uniaxial compression of spherical gels.** (A) Radial component of the gel displacement u_r in a spherical gel upon uniaxial confinement (see Fig.3.12). (B) Logarithm of the normalized radius change of a spherical gel upon compression as a function of the normalized time $\frac{t}{\tau_1}$ (Eq.3.87).

4.2 Applications to experimental data

Damien Cuvelier gave us the evolution of the radii $b(t)$ upon uniaxial compression for the beads characterised in the previous section. The radii were measured by hand for each individual beads and for each frame using the software ImageJ. At the difference of the osmotic-shock experiment, the initial time of compression is much better defined because there is no injection of fluid in the set-up that blurs the image for few seconds. We show in this section the results of our analysis on four beads mechanically compressed at h = 7.6 μm.

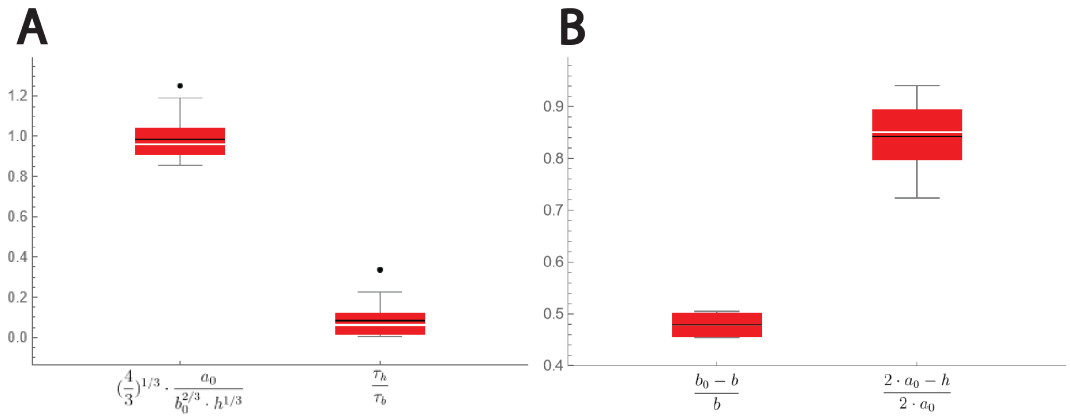

Figure 3.14: **Further characterisations of the polyacrylamide beads.** (A) Distribution of two quantities for the beads under study. The left chart accounts for the condition of conservation of volume (see Eq.3.89). The right chart shows the distribution of the ratio of the two diffusion timescales related to the two length scales in the confinement problem (see Fig.3.12). (B) Distribution of the radial and vertical deformations of the beads upon uniaxial confinement (see Fig.3.12).

The diffusion coefficient of the beads was estimated in the last section to lie between 10 to 80 $\mu m^2/s$. We obtain $\tau_h \sim 1s$, $\tau_b \sim 100s$. Although these estimates are crude, they show that there is a distinct separation of timescales in our problem.

$$\tau_c << \tau_h << \tau_b \tag{3.88}$$

As a matter of illustration, we show in Fig.3.14 the distribution of the ratio $\frac{\tau_h}{\tau_b}$ for the seven beads. This separation of timescales leads to two important predictions of the theory.
(1) There is no volume loss during the compression that takes place on timescales of order τ_c. Given the geometries of the gels before and after the compression Fig.3.12, the condition of no volume loss is equivalent to the following criterion:

$$V = V_0 \Leftrightarrow \left(\frac{4}{3}\right)^{1/3} \frac{a_0}{b_0^{2/3} \cdot h^{1/3}} = 1 \quad \text{With,} \quad \begin{cases} V_0 = \frac{4}{3}\pi a_0^3 \\ V = \pi b_0^2 h \end{cases} \tag{3.89}$$

We plot in Fig.3.14.A, the distribution of this criterion for the beads. The average of this criterion is 0.99 demonstrating that the volume is indeed conserved during the mechanical compression of the beads.
(2) The dynamic should be well described by Eq.3.51 as timescales longer than τ_h. We estimated that the time resolution of the experiments is of the order of τ_h. This implies that the dynamic that is observed should be entirely given by Eq.3.51. We provide on Fig.3.15 a summary of our analysis. Similarly to the last section, we fit the long-term dynamics of the shrinking by a single exponential to determine both α and τ_1 (see Fig.3.15.B and Eq.3.82). We verify that τ_1 scales with b^2 for the four beads. While τ_1 seems to indeed increase with b^2, the quality of the fit is poor. We provide two reasons for this. First,

the shrinking of the radius is exponential while the error on the radius measurement is constant. We thus expect the noise to increase with time in logarithmic scale and thus be an important source of error for τ_1 (see Fig.3.15 B and D). Second, less data points were measured on the long-term dynamics. The signal to precisely determine τ_1 is thus lowered.

From the slope of Fig.3.15.B, we obtain the coefficient $\frac{1}{D \cdot x_1(\alpha)^2}$ (see Eq.3.84). We thus plot in Fig.3.15.F the range of diffusion coefficient that can lead to such coefficient. The average α of the four beads is $\alpha = 1.5$. We thus estimate $D \sim 100 \mu m^2/s$. The diffusion coefficient is thus larger than the one estimated for the osmotic shock experiment Fig.3.10.D. We interpret this by the high deformations that the beads experience of respectively 80% in the vertical direction and of 50% in the radial direction (see Fig.3.14.B). It is thus likely that the response of the system is non-linear and what our linear theory is measuring is an effective diffusion coefficient. Finally, we verify that, as predicted by the theory Eq.3.82, the shrinking pattern of the normalized radii of the mechanically compressed beads collapse on the same master curve in the rescaled time $\frac{t}{\tau_1}$ Fig.3.15.C and D. Altogether, we conclude that the derived linear poroelastic theory, combined with effective parameters, provides a consistent quantitative description of the shrinking pattern of polyacrylamide beads upon uniaxial mechanical confinements.

4.3 Wall friction

In the last sections, we didn't consider the friction of the gel with the PDMS plates. We propose in this subsection to include such an effect into our framework. To simplify our discussion, we make a lubrification approximation and consider a 2D problem by integrating all the quantities over the height of confinement. We denote by $\tilde{x}$ the averaged value of this quantity. The force balance on the gel network, including the friction of the walls ξ_w, reads:

$$\vec{\nabla} \cdot \tilde{\bar{\sigma}}^{el} = \xi \cdot h \cdot (1 - \phi_0)^2 \cdot (\dot{\tilde{\vec{u}}} - \tilde{\vec{v}}^f) + \xi_w \cdot \dot{\tilde{\vec{u}}} \tag{3.90}$$

Using the non-rotational property of the flows under study to express the fluid velocity according to the gel velocity, it is straightforward to show that the effect of the friction on the walls is to renormalize the diffusion coefficient:

$$D^{eff} = \frac{K + \frac{4}{3} \cdot G}{\xi \cdot (1 - \phi_0) + \frac{\xi_w}{h}} \tag{3.91}$$

As expected the consideration of an additional friction slows down the dynamic. Yet, the only effect of this new friction is to renormalize the diffusion coefficient and as such our theoretical solution can still be used even if the friction with the plates was dominant.

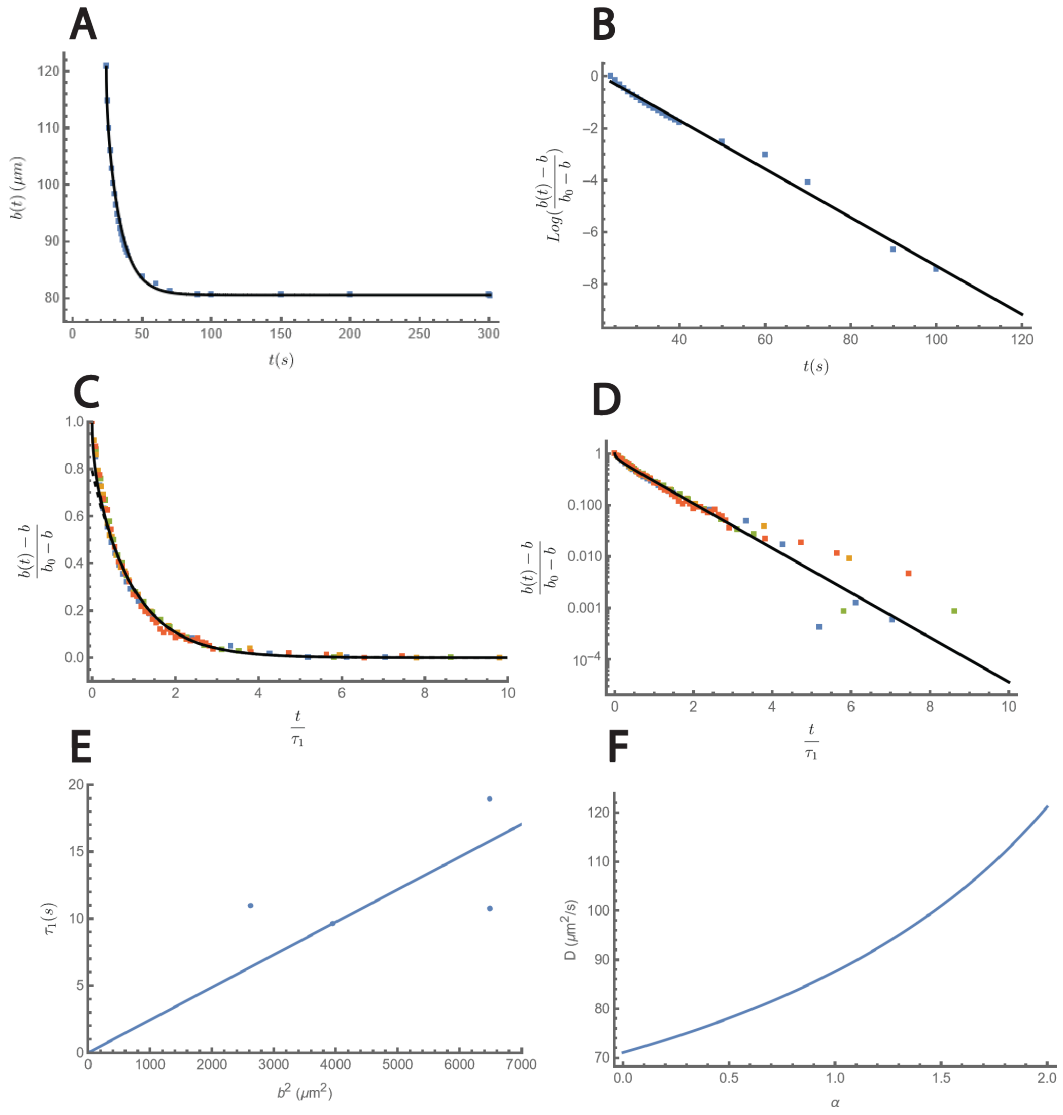

Figure 3.15: **Experimental validation of the linear poroelastic theory to the uniaxial confinement of polyacrylamide beads** (A) Evolution of the normalized radius change of one bead after the confinement. The black line is the theoretical solution Eq.3.82 with 100 modes, $\tau_1 = 10.8s$ and $\alpha = 1.4$ as determined by Fig.3.15.B. (B) Logarithmic evolution of the normalized radius change of the same bead. The blue dots are the experimental points and the black line the least mean square fit to a straight line. The slope of the straight line gives $\frac{1}{\tau_1}$ (see Eq.3.84 and 3.87). (C) and (D) Master curves as predicted by Eq.3.82 in real and logarithmic space. The colored squares are the experimental traces of the radius change of each bead in the re-scaled time $\frac{t}{\tau_1}$ upon confinement. The average of the elastic moduli of each bead, $< \alpha >= 1.51$, as inferred by our analysis, was used to plot the black theoretical line. (E) Characteristic diffusion time τ_1 as a function of the square of the equilibrium radius b. The continuous line account for the least mean square regression fit to a straight line. (F) Range of plausible diffusion constants of the beads according to the unknown elastic modulus α as obtained from the slope of the straight lines $\frac{1}{D \cdot x_1(\alpha)}$ measured in E combined with Eq.3.85.

5 General discussion and perspectives

In this chapter, we have aimed at understanding the dynamic of volume loss of nuclei on the timescale of seconds upon fast ($\sim ms$) uniaxial confinements. We showed in Chapter 1 and 2 that a host of factors influenced the steady-state volume of the nucleus. In front of such a complexity, we have decided to use both a simplified experimental model system of polyacrylamide beads and a simpler theory to focus on the effect of confining a gel. The choice of these models is motivated by four reasons. First, we estimate that the dynamic of permeation of a viscous flow through the nuclear membrane would be too fast to explain the timescale observed. This is mainly due to the large size of the nuclear pores coupled to their substantial number on the envelope of mammalian nuclei (~ 1000). Second, the data that were given to us shows that Hela cells lose $\sim 5\%$ of volume at height of confinement where they should still possess folds. The effect described in Chapter 2 of nuclear pressure increase and associated volume loss due to NE stretching is thus unlikely to be at the root of the observed nuclear shrinking and its associated dynamics. Third, the dynamics of volume loss of nuclei and of polyacrylamide beads displayed very similar distinctive features: they first deform at constant volume upon the millisecond compression and they then shrink following a quasi-exponential decrease on the second timescale. Finally, this effect was not observed for the cytoplasm - which do not possess chromatin - and which can lose up to 20% of its volume in 100 ms [Venkova, 2022].

To understand this peculiar dynamic, we have derived a linear poroelastic theory from entropy production and Onsager reciprocal relations. We show that the derived theory is equivalent to the stress diffusion coupling model developed 40 years ago [Tanaka, 1979]. The proposed derivation of the theory has two benefits. First, it clearly identifies what is the "fluid pressure" which appears in the Tanaka theory as being proportional to the difference between the hydrostatic pressure and the osmotic pressure arising from the steric repulsions of the gel Eq.3.29. Second, it can easily be adapted to include other species such as ions. A striking prediction of this theory is that the mesoscopic elements of volume constituting the gel evolve upon perturbation following a diffusion equation. Any volume variations on timescales faster than the diffusion timescale are thus impeded. The gel thus first deforms at constant volume under fast deformation and then relax by shrinking toward its equilibrium state following the diffusion timescale, the magnitude of this deformation being driven by the Poisson's ratio of the gel. Motivated by these early qualitative correlations, we have decided to quantitatively apply this theory to two distinct problems:

First, to the osmotic compression of the polyacrylamide beads. For simplicity, we neglected the gravity and the adhesion of the beads with the substrate such that we assumed that the beads are spherical. The radial symmetry of the problem allowed us to simplify the linear poroelastic theory and solve it analytically. We derived a solution for any given elastic shear and bulk modulus that satisfies both the no stress boundary condition and the initial condition of homogeneous stress. We compared our solution to the one proposed in the literature. Our solution is consistent with [Tanaka, 1979] when $K << G$. It is however nonequivalent to the solution proposed in [Peters, 1986] in the limit of $G \sim K$. We show that our solution is stronger since it enforces the initial condition of homogeneous stress. We thus chose our solution to characterize the beads from the dynamic of shrinking. We first extracted the bulk modulus of the beads. Our analysis showed that one set of experiment was done with beads with distinct elastic moduli. The signature of this mechanical disparity is genuinely observed in our dynamic characterization. Indeed, while we verified that the diffusion timescale increases linearly with the square of the equilibrium radius of the beads for each set of experiments, the experiment performed with the odd beads exhibited a clear different slope demonstrating that their diffusion coefficient was distinct. We estimated that the diffusion coefficient of the beads was in the range of 10 to 20 $\mu m^2/s$ for the regular ones and between 40 to 80 $\mu m^2/s$ for the odd ones. A thinner characterization of these coefficients would require a more precise extraction of the elastic modulus α and thus a higher time resolution.

Nevertheless, even with these inherent uncertainties, our analysis demonstrate that the linear poroelastic theory provides a good quantitative description of the dynamic of shrinking of the polyacrylamide beads upon osmotic compression as embodied by the master curves Fig.3.10 E and F.

Second, to the uniaxial compression of the same beads. This problem is more complicated as it displays two different length scales and thus two different timescales associated with distinct modes of deformation Fig.3.12. We take advantage of our previous experimental analysis to estimate those timescales. We show that they are separated by 2 orders of magnitudes. This clear separation of timescales allows us to make the same theoretical simplification as for the osmotic shock problem. Both shrinking dynamics are thus predicted to display very similar features, the only difference arising from the geometry. We thus generalize the previous solution to cylindrical geometry and apply it to experimental data. Our analysis shows that both the theory and the experiments are in good agreement. First, we verify that the beads deform at constant volume upon the millisecond confinement. Second, the long-term relaxation dynamic is described by a single timescale which scales with the square of the radius. Third, the shrinking pattern upon uniaxial confinement of any given bead is shown to be identical in the rescaled time $\frac{t}{\tau_1}$. However, we note that the diffusion timescale extracted from this confinement experiments is higher than the one estimated from the osmotic shock experiment, as it ranges from 70 to 120 $\mu m^2/s$. We interpret this disparity from the substantial deformations that the confined beads experiences of respectively 80% in the vertical direction and 50% in the radial direction. We propose that the measured higher diffusion coefficient is an effective coefficient that arise from the renormalization of both the elastic moduli K and G and the friction ξ as a result of the change of the volume fraction ϕ of the gel during its deformation. A natural improvement of the theory would be to consider the change of ϕ with the deformation. Such a theory was proposed in [Geng, 2012] based on the stress-diffusion coupling model. Yet, the resolution becomes numerical. Another improvement would be to change the elastic constitutive linear relation by a non-linear one. We point out that Tartara's theory [Tatara, 1993] goes in this direction.

Taken as a whole, our study suggest that the dynamic of volume loss of nuclei is influenced by the permeation of the nucleoplasm through the dense chromatin network. As a logical extension, we propose to use this framework as the basis to quantitatively describe the dynamic of volume loss of nuclei under compression. We emphasize that such a framework is amenable to further improvement such as the incorporation of the membrane using the right boundary conditions or to electrostatic effects through the consideration of ions [Yamaue, 2005].

Chapter 4

Nuclear Blebs

En schématisant à peine, on pourrait dire que l'art du théoricien est de savoir jusqu'où on peut aller trop loin en matière de simplification.

Pierre-Gilles de Gennes
Leçon inaugurale au Collège de France
1971

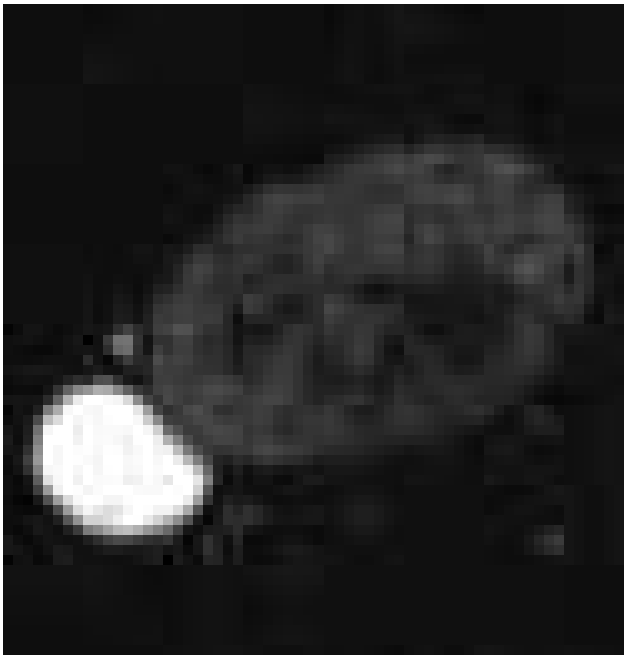

Nuclear bleb, Guilherme Nader

1 Introduction

1.1 Objectives

In Chapter 2, we investigated the consequences of the uniaxial confinement of nuclei. We showed that nuclei have two different regimes of deformation upon confinement. A first "safe" regime, where nuclear folds are unfolding at constant volume followed by a second regime of stretched nuclear envelope and volume loss. In this chapter we study the response of nuclei at even higher confinement: nuclear envelope ruptures and nuclear blebs appear.

1.2 Physiological consequences of nuclear blebs

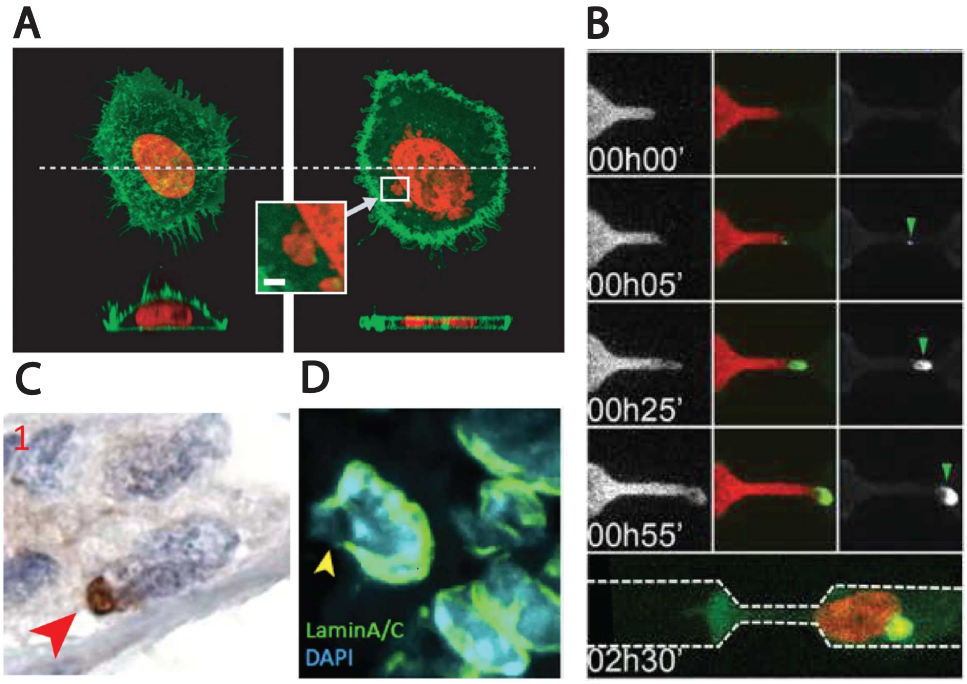

Figure 4.1: **Observation of nuclear blebs in different contexts.** (A) Hela cells before (left) and 30 minutes after (right) a 3.5nm confinement. The plasma membrane is stained in green, and chromatin is stained in red. Extracted from [Le Berre, 2014]. (B) Sequential images of a HeLa cell migrating through a constriction. H2b Histones are stained in red while the cytosolic binding protein cGAS is stained in green. The green arrows show the entry of cGAS at the nuclear tip and is an indicator of nuclear envelope rupture. Extracted from [Raab, 2016]. (C) Human tumor sample of a breast ductal carcinoma cancer cells. cGAS is stained in brown. The red arrow shows the location of NE rupture. (D) Zoom of a mouse xenograft showing breast ductal carcinoma tumor cells. The green arrow shows the location of nuclear envelope rupture. (C) and (D) are both extracted from [Nader, 2021].

Nuclear blebs have attracted attention in the recent years [Srivastava, 2021]. They have been observed both in vitro and in vivo in a variety of context ranging from constrained migration Fig.4.1(B), uniaxial confinement Fig.4.1(A) and diseases such as cancer Fig.4.1(C) and (D) and laminopathies [De Vos, 2011].

Contrary to the more studied plasma membrane blebs which benefit cells for example by providing them a way to migrate without adhesion to a substrate (amoeboid migration) [García-Arcos, 2022], the function of nuclear blebs, if they have one, is still unknown. They instead appear as a side consequence of nuclear envelope disruption due to strong nuclear deformation or diseases associated to the weakening of the nuclear envelope [Srivastava, 2021]. Recent studies have even highlighted the deleterious conse-

quences of nuclear blebs in breast cancer [Nader, 2021]. Upon strong confinement, blebs are unstable and repeatedly grow, burst and repair Fig.4.2. In the case of breast carcinoma, tumor cells proliferate in the mammary duct which confines the growth and lead to similar nuclear deformation and nuclear envelope ruptures. Nuclear envelope ruptures in turn provoke: loss of nuclear envelope permeability, entry of cytosolic proteins such as exonucleases, DNA damage, genetic instabilities and a switch from an in situ to an invasive tumor [Nader, 2021].

Although widely acknowledged as a major source of genetic and nuclear instability, nuclear blebs are comparatively poorly understood. This is what motivates the current chapter.

1.3 Experimental observations

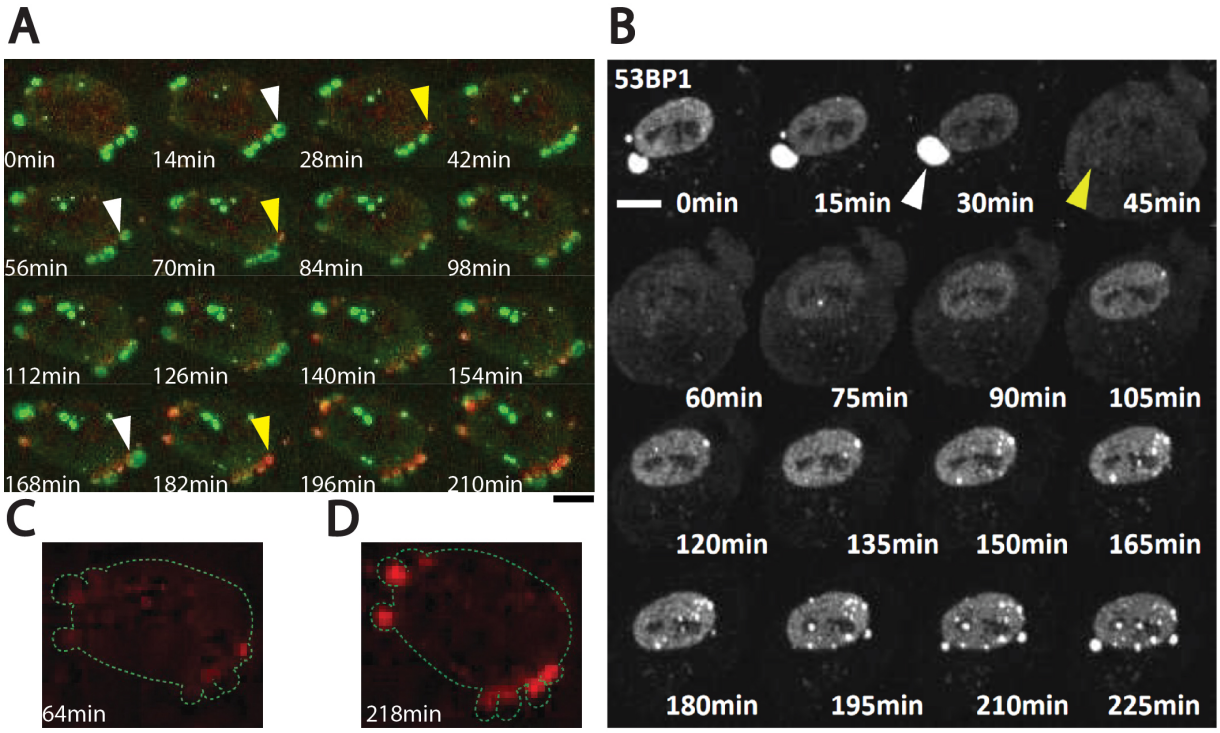

Figure 4.2: **Sequential images of RPE1 nuclei confined at 2μm.** Courtesy of Guilherme Nader. The origin of time is indexed on the time of first observation which occurs typically 40 to 60 min after confinement. Cells express 53BP1-EGFP which appear in green in (A) and white in (B). White arrowheads point to a bleb before its rupture while yellow arrowheads points to the same bleb after its rupture. (C) and (D) cGas becomes red when it comes into contact with DNA. Dashed green lines show the corresponding position of the nuclear membrane.

In this chapter we focus on understanding the physical origins of the instability of blebs that are observed upon strong uniaxial confinements Fig.4.2. We list below a number of significant experimental observations that characterize the blebbing process.

- Blebs are unstable and repeatedly grow, burst and repair. Fig.4.2.A
- The growth that occurs after a bursting event is always located at the same position as the previous bleb Fig.4.2.A.
- After a bursting event, 53BP1 leaks into the cytosol and is then reimported into the nucleus Fig.4.2.B.

- The radius of the hole at the tip of the bleb is constant during bleb growth and its value is about 500nm.
- The time of growth before the bleb rupture is about 30min but tends to slow down after 6 hours of confinement Fig.4.2.A. This is typically 100 times slower than the growth of plasma membrane blebs [Tinevez, 2009].
- The growing volumes and number of blebs depend on the nucleus observed Fig.4.2.A and B.
- New blebs can appear long after the confinement Fig.4.2.B.
- Chromatin herniates out of the nucleus. However, the timescale of herniation is much slower than the timescale of individual bleb growth Fig.4.2.C and D

2 Results

2.1 Preamble

2.1.1 The working model

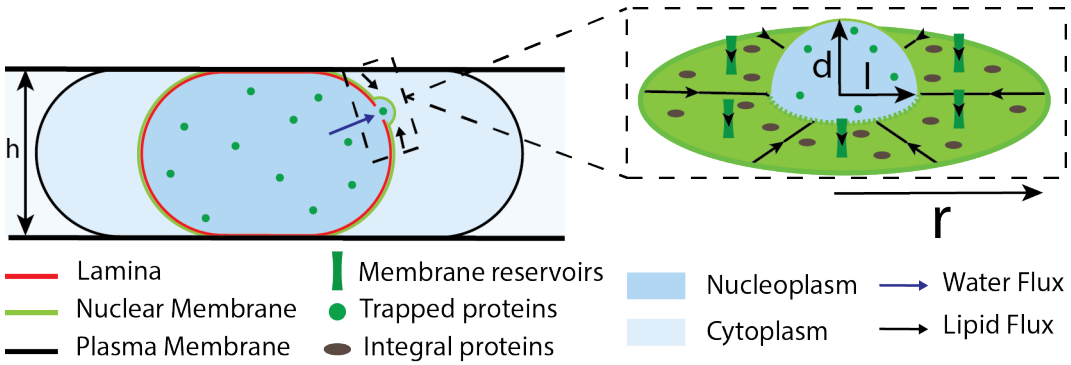

Figure 4.3: **Schematic of the bleb growth model.**

The model that we will formalize mathematically in Section.2.2 and Section.2.3 is the following. The confinement increases the tension in the lamina up to its rupture (see Chapter.2). The resulting difference of pressure between the nucleus and the cytoplasm ΔP_n initiates the growth of the bleb. Such a growth must be accompanied by an influx of lipid inside the bleb (see Sec.2.1.2). Importantly, we consider a scenario where the dynamic of growth is dominated by the friction between this lipid flow and the network of integral membrane proteins, assumed fixed in our model as they are embedded in the lamina layer. As such, we make a quasi-static approximation for the water flux and impose that it equilibrates instantaneously compared to the timescale of bleb growth (see Sec.2.2). Note that there are no integral membrane proteins in the bleb membrane and thus no associated friction. Hence, we assume that the tension in the bleb membrane is homogeneous. We further model the lipid flow as a axisymmetric planar flux fed by homogeneously partitioned membrane reservoirs. This flux is caracterized by one coordinate r which denotes the distance from a point on the membrane and the center of the hole at the basis of the bleb. We finally caracterize the geometry of the hemispherical bleb by two coordinates d and l. Based on the experimental recordings we assume that l remains constant during the bleb growth. Note however that when the bleb is large enough it touches the PDMS plates and thus transition from a hemispherical to a pancake geometry (see Sec.2.4.1). We justify in the next section (Sec.2.1.2) our modelling choices.

2.1.2 Motivations of our modelling

Nuclear membrane reservoirs The total surface of the system $\{Nucleus + Bleb\}$ is not conserved during bleb growth. For example, from the film displayed in Fig.4.2.B, we estimate that at the time of the bleb rupture, the total surface of the system $\{Nucleus + Bleb\}$ has increased by $\sim 30\%$. Alternatively, taken separately, the surface of the bleb has increased by more than 100 times. This has two important consequences. First, the growth of the bleb must be fed by a flow of lipid (see Fig.4.3). Second, it is likely that membrane reservoirs provide lipids to the nuclear envelope during the growth of the bleb. Indeed, membranes are quasi-inextensible. Their area stretching modulus is high ranging between 100-300 mN/m [Picas, 2012]. A small strain of 1 to 10% would thus be enough to rupture the membrane for which rupture stresses typically range from 1 to 10 mN/m [Evans, 2011]. We discuss in Sec.3 the possible biological origins of such membrane reservoirs for the nucleus.

Fluxes of water are equilibrated during bleb growth. The role of this subsection is to show that water fluxes equilibrate must faster than the observed bleb growth dynamic of about $Q \sim 1.7 \cdot 10^{-2} \mu\text{m}^3/\text{s}$. We consider two kinds of bulk dissipation processes. The friction induced by the nucleosolic flow through the chromatin network and the friction due to the flow through the hole at the tip of the bleb. Here, we assume that the tension in the nuclear membrane is homogeneous and small compared to the tension in the lamina. Hence, the difference of pressure across the hole is of the same order as the nuclear pressure difference ΔP_n far from the bleb. Moreover, the size of the hole at the tip of the bleb is large enough that proteins can pass through it. Indeed, the average protein size is typically 5nm [Rob Philipps, 2015] which is 100 times smaller than the size of the hole $l \sim 500\text{nm}$. The volumetric flow rate through a permeable hole can thus be written as:

$$Q = l_p \cdot \Delta P_n \tag{4.1}$$

With, l_p a permeation coefficient. Typical values of nuclear pressure differences for a 2μm confinement range from 10^3 Pa to 10^4 Pa (see Chapter.2). To further estimate l_p we consider two scenarios.

- Scenario 1: the dynamics of bleb growth is ruled by the bulk friction between the nucleosol and the chromatin network. The volumetric flow rate reads:

  $$Q = v \cdot \pi l^2 \tag{4.2}$$

  With v the velocity at the bleb entrance. Using a Darcy law we express $\vec{v}$ as:

  $$\vec{v} = \frac{\vec{\nabla} P}{\xi_b} \sim \frac{\Delta P_n}{\xi_b \cdot l} \tag{4.3}$$

  With, ξ_b a dissipation coefficient due to the friction between the chromatin network and the nucleosol. This coefficient should scale as $\frac{\eta_n}{\lambda_b^2}$ (see Sec.2.5.2) where η_n is the effective viscosity of the nucleosol and λ_b is the typical mesh-size of the chromatin network. We estimate a lower bond for Q assuming this dynamical process. We use $\Delta P_n = 10^3$ Pa and $\eta_n = 5 \cdot 10^{-3}$ Pa.s. Trapped nuclear proteins are observed in the bleb (see 53BP1 in Fig.4.2.B). These proteins must be big in order not to leak through the passive channel of nuclear pores which is typically of size 10nm [Ma, 2012]. It thus seems reasonable to use a lower bond of λ of order 10nm. Using these values, we find a lower bond for the flow rate to be 600 times faster than the one observed:

  $$Q \sim \frac{l \cdot \lambda^2}{\eta_n} \cdot \Delta P_n \sim 10\, \mu\text{m}^3.\text{s}^{-1} \tag{4.4}$$

- Scenario 2: the dynamics of bleb growth is ruled by the viscous flow across a hole. We assume that the thickness of the lamina is smaller than the size of the hole at the bleb tip. The permeation coefficient should scale as $l_p \sim \frac{l^3}{\eta_n}$ and the resulting flow rate is estimated to be:

$$Q \sim \frac{l^3}{\eta_n} \cdot \Delta P_n \sim 2.5 \cdot 10^4 \, \mu m^3.s^{-1} \tag{4.5}$$

  The flow rate obtained would be at least 6 order of magnitudes larger than the one observed in experiment. Collectively, these estimates clearly demonstrate that a hypothetical bulk flow dissipation would be too fast to explain the dynamic of bleb growth. In section Sec.2.2, we will thus assume that water fluxes are equilibrated during bleb growth and that the dissipation that dominates the dynamics originates from the friction between the flow of lipids and the integral proteins which are embedded in the lamina layer and thus considered as fixed.

Nucleation pressure to grow a bleb We end this preamble section by showing that, to observe a bleb, the tension in the lamina γ^l far from the bleb must be greater than the homeostatic tension of the membrane far from the bleb γ_0^m. As a thought experiment, we assume that the bleb is at equilibrium in a state where $d < l$ Fig.4.4. In this state, equality of pressures between the bleb and the nucleus leads to the constraint: $\Delta P_n = \Delta P_b = \frac{2\gamma_0^m}{R_b}$. We now imagine that the nuclear pressure is increased by small increments and want to assess how the equilibrium is changed. The balance of pressure implies that the radius of curvature of the bleb must decrease. This is achieved as long as the bleb has not reached the hemisphere Eq.4.33. Once the bleb becomes larger than a hemisphere - i.e., $d > l$ - the radius of curvature of the bleb can only grow and no further equilibrium state can be found assuming the pressure difference constant. This implies that there is a nucleation pressure above which the bleb grows $\Delta P_n^* = \frac{2\gamma_0^m}{l}$. Experimentally, blebs never reach their equilibrium state. It thus means that the regime where $\Delta P_n > \Delta P_n^*$ is the biologically relevant regime.

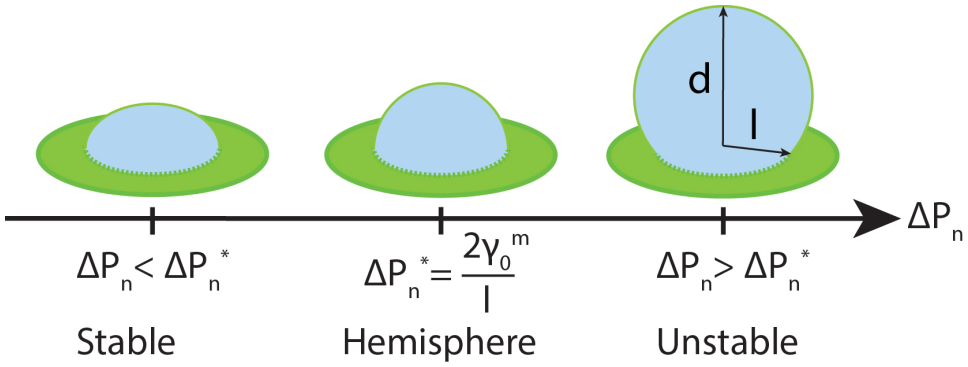

Figure 4.4: **Bleb nucleation pressure.** Schematic of the thought experiment. We imagine an initial equilibrium state where the bleb forms a small bulge above the membrane. We then assume that the pressure in the nucleus is increased incrementally. Due to the non-monotonic variations of the radius of curvature (see Eq.4.33 and Fig.4.6.B), an equilibrium state can only be found as long as the bleb has not reached the hemisphere demonstrating that there is a nucleation pressure of order $\sim \frac{2\gamma_0^m}{l}$ to grow a bleb.

This implies that the tension in the lamina must exceed the value:

$$\gamma^l > \gamma_0^m \cdot \left(\frac{h}{l} - 1 \right) \tag{4.6}$$

Experimentally, we observe that $\frac{h}{l} \sim 4$ such that $\gamma_l > 3 \cdot \gamma_0^m$. For simplicity, we will neglect γ_0^m

before γ_l^0 in the next sections. Note that this thought experiment was performed assuming that ΔP_n is constant. This will turn out to be a good approximation later (see Sec.2.5).

2.2 Bleb growth is accompanied by an influx of water inside the system $\{Nucleus + Bleb\}$

For clarity, we use the simplest model of one neutral osmolyte representing the nuclear trapped proteins to model bleb growth. However, qualitatively similar features are obtained when metabolites, ions and chromatin are included or when we only authorize a fraction of the trapped proteins to enter the bleb.

We assume that the fluxes of water and proteins are equilibrated. As the bleb grows, proteins enter into the bleb. At equilibrium, the partitioning of the proteins between the bleb - subscript b - and the nucleus - subscript n - is given by the balance of the chemical potential which, in the case of neutral osmolytes, is equivalent to the balance of concentrations. It is then straightforward to express the number of trapped proteins in the nucleus X_n at time t of growth with respect to their respective number $X_n(0)$ at the initial stage of growth.

$$X_n = \frac{X_n(0)}{1 + \frac{V_b}{V_n}} \tag{4.7}$$

The balance of the chemical potential of water between the nucleus and the cytoplasm reads:

$$\frac{2 \cdot \gamma^l}{h} = kT \cdot (x_n - 2n_0) \tag{4.8}$$

Where, we assumed a "pancake shape" for the nucleus. Hence, the volume and the apparent surface of the nucleus scale as $V_n = S_n^{proj} \cdot h$. And, the average curvature at the edge of the nucleus is $\frac{1}{h}$ since the radius of contact is assumed much larger than the confinement height (see Fig.4.3 and Chapter.2). We further use the constitutive elastic equation Eq.S.112 of the lamina to express γ^l as:

$$\gamma^l = K \cdot \left(\frac{2V_n}{h \cdot S^*} - 1 \right) \tag{4.9}$$

With, K and S^* the nuclear envelope stretching modulus and the nuclear surface at which the envelope starts to get tensed. Note that we also used that $V_n \approx \frac{S_n}{2} \cdot h$. Combining Eq.4.7, Eq.4.8, we further establish a relationship between the volume of the bleb and the volume of the nucleus during the growth of the bleb. For clarity, we normalize the volumes by the initial volume of the nucleus before blebbing - e.g., $\bar{V}_n = \frac{V_n}{V_n^0}$.

$$\begin{cases} \bar{K} \cdot c_1 \cdot \bar{V}_n^2 + \left(\bar{K} \cdot c_1 \cdot \bar{V}_b + (1 - \bar{K})\right) \cdot \bar{V}_n + \left((1 - \bar{K}) \cdot \bar{V}_b - c_2\right) = 0 \\ \text{With : } \bar{K} = \frac{K}{h \cdot kT n_0}, \quad c_1 = \frac{2V_n^0}{hS^*}, \quad c_2 = \frac{X_n(0)}{2n_0 V_n^0} \end{cases} \tag{4.10}$$

We further take advantage of the fact that blebs tend to be much smaller than the nucleus - i.e., $\bar{V}_b << 1$ - to use a perturbative approach and look for a solution of Eq.4.10 of the form $\bar{V}_n = 1 + \delta \cdot \bar{V}_b$. Only considering linear terms in $\bar{V}_b$ allows to express δ as:

$$V_n^0 = V_n(t) + \delta \cdot V_b(t) \quad \text{With,} \quad \delta = \frac{1}{1 + \frac{1}{\pi_n^0} \cdot \frac{2K}{h} \cdot (1 + \frac{S_n^0}{S^*})} \tag{4.11}$$

Where, h is the height of confinement; π_n^0 and S_n^0, the nuclear osmotic pressure and the nuclear surface at the initial stage of growth. Importantly, δ is bounded between 0 and 1. This implies that there is an influx of water inside the system $\{Bleb, Nucleus\}$ during the growth of the bleb. This can be seen from the following inequality $V_n^0 = V_n(t) + \delta \cdot V_b(t) \leq V_n(t) + V_b(t)$. Note that we find back the regime invoked

for the plasma membrane: if $\frac{K}{h} << \pi_n^0$, i.e. osmotic pressures are much larger than mechanical pressures, then $\delta = 1$ and volume is conserved. Finally, we emphasize that the precise expression of δ will change if we add more complexity into the model such as ions, chromatin and metabolites. However, we expect the conclusion that $V_n^0 = V_n(t) + \delta \cdot V_b(t)$, with $\delta \leq 1$, to hold.

2.3 A dynamic model for membrane flow

We hypothesize that the slow dynamic of growth of the blebs originates from the friction between the flow of lipids and the fixed integral membrane proteins embedded in the lamina layer Fig.4.3. We model this flow in this section.

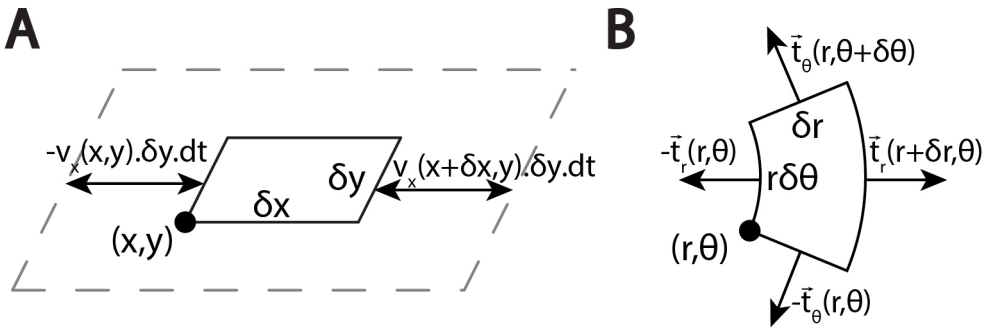

Figure 4.5: **Derivation of the equations describing nuclear membrane flow.** (A) Surface increase rate of a small element of surface initially measuring $\delta x \delta y$. The geometrical representation depicted leads to Eq.4.14. (B) Forces applied on a small element of surface in cylindrical coordinates.

2.3.1 Derivation of the equations

Continuity equation. We assume the membrane to be 3D incompressible:

$$\vec{\nabla} \cdot \vec{v}^{3D} = 0 \longrightarrow \partial_z v_z^{3D} + \partial_r v_r^{3D} + \frac{v_r^{3D}}{r} = 0 \tag{4.12}$$

We further show that this 3D incompressibility - i.e, ρ^{3D} constant - becomes a 2D continuity equation for the surface mass density of the membrane $\rho^m = \rho^{3D} \cdot e$. With e the thickness of the nuclear membrane which varies depending on the membrane tension. We use a Lagrangian approach and follow the deformation of a small element of volume of mass $\delta m = \rho^m \cdot \delta x \delta y$ (see Fig.4.5.A).

$$\frac{\mathbf{d}\delta m}{\mathbf{d}t} = 0 = \frac{\mathbf{d}\rho^m}{\mathbf{d}t} + \rho^m \cdot \frac{\mathbf{d}\left(\delta x \delta y\right)}{\mathbf{d}t} \tag{4.13}$$

The rate of variation of the small element of surface $\frac{\mathbf{d}(\delta x \delta y)}{\mathbf{d}t}$ can be expressed according to the 2D velocities $v_i \sim \frac{\int_0^{e_0} v_i^{3D}\, \mathrm{d}z}{e_0}$. Where, at linear order, it is sufficient to integrate over the homeostatic thickness of the nuclear membrane e_0. Without loss of generality we use cartesian coordinates to demonstrate the following formula (see Fig.4.5.A).

$$\frac{\mathbf{d}\left(\delta x \delta y\right)}{\mathbf{d}t} = (v_x(x+\delta x) - v_x(x)) \cdot \delta y + (v_y(y+\delta y) - v_y(y)) \cdot \delta x = \left(\vec{\nabla} \cdot \vec{v}\right) \cdot \delta x \delta y \tag{4.14}$$

We thus obtain:

$$\frac{\mathbf{d}\rho^m}{\mathbf{d}t} + \rho^m \cdot \left(\vec{\nabla} \cdot \vec{v}\right) = 0 \tag{4.15}$$

The previous equation was derived assuming mass conservation. As explained in Sec.2.1.2, the total surface of the system $\{Bleb + Nucleus\}$ is likely not conserved during the growth of the bleb because

of the inextensibility of lipid bilayers. Here, we choose to model the nuclear membrane reservoirs in an abstract way because the biological origin of these reservoirs is not clear at the time of redaction of the thesis. We discuss in Sec.3 the possible biological origins of such reservoirs. In the model, reservoirs allow to set the surface mass density to target a given surface mass density ρ_0^m. The dynamics of relaxation toward this target value is described by a relaxation time τ_r. The simplest linearized source term that we can write reads:

$$\frac{\mathbf{d}\rho^m}{\mathbf{d}t} + \rho^m \cdot \left(\vec{\nabla} \cdot \vec{v}\right) = \frac{\rho_0^m - \rho^m}{\tau_r} \tag{4.16}$$

For simplicity, we further assume that the bleb growth is slower than the dynamics of relaxation of the reservoirs - i.e., $\tau_r << 10min$. At steady-state, the continuity thus simplifies as:

$$\rho_0^m \cdot \left(\vec{\nabla} \cdot \vec{v}\right) = \frac{\rho_0^m - \rho^m}{\tau_r} \tag{4.17}$$

Constitutive equations. The nuclear membrane is modelled as a viscous Newtonian fluid with a shear viscosity η, a velocity $\vec{v}$ and a pressure P. The stress in the membrane reads:

$$\overline{\overline{\sigma}} = -P \cdot \overline{\overline{\mathbb{1}}} + \eta \cdot \left[\left(\overline{\overline{\nabla}}\vec{v}^{3D}\right) + \cdot \left(\overline{\overline{\nabla}}\vec{v}^{3D}\right)^T\right] \tag{4.18}$$

We assume the flow to be axisymmetric such that $\sigma_{r\theta} = 0$, $\sigma_{\theta z} = 0$ and $\vec{v} = v_r(r,z) \cdot \vec{e}_r$. We further make a thin shell approximation because we assume that the width of the membrane $\sim 50nm$ is smaller than its typical radius of curvature $\sim \mu m$. We thus impose $\sigma_{zz} = \sigma^m$ to be independent of z. Using the assumed 3D incrompressibility of the membrane and Eq.4.18 we express the pressure as:

$$-P = \sigma^m + \eta \cdot \left(\partial_r v_r^{3D} + \frac{v_r^{3D}}{r}\right) \tag{4.19}$$

Integrating over the membrane width e, we finally derive the 2D constitutive equations relating the in plane tensions with the radial velocity of the flow v_r:

$$\begin{cases} t_r = \gamma + 4\eta^m \cdot \partial_r v_r + 2\eta^m \cdot \frac{v_r}{r} \\ t_\theta = \gamma + 2\eta^m \cdot \partial_r v_r + 4\eta^m \cdot \frac{v_r}{r} \end{cases} \tag{4.20}$$

Where, $\gamma^m = \sigma^m \cdot e_0$ and $\eta^m = \eta \cdot e_0$ are respectively the bulk tension and the 2D shear viscosity of the membrane. Note that v_r now refers to the 2D average velocity of the flow over the width of the membrane. t_r and t_θ are the in-plane tensions in the nuclear membrane. They can be expressed according to the in plane stresses σ_{rr} and $\sigma_{\theta\theta}$ as:

$$\begin{cases} t_r = \int_0^e \sigma_{rr}\, \mathrm{d}z \\ t_\theta = \int_0^e \sigma_{\theta\theta}\, \mathrm{d}z \end{cases} \tag{4.21}$$

We add another constitutive equation to model the area elasticity of the membrane. This elasticity originates from the fact that, by stretching the nuclear membrane, the width must decrease by virtue of the 3D incompressibility and there is thus an energetic cost associated to this thinning. In the case of a simple lipid bilayer, we can interpret this energy penalty as the energy required to compress the lipids out of their resting length. In the case of the nuclear membrane which is constituted by a double lipid bilayer we instead think that the cost is more likely to originate from the fact that there are spacer proteins such as NPC or LINC complexes that imposes a certain perinuclear space. This 2D bulk compressibility reads:

$$\gamma^m = \gamma_0^m + K^m \cdot \frac{\rho_0^m - \rho^m}{\rho_0^m} \tag{4.22}$$

Where, γ_0^m is the resting surface tension of the nuclear membrane; K^m its stretching modulus - analogous for the membrane to the parameter K used in Chapter.2 to describe the lamina elasticity; And ρ_0^m, and ρ^m, the surface mass density of the membrane in a resting state, and in a stretched state. Note that K^m for a single lipid bilayer range from 100 to 300 mN/m [Picas, 2012]. For the nuclear membrane, it was measured to have a slightly higher value of $K^m = 390$mN/m for Oocyte Xenopus nuclei [Dahl, 2004].

Force balance in the radial direction. We make a force balance on a small element of volume comprised between r and $r + \delta r$ and θ and $\theta + \delta\theta$ (see Fig.4.5.B). For clarity, we only show the terms relevant for the radial direction. Note that the orthogonal force balance was already taken into account through the use of Laplace law far from the bleb and lead to the derivation of the constraint $V_n^0 = V_n + \delta \cdot V_b$ (see Eq.4.11).

$$t_r(r+\delta r,\theta)\cdot\vec{e}_r\cdot(r+\delta r)\delta\theta - t_r(r)\cdot\vec{e}_r\cdot r\delta\theta + t_\theta(r,\theta)\cdot(\vec{e}(r,\theta+\delta\theta)-\vec{e}(r,\theta)) = \xi^m\cdot v_r(r,\theta)\cdot r\delta r\delta\theta\vec{e}_r \tag{4.23}$$

Where, we call ξ^m the friction resulting from the lipid flow on the fixed network of integral proteins. Only keeping the lowest order terms in $\delta r \cdot \delta\theta$ leads to :

$$\partial_r t_r + \frac{t_r - t_\theta}{r} = \xi^m \cdot v_r \tag{4.24}$$

Boundary conditions. The continuity of mass at the junction between the nucleus and the bleb leads to a relationship between the velocity at the bleb entrance $v_r(l)$ and the rate of surface change of the bleb $\dot{S}_b$:

$$-2\pi l \cdot v_r(l) = \dot{S}_b \tag{4.25}$$

There are no integral proteins in the bleb membrane and thus no associated friction. Hence, we assume the tension in the bleb γ_b is homogeneous during the growth of the bleb. The continuity of tensions at the bleb junction further reads:

$$\gamma_b = t_r(l) \tag{4.26}$$

We finally assume that the velocity of the lipids far from the bleb vanishes:

$$v_r(r \longrightarrow \infty) = 0 \tag{4.27}$$

2.3.2 Membrane velocity field

The closed problem to solve thus reads:

$$\partial_r t_r + \frac{t_r - t_\theta}{r} = \xi^m \cdot v_r \quad \text{With,} \quad \begin{cases} t_r = \gamma^m + 4\eta^m \cdot \partial_r v_r + 2\eta^m \cdot \frac{v_r}{r} \\ t_\theta = \gamma^m + 2\eta^m \cdot \partial_r v_r + 4\eta^m \cdot \frac{v_r}{r} \\ \gamma^m = \gamma_0^m + K^m \cdot \frac{\rho_0^m - \rho^m}{\rho_0^m} \\ \rho_0^m \cdot \left(\vec{\nabla}\cdot\vec{v}\right) = \frac{\rho_0^m - \rho^m}{\tau_r} \end{cases}, \quad \begin{cases} -2\pi l \cdot v_r(l) = \dot{S}_b \\ \gamma_b = t_r(l) \\ v_r(r \longrightarrow \infty) = 0 \end{cases} \tag{4.28}$$

Note that the 2D problem formulated in Eq.4.28 is reminiscent of the equations used to describe compressible flows. By analogy we can identify $K^m \cdot \tau_r$ as a 2D bulk viscosity. Combining the force balance with the constitutive equations allows to derive a Bessel partial differential equation for v_r.

$$r^2 \cdot \partial_r^2 v_r + r \cdot \partial_r v_r - \left(1 + \left(\frac{r}{\mathcal{L}}\right)^2\right) \cdot v_r = 0 \quad \text{with,} \quad \mathcal{L}^2 = \mathcal{L}_1^2 + \mathcal{L}_2^2 = \frac{4\eta^m}{\xi^m} + \frac{K^m \tau_r}{\xi^m} \tag{4.29}$$

The two linearly independent solutions of this differential equation are the modified Bessel functions of the first and second kind of order one $\mathcal{I}_1$ and $\mathcal{K}_1$. The vanishing velocity far from the bleb imposes that the constant in front of $\mathcal{I}_1$ must vanish. We then use the continuity of tensions at the bleb junction to express v_r according to γ_b:

$$v_r = -\frac{(\gamma_b - \gamma_0^m)}{\xi^m \cdot \left[\mathcal{L} \cdot K_0(\frac{l}{\mathcal{L}}) + \frac{\mathcal{L}_1^2}{2l} \cdot K_1(\frac{l}{\mathcal{L}})\right]} \cdot K_1(\frac{r}{\mathcal{L}}) \tag{4.30}$$

Finally, we use the last boundary condition to express the tension in the bleb according to the rate of surface change of the bleb. The result reads:

$$\gamma_b = \gamma_0^m + \xi^{m,eff} \cdot \frac{\dot{S}_b}{\pi} \quad \text{with,} \quad \xi^{m,eff} = \xi^m \cdot \left[\frac{\mathcal{L}}{2l} \cdot \frac{K_0(\frac{l}{\mathcal{L}})}{K_1(\frac{l}{\mathcal{L}})} + \left(\frac{\mathcal{L}_1}{2l}\right)^2\right] \tag{4.31}$$

The coefficient relating $\xi^{m,eff}$ to ξ^m Eq.4.31 varies between two limiting regimes depending on the ratio $\frac{l}{\mathcal{L}}$. (1) When $l >> \mathcal{L}$, all the Bessel functions are equivalent at infinity such that $\xi^{m,eff} \sim \frac{\mathcal{L}}{2l} \cdot \xi^m$ (2) When $l << \mathcal{L}$, $K_0(\frac{l}{\mathcal{L}}) \sim ln\left(\frac{2\mathcal{L}}{l}\right)$ and $K_1(\frac{l}{\mathcal{L}}) \sim \frac{\Gamma(1)\cdot\mathcal{L}}{l}$, with Γ the Gamma function, such that $\xi^{m,eff} \sim \frac{1}{2\cdot\Gamma(1)} \cdot ln\left(\frac{2\mathcal{L}}{l}\right) \cdot \xi^m$. For simplicity, in the following we will assume that ξ^m is of the same order of $\xi^{m,eff}$. As a side note, we can easily verify that the qualitative argument presented in Sec.2.5.2 holds, namely that when $\lambda_m^2 << l^2$, only one dissipation coefficient, ξ^m, is sufficient to describe the dynamics. Here, we call λ_m the average distance between two integral proteins. $\frac{1}{\lambda_m^2}$ is thus the typical integral protein density. This parameter is analogous, for the membrane, to λ_b which refers to the typical mesh size of the chromatin.

2.4 Tension in the bleb during its growth

We close the problem by imposing the balance of water chemical potential between the bleb and the nucleus. In our qualitative model taking into account a single neutral compound that can freely go inside the bleb, this constraint simply becomes equivalent to the constraint of equality of hydrostatic pressure between the bleb and the nucleus. Neglecting γ_0^m (see Sec.2.1.2), Laplace law in each compartment reads:

$$\frac{\gamma^l}{h} = \frac{\gamma_b}{R_b} \tag{4.32}$$

Where, R_b is the averaged radius of curvature of the bleb. We show in the next subsection that there are two important limits for the geometry of the bleb and thus for R_b.

2.4.1 Geometry of the bleb

When the bleb is "small", the bleb is considered to be a spherical cap. This geometry is the one that minimizes the energy of the bleb (surface energy + curvature energy) if the tension in the bleb membrane is homogeneous. As mentioned above, this is justified because there are no integral proteins in the bleb membrane nor chromatin filling the bleb in most of the recording, such that the tension and

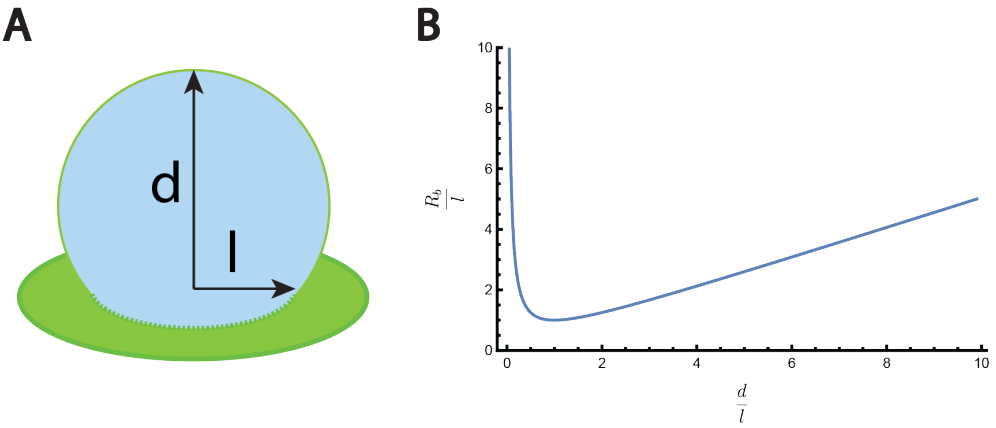

Figure 4.6: **Geometry of the bleb.** (A) As long as the bleb does not touch the PDMS plates, i.e., $d \leq d_{max}$ (see Eq.4.35). we model it as a spherical cap fully described by two parameters: l, the radius of the hole at the basis of the bleb. And d, the height of the bleb. (B) In the spherical cap regime, the radius of curvature of the bleb R_b is non monotonous (see Eq.4.33): it first decreases up to the hemispherical geometry, i.e., $d = l$ and then increases back again. This has important consequence for the dynamic of growth. Note that when the bleb touches the PDMS plates, i.e, $d \geq d_{max}$, R_b must saturate to a value close to the height of confinement h.

pressure are much faster to equilibrate inside the bleb. Note that experimentally, this approximation seems to be well observed for small blebs Fig.4.2.A. Following this geometry, the radius of curvature, the surface and the volume of the bleb can be expressed as:

$$\begin{cases} R_b = \frac{d^2+l^2}{2d} \\ S_b = \pi \cdot (d^2 + l^2) \\ V_b = \frac{\pi}{6} \cdot d \cdot (d^2 + 3l^2) \end{cases} \tag{4.33}$$

Only two independent parameters describing the bleb are necessary to fully describe its growth. For practical reasons we choose d, and l to be these parameters Fig.4.6. From experimental observations, we choose l to be constant, of order $\sim 500nm$. At time 0, the curvature of the bleb must match the curvature of the nucleus $R_b(t = 0) = h$ Fig.4.7.B. This imposes a constraint on d at the initial stage of growth:

$$d(t = 0) = h \cdot \left(1 - \sqrt{1 - \left(\frac{l}{h}\right)^2}\right) \tag{4.34}$$

We emphasize that in such a geometry, the radius of curvature of the bleb is non monotonous during growth. Before reaching the hemisphere $d < l$, the radius of curvature of the bleb decreases from h to l and then grows back again from l to d_{max} (see Fig.4.6.B). This will turn out to be of importance for the dynamic of growth of the bleb. Finally, we call d_{max} the value of the parameter d when the bleb touches the PDMS plates and thus stops to be a spherical cap. This happens when the radius of curvature of the bleb is of order $\frac{h}{2}$ which leads to a constraint on d :

$$d \leq d_{max} = \frac{h}{2} \cdot \left(1 + \sqrt{1 - \left(\frac{2l}{h}\right)^2}\right) \tag{4.35}$$

When the bleb is large, the bleb is considered to be a pancake Similarly to Chapter.2, if the bleb is large enough it tends to adopt a pancake shape. In this limit, the radius of curvature at the edges of the bleb is proportional to h:

$$R_b \approx h \tag{4.36}$$

2.4.2 Resolution

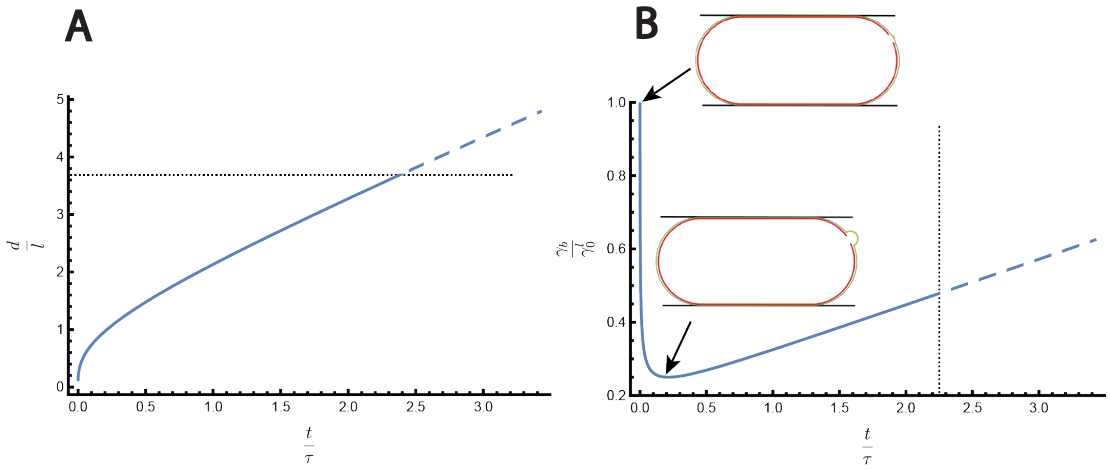

Figure 4.7: **Tension in the bleb during its hemispherical growth.** (A) Evolution of the height of the bleb with time (see Fig.4.6.A). The blue curve was obtained by solving numerically Eq.4.38. The length d is normalized by the radius of the hole l and the time is normalized by τ Eq.4.37. (B) Tension in the bleb membrane with time as computed from Eq.4.31. The tension is normalized by the tension in the lamina before blebbing γ_0^l. The minimum of tension is achieved for the hemisphere. In both panels, the black dashed line shows the time at which the bleb is predicted to touch the PDMS plates, i.e., $d = d_{max}$ Eq.4.35.

When the Bleb is hemispherical. We combine Eq.4.32 and Eq.4.33 to derive a differential equation for d. We identify the natural timescale ruling the growth of the bleb to be:

$$\tau = \frac{4 \cdot l \cdot h \cdot \xi^{m,eff}}{\gamma_0^l} \tag{4.37}$$

The problem to solve for $\bar{d} = \frac{d}{l}$ in the nondimensional time unit $\frac{t}{\tau}$ becomes:

$$\dot{\bar{d}} = \left(1 + \frac{1}{\bar{d}^2}\right) \quad \text{with,} \quad \bar{d}(0) = \bar{h} \cdot \left(1 - \sqrt{1 - \left(\frac{1}{\bar{h}}\right)^2}\right) \tag{4.38}$$

There are two important limit solutions to the previous differential equation. (1) For $\bar{d} << 1$ or equivalently $\bar{t} << 1$, $\bar{d}$ will scale as $\bar{d} \sim \bar{t}^{1/3}$ and γ_b as $\gamma_b \sim \bar{t}^{-1/3}$. This supra linear scaling for $\bar{d}$ can be qualitatively understood as follow: as long as the bleb has not reached the hemisphere, the radius of curvature decreases. Laplace law states that $\gamma_b = \Delta P_n \cdot \frac{R_b}{2}$. This implies that, at constant pressure ΔP_n, the tension in the bleb membrane decreases. This situation is unstable, the force resisting the deformation γ_b is fading which leads to an initial vertical asymptote for d and an infinite acceleration. We will see later that this divergence is an artefact resulting from our approximation that the pressure is equilibrated at each time step of growth (see Sec.2.6). (2) For $\bar{d} >> 1$, the growth will be linear with time up until $\bar{d}$ reaches $\bar{d}_{max}$. The solutions d and γ_b are plotted in Fig.4.7.

When the Bleb is a pancake. Using equation Eq.4.36, Eq.4.32 and Eq.4.31, it is straightforward to show that the tension in the bleb must equate the tension in the lamina and we thus predict that the surface of the bleb should scale linearly with time :

$$\dot{S}_b = \frac{\pi \cdot \gamma_l^0}{\xi_m^{eff}} \tag{4.39}$$

2.5 Preliminary Experimental validations

The story is under development at the time of redaction of the thesis. We nevertheless provide here a preliminary analysis based on one film Fig.4.2.B to give support to our modelling choices and results.

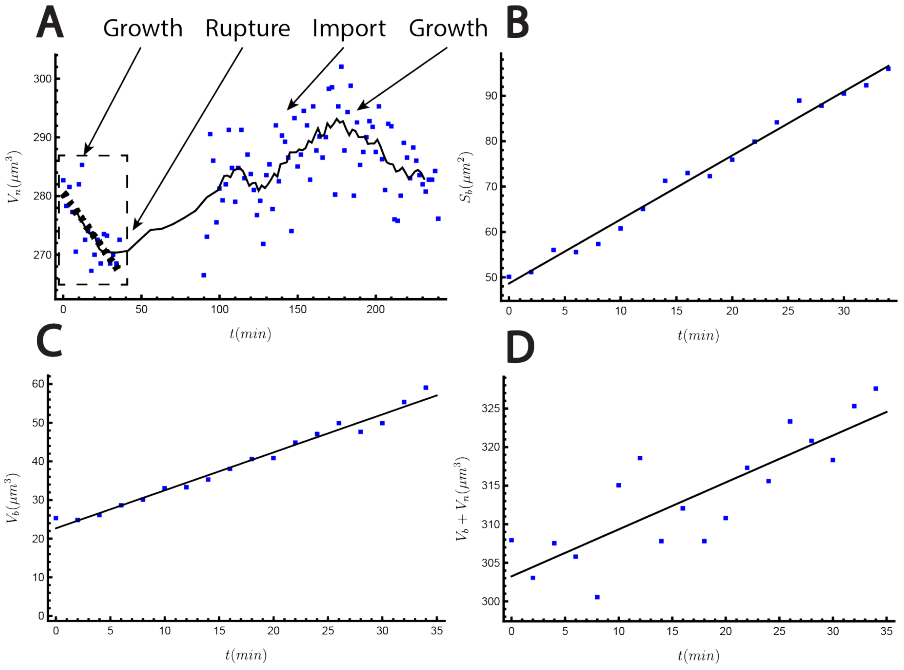

Figure 4.8: **Dynamic of bleb growth.** (A) Volume of the nucleus during blebbing over 240min as displayed in Fig.4.2.B. The volume was estimated from the formula $V_n = h \cdot S_n^{proj}$, with S_n^{proj} the apparent surface of the nucleus. The film can be divided into four observable events. First, the growth of one bleb. Note that the bleb is already large enough to touch the PDMS plates at the beginning of the recording. Inset: comparison with our model. The thick black dashed line is a linear fit of the volume of the nucleus during the growth of the bleb. A least mean square regression leads to: $V_n = 280.552 - 0.373076 \cdot t\ \mu m^3$ and the R^2 of the regression is 0.5. After 36 minutes, the bleb ruptures and the image of the nucleus disappear due to the mixing of the 53BP1 die with the cytoplasm. During this period the nuclear membrane heals. Then, we observe the importation of 53BP1 into the nucleus. And finally, at about 180 minutes, many blebs appear, one of them appearing at the exact same position as the one before. (B) Surface of the bleb during its growth using the approximate forumla $S_b = 2 \cdot S_b^{proj} + p \cdot h$. A least mean square regression leads to: $S_b = 48.6328 + 1.411 \cdot t\ \mu m^2$ and the R^2 of the regression is 0.98. (C) Evolution of the volume of the Bleb before its rupture (see Fig.4.2.B). V_b was also estimated assuming an elliptic cylindrical shape. A least mean square regression leads to: $V_b = 22.6898 + 0.981914 \cdot t\ \mu m^3$ with a $R^2 = 0.98$. (D) Evolution of the volume of the system $\{Bleb + Nucleus\}$ during the growth of the bleb.

Estimation of δ. We remind that δ was defined in Eq.4.11 as $V_n(t) = V_n^0 - \delta \cdot V_b(t)$. One important prediction of our model is that the growth of the bleb should be accompanied by an influx of water toward the system $\{Bleb + Nucleus\}$, i.e. $\delta < 1$. This is indeed verified in Fig.4.8.D. From the fit of Fig.4.8.A

and C, we estimate that $\delta \approx 0.38$.

Estimation of the apparent friction ξ_m^{eff}. Another important prediction of our model is that when the bleb is large enough to be also confined by the plates, the surface should grow linearly with time Eq.4.39. This is in line with the analysis we made from the recording displayed in Fig.4.2.B. Indeed, we estimate that the bleb is large enough to touch the PDMS plates from Fig.4.8.C. This also correlates with the linear increase of the surface Fig.4.8.B.

From Eq.4.39 and Fig.4.8.B we further estimate that the ratio $\frac{\gamma_l^0}{\xi_m^{eff}} = 0.45\mu\text{m}^2/\text{min}$. This leads to an effective friction coefficient ξ^{eff} of order $10^{11} - 10^{12}\text{Pa.s.m}^{-1}$, assuming a tension in the lamina to be $\sim 1 - 10\text{mN/m}$. If we further assume that the microscopic origin of the friction arise from the friction between the integral proteins and the flow of lipids then $\xi_m \sim \frac{\eta_m}{\lambda_m^2}$ (see Sec.2.5.2 for a justification), with $\frac{1}{\lambda_m^2}$ the typical integral protein density. There are about 1000 NPC per mammalian nuclei each occupying a circular region of radius $\sim$ 50nm on the nuclear envelope. The surface of the blebbing nucleus is $\sim 300\mu\text{m}^2$ such that the typical distance between two NPC is 100nm. NPCs are only one of the numerous integral proteins observed on the nuclear envelope. It thus seems reasonable to choose $\lambda \sim 10\text{nm}$. Assuming that the prefactor relating ξ^m with ξ_{eff}^m is of order one (see Eq.4.31), we estimate that the resulting membrane viscosity is of order $10^{-4} - 10^{-5}\text{Pa.s.m}$. Although this membrane viscosity was observed in certain types of cells [Brochard-Wyart, 2006], such a high value of nuclear membrane viscosity challenges our qualitative dynamic model. We discuss in Sec.3 the possible reasons of such a high apparent friction ξ_m^{eff} for the nuclear membrane.

Other experimental corroborations. One crucial approximation that we have made is to suppose the nuclear pressure difference to be constant during the growth of the bleb. In our model, the nuclear pressure difference is driven by the stretching of the nuclear envelope and in particular of the lamina. We estimate from Fig.4.8 that the loss of surface over the lifetime of the bleb to be $5\mu\text{m}^2$. This is negligibly small compared to the surface S^* at which the surface is stretched that should be at least $300\mu\text{m}^2$. Assuming $K = 25\text{mN/m}$, this would release a tension in the lamina of order $\sim 0.1\text{mN/m}$ which is again small compared to the tension γ_0^l that we estimated to be of order $1 - 10\text{mN/m}$.

Moreover, the time τ Eq.4.37 that we estimate is of order 10 minutes. Our model further predicts that the time to grow an hemispherical bleb is $\sim 0.1 \cdot \tau$ which would correspond to one minute (see Fig.4.7.B). The time resolution of the experiment is 2min which means that we should not be able to observe two frames in which the bleb is smaller than the hemisphere. This is indeed in line with what is observed in the films shown in Fig.4.2.A and B.

2.6 Rupture of the bleb.

In the current model, the tension is maximum at the beginning of the growth Fig.4.7.B. The natural question that arises is: why wouldn't the blebs burst at the early stages of their growth ? We investigate in this section two hypothesis that could theoretically explain this feature.

Permeation of the nucleoplasm We first hypothesize that the observed maximum of tension was an artefact of considering that the pressure is equilibrated in the bleb at all times. At small timescales, this hypothesis must break down. This can be captured by considering the rate of surface and volume changes which respectively scale as: $\dot{V}_b \sim \dot{d}$ and $\dot{S}_b \sim d\dot{d}$ at small d. Hence, there must be a regime at short timescale where the dynamics is dominated by the bulk dissipation and not the surface dissipation. We thus discuss qualitatively the consequences of the addition of such a bulk permeation to the previous model. Using Darcy's law with a bulk friction denoted by ξ_b, the volume growth rate of the bleb reads:

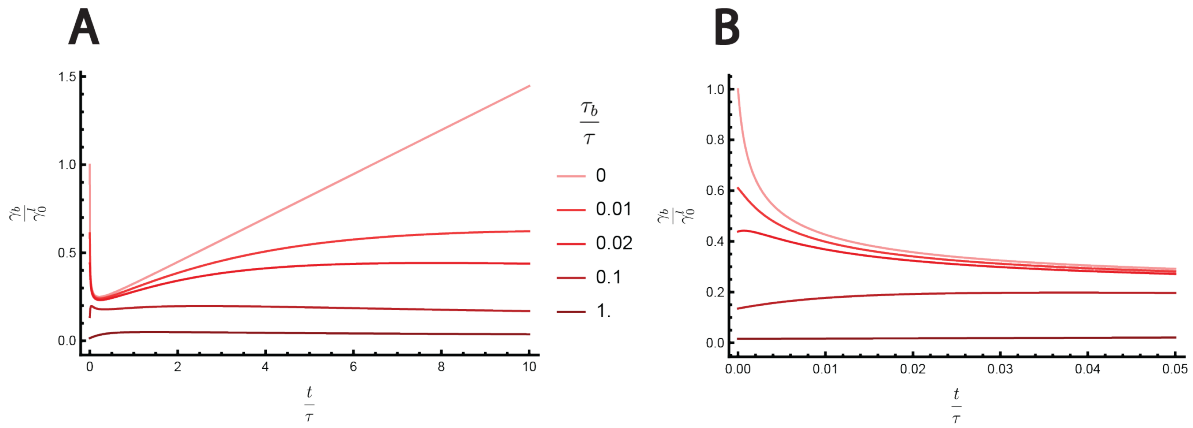

Figure 4.9: **Tension in the bleb during growth depending on the relative importance of the bulk to membrane friction.** (A) and (B) Tension in the bleb membrane for different value of $\frac{\tau_b}{\tau}$ as computed numerically from Eq.4.41 and Eq.4.31. (B) is zoomed on the early stages of growth. We estimate that the biological regime is achieved for $\frac{\tau_b}{\tau} \sim 10^{-5}$. Note that we neglected γ_0^m before γ_0^l.

$$\dot{V}_b = \frac{\pi l^2}{\xi_b} \cdot \frac{(P_n - P_b)}{l} \tag{4.40}$$

The new differential equation ruling the evolution of d becomes:

$$\dot{\bar{d}} = \frac{1}{\frac{\tau_b}{\tau} \cdot (1 + \bar{d}^2) + \frac{\bar{d}^2}{(1+\bar{d}^2)}} \tag{4.41}$$

The effect of adding the permeation of the nucleoplasm is to add a new timescale $\tau_b = \frac{\xi_b h l^2}{\gamma_0^l}$. Note that when $\tau_b = 0$ we find back Eq.4.38. As predicted, the maximum of tension observed at early stages of the bleb growth is decreased. We display for illustration, in Fig.4.9, the evolution of the tension for different values of the parameter $\frac{\tau_b}{\tau}$. When $\frac{\tau_b}{\tau}$ is high enough, e.g. ~ 1, the tension in the bleb stays constant. At intermediate values, e.g., $\frac{\tau_b}{\tau} \sim 10^{-2}$, the tension exhibits a maximum at short timescale but of smaller amplitude. Nevertheless, using the friction coefficient extracted earlier $\xi_m \sim 10^{11} - 10^{12}$Pa.s.m^{-1} from experiments, we estimate the ratio to be even smaller, of order 10^{-5}. With such a low value of $\frac{\tau_b}{\tau}$, our numerical solutions predict no difference with the limiting regime $\tau_b \longrightarrow 0$. Note that to obtain this estimation, we determined an upper bound for the friction coefficient of the bulk. The bulk friction should scale as $\xi \sim \frac{\eta_b}{\lambda_b^2}$, with $\eta_b \sim 5 \cdot 10^{-3} Pa.s$ the bulk viscosity of the nucleoplasm and λ_b the typical chromatin mesh size of order $10nm$. To further validate that we can indeed neglect the permeation of the bulk we adopted the complementary approach. Instead of assuming that the membrane restricts the dynamic, we assumed that the dynamic is ruled entirely by the permeation of the nucleoplasm. Using $\dot{V}_b \sim 1\mu\text{m}^3 \cdot \text{min}^{-1}$, we estimate that the viscosity of the bulk should be of order $\eta_b \sim 10^1 Pa.s$ which would be equivalent to honey and thus not realistic. Although, the permeation of the bulk could allow to explain why the bleb do not burst at the beginning of its growth, our estimates seem to refute this hypothesis.

Kinetics of nucleation of a hole in the nuclear membrane. The second hypothesis is that the rupture process is not only driven by the absolute value of the tension but also by the kinetics of nucleation of the hole. This hypothesis seems realistic since experimental studies have shown that double lipid bilayers could sustain tensions of 1- 10 mN/m over tenth of minutes [Evans, 2011].

3 Discussion and perspectives

In this chapter, we have studied the physical origins of the mechanical instability of nuclear blebs. Contrary to cortical actin, lamina is stiff and has a turnover rate of the order of few hours ([Moir, 2000] and [Guilluy, 2014]) allowing it to sustain relatively high tensions on long timescales. The pressure built up in the nucleus after confinement is thus maintained over long periods. Blebs should in principle allow to release such a pressure by decreasing the volume of the nucleus and thus its surface. This pressure release is nevertheless counteracted by two factors. First, we show that the growth of the bleb is accompanied by an influx of water which impedes the nuclear pressure release. Second, proteins expelled after the bleb rupture are imported again leading to the restoration of the nuclear pressure.

Another key feature of nuclear blebs is that their dynamic of growth takes place on the tenth of minutes timescale against tenth of seconds for their plasma membrane homolog. This is to be noticed since the nuclear pressure difference is estimated to be at least ten times greater than the cytoplasmic pressure difference [Tinevez, 2009]. Plasma membrane can expand by more than three times before rupturing demonstrating the existence of membrane reservoirs [Venkova, 2022]. These membrane reservoirs originate from invaginations mediated by specific proteins such as caveolae which span over the entire surface of the cell [Sinha, 2011]. When the cortex ruptures or is ablated, the bleb grows by unfolding these invaginations and the initial dynamic of growth is likely driven by this unfolding. For confined nuclei, we showed that nuclei have lost their invaginations (see Chapter.2). Nuclear membrane is smooth, and the growth of the bleb must be accompanied by a flux of lipids towards the bleb. Our results show that the slow growth of blebs cannot be explained by the permeation of the nucleoplasm through the dense chromatin network nor through the hole in the lamina. We thus propose that the dynamic is limited by the friction between lipids which flow towards the blebs and integral proteins such as nuclear pore complexes which are embedded in the lamina. We show that this model can explain the dynamic of growth if the associated friction coefficient ξ_m is high of order $10^{11} - 10^{12}$Pa.s.m^{-1} resulting in a nuclear membrane viscosity of order $10^{-5} - 10^{-4}$Pa.s.m. We emphasize that this viscosity is high when compared to single lipid bilayers although compatible with values for the plasma membrane observed in certain cell types [Brochard-Wyart, 2006].

The slow dynamics of bleb growth contributes to its instability. It indeed allows to equilibrate the pressure between the nucleus and the bleb. Tension in the bleb is thus predicted to be of the order of the tension in the lamina whose value typically matches the tensions of rupture observed in lipid bilayers (1-10 mN/m) (see Fig.4.7.B and [Evans, 2011]). In our model, the lipid flow is driven by the gradient of membrane tension between the bleb and the nucleus Eq.4.31. A natural consequence is that it makes more likely the rupture to happen in the bleb. This may explain why membrane ruptures are exclusively observed inside blebs. Another reason may be that the energy barrier to nucleate a hole in the bleb membrane is lower than the one in the nuclear membrane. Indeed, the loss of transmembrane proteins in the bleb which normally ensures a spacing between the two nuclear membranes, could lead to the close proximity of the tensed inner and outer nuclear membranes, and eventually to their fusion [Srivastava, 2021] and [Chernomordik, 2008]. This would in turn ease the formation of a pore and thus lead to the rupture of the membrane in the bleb.

Although our model shows good success at explaining key experimental observations, the required high value of apparent nuclear membrane viscosity challenges it. We propose two explanations for this observation. (1) The nuclear envelope is a double lipid bilayer. Both membranes are continuous with each other, and the junction happens at the location of the NPC insertion. Importantly, only the outer nuclear membrane is continuous with the endoplasmic reticulum membrane which we propose provides lipids during the growth of the bleb. This implies that there must also be a flow of lipid from the outer nuclear membrane to the inner nuclear membrane. This flow is likely to happen with an additional

friction at the nuclear pore junction. We thus hypothesize that this process might slow down the dynamic and in turn increase the apparent friction estimated from our model. Further finer modelling as well as experimental characterization of the nuclear membrane remain an exciting area for future studies. (2) An additional effect that would slow down the dynamic of bleb growth is the explicit consideration of the diffusion of large proteins through the network of chromatin. The nested Pump-leak model states that the driving force of bleb growth is the entry of osmolytes that were previously trapped in the nucleus. In its current version, our model assumes that trapped proteins equilibrate rapidly and we thus set the concentration of proteins to be the same across the bleb hole Eq.4.7. The immediate next step of our future research is to relax this assumption. Indeed, studies have shown that the diffusion of large objects can be slow in the nucleus. For example, the diffusion coefficient of mRNAs in the nucleus was measured to be 0.12 $\mu m^2/s$, or equivalently, the typical timescale for an mRNA to exit the nucleus is in the minutes range [Coulon, 2014].

Finally, we conclude this chapter by highlighting possible extensions of our study. In this chapter, we have focused on the growth of nuclear blebs and have evoked the reasons of their rupture in the tenth of minutes after confinement. The events that occur after the bleb rupture, namely nuclear membrane healing and protein import are exciting avenues for future research. Moreover, the appearance of new blebs 4 hours after confinement (see Fig.4.2.B) is interesting because their origin is likely different from the one observed just after confinements. We propose two hypotheses that we would like to investigate in the future. (1) First, a biological hypothesis where the lamina would be biologically degraded by the action of phosphorylase enzymes produced by the cell in response to the long term confinement. (2) Second, a physical hypothesis where the lamina would naturally depolymerize because of the tension which increases the energy of the "polymerised" state compared to the "unpolymerized" state. This mechanism would be in essence similar to a phase transition undergone by the lamina.

Conclusion

Comme je l'ai réalisé avec le temps, [ma recherche] traverse [des] cycles comme une respiration : un temps pour l'action et un temps pour la contemplation. Il n'y a pas moyen d'y échapper.

Nathalie Cabrol
Voyage aux frontières de la vie
2021

In this thesis, we have investigated the physical principles at the root of size and density regulation in the cell and the cell nucleus. The cornerstone of our work is based on a model for cell volume developed 60 years ago named the Pump-Leak model [Tosteson, 1960]. Although being well established, the model exhibits a high number of parameters which has mainly precluded its dissemination and use in the community of biologists.

The first part of our work was thus to design the minimal formulation of such a model. Based on order of magnitude estimates, we make four important approximations. (1) To study size variations on timescales of the order of minutes, steady states on the water and ionic fluxes can be assumed. This implies that the Pump-Leak model reduces to three simple physical constraints: electroneutrality, osmotic balance at the plasma membrane and balance of ionic fluxes Eq.1.1, Eq.1.2, Eq.1.3. (2) The osmotic pressure expression of non-ideal solutions can be highly non-linear and complex [Barrat, 1996]. Yet, estimations of the steric contribution of large osmolytes such as proteins suggest that these effects are negligible compared to the ideal gas law contribution (see Section.3.12). This originates from the fact that small osmolytes such as ions and metabolites are typically one hundred times more concentrated than large proteins in the cell Fig.1.1. (3) The theory is insensitive to the number of ionic species taken into account. Indeed, the expressions of volume takes the same functional form provided that the ionic species considered are monovalent Eq.S.59. The latter approximation is very robust, multivalent ions such as calcium are typically 5 orders of magnitude less concentrated than their monovalent homolog [Rob Philipps, 2015]. The huge complexity of ionic transport at the plasma membrane can thus be reduced in one effective parameter α_0 which, in the two-ions model, characterizes the pumping efficiency of cations by comparing their active export with their passive leakage at the plasma membrane Eq.1.3. (4) Estimations of this parameter for mammalian cells demonstrate that it is close to 0, i.e., cells are in a regime of high pumping such that the only ions that remains in the cell are the counterions of the impermeant molecules. These approximations significantly simplify the model and make the results much more intuitive. The volume of the cell can simply be expressed as the sum of two contributions: a dry volume, resulting mainly from proteins and estimated to occupy 30% of the volume of the cell, and a "wet" volume, which is the volume occupied by water Eq.1.4. The latter volume, in the regime described before, is simply proportional to the number of impermeant cellular macromolecules, which were shown to be mainly accounted for by metabolites and in particular amino-acids Fig.1.1.

Based on this new reductionist interpretation of the Pump-Leak model, we studied the origin of the ubiquitous cell size scaling laws which linearly relates cell volume with the cellular protein content and the nucleus volume. Importantly, we show that both scaling laws arise from the same three physical constraints, namely the electroneutrality, the osmotic balance, and the balance of ionic fluxes. For the density homeostasis, i.e., the linear scaling between cell volume and protein number, given that the cell volume is at first order accounted by amino-acids (mainly glutamate), the problem reduces to understanding how the proteins and the amino-acids scale with each other. We thus complemented the Pump-Leak model with a model of amino-acid and protein biosynthesis (see Section.2.3). This model makes two important predictions. (1) The density homeostasis is naturally achieved in the exponential growth regime of the cell by virtue of the enzymatic control of the amino-acid production. (2) The density homeostasis however breaks down when cells exit this exponential regime. The model further predicts that the change of regimes naturally occurs when cells are prevented from dividing. In this case, DNA and mRNAs become saturated by RNA polymerases and ribosomes, which leads to a drastic change of regime of growth: the protein number saturates while the amino-acid number increases linearly with time, resulting in the dilution of the protein content. These predictions are reminiscent of the intracellular dilution at senescence recently reported in fibroblasts and yeast cells [Neurohr, 2019]. We thus naturally compared our predictions with these recent, yet unexplained data. The agreement between

the theory and the experiment is striking as the model is able, without adjustable parameters, to predict with good precision both the evolution of the protein number and the dry mass density during the growth of yeast cell prevented from dividing Fig.1.2. We highlight that our conclusions resolve a known paradox in the field, namely, the proportionality between cellular volume and protein content although protein concentration is relatively low in the cell. In addition, we proposed a novel interpretation of the dilution that occurs at the beginning of mitosis as originating from the interplay between the Pump-Leak model and a subtle electrostatic mechanism associated to the release of the condensed counterions of the chromosomes induced by histone tail modifications Fig.1.3.

For the nuclear scaling, we generalized the Pump-Leak model by nesting it. Similarly to recent studies, our model shows that one necessary condition for the nuclear scaling is the osmotic balance at the nuclear envelope Eq.1.12. Yet, we emphasize that this condition is not sufficient. Indeed, how to explain that the nucleus scales while the counterions of chromatin (which do not scale during growth) cannot be neglected compared to the number of trapped nuclear protein (which do scale)? Here again, we resolve this apparent paradox by the consideration of metabolites and their counterions. Counterintuitively, metabolites, though permeable to the nuclear envelope, play an essential role in the NC ratio. Their high concentrations in cells, a conserved feature throughout biology, is shown to dilute the chromatin counterions, thereby allowing the scaling of nuclear size with cell size both at the population level and during individual cell growth Fig.1.4. However, why would the osmotic pressure be balanced at the nuclear envelope? This is even more surprising because, at the difference of the plasma membrane, the typical criterion for the nuclear envelope to play a role in the regulation of the nucleus volume is that the Laplace pressure originating from the tension in the envelope is of the order of the osmotic pressure created by the nuclear trapped proteins Eq.1.16. The magnitude of this osmotic pressure was estimated to lie in the kPa range which was shown to be easily achieved for small elastic deformations of the stiff lamina. The paradox can be resolved phenomenologically by assuming a non-linear elastic response of the nuclear envelope: the tension in the envelope only increases when the surface of the nucleus exceeds a certain threshold surface Eq.S.112. This phenomenological answer was further supported by published hypo-osmotic shock experiments showing that the osmotic response of nuclei was non-linear [Finan, 2009]. For low osmotic shocks, both the nucleus volume and the cytoplasm volume inversely scale with the magnitude of the shock enforcing a constant NC ratio. On the other hand, after a sharp transition, while the cytoplasm keeps its scaling, the nucleus starts to grow sublinearly leading to a decrease of the NC ratio Fig.1.4.D.

Although the nested Pump-Leak model makes interesting predictions, it remained mainly theoretical at that stage and based on a phenomenological equation to describe the mechanical response of the nuclear envelope. We therefore propose in Chapter.2 a quantitative confrontation of our theory to the unpublished data from Matthieu Piel's team studying the consequences of "moderate" uniaxial confinement of nuclei on the minute timescale. The main experimental observations are twofold. (1) The response of the nucleus can be divided into two clearly distinct regimes: a first "safe" regime, at low confinements, for which the surface of the nucleus increases at constant volume; And a second regime, at moderate confinements, for which the surface keeps increasing but at decreasing nuclear volume Fig.2.2. (2) Nuclei smoothen upon confinement and the transition between the two regimes of deformation occurs precisely at the confinement height for which nuclei have entirely lost their folds. We propose a theoretical answer to these observations in two steps. First, we complemented the nested Pump-Leak with an equation that describes the shape of the confined nuclei Eq.2.3. Together, the theory shows good quantitative agreement with the data. Importantly, it predicts that the nucleus starts to lose volume at the height for which the tension in the envelope starts to increase. But what is the origin of such a sharp transition for the nuclear envelope tension? Following the second experimental observation, namely the causality between the nuclear folds

disappearance and the abrupt volume decrease, we propose a mechanical model to explain the origin of nuclear folds. Our theoretical answer is based on a well-known mechanical instability: soft substrates bound to thin stiff elastic layers buckle upon compression. Estimates using typical values of the chromatin and lamina elastic moduli confirm that such a scenario is likely relevant for the nucleus. Lamina is indeed a thousand time stiffer than the chromatin such that wrinkling is energetically favorable even for low compressive strains Table.2.2. Importantly, the model is consistent with the phenomenological equation used in the Pump-Leak model. Indeed, it predicts that the folds set the tension in the nuclear envelope to small values compared to the osmotic tensions and that they disappear with uniaxial confinements Fig.2.11. However, the mechanical model relies on a key hypothesis: the system must be compressed for the folds to appear. What is the biological origin of such compression? We propose that it originates from two essential features of the nuclear envelope. (1) The nuclear envelope forms on the condensed chromosome cluster (see Fig.2.12). This can lead to frustrations during the geometric transition following chromosome decondensation. (2) The lamina, contrary to cortical actin, was shown to have a low turnover rate of the order of few hours ([Moir, 2000],[Guilluy, 2014]) which we propose explains the conservation of stress over long period of time. Collectively, the previous models provide a self-consistent framework to explain the nuclear envelope smoothening followed by the nuclear volume loss upon uniaxial compression on the timescale of minutes. Importantly, our study adds to a growing number of recent papers that demonstrate the fundamental contribution of nuclear shapes and in particular of nuclear wrinkles and folds to the cell homeostasis ([Lomakin, 2020],[Venturini, 2020],[Cosgrove, 2021]). In this thesis, we have demonstrated the fundamental role of these folds on the nuclear volume homeostasis and by extension on the robustness of the nuclear scaling law.

So far, we have demonstrated that *a single model of size regulation*, namely the nested Pump-Leak model, coupled to an appropriate mapping between the cellular processes and the coarse-grained model parameters can successfully predict a large variety of independent biological processes such as the cell density homeostasis and dilution, the mitotic swelling, and the nuclear scaling and its subsequent breakdown upon perturbation. The common feature of these biological phenomena is that they happen on timescale of minutes to hours. But how to extend our theory to encompass faster size variations? This question is motivated by the data of the team of Matthieu Piel which show that the volume response of confined nuclei on the seconds timescale is non-trivial: the nucleus first deforms at constant volume following a millisecond compression and then shrinks with a dynamic governed by a timescale of about 10s. Interestingly, this dynamic is 1000 slower than that of the cytoplasm and happens at height of confinement where the nuclear envelope should not be stretched. The major challenge in proposing a dynamical model for the nucleus volume is the multiplicity of factors that were shown to play a crucial role in its regulation such as ions, proteins, metabolites and lamina. To go in this direction, we decided to study the response to confinement of a simplified model system constituted by only 2 components: a neutral polyacrylamide network and a fluid. This system was shown to exhibit qualitatively similar response to confinement, namely the deformation at constant volume followed by a network shrinkage. To understand this peculiar dynamic, we have derived a linear poroelastic theory from entropy production and Onsager reciprocal relations. We show that the derived theory is equivalent to the stress diffusion coupling model developed 40 years ago [Tanaka, 1979]. The proposed derivation of the theory has two benefits. First, it clearly identifies what is the "fluid pressure" which appears in the Tanaka theory as being proportional to the difference between the hydrostatic pressure and the osmotic pressure arising from the steric repulsions of the gel Eq.3.29. Second, it can easily be adapted to include other species such as ions. A striking prediction of this theory is that the mesoscopic elements of volume constituting the gel evolve following a diffusion equation Eq.3.47. Any significant volume variations on timescales faster than the diffusion timescale are thus impeded. The gel hence first deforms at constant volume

under fast deformation and then relaxes by shrinkage toward its equilibrium state following the diffusion timescale, the magnitude of this deformation being driven by the Poisson's ratio of the gel. Motivated by these qualitative conclusions, we next quantitatively apply this theory to two distinct problems: the osmotic compression and the uniaxial compression of the polyacrylamide beads. Our analytical solutions demonstrate that both experiments are well described by the theory, as embodied by the superposition of the experimental data on master curves describing the shrinkage of beads of different size upon osmotic and mechanical compression Fig.3.10 and 3.15.

One important consequence of moderate nuclear uniaxial confinements is the tension increase in the nuclear envelope. We explained that this increase was at the root of the volume loss of moderately confined nuclei. However, if the confinement is increased even more, the tension becomes high enough to rupture the nuclear envelope and leads to the appearance of nuclear blebs Fig.4.2. Intriguingly, the nuclear blebs are unstable: they repeatedly grow, burst and repair. This instability of the nuclear envelope was shown to be deleterious since it is associated to genetic instabilities and to an increase of cancer invasiveness in breast carcinoma. Why are nuclear blebs unstable? Here again, the nested Pump-Leak model provides enlightening answers. The model shows that the bleb growth is necessarily induced by the passage of trapped nuclear osmolytes, mainly large proteins, into the bleb. The bleb growth in turn allows to release the nuclear pressure, here induced by the stretching of the nuclear envelope upon confinement, by reducing the nucleus volume and thus the tension in the nuclear envelope. However, the magnitude of this pressure release is in average negligible due to the combined effect of two factors. First, the nested Pump-Leak model predicts that the bleb growth is accompanied by an influx of water inside the nucleus which partially impedes the pressure release. Second, after bleb burst, the large proteins, which possess a nuclear localization signal, are imported back into the nucleus, thus restoring the initial nuclear pressure. Together, these effects, combined with the low turnover rate of lamina, explain why blebbing is periodic. Another key feature of nuclear blebs is that their dynamic of growth is slow, on the tenth of minutes range. Our estimations strongly refute the hypothesis that the dynamic of growth is driven by the permeation of water through the network of chromatin. We thus proposed an alternative model where the growth is slowed down by the friction between lipids which flow toward the bleb and the integral nuclear membrane proteins which are embedded in the lamina layer (see Section.2.3). We show that this model can quantitatively explain the dynamic of growth if the associated friction coefficient ξ_m is high of order $10^{11} - 10^{12}$Pa.s.m^{-1} resulting in a nuclear membrane viscosity of order $10^{-5} - 10^{-4}$Pa.s.m. Such a high value of nuclear membrane viscosity challenges our dynamic model. We propose two explanations for this observation. (1) The nuclear envelope is a double lipid bilayer. Both membranes are continuous with each other, and the junction happens at the location of the nuclear pore insertion. Importantly, only the outer nuclear membrane is continuous with the endoplasmic reticulum membrane which we propose provides lipids during the growth of the bleb. This implies that there must also be a flow of lipid from the outer nuclear membrane to the inner nuclear membrane. This flow is likely to happen with an additional friction at the nuclear pore junction. We thus hypothesize that this process might slow down the dynamic and in turn increase the apparent friction estimated from our model. Further finer modelling as well as experimental characterization of the nuclear membrane remain an exciting area for future studies. (2) An additional effect that would slow down the dynamic of bleb growth is the explicit consideration of the diffusion of large proteins through the network of chromatin. The nested Pump-leak model states that the driving force of bleb growth is the entry of osmolytes that were previously trapped in the nucleus. In its current version, our model assumes that trapped proteins equilibrate rapidly and we thus set the concentration of proteins to be the same across the bleb hole Eq.4.7. The immediate next step of our future research is to relax this assumption. Indeed, studies have shown that the diffusion of large objects can be slow in the nucleus. For example, the diffusion coefficient of mRNAs in the nucleus was measured

to be 0.12 $\mu m^2/s$, or equivalently, the typical timescale for an mRNA to exit the nucleus is in the minutes range [Coulon, 2014].

To conclude, in this thesis, I have provided a broad theoretical picture of cell volume, nucleus volume and cellular density, and a particular attention has been given to the experimental verification of the predictions of our models. Although showing good quantitative agreement with experiments, the models presented in this thesis can be extended in a number of different and exciting directions. In chapter 1, we complemented the nested Pump-Leak model with a model of amino-acid and protein biosynthesis to assess how cell density evolves during growth. The natural extension of this model of growth is to add a mechanism for cell division. Several factors were shown to act as a signal to induce cell division such as the dilution of the cell cycle inhibitor Rb in human cells [Zatulovskiy, 2020] or cell wall tension [Harris, 2016]. Another interesting path would be to couple the nested Pump-Leak model to a model of nucleocytoplasmic transport. I think that this may reveal a promising new mechanism for the translocation of protein into the nucleus upon perturbation which is independent of the tension in the nuclear envelope. In Chapter.2, we proposed a mechanical model to understand the folds at the root of the nuclear scaling law. This model is purposely simplified to obtain scaling relations and to subsequently check if it is likely relevant for the nucleus. A natural extension of this model would be to conduct simulations to include geometrical effects and solve the full system of equations without approximations. We can also assess other mechanical instability such as creasing [1]that can emerge in these mechanical systems [Ciarletta, 2019]. In chapter 3, we derived a linear poroelastic theory for a neutral two components gel. As a logical extension, we propose to incorporate: the membrane using appropriate boundary conditions Eq.3.44, non-linear effects ([Geng, 2012],[Tatara, 1993]), or electrostatic effects through the consideration of ions [Yamaue, 2005]. Finally, in Chapter 4, we have started to solve a model that couples both nucleosol flow and nuclear membrane flow. We propose to complexify the nucleosol flow by adding the diffusion of large proteins through the network of chromatin.

[1]A crease is a localized, sharped tip, self-contact region of large strain relative to the homogeneous state. Interestingly, creasing is one peculiar instability in the sense that the system sharply transitions from an undeformed to a highly deformed state such that linear elasticity cannot describe it.

Supplementary information

La vie c'est comme une boîte de chocolat, on ne sait jamais sur quoi on va tomber.

Winston Groom
Forrest Gump
1986

1 PLM fundamental equations

In this section we derive and discuss the three physical constraints we used throughout our paper to study cell volume regulation. These results are classical and can be found in a reference textbook such as [Sten-Knudsen, 2002].

1.1 Electroneutrality

The intrinsic length scale associated to the Poisson equation is the Debye length. It appears explicitly in the linearized version of the Poisson equation also called the Debye-Huckel equation. It reads:

$$\lambda_D = \left(\frac{1}{4\pi \cdot l_b \cdot (n^+ + n^-)} \right)^{\frac{1}{2}} \tag{S.42}$$

Where: $l_B = \frac{e^2}{4\pi k T \epsilon_r \epsilon_0}$ is the Bjerrum length - which qualitatively corresponds to the distance between two elementary charges at which the electrostatic energy will be comparable to the thermal energy. $l_B \approx 0.7$nm in water at 300K. In the unit used in this paper (concentrations in mMol) the Debye length can be estimated using the following formula:

$$\lambda_D \approx \frac{9.7}{\sqrt{n^+(mM) + n^-(mM)}} \cdot nm \tag{S.43}$$

For a typical mammalian cell $n^+(\text{mM}) + n^-(\text{mM}) \approx 180$mM (Fig.1.1) which leads to a Debye length $\lambda_D \approx 0.7$nm. Thus, the Debye length is at least 3 orders of magnitude smaller than the typical radius of a cell or of a nucleus. This justifies the approximation of electroneutrality used throughout the main paper for length scales much larger than the Debye length.

1.2 Balance of water chemical potential

We define the osmotic pressure as:

$$\Pi = -\frac{1}{v_w} \cdot (\mu_w - \mu_w^*) \tag{S.44}$$

where : v_w is the molecular volume of water, μ_w, μ_w^* are the chemical potential of water respectively in the real solution and in a pure water solution. Assuming that water is incompressible, $\mu_w^* = \mu_0(T) + v_w \cdot P$, where P is the hydrostatic pressure. When water is equilibrated, thermodynamics imposes that the chemical potential of water is equal on both sides of the membrane. From the previous equations it is straightforward to derive Eq.1.2 in the main text.

1.3 Balance of ionic fluxes

The total flux J of cations - respectively anions - is decomposed between 3 main contributions: active pumping, electrical conduction and entropic diffusion. For simplicity we assumed that only cations are pumped out of the cell. This simplifying choice was made to model the Na/K pump which is one of the most relevant cationic pumps. Though, we show in subsection.2 that this assumption is not critical since the equations keep the same functional form if it is relaxed. As a convention, we choose J to be positive when ions are entering the cell. At steady-state, the fluxes vanish:

$$\begin{cases} J_{+,tot} = g^+ \cdot \left[-e \cdot U_c - kT \cdot ln\left(\frac{n^+}{n_0}\right) \right] - p = 0 \\ J_{-,tot} = g^- \cdot \left[e \cdot U_c - kT \cdot ln\left(\frac{n^-}{n_0}\right) \right] = 0 \end{cases} \tag{S.45}$$

where p is the pumping flux, $g^{\pm}$ are the membrane conductivities for cations and anions, and U_c is the cell transmembrane potential, which can be expressed as:

$$U_c = -\frac{kT}{e} \cdot ln\left(\frac{n^+}{n_0}\right) - \frac{p}{g_+} = \frac{kT}{e} \cdot ln\left(\frac{n^-}{n_0}\right) \tag{S.46}$$

For Eq.S.46 to be verified, the following relationship between n^+ and n^- must be imposed :

$$\begin{cases} n^+ \cdot n^- = \alpha_0 \cdot n_0^2 \\ \alpha_0 = e^{-\frac{p}{g^+}} \end{cases} \tag{S.47}$$

The latter equation takes the form of a generalized Donnan ratio that includes the active pumping of cations. The usual Donan ratio [Sten-Knudsen, 2002] is recovered when $p = 0$. The generalized Donnan ratio Eq.1.3 together with the electroneutrality condition Eq.1.1 yield analytic expressions for the ionic densities n^+ and n^- (the notations are defined in the main text):

$$\begin{cases} n^+ = \frac{zx+\sqrt{(zx)^2+4\alpha_0 n_0^2}}{2} \\ n^- = \frac{-zx+\sqrt{(zx)^2+4\alpha_0 n_0^2}}{2} \end{cases} \tag{S.48}$$

The cell osmotic pressure can thus be expressed as:

$$\frac{\pi}{kT} = \sqrt{(zx)^2 + 4\alpha_0 n_0^2} + x \tag{S.49}$$

2 General expressions of the volume in the PLM model

The system of equation formed by Eq.1.1,1.2,1.3 is nonlinear and cannot be solved analytically in its full generality. One complexity arises from the difference of hydrostatic pressure ΔP. Intuitively, if the volume increases, the surface increases which may in some situations increase the tension of the envelope and in turn impede the volume growth. Mathematically, Laplace law relates the difference of hydrostatic pressure to the tension γ and the mean curvature of the interface - which simplifies to the radius of the cell R in a spherical geometry. The difference of hydrostatic pressure then reads:

$$\Delta P = \frac{2\gamma}{R} \tag{S.50}$$

In the case where the interface exhibits a constitutive law which is elastic $\gamma = K \cdot \frac{S-S_0}{S_0}$, it is easy to see that ΔP exhibits power of V which makes the problem non analytical. However, we can get around this limitation in two biologically relevant situations :

- When ΔP is negligible. As shown in Fig1.1.B this happens for mammalian cells that do not possess cellular walls.
- When ΔP is buffered by biological processes. We argue that this situation applies for yeasts and bacteria during growth. Indeed, if the volume increase is sufficiently slow, one can hypothesize that cells have time to add materials to their cellular walls such that the tension does not increase during growth.

We give the corresponding analytical expressions under these two hypotheses in the next two paragraphs.

2.1 Analytical expression of the volume when hydrostatic pressure difference is negligible

The balance of water chemical potential Eq.1.2, neglecting the difference of pressure and injecting the expressions for the ionic densities Eq.S.48 leads to the following equation for the density of impermeant molecules x :

$$(z^2-1)\cdot x^2 + 4n_0\cdot x - 4\cdot(1-\alpha_0)\cdot n_0^2 = 0 \tag{S.51}$$

Solving this equation and using the definition of the density of impermeant molecules $x = \frac{X}{V-R}$ yield the expression for the volume of the cytoplasm :

$$\begin{cases} V - R = \frac{kT\cdot N^{tot}}{\Pi_0} \\ N^{tot} = X\cdot\frac{(z^2-1)}{-1+\sqrt{1+(1-\alpha_0)(z^2-1)}} \end{cases} \tag{S.52}$$

The volume can thus be written as an ideal gas law with a totel number of free osmolytes N^{tot}. This number takes into account the different ions and is thus larger than the actual number of impermeant molecules X. In the limit of very fast pumping - $\alpha_0 \to 0$ - Eq.S.52 reduces to the expression given in the main text Eq.1.4

2.2 Analytical expression of the volume when ΔP is buffered

The same procedure can be used when ΔP is buffered (independent of the volume). The final expression reads:

$$\begin{cases} V - R = \frac{kT\cdot N^{tot}(\Delta P)}{(\pi_0+\Delta P)} \\ N^{tot}(\Delta P) = X\cdot\frac{z^2-1}{-1+\sqrt{1+(z^2-1)\cdot\left(1-\frac{\alpha_0}{\left(1+\frac{\Delta P}{kT\cdot 2n_0}\right)^2}\right)}} \end{cases} \tag{S.53}$$

Interestingly, the wet volume $V-R$ remains proportional to the number of impermeant molecules X in this limit.

2.3 Analytical expression of the volume for an arbitrary number of ions and active transports

In this subsection, we generalize the PLM to any type of ions and any ionic transport. Each ion can be actively transported throughout the membrane. Importantly, we show that - as long as ions are monovalent - the PLM equations and solutions take the same functional form as the two-ions model used in the main text. We use the same notations as in the main text (Section 2.1 and Fig.1.1), except that we now add subscript i to refer to the ion of type i. For instance, z_i^- - respectively n_i^- - refers to the valancy - respectively the concentration - of the anion i. The densities of positive / negative charges in the cell read:

$$\begin{cases} d^+ = \sum_j z_j^+\cdot n_j^+ \\ d^- = \sum_j z_j^-\cdot n_j^- \end{cases} \tag{S.54}$$

Electroneutrality thus simply reads:

$$d^+ - d^- - z \cdot x = 0 \tag{S.55}$$

Balancing ionic fluxes for each ion types, as in Eq.S.45, leads to :

$$\begin{cases} n_j^{+/-} = n_j^0 \cdot \alpha_j \cdot e^{(-/+) \cdot z_j \cdot \frac{e \cdot U_c}{kT}} \\ \alpha_j = e^{-\frac{p_j}{g_j}} \end{cases} \tag{S.56}$$

Using Eqs.S.54,S.55, S.56 and assuming that all ions are monovalent, the product of the cationic and anionic densities can be expressed as :

$$d^+ \cdot d^- = \underbrace{\left(\sum_j n_j^{+,0} \cdot \alpha_j \right) \cdot \left(\sum_i n_i^{-,0} \cdot \alpha_i \right)}_{\underset{def}{\equiv} \tilde{\alpha}(n_i^0)} \tag{S.57}$$

and the analytical solution of the full problem reads:

$$\begin{cases} d^+ = \frac{zx + \sqrt{(zx)^2 + 4\tilde{\alpha}(n_i^0)}}{2} \\ \\ d^- = \frac{-zx + \sqrt{(zx)^2 + 4\tilde{\alpha}(n_i^0)}}{2} \end{cases} \tag{S.58}$$

$$\begin{cases} V - R = \frac{kT \cdot N^{tot}(\Delta P)}{(\pi_0 + \Delta P)} \\ \\ N^{tot}(\Delta P) = X \cdot \frac{z^2 - 1}{-1 + \sqrt{1 + (z^2 - 1) \cdot \left(1 - \frac{4\tilde{\alpha}(n_i^0)}{\left(\frac{1}{kT} \cdot \Pi_0 + \frac{1}{kT} \cdot \Delta P \right)^2} \right)}} \end{cases} \tag{S.59}$$

which shows a similar form as the two-ion model, Eqs.S.48,S.53.

3 Order of magnitudes

Throughout the main text, we used order of magnitudes to guide our investigations and justify our approximations. For the sake of readability we gather all the parameter significations, values, and origins in Table S1.

Table S1: Description and values of the parameters used for the order of magnitudes.

Symbol	Typical Value	Meaning
ρ	0.1kg.L^{-1}	Typical dry mass density in a mammalian cell [Zlotek-Zlotkiewicz, 2015]
$\mathcal{M}_a$	100Da	Average mass of an amino-acid [Rob Philipps, 2015]
l_p	400a.a	Average length of an eukaryotic protein [Rob Philipps, 2015]
$\mathcal{M}_{mRNA}$	$3 \cdot \mathcal{M}_a$	Average mass of a mRNA [Rob Philipps, 2015]
l_{mRNA}	$3 \cdot l_p$	Average length of a mRNA [Rob Philipps, 2015]
l_{bp}	1/3nm	Average length of one base pair
Q_{bp}	2	Average number of negative charge per base pair
$L_{nucleosome}$	200bp	Average length of DNA per nucleosome
L_{link}	53bp	Length of the DNA linking two histones
L_{wrap}	147bp	Length of the DNA wrapped around one histone
u_{DNA}	4	Manning parameter for pure DNA, i.e., 75% of the charges will be screened by manning condensation.
L_{tot}	$6 \cdot 10^9$bp	Total length of the DNA within a diploid human cell
Q_{hist}	76	Average number of positive charges per histone at less than 1nm from the wrapped DNA backbone[Materese, 2009]
Q_{wrap}	174	Average number of condensed counterions around the wrapped DNA [Materese, 2009]
l_b	0.7nm	Bjerrum length in water at 300k
K	25mN/m	Stretching modulus of Lamina [Dahl, 2004]

3.1 Protein concentration

We use data published in [Zlotek-Zlotkiewicz, 2015] to estimate the typical concentration of proteins in mammalian cell p_{tot} as :

$$p_{tot} = \%_p^{mass} \cdot \frac{\rho}{\mathcal{M}_a \cdot l_p \cdot (1 - \frac{R}{V})} \sim 2mMol \tag{S.60}$$

where, $\%_p^{mass}$ is the fraction of dry mass occupied by proteins Fig.1.1.D.

3.2 mRNA to protein fraction

In figure 1.1.C we neglected the contribution of mRNAs to the wet volume of the cell. The rationale behind this choice is twofold. (1) Proteins represent less than 1% of the wet volume (2) The mRNA to

protein number fraction is estimated to be small, due to the fact that the mass of one mRNA is 9 times greater than the one of a protein while the measured fraction of mRNA to dry mass is of the order 1% [Rob Philipps, 2015] :

$$\frac{M_{tot}}{P_{tot}} = \frac{\mathcal{M}_p}{\mathcal{M}_{mRNA}} \cdot \frac{\%^{mass}_{mRNA}}{\%^{mass}_{p}} \sim \frac{1}{500} \tag{S.61}$$

Thus, mRNAs contribute even less than proteins to the wet volume.

3.3 Metabolite concentration

We find the metabolite concentration self-consistently by enforcing balance of osmotic pressure at the plasma membrane Eq.1.2 :

$$a^f = 2n_0 - p_{tot} - n^+ - n^- \sim 118mMol \tag{S.62}$$

where the concentrations of ions were reported in [Rob Philipps, 2015] (see Fig.1.1). This high value of metabolite concentration is coherent with reported measurements [Park, 2016].

3.4 Contribution of osmolytes to the wet volume of the cell Fig.1.1.C

The contribution of osmolytes to the wet volume fraction is simply equal to the ratio of the osmolyte concentration to the external osmotic pressure, here equal to $2n_0$ Eq.1.4. The concentration of specific amino-acids and metabolites were estimated using their measured proportion in the metabolite pool [Park, 2016] times the total concentration of metabolites a^f (Eq.S.62).

3.5 Amino-acids contribution to the dry mass

One of the main conclusions from our order of magnitude estimates is that amino-acids play an essential role in controlling the volume but have a negligible contribution to the cell's dry mass. This originates from the large average size of proteins $l_p \sim 400$a.a. The contribution of amino-acids to the dry mass reads:

$$\%^{mass}_{a.a} = \%^{number}_{a.a} \cdot \frac{a^f}{p_{tot}} \cdot \frac{\%^{mass}_{p}}{l_p} \sim 6\% \tag{S.63}$$

where, $\%^{number}_{a.a} \sim 73\%$ is the number fraction of amino-acids among metabolites.

3.6 Effective charge of chromatin

The average effective charge per nucleosome is estimated to be:

$$Q^{eff}_{pernucleosome} = L_{Link} \cdot \frac{Q_{bp}}{u_{DNA}} + L_{wrap} \cdot Q_{bp} - Q_{hist} - Q_{wrap} = 71 \tag{S.64}$$

where, the right hand side can be understood as the total negative charge of pure DNA, screened in part by histone positive charges and by the manning condensed counterions. Note that the number of condensed counterions Q_{wrap} around the wrapped DNA simulated in [Materese, 2009] is similar to the value expected by the manning theory which we estimate to be 164 elementary charges.

The number of nucleosomes is simply $N_{hist} = \frac{L_{tot}}{L_{nucleosomes}} = 3 \cdot 10^7$ such that the effective charge of chromatin is estimated to be :

$$Q^{eff} = 2 \cdot 10^9 \tag{S.65}$$

3.7 Condensed counterions on chromatin

The condensed counterions on chromatin can simply be found from the effective charge of the chromatin, the total charge of pure DNA and the charge of histones. We obtain:

$$Q^{cond} = Q_{bp} \cdot L_{tot} - Q^{eff} - Q_{hist} \cdot N_{hist} \sim 8 \cdot 10^9 \tag{S.66}$$

3.8 Estimation of the amplitude of the Mitotic Swelling

At mitosis cells have doubled their genome content such that we double the number of condensed counterions estimated earlier for a diploid mammalian cell. Using the PLM, we compute the amplitude of swelling if all the chromatin condensed counterions were released at the same time, assuming an external osmolarity of $n_0 = 100 - 150$mM.

$$\Delta V = \frac{2 \cdot Q^{cond}}{2n_0} \sim 100 \mu \text{m}^3 \tag{S.67}$$

Note that ΔV must scale with the number of genome duplications. For instance, for tetraploid cells, the previous amplitude must be doubled.

3.9 Average charge of proteins and metabolites

The average charge of proteins used in the paper, $z_p \sim 0.8$, was estimated from [Requião, 2017] assuming that Histidines are neutral. This is reasonable because their Pka is of order 6 while typical physiological pH is of order 7.4, so that only 4% of histidines are charged in the cell.

The average charge of metabolites is assumed to be $z_a \sim 1$ since glutamate is the most abundant [Park, 2016]. We have checked that changing this parameter does not alter our conclusions.

3.10 Absolute number of osmolytes

To obtain the Figure.1.4, we had to estimate the parameter $NC_1 = \frac{P_n}{P_c}$ and thus, the number of protein trapped inside the nucleus P_n at the beginning of interphase. The total number of proteins and metabolites at the beginning of interphase is simply obtained by multiplying the concentration of proteins p_{tot}, m_{tot} estimated earlier by the volume at the beginning of interphase, measured to be equal to $1250 \mu\text{m}^3$, minus the dry volume which roughly represent 30% of the total volume [Zlotek-Zlotkiewicz, 2015] and Fig.1.1.B.

$$P_{tot} = p_{tot} \cdot (V - R) \sim 10^9 \tag{S.68}$$

$$A^f = \frac{a^f}{p_{tot}} \cdot P_{tot} \sim 60 \cdot 10^9 \tag{S.69}$$

In the regime where the chromatin is diluted (large amount of metabolites), the NC ratio can be well approximated by $NC_1 = \frac{P_n}{P_c}$. Usual values of NC reported in the literature typically range from 0.3 to 0.6 [Guo, 2017], [Wu, 2022]. We thus estimate reasonable values of P_n as:

$$P_n = \frac{NC}{1 + NC} \cdot P_{tot} \sim 3 \cdot 10^8 \tag{S.70}$$

Note that we also used the numerical solutions of Eq.S.93 in Section 6 to infer NC_1 from NC exactly. This method made no qualitative difference to the results plotted in Fig.1.4.

3.11 Estimation of an upper bound for the hydrostatic pressure difference of the nucleus

Even though the stiffness of the lamina layer is susceptible to vary according to the tissue the cell is belonging to [Swift, 2013], its stretching modulus was reported to range from 1 to 25mN/m [Dahl, 2004], [Stephens, 2017]. Also, Lamina turnover rate is much slower than the actin turnover rate. Together, this suggests that Lamina - at the difference to the cortical actin - can sustain bigger pressure difference on longer timescales. This solid-like behavior of Lamina was observed during micropipette aspiration of Oocyte nuclei through the formation of membrane wrinkles at the pipette entrance [Dahl, 2004]. We thus chose to mathematically model lamina with an elastic constitutive equation when it is tensed Eq.S.112. Using Laplace law, we estimate an upper bound for ΔP_n, assuming a typical nuclear radius of 5 μm, to be:

$$\Delta P_n \sim \frac{2K}{R} \sim 10^4 Pa \tag{S.71}$$

3.12 Estimation of the second virial term in the osmotic pressure

We estimate the steric term in the osmotic pressure to be:

$$\pi_{steric} \sim kT \cdot v_p \cdot p_{tot}^2 \sim 2kPa \tag{S.72}$$

where, v_p is the excluded volume per protein, estimated to be $v_p \sim \frac{R}{P_{tot}} \sim 375nm^3$. This corresponds to a protein radius of 4.5nm, a value coherent with observations [Rob Philipps, 2015]. This steric contribution in the osmotic pressure may thus safely be neglected, as $\pi_{steric} << \pi_0$.

4 A cell growth model

We summarize here the equations derived and discussed in the main text (Eqs.1.6,1.7). The rates of production of mRNAs and proteins in the non-saturated and saturated regimes read:

$$\dot{M}_j = \begin{cases} k_0 \cdot \phi_j \cdot P_p - \frac{M_j}{\tau_m}, & if \quad P_p \leq P_p^* \\ k_0 \cdot g_j \cdot \mathcal{N}_p^{max} - \frac{M_j}{\tau_m}, & if \quad P_p \geq P_p^* \end{cases} \tag{S.73}$$

$$\dot{P}_j = \begin{cases} k_t \cdot \frac{M_j}{\sum M_j} \cdot P_r - \frac{P_j}{\tau_p}, & if \quad P_r \leq P_r^* \\ k_t \cdot M_j \cdot \mathcal{N}_r^{max} - \frac{P_j}{\tau_p}, & if \quad P_r \geq P_r^* \end{cases} \tag{S.74}$$

The cut-off values - P_p^*, P_r^* - above which the substrates become saturated are obtained by imposing continuities of the production rates at the transition:

$$\begin{cases} P_p^* = \mathcal{N}_p^{max} \cdot \sum g_j \\ P_r^* = \mathcal{N}_r^{max} \cdot \sum M_j \end{cases} \tag{S.75}$$

4.1 Neither DNA nor mRNAs are saturated: $P_p \leq P_p^*$ and $P_r \leq P_r^*$

The fast degradation rate of mRNAs ensures that their number reach steady-state during growth (Eq.1.8 which with Eq.1.7 yield an exponential growth for the number of ribosomes $P_r = P_{r,0} \cdot e^{k_r \cdot t}$ (with $k_r = k_t \cdot \phi_r - 1/\tau_p$) and of any other protein, $P_j = \frac{\phi_j}{\phi_r} \cdot P_r$; where we neglected the initial conditions on proteins other than ribosomes due to the exponential nature of the growth. Incorporating the dynamics

of growth of the enzyme catalyzing the amino-acid biosynthesis P_e into Eq.1.9, we obtain the number of free amino-acids in the cell:

$$A^f = \left(\phi_e \cdot \frac{k_{cat}}{k_r} - l_p\right) \cdot \frac{P_r}{\phi_r} \tag{S.76}$$

Using the expression of the volume Eq.1.4 derived from the PLM coupled to our quantitative order of magnitudes, it is straightforward to show that the volume grows exponentially :

$$V = \left(v_p + \frac{(z_{A,f}+1)\cdot\left(\phi_e \cdot \frac{k_{cat}}{k_r} - l_p\right)}{2n_0}\right) \cdot \frac{P_r}{\phi_r} \tag{S.77}$$

where we assumed the dry volume to be mainly accounted by proteins. Incorporating the previous expressions in the equation for the dry mass density Eq.1.5, we obtain the homeostatic dry mass density written in the main text Eq.1.10. These expressions were obtained assuming that neither the DNA nor the mRNA were saturated. Importantly, mRNAs cannot be saturated if DNA is not saturated because the cut-off value P_r^* for which ribosomes saturates mRNAs grows at the same speed as the number of ribosomes : $P_r^* = \mathcal{N}_r^{max} \cdot k_0 \cdot \tau_m \cdot \frac{\phi_p}{\phi_r} \cdot P_r$. Hence, DNA will saturate before mRNAs during interphase, at a time t^* given by:

$$t^* = \frac{1}{k_r} \cdot ln\left(\frac{g_r}{g_p} \cdot \frac{\mathcal{N}_p^{max} \cdot \sum g_j}{P_{r,0}}\right) \tag{S.78}$$

4.2 DNA is saturated but not mRNAs: $P_p \geq P_p^*$ and $P_r \leq P_r^*$

The only difference with the previous regime is that mRNA number saturates to the value $M_j = k_0 \cdot g_j \cdot \tau_m \cdot \mathcal{N}_p^{max}$. Hence, the threshold P_r^* will saturate to the value:

$$P_r^* = \mathcal{N}_r^{max} \cdot \mathcal{N}_p^{max} \cdot k_0 \cdot \tau_m \cdot \sum g_j \tag{S.79}$$

This allows for the subsequent saturation of mRNAs by ribosomes after a time t^{**}; whose expression can be derived after simple algebra as :

$$t^{**} = t^* + \frac{1}{k_r} \cdot ln\left(\frac{g_p}{g_r} \cdot \mathcal{N}_r^{max} \cdot k_0 \cdot \tau_m\right) \tag{S.80}$$

However, before reaching this time, there won't be any consequence on the proteomic dynamics, which still scales with the number of ribosomes $P_j = \frac{\phi_j}{\phi_r} \cdot P_r$. This regime thus still corresponds to an exponential growth and the dry mass density remains at its homeostatic value Eq.1.10.

4.3 Both DNA and mRNAs are saturated: $P_p \geq P_p^*$ and $P_r \geq P_r^*$

The dynamics of growth is profoundly impacted by mRNA saturation. The protein number no longer grows exponentially, but saturates to the stationary value $P_j^{stat} = k_t \cdot k_0 \cdot \tau_p \cdot \tau_m \cdot \mathcal{N}_r^{max} \cdot \mathcal{N}_p^{max} \cdot g_j$ after a typical time $t^{**} + \tau_p$ according to:

$$P_j = P_j^{stat} + \left(P_j(t^{**}) - P_j^{stat}\right) \cdot e^{-\frac{t-t^{**}}{\tau_p}} \tag{S.81}$$

The loss of the exponential scaling of proteins implies a breakdown of the proportionality between amino-acid and protein numbers as predicted by the amino-acid biosynthesis equation Eq.1.9. The total amino-acid pool in the cell $A_{tot} = A_f + l_p \cdot P_{tot}$ now scales as:

$$A_{tot} = A_{tot}(t^{**}) + k_{cat} \cdot \left[P_e^{stat} \cdot (t - t^{**}) - \tau_p \cdot (P_e(t^{**}) - P_e^{stat}) \cdot \left(e^{-(t-t^{**})/\tau_p} - 1 \right) \right] \tag{S.82}$$

with, $A_{tot}(t^{**}) = \frac{\phi_e}{\phi_r} \cdot \frac{k_{cat}}{k_r} \cdot \mathcal{N}_r^{max} \cdot \mathcal{N}_p^{max} \cdot k_0 \cdot \tau_m \cdot \sum g_j$. Although, expressions still remain analytical in the transient regime and were implemented in Fig.1.2 in order to quantitatively test our theory, we avoid analytical complications here, by writing expressions after saturation has been reached, i.e., after a typical time $t^{**} + \tau_p$. The volume thus increases linearly with time:

$$V^{lin} = v_p \cdot P_{tot}^{stat} + \frac{(z_{A^f} + 1) \cdot (A_{tot}(t^{**}) + k_{cat} \cdot P_e^{stat} \cdot (t - t^{**}) - l_p \cdot P_{tot}^{stat})}{2n_0} \tag{S.83}$$

As emphasized in the main text, the fundamental property of this regime is that the dry mass density is predicted to decrease with time with no other mechanism than a simple crowding effect on mRNAs (see Eq.1.11 in the main text).

4.4 Quantification of the model of growth with published data

Many of the parameters involved in the growth model can be obtained independently, so that four parameters suffice to fully determine the volume, the amount of protein and the dry mass density during interphase growth. Here, we summarize the equations used to fit the data displayed in Fig.1.2. The volume can be expressed as:

$$V = \begin{cases} v_1 \cdot e^{k_r \cdot t}, & if \quad t \leq t^{**} \\ v_2 \cdot (t - t^{**}) + v_3 \cdot e^{-(t-t^{**})/\tau_p} + v_4, & if \quad t \geq t^{**} \end{cases} \tag{S.84}$$

in which ($v_1,\ v_2,\ v_3,\ v_4$) are volumes that can be, if needed, expressed function of the previously defined parameters. We obtain ($v_2,\ v_3,\ v_4$) as a function of $v_1,\ \tau_p$ and t^{**} by imposing regularity constraints on the volume and growth rate:

$$\begin{cases} v_3 = \tau_p^2 \cdot k_r^2 \cdot v_1 \cdot e^{k_r \cdot t^{**}} \\ v_2 = \frac{v3}{\tau_p} + k_r \cdot v_1 \cdot e^{k_r \cdot t^{**}} \\ v_4 = v_1 \cdot e^{k_r \cdot t^{**}} - v_3 \end{cases} \tag{S.85}$$

Similarly, the normalized total number of protein can be expressed as:

$$\frac{P_{tot}}{P_{tot}(1h)} = \begin{cases} e^{k_r \cdot (t-1)}, & if \quad t \leq t^{**} \\ p_1 + p_2 \cdot e^{-(t-t^{**})/\tau_p}, & if \quad t \geq t^{**} \end{cases} \tag{S.86}$$

Again imposing regularity constraints at the mRNA saturating transition, allows us to relate p_1 and p_2 to k_r, τ_p and t^{**}.

$$\begin{cases} p_2 = -\tau_p \cdot k_r \cdot e^{k_r \cdot (t^{**}-1)} \\ p_1 = e^{k_r \cdot (t^{**}-1)} - p_2 \end{cases} \tag{S.87}$$

Finally, we can express the buoyant mass density ρ^b of the cell (see Fig.1.2 for a definition) using the expressions of total protein number and volume Eq.S.86,S.84 :

$$\frac{\rho^b - \rho^w}{\rho^{b,0} - \rho^w} = \begin{cases} 1, & if \quad t \leq t^{**} \\ \frac{P_{tot}}{P_{tot}(0h)} \cdot \frac{v_1}{V}, & if \quad t \geq t^{**} \end{cases} \tag{S.88}$$

We use a density of water 4% larger than that of pure water ($\rho^{w,eff} = 1.04$kg/L instead of ~ 1kg/L)

to compensate for our approximation to consider the dry mass as entirely made of proteins. Proteins are known to only occupy $\%_p^{mass} = 0.6$ of the dry mass, itself being of order $\rho = 0.1$kg/L Tab.S1. Thus, we simply use as the effective water mass density, $\rho^{w,eff} = \rho^w + (1 - \%_p^{mass}) \cdot \rho \sim 1.04$kg/L.

4.5 Fitting procedure

We detail in this appendix the method used to determine the four fitting parameters: τ_p, t^{**}, k_r, v_1 from the cell volume data Fig.1.2.B. Our model (Eq.S.84,S.85) displays two different regimes of growth according to the saturation state of mRNAs. Our fitting procedure is thus divided into two steps. First, we impose an arbitrary transition time t^{**} to determine by a least mean square minimization the three other parameters. Then, we minimize the variance between the obtained solution with the data to determine t^{**}. The optimal values of the fitting parameters are:

$$t^{**} = 2h44\text{min} \quad , \quad \tau_p = 1h9\text{min} \quad , \quad k_r = 0.62\text{h}^{-1} \quad , \quad v_1 = 30\text{fL} \tag{S.89}$$

5 Manning condensation

We give a simple description of the phenomenon of Manning condensation, based on [Barrat, 1996]. The electrostatic potential close to an infinitely charged thin rod, in a salt bath, reads:

$$\psi = \frac{2 \cdot l_b}{A} \cdot ln(\kappa r) \tag{S.90}$$

where, l_b is the Bjerrum length. It is the length at which the elecrostatic interaction between two elementary particles is on the order of kT. Its value in water at room temperature is $l_B \approx 0.7$nm. A is the average distance between two charges on the polymer. $\kappa^2 = 8\pi l_B(n^+ + n^-)$ is the inverse of the Debye length. At equilibrium, the distribution of charges around the rod follows a Boltzmann distribution:

$$n^+ = n_0 \cdot e^{-\Psi} = \frac{n_0}{(\kappa r)^{2 \cdot \frac{l_b}{A}}} \tag{S.91}$$

The total number of positive charges per unit length of the rod reads within a distance $\mathcal{R}$:

$$N(\mathcal{R}) = \int_0^{\mathcal{R}} n^+ 2\pi r dr = \frac{2\pi \cdot n_0}{\kappa^{2 \cdot \frac{l_b}{A}}} \cdot \int_0^{\mathcal{R}} \frac{1}{(r)^{2\frac{l_b}{A}-1}} dr \tag{S.92}$$

When $u = \frac{l_B}{A} < 1$, $N(\mathcal{R})$ is dominated by its upper bond and goes to 0 close to the rod. On the other hand, when $u = \frac{l_B}{A} > 1$, $N(\mathcal{R})$ diverges as $\mathcal{R} \to 0$ indicating a strong condensation of the counterions on the rod. This singularity is symptomatic of the breakdown of the linear Debye-Huckel theory. The solution of the nonlinear Poisson-Boltzmann equation shows that there is formation of a tighly bound layer of counterions very near the rod, which effectively decreases the charge density (increases A) up to the value $u_{eff} = 1$ [Schiessel, 2014]. It means that if A is smaller than l_B the manning condensation will renormalize A to $A^{eff} = l_B$. The rationale behind this renormalization is to decrease the electrostatic energy of the system by condensing free ions on the polymer. Note that there is an energy penalty associated to the loss of entropy of the condensed counterions. For weakly charged polymers this loss of entropy is not energetically favorable - case where $u = \frac{l_B}{A} < 1$ and no condensation occurs. If the density of charge of the polymer increases, Manning condensation becomes energetically favorable - case where $u = \frac{l_B}{A} > 1$. By virtue of the high lineic charge of DNA, Manning condensation will be favorable, $u^{DNA} \sim 4$.

6 The Nested PLM Model

The nested PLM is described by a set of non-linear equations, i.e., the electroneutrality, the balance of pressures, and the balance of ionic fluxes, in the cytoplasm, subscript c, and in the nucleus, subscript n. In its most general form the system reads:

$$\begin{cases} n_c^+ - n_c^- - z_p \cdot p_c - z_a \cdot a_c = 0 \\ n_n^+ - n_n^- - z_p \cdot p_n - z_a \cdot a_n - q = 0 \\ \Delta\Pi_c = \Delta P_c \\ \Delta\Pi_n = \Delta P_n \\ n_c^+ \cdot n_c^- = \alpha_0 \cdot n_0^2 \\ n_n^+ \cdot n_n^- = \alpha_0 \cdot n_0^2 \\ (n_n^+)^{z_a} \cdot a_n = (n_c^+)^{z_a} \cdot a_c \end{cases} \tag{S.93}$$

Here, we apply the nested PLM to mammalian cells, such that we can neglect the cytoplasmic difference of hydrostatic pressure with respect to the external osmotic pressure. If the NE is not under tension, the condition of osmotic balance at the NE simply implies that the volume of each compartment takes the same functional form as in the PLM model:

$$\begin{cases} V_n = R_n + \frac{N_n^{tot}}{2n_0} \\ V_c = R_c + \frac{N_c^{tot}}{2n_0} \end{cases} \tag{S.94}$$

It is thus straightforward to show that both the volume of the nucleus and the volume of the cytoplasm scale with each other Eq.1.12.

6.1 Dry volumes in the nucleus and in the cytoplasm

We assume that the dry volumes in the nucleus and in the cytoplasm are proportional to the total volumes of each compartments and are equal to each other: $R_n = r \cdot V_n$ and $R_c = r \cdot V_c$. Under this assumption the NC ratio simply becomes the ratio of the wet volumes:

$$NC = \frac{V_n}{V_c} = \frac{V_n - R_n}{V_c - R_c} \tag{S.95}$$

This hypothesis is practical rather than purely rigorous. It is based on experiments that suggest that dry mass occupies about 30% of the volume of both the nucleus and the cytoplasm for several cell types and conditions [Lemière, 2022], [Venkova, 2022],[Rowat, 2006]. Nonetheless, even if this assumption were to be inexact, our discussion would then rigorously describe the slope of the linear relationship between nucleus and cell volume (Eq.1.12) which was shown to be robust to perturbation [Guo, 2017].

6.2 Membrane potential in the simple PLM model

Using the results provided earlier we find that a transmembrane potential exists as soon as there are trapped charged particles. The plasma membrane potential reads:

$$\begin{cases} U = ln\left(\frac{-z\cdot(-1+r)+\sqrt{z^4+\alpha_0-z^2\cdot(-1+\alpha_0+2\cdot r)}}{z^2-1}\right) \\ \text{With,} \quad r = \sqrt{1+(z^2-1)\cdot(1-\alpha_0)} \end{cases} \tag{S.96}$$

We find that U monotonically increases (in absolute value) with the average charge of the cell trapped components. This differs from the nuclear membrane potential that vanishes when the charge of the chromatin is diluted regardless of the properties of the trapped proteins Eq.1.14.

6.3 General Formula for the regime NC_2, i.e., no metabolites

As stated in the main text an important limit regime, NC_2, is achieved when there are no metabolites in the cell. Specifically, the previous system of equations becomes uncoupled with respect to the nuclear and cytoplasmic set of variables such that we can solve the system analytically. Using the exact same algebra as used in the simple PLM we express the volumes and the NC ratio as:

$$\begin{cases} V_{tot} = (R_c + R_n) + \frac{N_n^{tot} + N_c^{tot}}{2n_0} \\ N_c^{tot} = P_c \cdot \frac{z_p^2 - 1}{-1 + \sqrt{1 + (1-\alpha_0)\cdot(z_p^2 - 1)}} \\ N_n^{tot} = P_n \cdot \frac{(z_{n,eff}^2 - 1)}{-1 + \sqrt{1 + (1-\alpha_0)(z_{n,eff}^2 - 1)}} \\ z_{n,eff} = z_p + \frac{Q^{eff}}{P_n} \\ NC_2 = NC_1 \cdot \frac{(z_{n,eff}^2 - 1)}{(z_p^2 - 1)} \cdot \frac{-1 + \sqrt{1 + (1-\alpha_0)(z_p^2 - 1)}}{-1 + \sqrt{1 + (1-\alpha_0)(z_{n,eff}^2 - 1)}} \end{cases} \tag{S.97}$$

6.4 Analytical solutions in the regime $z_p = 1$, $z_a = 1$, and $\alpha_0 \sim 0$

In this regime of high pumping, no anions occupy the cell. We simplify the notations by denoting by n the concentration of cations. The system of equation to solve is stated in the main text Eq.1.13. We first express the concentrations of cations and metabolites in the cytoplasm and nucleus as a function of n_0, q, and p thanks to the electroneutrality equations and balance of osmotic pressures:

$$\begin{cases} n_n = n_0 + \frac{q}{2} \\ a_n^f = \left(n_0 - \frac{q}{2}\right) - p_n \\ n_c = n_0 \\ a_c^f = n_0 - p_c \end{cases} \tag{S.98}$$

This allows us to write the NE potential as Eq.1.14 in the main text. Using the balance of nuclear osmotic pressure we express the nuclear volume function of the number of nuclear osmolytes:

$$V_n - R_n = \frac{Q^{eff} + 2A_n^f + 2P_n}{2n_0} \tag{S.99}$$

This implies that the NE potential can be written without the dependence on n_0 as in Eq.1.14. We then express the NC ratio in two different manners. First, using the interpretation of wet volumes namely, the total number of osmolytes in the compartments over $2n_0$. Second, we take advantage of the concentrations of metabolites and cations in Eq.S.98 to express the ratio of protein concentrations. After simple algebra we obtain:

$$\begin{cases} NC = \frac{P_n}{P_c} \cdot \frac{p_c}{p_n} = NC_1 \cdot \left(1 + \frac{Q^{eff}}{2P_n + 2A_n^f + Q^{eff}} + \frac{Q^{eff\,2}}{2P_n + 2A_n^f + Q^{eff}}\right) \\ NC = \frac{1}{2} \cdot \frac{2A_n^f + 2P_n + Q^{eff}}{A_{tot}^f - A_n^f + P_c} \end{cases} \tag{S.100}$$

For clarity, we now normalize each number by $2P_n$, e.g, $\overline{A}_{tot} = \frac{Atot}{2P_n}$. Equating both expressions of the NC ratio leads to a second order polynomial in $\overline{A}_n$:

$$2(1 + \frac{1}{NC_1}) \cdot \overline{A}_n^2 + \left(-2\overline{A}_{tot} + (1 + \overline{Q}^{eff})^2 + \frac{1}{NC_1} \cdot (1 + 2\overline{Q}^{eff})\right) \cdot \overline{A}_n - \overline{A}_{tot} \cdot (1 + \overline{Q}^{eff})^2 = 0 \tag{S.101}$$

The solution $\overline{A}_n$ now reads:

$$\overline{A}_n = \frac{2\overline{A}_{tot} - \frac{1}{NC_1}\cdot(1+2\overline{Q}^{eff}) - (1+\overline{Q}^{eff})^2 + \sqrt{\left(2\overline{A}_{tot} - \frac{1}{NC_1}\cdot(1+2\overline{Q}^{eff}) - (1+\overline{Q}^{eff})^2\right)^2 + 8\cdot(1+\frac{1}{NC_1})\cdot\overline{A}_{tot}\cdot(1+\overline{Q}^{eff})^2}}{4\cdot(1+\frac{1}{NC_1})} \tag{S.102}$$

Which leads to the following expression for NC:

$$NC = NC_1 \cdot \frac{2\overline{A}_{tot} + \frac{1}{NC_1} + (1+\overline{Q}^{eff})^2 + \sqrt{\left(2\overline{A}_{tot} - \frac{1}{NC_1}\cdot(1+2\overline{Q}^{eff}) - (1+\overline{Q}^{eff})^2\right)^2 + 8\cdot(1+\frac{1}{NC_1})\cdot\overline{A}_{tot}\cdot(1+\overline{Q}^{eff})^2}}{2\cdot\left(1+2\overline{A}_{tot} + \frac{1}{NC_1} + \overline{Q}^{eff}\right)} \tag{S.103}$$

As a sanity check, we verify some asymptotic expressions discussed in the main text. For example, when $\overline{Q}^{eff} << 1$ or $\overline{A}_{tot} >> 1$ we recover that NC becomes equal to NC_1. On the other hand, when $\overline{A}_{tot} << 1$, we recover that $NC = NC_1 \cdot (1 + \overline{Q}^{eff}) = NC_2$

6.5 Control parameters of the nested PLM during growth

The precise value of the parameter $NC_1 = \frac{P_n}{P_c}$ is biologically set by an ensemble of complex active processes ranging from transcription, translation to the Ran GTPase cycle and nuclear transport. The precise modelling of nucleo-cytoplasmic transport is out of the scope of this paper but could easily be incorporated to our framework. Nonetheless, we can safely assume that nucleo-cytoplasmic transport is fast compared to the typical timescale of growth. In this case, neglecting protein degradation on the timescale of the G1 phase, the total number of proteins in the nucleus is simply the number of proteins assembled that possessed a nuclear import signal (NIS) in their sequence. Using the same notation as earlier, in the exponential growth regime, the total number of proteins in the nucleus reads:

$$P_{tot,n}(t) = \sum_{j \in NIS} \frac{\phi_j}{\phi_r} \cdot P_r(t) \tag{S.104}$$

where $P_r(t)$ accounts for the number of ribosomes, ϕ_j is the fraction of genes coding for the protein j (see Appendix 4). The subscript j is summed over the genes coding for proteins having nuclear import signals in their sequence. Proteins in the nucleus can either be DNA bound or unbound. For example, histones or DNA polymerases bind to the DNA. Only the unbound proteins contribute to the osmotic pressure. Denoting $k_{u,j}$ and $k_{b,j}$ the reaction rate of binding and unbinding of protein j and assuming that the reactions of binding and unbinding are fast compared to the timescale of growth, we finally express the number of free proteins in the nucleus as :

$$P_{free,n}(t) = \sum_{j \in NIS} \frac{k_{u,j}}{k_{b,j} + k_{u,j}} \cdot \frac{\phi_j}{\phi_r} \cdot P_r(t) \tag{S.105}$$

It is then straightforward to express NC_1 as:

$$NC_1 = \frac{\sum_{j \in NIS} \frac{k_{u,j}}{k_{b,j}+k_{u,j}} \cdot \frac{\phi_j}{\phi_r}}{\sum_{j \notin NIS} \frac{k_{u,j}}{k_{b,j}+k_{u,j}} \cdot \frac{\phi_j}{\phi_r}} \tag{S.106}$$

An important result of this abstract modelling is that NC_1 is independent of time during the exponential growth due to the fact that both $P_n(t)$ and $P_c(t)$ are proportional to $P_r(t)$, which is why we adopted it as a control parameter. The same goes for our second control parameter $\frac{A_{tot}}{2P_n}$, which is also constant during exponential growth.

6.6 Phase Diagram

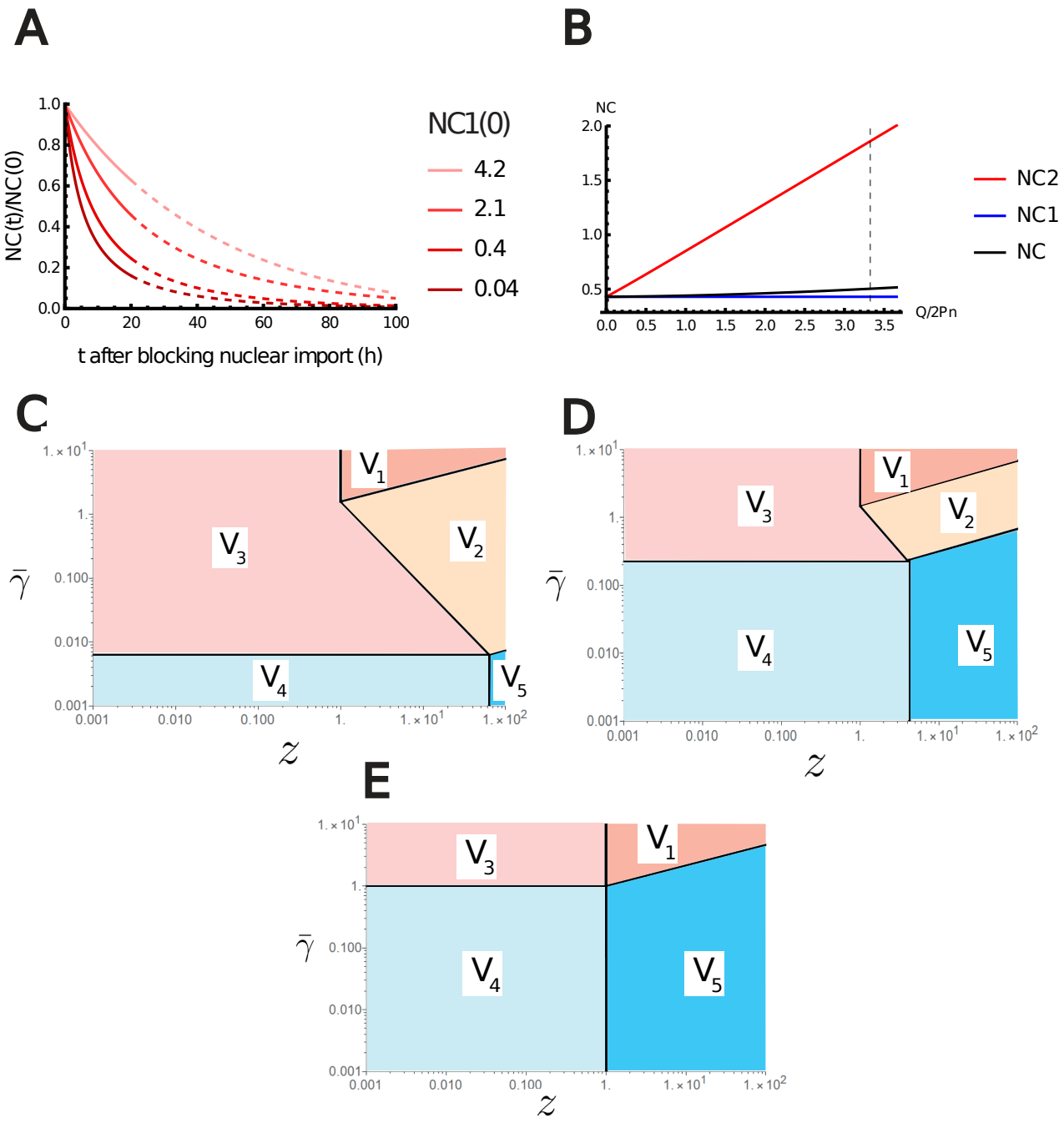

Figure S1: **Additional results of the Nested PLM.** (A) Variation of the NC ratio during growth after blocking nuclear import. (B) Variations of the NC ratio according to the effective charge of the chromatin normalized by the number of trapped proteins in the nucleus $\frac{Q}{2P_n}$. The NC ratio is bounded by two limit regimes. NC1, if the number of metabolites is assumed infinite. NC2, if there are no metabolites. The vertical black dashed line depicts the value of $\frac{Q}{2P_n}$ estimated in Appendix 3 for diploid mammalian cells (C) to (E) Log-Log plot of the different regimes of V Eq.S.110 in the plan $(z_n, \overline{\gamma}_n)$ for α_0 fixed (C) $\alpha_0 = 0.99$ (D) $\alpha_0 = 0.8$ (E) $\alpha_0 = 0.001$. The crossover lines plotted are given in Eq.S.111

In this paragraph we address the case $\Delta P_n \neq 0$ and assume that the cell does not adhere to the substrate such that we consider the nucleus to be spherical. For simplicity, we neglect the dry volume because we want to consider hypo-osmotic shock experiment where dry mass will be diluted, making a dry volume a second order effect of the order 10%. We first make the problem dimensionless. There are two dimensions in our problem: an energy and a length. This means that we can express all our parameters that possess a dimension with a unit energy and a unit length. Moreover, we have three parameters with physical dimensions: the extracellular osmolarity n_0, the NE tension γ, and the thermal energy kT. The theorem of Buckingham [Buckingham, 1914] tells us that we can fully describe our problem with a single dimensionless parameter and the 3 parameters with by definition no dimensions. In this geometry, we choose, $[\left(\frac{4\pi}{3}\right)^{1/3} \cdot \frac{\gamma_0}{kTX_n^{1/3} n_0^{2/3}}, \alpha_0, z_n, X_n]$. Laplace law reads:

$$\Delta P_n = \frac{2\gamma_n}{(\frac{3}{4\pi} V_n)^{1/3}} \tag{S.107}$$

Using the following dimensionless quantities:

$$\begin{cases} \overline{V}_n = \frac{2n0}{X_n} \cdot V_n \\ \overline{\gamma}_n = \left(\frac{4\pi}{3}\right)^{1/3} \cdot \frac{\gamma_0}{kTX_n^{1/3} n_0^{2/3}} \end{cases} \tag{S.108}$$

Equality of pressures becomes:

$$\sqrt{\left(\frac{z_n}{\overline{V}_n}\right)^2 + \alpha_0} + \frac{1}{\overline{V}_n} - 1 - \frac{\overline{\gamma}_n}{\overline{V}_n^{1/3}} = 0 \tag{S.109}$$

Eq.S.109 cannot be solved analytically for $\overline{V}_n$. However, five asymptotic regimes can be identified (see Fig.S1):

$$\begin{cases} V_1 = \left(\frac{3}{16\pi}\right)^{\frac{1}{2}} \cdot \left(\frac{kTX_n}{z_n \cdot \gamma_n}\right)^{\frac{3}{2}} \\ V_2 = \left(\frac{3}{2^{10} \cdot \pi}\right)^{\frac{1}{5}} \cdot \left(\frac{kT \cdot z_n^2 \cdot X_n^2}{n_0 \cdot \sqrt{\alpha_0} \cdot \gamma_n}\right)^{\frac{3}{5}} \\ V_3 = \left(\frac{3}{16\pi}\right)^{\frac{1}{2}} \cdot \left(\frac{kT \cdot X_n}{\gamma_n}\right)^{\frac{3}{2}} \\ V_4 = \frac{X_n}{2n_0} \cdot \frac{1}{1-\sqrt{\alpha_0}} \\ V_5 = \frac{X_n}{2n_0} \cdot \frac{z_n}{\sqrt{1-\alpha_0}} \end{cases} \tag{S.110}$$

- V_4 and V_5 are the limit regimes where osmotic pressure is balanced at the NE.
- V_3 is the limit regime where the difference of osmotic pressure is dominated by the impermeant molecules trapped inside the nucleus. This happens when the proteins are not or very weakly charged. This difference of osmotic pressure is balanced by the Laplace pressure of the lamina.
- V_1 is the limit regime where the difference of osmotic pressure is dominated by the counterions of the impermeant molecules. This difference of osmotic pressure is balanced by the Laplace pressure of the lamina.
- V_2 is an intermediate regime that can arise when $\alpha_0 \approx 1$. The difference of osmotic pressure takes the form of $\Delta\Pi_n \approx kT \cdot \frac{1}{\sqrt{\alpha_0}} \cdot \frac{(z_n \cdot x_n)^2}{4n_0}$. This osmotic pressure defines an effective virial coefficient between monomers of DNA and proteins $v_{el} = \frac{1}{\sqrt{\alpha_0}} \frac{z_n^2}{2n_0}$. This difference of osmotic pressure is balanced by the Laplace pressure at the NE.
- Note that when $\alpha_0 \approx 0$ (strong pumping), only the counterion necessary for electroneutrality remain in the nucleus. Π_n is simply $(z_n + 1) \cdot x_n$ and is either balanced by the Laplace pressure of the

lamina or the external osmotic pressure (see Fig.S1)

Finally, the analytical expressions for the crossover lines $\overline{\gamma}_{i,j}$ between regime of volume V_i and volume V_j, plotted in Fig.S1 read :

$$\begin{cases} \overline{\gamma}_{1,2} = (4 \cdot \alpha_0 \cdot z_n)^{\frac{1}{3}} \\ \overline{\gamma}_{1,4} = z_n \cdot (1 - \sqrt{\alpha_0})^{\frac{2}{3}} \\ \overline{\gamma}_{1,5} = z_n^{\frac{1}{3}} \cdot (1 - \alpha_0)^{\frac{1}{3}} \\ \overline{\gamma}_{2,5} = \frac{z_n^{\frac{1}{3}} \cdot (1-\alpha_0)^{\frac{5}{6}}}{2 \cdot \sqrt{\alpha_0}} \\ \overline{\gamma}_{2,4} = \frac{z_n^{2} \cdot (1-\sqrt{\alpha_0})^{\frac{5}{3}}}{2 \cdot \sqrt{\alpha_0}} \\ \overline{\gamma}_{2,3} = z_n^{-\frac{4}{3}} \cdot (4 \cdot \alpha_0)^{\frac{1}{3}} \\ \overline{\gamma}_{3,5} = z_n^{-\frac{2}{3}} \cdot (1 - \alpha_0)^{\frac{1}{3}} \\ \overline{\gamma}_{3,4} = (1 - \sqrt{\alpha_0})^{\frac{2}{3}} \\ z_{1,3} = 1 \\ z_{4,5} = \frac{\sqrt{1-\alpha_0}}{1-\sqrt{\alpha_0}} \end{cases} \tag{S.111}$$

6.7 Saturating volume after a hypo-osmotic shock

The saturation occurs when the nuclear osmotic pressure is balanced by the Laplace pressure making nuclear volume insensitive to the external osmolarity Eq.S.110. We assume that the NE behaves elastically with a stretching modulus K beyond a surface area S^* for which NE folds are flattened:

$$\gamma_n = \begin{cases} 0 & , if \quad S_n \leq S^* \\ K \cdot \left(\frac{S_n}{S^*} - 1\right) & , if \quad S_n \geq S^* \end{cases} \tag{S.112}$$

As justified in the main text, metabolites tend to leave the nucleus with decreasing external osmolarity. The saturating volume is obtained when $\Delta P_n >> \pi_0$ and $A_n^f << P_n$. From Eq.S.53 applied to the volume of the nucleus, we thus obtain :

$$\Delta P = (z_n^{eff} + 1) \cdot \frac{P_n}{V_n^{max}} \tag{S.113}$$

where, $z_n^{eff} = z_p + \frac{Q}{P_n}$. Similarly to the last subsection, we normalize tensions by $(\frac{3}{4\pi})^{1/3} \cdot kT \cdot P_n^{1/3} \cdot n_0^{2/3}$ and volumes by $\frac{2 \cdot P_n}{2 n_0}$. Eq.S.113 leads to the equation ruling the saturating volume :

$$(v_n^{max})^{4/3} - (v_n^{iso})^{2/3} \cdot (1+s) \cdot (\frac{n_0}{n_0^{iso}})^{2/3} \cdot (v_n^{max})^{2/3} - (v_n^{iso})^{2/3} \cdot (1+s) \cdot (\frac{n_0}{n_0^{iso}})^{2/3} \cdot \frac{\frac{1}{2} \cdot (z_n^{eff} + 1)}{\overline{K}} = 0 \tag{S.114}$$

where, $s = \frac{S^*}{S_n^{iso}} - 1$ is the fraction of folds that the nucleus possesses at the isotonic osmolarity. $v_n^{max} = \frac{2 n_0 \cdot V_n^{max}}{2 P_n}$ is the normalized saturating nuclear volume and v_n^{iso} the normalized nuclear volume at the isotonic osmolarity. $\overline{K} = \frac{K}{(\frac{3}{4\pi})^{1/3} \cdot kT \cdot P_n^{1/3} \cdot n_0^{2/3}}$ is the normalized effective stretching modulus of the NE. Solving the previous equation, coming back to real volumes $\frac{V_n^{max}}{V_n^{iso}} = \frac{v_n^{max}}{v_n^{iso}} \cdot \frac{n_0^{iso}}{n_0}$ and taylor develop the result for $n_0 \longrightarrow 0$ leads to Eq.1.17 in the main text.

6.8 Geometrical impact

The previous equations were conducted for a spherical geometry. Interestingly, while the precise geometry does not qualitatively change our results, we expect the saturation of nuclear volume to occur more easily

for a pancake shape - a shape closer to the shape of adhered cells. Indeed, the scaling between surface and volume is approximatively linear in this case: $V \sim h \cdot S$, while it is sub-linear for spheres $S \sim V^{2/3}$. Thus, smaller osmotic shocks will be required to tense the NE and so as to reach the saturating regime.

7 Electrostatic interactions are encompassed within our framework

We directly compute the contribution of electrostatic interactions to the osmotic pressure based on [Barrat, 1996]. The total interaction energy of a solution of charged particles of average density x within a volume V is, using the Poisson-Boltzmann framework:

$$\frac{E_{el}}{kT} = \frac{l_B \cdot z^2}{2} \int\int x(\vec{r}) \cdot x(\vec{r'}) \cdot \frac{e^{-\kappa|\vec{r}-\vec{r'}|}}{|\vec{r}-\vec{r'}|} \quad d^3\vec{r} \cdot d^3\vec{r'} \tag{S.115}$$

where $x(\vec{r})$ is the local density of impermeant molecules in the cell. Fourier analysis allows us to rewrite this equation:

$$\frac{E_{el}}{kT} = \frac{l_B \cdot z^2}{2} \int x(\vec{k}) \cdot x(\vec{-k}) \cdot \frac{4\pi}{k^2+\kappa^2} \quad d^3\vec{k} \approx \frac{l_B \cdot z^2}{2} \cdot x^2 \cdot \frac{4\pi}{\kappa^2} \cdot V \tag{S.116}$$

From which we derive the expression of the osmotic pressure:

$$\frac{\pi_{el}}{kT} \approx \frac{1}{2} \cdot \frac{z^2}{2n_0} \cdot x^2 \tag{S.117}$$

We now show that this term is already encompassed within our framework. For the simplicity of the discussion we neglect pumping, i.e., $\alpha_0 \sim 1$. The difference of osmotic pressure then reads (see Eq.S.49):

$$\frac{\Delta\pi}{kT} = \sqrt{(zx)^2 + 4n_0^2} + x - 2n_0 \tag{S.118}$$

which, under the right regime, i.e., $zx << 2n_0$, leads to the same term. As mentioned above, this osmotic pressure defines an effective electrostatic virial coefficient between monomers:

$$v_{el} = \frac{z^2}{2n_0} \tag{S.119}$$

8 Possible extension to explain the scaling of other organelles

Organelles are also known to display characteristic scaling trends with cell size ([Chan, 2010]). Even-though these scalings may be of different origins and would require much careful treatment with respect to the specificity of the organelle, we highlight in this subsection that our model can easily be extended to also include organelles.

We model an organelle in our theory by a compartment bound by a membrane that trap some molecules. For the sake of generality we assume that there is an active transport of cations through this membrane. As a matter of coherence with the previous notations we will call by $\alpha_{org} = e^{-\frac{p_{org}}{g+}}$ the parameter that compares the active pumping through the organelle's membrane versus the passive leakage. Donnan Equilibrium on both side of the organelle reads :

$$n^+_{org} \cdot n^-_{org} = \alpha_{org} \cdot (n^+_c \cdot n^-_c) = \alpha_{org} \cdot \alpha_0 \cdot n_0^2 \tag{S.120}$$

Hence, the results derived previously also apply to the organelle provided the parameter α_0 is changed into $\alpha_{org} \cdot \alpha_0$. Interestingly, in the case of osmotic balance at the membrane of the organelle, it is straightforward to show that the the volume of the organelle also scales with the cell volume:

$$\begin{cases} V_{org} = \left(\frac{N_{org}^{tot}}{N^{tot}}\right) \cdot V_{tot} + \left[\left(\frac{N_c^{tot}+N_n^{tot}}{N^{tot}}\right) \cdot R_{org} - \left(\frac{N_{org}^{tot}}{N^{tot}}\right) \cdot (R_c + R_n)\right] \\ N^{tot} = N_c^{tot} + N_n^{tot} + N_{org}^{tot} \\ N_{org}^{tot} = X_{org} \cdot \frac{(z_{org}^2-1)}{-1+\sqrt{1+(1-\alpha_0 \cdot \alpha_{org})(z_{org}^2-1)}} \end{cases} \tag{S.121}$$

Bibliography

[Adar, 2020] Ram M. Adar and Samuel A. Safran. "Active volume regulation in adhered cells". *Proceedings of the National Academy of Sciences* (2020) (cit. on pp. 3, 6).

[Alberts, 2002] Bruce Alberts, Alexander Johnson, Julian Lewis, Martin Raff, Keith Roberts, and Peter Walter. *Molecular Biology of the Cell*. 4th. Garland Science, 2002 (cit. on pp. 8, 11, 16, 134).

[Altman, 2016] Brian J. Altman, Zachary E. Stine, and Chi V. Dang. "From Krebs to clinic: glutamine metabolism to cancer therapy". *Nature Reviews Cancer* 16.10 (2016), pp. 619–634 (cit. on pp. 21, 24).

[Anderson, 2007] Daniel J. Anderson and Martin W. Hetzer. "Nuclear envelope formation by chromatin-mediated reorganization of the endoplasmic reticulum". *Nature Cell Biology* 9.10 (2007), pp. 1160–1166 (cit. on p. 52).

[Andreu, 2022] Ion Andreu, Ignasi Granero-Moya, Nimesh R. Chahare, Kessem Clein, Marc Molina-Jordán, Amy E. M. Beedle, et al. "Mechanical force application to the nucleus regulates nucleocytoplasmic transport". *Nature Cell Biology* 24.6 (2022), pp. 896–905 (cit. on pp. 39, 40).

[Barrat, 1996] Jean-Louis Barrat and François Joanny. "Theory of Polyelectrolyte Solutions". *Advances in Chemical Physics*. John Wiley & Sons, Ltd, 1996, pp. 1–66 (cit. on pp. v, 26, 103, 119, 126).

[Belle, 2006] Archana Belle, Amos Tanay, Ledion Bitincka, Ron Shamir, and Erin K. O'Shea. "Quantification of protein half-lives in the budding yeast proteome". *Proceedings of the National Academy of Sciences* 103.35 (2006), pp. 13004–13009 (cit. on p. 14).

[Betzig, 2006] Eric Betzig, George H. Patterson, Rachid Sougrat, O. Wolf Lindwasser, Scott Olenych, Juan S. Bonifacino, et al. "Imaging Intracellular Fluorescent Proteins at Nanometer Resolution". *Science* 313.5793 (2006), pp. 1642–1645 (cit. on p. 3).

[Biedzinski, 2020] Stefan Biedzinski, Gökçe Agsu, Benoit Vianay, Marc Delord, Laurent Blanchoin, Jerome Larghero, et al. "Microtubules control nuclear shape and gene expression during early stages of hematopoietic differentiation". *The EMBO Journal* 39.23 (2020), e103957 (cit. on p. 53).

[Brau, 2011] Fabian Brau, Hugues Vandeparre, Abbas Sabbah, Christophe Poulard, Arezki Boudaoud, and Pascal Damman. "Multiple-length-scale elastic instability mimics parametric resonance of nonlinear oscillators". *Nature Physics* 7.1 (2011), pp. 56–60 (cit. on pp. 43, 44, 49, 50).

[Brochard-Wyart, 2006] F. Brochard-Wyart, N. Borghi, D. Cuvelier, and P. Nassoy. "Hydrodynamic narrowing of tubes extruded from cells". *Proceedings of the National Academy of Sciences* 103.20 (2006), pp. 7660–7663 (cit. on pp. 98, 100).

[Buckingham, 1914] E. Buckingham. "On Physically Similar Systems; Illustrations of the Use of Dimensional Equations". *Physical Review* 4.4 (1914), pp. 345–376 (cit. on p. 124).

[Burg, 2007] Thomas P. Burg, Michel Godin, Scott M. Knudsen, Wenjiang Shen, Greg Carlson, John S. Foster, et al. "Weighing of biomolecules, single cells and single nanoparticles in fluid". *Nature* 446.7139 (2007), pp. 1066–1069 (cit. on pp. 3, 5).

[Cadart, 2017] C. Cadart, E. Zlotek-Zlotkiewicz, L. Venkova, O. Thouvenin, V. Racine, M. Le Berre, et al. "Fluorescence eXclusion Measurement of volume in live cells". *Methods in Cell Biology* 139 (2017), pp. 103–120 (cit. on pp. 3, 5).

[Cadart, 2019] Clotilde Cadart, Larisa Venkova, Pierre Recho, Marco Cosentino Lagomarsino, and Matthieu Piel. "The physics of cell-size regulation across timescales". *Nature Physics* 15.10 (2019), pp. 993–1004 (cit. on pp. 3, 5, 6).

[Cantwell, 2019] Helena Cantwell and Paul Nurse. "Unravelling nuclear size control". *Current Genetics* 65.6 (2019), pp. 1281–1285 (cit. on pp. 5, 6, 17, 23–25).

[Chan, 2010] Yee-Hung M. Chan and Wallace F. Marshall. "Scaling properties of cell and organelle size". *Organogenesis* 6.2 (2010), pp. 88–96 (cit. on pp. 2, 17, 26, 126).

[Chernomordik, 2008] Leonid V. Chernomordik and Michael M. Kozlov. "Mechanics of membrane fusion". *Nature Structural & Molecular Biology* 15.7 (2008), pp. 675–683 (cit. on p. 100).

[Ciarletta, 2019] P. Ciarletta and L. Truskinovsky. "Soft Nucleation of an Elastic Crease". *Physical Review Letters* 122.24 (2019), p. 248001 (cit. on pp. ix, 53, 107).

[Conklin, 1912] Edwin G. Conklin. "Cell size and nuclear size". *Journal of Experimental Zoology* 12.1 (1912), pp. 1–98 (cit. on p. 5).

[Cosgrove, 2021] Brian D. Cosgrove, Claudia Loebel, Tristan P. Driscoll, Tonia K. Tsinman, Eric N. Dai, Su-Jin Heo, et al. "Nuclear envelope wrinkling predicts mesenchymal progenitor cell mechano-response in 2D and 3D microenvironments". *Biomaterials* 270 (2021), p. 120662 (cit. on pp. vii, 41, 54, 105).

[Coulon, 2014] Antoine Coulon, Matthew L Ferguson, Valeria de Turris, Murali Palangat, Carson C Chow, and Daniel R Larson. "Kinetic competition during the transcription cycle results in stochastic RNA processing". *eLife* 3 (2014). Ed. by Douglas L Black, e03939 (cit. on pp. ix, 101, 107).

[Cuylen-Haering, 2020] Sara Cuylen-Haering, Mina Petrovic, Alberto Hernandez-Armendariz, Maximilian W. G. Schneider, Matthias Samwer, Claudia Blaukopf, et al. "Chromosome clustering by Ki-67 excludes cytoplasm during nuclear assembly". *Nature* 587.7833 (2020), pp. 285–290 (cit. on p. 52).

[Dahl, 2004] Kris Noel Dahl, Samuel M. Kahn, Katherine L. Wilson, and Dennis E. Discher. "The nuclear envelope lamina network has elasticity and a compressibility limit suggestive of a molecular shock absorber". *Journal of Cell Science* 117.20 (2004), pp. 4779–4786 (cit. on pp. 18, 20, 35, 48, 51, 93, 113, 116).

[Dal Molin, 2015] Marta Dal Molin, Quentin Verolet, Adai Colom, Romain Letrun, Emmanuel Derivery, Marcos Gonzalez-Gaitan, et al. "Fluorescent Flippers for Mechanosensitive Membrane Probes". *Journal of the American Chemical Society* 137.2 (2015), pp. 568–571 (cit. on p. 38).

[De Vos, 2011] Winnok H. De Vos, Frederik Houben, Miriam Kamps, Ashraf Malhas, Fons Verheyen, Juliën Cox, et al. "Repetitive disruptions of the nuclear envelope invoke temporary loss of cellular compartmentalization in laminopathies". *Human Molecular Genetics* 20.21 (2011), pp. 4175–4186 (cit. on p. 85).

[Deviri, 2019] Dan Deviri, Charlotte R. Pfeifer, Lawrence J. Dooling, Irena L. Ivanovska, Dennis E. Discher, and Samuel A. Safran. "Scaling laws indicate distinct nucleation mechanisms of holes in the nuclear lamina". *Nature Physics* 15.8 (2019), pp. 823–829 (cit. on p. 30).

[Deviri, 2022] Dan Deviri and Samuel A. Safran. "Balance of osmotic pressures determines the nuclear-to-cytoplasmic volume ratio of the cell". *Proceedings of the National Academy of Sciences* 119.21 (2022), e2118301119 (cit. on pp. 17, 20, 24).

[Dey, 2021] Gautam Dey and Buzz Baum. "Nuclear envelope remodelling during mitosis". *Current Opinion in Cell Biology* 70 (2021), pp. 67–74 (cit. on p. 52).

[Doi, 2009] Masao Doi. "Gel Dynamics". *Journal of the Physical Society of Japan* 78.5 (2009), p. 052001 (cit. on p. 65).

[Donahue, 2016] Daniel A. Donahue, Sonia Amraoui, Francesca di Nunzio, Camille Kieffer, Françoise Porrot, Silvana Opp, et al. "SUN2 Overexpression Deforms Nuclear Shape and Inhibits HIV". *Journal of Virology* 90.8 (2016), pp. 4199–4214 (cit. on p. 41).

[Economos, 1983] A. C. Economos. "Elastic and/or geometric similarity in mammalian design?" *Journal of Theoretical Biology* 103.1 (1983), pp. 167–172 (cit. on p. 2).

[Elosegui-Artola, 2017] Alberto Elosegui-Artola, Ion Andreu, Amy E. M. Beedle, Ainhoa Lezamiz, Marina Uroz, Anita J. Kosmalska, et al. "Force Triggers YAP Nuclear Entry by Regulating Transport across Nuclear Pores". *Cell* 171.6 (2017), 1397–1410.e14 (cit. on p. 39).

[Evans, 2011] Evan Evans and Benjamin A. Smith. "Kinetics of Hole Nucleation in Biomembrane Rupture". *New Journal of Physics* 13 (2011), p. 095010 (cit. on pp. 88, 99, 100).

[Feig, 2015] Michael Feig, Ryuhei Harada, Takaharu Mori, Isseki Yu, Koichi Takahashi, and Yuji Sugita. "Complete atomistic model of a bacterial cytoplasm for integrating physics, biochemistry, and systems biology". *Journal of Molecular Graphics and Modelling* 58 (2015), pp. 1–9 (cit. on p. 25).

[Finan, 2009] John D. Finan, Kevin J. Chalut, Adam Wax, and Farshid Guilak. "Nonlinear osmotic properties of the cell nucleus". *Annals of Biomedical Engineering* 37.3 (2009), pp. 477–491 (cit. on pp. vi, 18, 22, 24, 104).

[Fujita, 2020] Mayumi Fujita, Kaori Imadome, Veena Somasundaram, Miki Kawanishi, Kumiko Karasawa, and David A. Wink. "Metabolic characterization of aggressive breast cancer cells exhibiting invasive phenotype: impact of non-cytotoxic doses of 2-DG on diminishing invasiveness". *BMC Cancer* 20.1 (2020), p. 929 (cit. on p. 21).

[Fukuda, 2005] Ryu-ichi Fukuda, Ayako Hayashi, Atae Utsunomiya, Yuko Nukada, Rie Fukui, Katsuhiko Itoh, et al. "Alteration of phosphatidylinositol 3-kinase cascade in the multilobulated nuclear formation of adult T cell leukemia/lymphoma (ATLL)". *Proceedings of the National Academy of Sciences* 102.42 (2005), pp. 15213–15218 (cit. on p. 41).

[Galilei, 1638] Galileo Galilei and Maurice Clavelin. *Discours et démonstrations mathématiques concernant deux sciences nouvelles*. Epiméthée. Presses universitaires de France. Paris, 1638 (cit. on p. 2).

[García-Arcos, 2022] Juan Manuel García-Arcos, Johannes Ziegler, Silvia Grigolon, Loïc Reymond, Gaurav Shajepal, Cédric J. Cattin, et al. *Advected percolation in the actomyosin cortex drives amoeboid cell motility*. 2022 (cit. on p. 85).

[Gemble, 2022] Simon Gemble, René Wardenaar, Kristina Keuper, Nishit Srivastava, Maddalena Nano, Anne-Sophie Macé, et al. "Genetic instability from a single S phase after whole-genome duplication". *Nature* 604.7904 (2022), pp. 146–151 (cit. on p. 17).

[Geng, 2012] Jiasong Geng, Meie Li, and Jinxiong Zhou. "Extended Stress-Diffusion Coupling Model for Swelling Dynamics of Polymer Gels". *Industrial & Engineering Chemistry Research* 51.8 (2012), pp. 3466–3471 (cit. on pp. x, 83, 107).

[Gennes, 1979] P. G. de Gennes. *Scaling Concepts in Polymer Physics*. Cornell University Press, 1979 (cit. on p. 19).

[Gray, 2019] William T. Gray, Sander K. Govers, Yingjie Xiang, Bradley R. Parry, Manuel Campos, Sangjin Kim, et al. "Nucleoid Size Scaling and Intracellular Organization of Translation across Bacteria". *Cell* 177.6 (2019), 1632–1648.e20 (cit. on p. 26).

[Groot, 1984] S. R. de Groot and P. Mazur. *Non-Equilibrium Thermodynamics*. New York, NY: Dover Publications, 1984 (cit. on p. 58).

[Guilluy, 2014] Christophe Guilluy, Lukas D. Osborne, Laurianne Van Landeghem, Lisa Sharek, Richard Superfine, Rafael Garcia-Mata, et al. "Isolated nuclei adapt to force and reveal a mechanotransduction pathway in the nucleus". *Nature Cell Biology* 16.4 (2014), pp. 376–381 (cit. on pp. vii, 53, 100, 105).

[Guo, 2017] Ming Guo, Adrian F. Pegoraro, Angelo Mao, Enhua H. Zhou, Praveen R. Arany, Yulong Han, et al. "Cell volume change through water efflux impacts cell stiffness and stem cell fate". *Proceedings of the National Academy of Sciences* 114.41 (2017), E8618–E8627 (cit. on pp. 5, 21, 115, 120).

[Haldane, 1985] J. B. S. Haldane. *On Being the Right Size and Other Essays*. Ed. by John Maynard Smith. Oxford ; New York: Oxford University Press, 1985 (cit. on p. 2).

[Hampoelz, 2011] Bernhard Hampoelz, Yannick Azou-Gros, Roxane Fabre, Olga Markova, Pierre-Henri Puech, and Thomas Lecuit. "Microtubule-induced nuclear envelope fluctuations control chromatin dynamics in Drosophila embryos". *Development* 138.16 (2011), pp. 3377–3386 (cit. on p. 48).

[Harris, 2016] Leigh K. Harris and Julie A. Theriot. "Relative Rates of Surface and Volume Synthesis Set Bacterial Cell Size". *Cell* 165.6 (2016), pp. 1479–1492 (cit. on pp. ix, 107).

[Hoffmann, 2009] Else K. Hoffmann, Ian H. Lambert, and Stine F. Pedersen. "Physiology of cell volume regulation in vertebrates". *Physiological Reviews* 89.1 (2009), pp. 193–277 (cit. on pp. 3, 7).

[Holzapfel, 2000] Gerhard A. Holzapfel. *Nonlinear Solid Mechanics: A Continuum Approach for Engineering*. 1st edition. Chichester ; New York: Wiley, 2000 (cit. on pp. 49, 59).

[Hooke, 1665] Robert (1635-1703) Auteur du texte Hooke. *Micrographia or Some physiological descriptions of minutes bodies made by magnifying glasses : with observations and inquiries thereupon ([Reprod.]) / by R. Hooke,...* 1665 (cit. on p. 3).

[Jevtić, 2014] Predrag Jevtić and Daniel L. Levy. "Mechanisms of nuclear size regulation in model systems and cancer". *Advances in Experimental Medicine and Biology* 773 (2014), pp. 537–569 (cit. on p. 5).

[Jülicher, 2018] Frank Jülicher, Stephan W. Grill, and Guillaume Salbreux. "Hydrodynamic theory of active matter". *Reports on Progress in Physics* 81.7 (2018), p. 076601 (cit. on pp. 58, 60).

[Kay, 2017] Alan R. Kay. "How Cells Can Control Their Size by Pumping Ions". *Frontiers in Cell and Developmental Biology* 5 (2017) (cit. on p. 9).

[Kedem, 1958] O. Kedem and A. Katchalsky. "Thermodynamic analysis of the permeability of biological membranes to non-electrolytes". *Biochimica et Biophysica Acta* 27 (1958), pp. 229–246 (cit. on p. 6).

[Kim, 2015] Dong-Hwee Kim, Bo Li, Fangwei Si, Jude M. Phillip, Denis Wirtz, and Sean X. Sun. "Volume regulation and shape bifurcation in the cell nucleus". *Journal of Cell Science* 128.18 (2015), pp. 3375–3385 (cit. on pp. 41, 42).

[King, 1969] Jack Lester King and Thomas H. Jukes. "Non-Darwinian Evolution". *Science* 164.3881 (1969), pp. 788–798 (cit. on p. 9).

[Kleiber, 1947] Max Kleiber. "Body size and metabolic rate". *Physiological Reviews* 27.4 (1947), pp. 511–541 (cit. on p. 2).

[Kuang, 2015] Qie Kuang, Pasi Purhonen, and Hans Hebert. "Structure of potassium channels". *Cellular and Molecular Life Sciences* 72 (2015), pp. 3677–3693 (cit. on p. 40).

[Landau, 1959] L. D. Landau and E. M. Lifshitz. *Theory of elasticity*. Course of theoretical physics 7. London: Pergamon, 1959 (cit. on p. 48).

[Lang, 1998] Florian Lang, Gillian L. Busch, Markus Ritter, Harald Völkl, Siegfried Waldegger, Erich Gulbins, et al. "Functional Significance of Cell Volume Regulatory Mechanisms". *Physiological Reviews* 78.1 (1998), pp. 247–306 (cit. on p. 3).

[Le Berre, 2014] Maël Le Berre, Ewa Zlotek-Zlotkiewicz, Daria Bonazzi, Franziska Lautenschlaeger, and Matthieu Piel. "Chapter 14 - Methods for Two-Dimensional Cell Confinement". *Methods in Cell Biology*. Ed. by Matthieu Piel and Manuel Théry. Vol. 121. Micropatterning in Cell Biology Part C. Academic Press, 2014, pp. 213–229 (cit. on pp. 25, 28, 56, 85).

[Lemière, 2022] Joël Lemière, Paula Real-Calderon, Liam J Holt, Thomas G Fai, and Fred Chang. "Control of nuclear size by osmotic forces in *Schizosaccharomyces pombe*". *eLife* 11 (2022). Ed. by Naama Barkai, e76075 (cit. on pp. 9, 17, 20, 21, 24, 120).

[Lengefeld, 2021] Jette Lengefeld, Chia-Wei Cheng, Pema Maretich, Marguerite Blair, Hannah Hagen, Melanie R. McReynolds, et al. "Cell size is a determinant of stem cell potential during aging". *Science Advances* 7.46 (2021), eabk0271 (cit. on pp. 5, 12, 23).

[Levin, 2013] Michael Levin. "Reprogramming cells and tissue patterning via bioelectrical pathways: molecular mechanisms and biomedical opportunities". *WIREs Systems Biology and Medicine* 5.6 (2013), pp. 657–676 (cit. on p. 3).

[Lin, 2018] Jie Lin and Ariel Amir. "Homeostasis of protein and mRNA concentrations in growing cells". *Nature Communications* 9.1 (2018), p. 4496 (cit. on pp. 9, 10).

[Lionetti, 2020] Maria Chiara Lionetti, Silvia Bonfanti, Maria Rita Fumagalli, Zoe Budrikis, Francesc Font-Clos, Giulio Costantini, et al. "Chromatin and Cytoskeletal Tethering Determine Nuclear Morphology in Progerin-Expressing Cells". *Biophysical Journal* 118.9 (2020), pp. 2319–2332 (cit. on p. 53).

[Lomakin, 2020] A. J. Lomakin, C. J. Cattin, D. Cuvelier, Z. Alraies, M. Molina, G. P. F. Nader, et al. "The nucleus acts as a ruler tailoring cell responses to spatial constraints". *Science (New York, N.Y.)* 370.6514 (2020), eaba2894 (cit. on pp. vii, 6, 22, 41, 42, 54, 105).

[Ma, 2012] Jiong Ma, Alexander Goryaynov, Ashapurna Sarma, and Weidong Yang. "Self-regulated viscous channel in the nuclear pore complex". *Proceedings of the National Academy of Sciences* 109.19 (2012), pp. 7326–7331 (cit. on pp. 57, 88).

[Manning, 1969] Gerald S. Manning. "Limiting Laws and Counterion Condensation in Polyelectrolyte Solutions I. Colligative Properties". *The Journal of Chemical Physics* 51.3 (1969), pp. 924–933 (cit. on p. 14).

[Marbach, 2019] Sophie Marbach and Lyderic Bocquet. "Osmosis, from molecular insights to large-scale applications". *Chemical Society Reviews* 48 (2019) (cit. on p. 6).

[Materese, 2009] Christopher K. Materese, Alexey Savelyev, and Garegin A. Papoian. "Counterion Atmosphere and Hydration Patterns near a Nucleosome Core Particle". *Journal of the American Chemical Society* 131.41 (2009), pp. 15005–15013 (cit. on pp. 16, 113, 114).

[Matsuoka, 2005] Masao Matsuoka. "Human T-cell leukemia virus type I (HTLV-I) infection and the onset of adult T-cell leukemia (ATL)". *Retrovirology* 2.1 (2005), p. 27 (cit. on p. 41).

[Mazzanti, 2001] Michele Mazzanti, José Omar Bustamante, and Hans Oberleithner. "Electrical Dimension of the Nuclear Envelope". *Physiological Reviews* 81.1 (2001), pp. 1–19 (cit. on pp. 19, 38).

[McGuffee, 2010] Sean R. McGuffee and Adrian H. Elcock. "Diffusion, Crowding & Protein Stability in a Dynamic Molecular Model of the Bacterial Cytoplasm". *PLOS Computational Biology* 6.3 (2010), e1000694 (cit. on p. 25).

[Model, 2018] Michael A. Model. "Methods for cell volume measurement". *Cytometry Part A* 93.3 (2018), pp. 281–296 (cit. on pp. 3, 5).

[Moir, 2000] Robert D. Moir, Miri Yoon, Satya Khuon, and Robert D. Goldman. "Nuclear Lamins a and B1: Different Pathways of Assembly during Nuclear Envelope Formation in Living Cells". *Journal of Cell Biology* 151.6 (2000), pp. 1155–1168 (cit. on pp. vii, 53, 100, 105).

[Mori, 2012] Yoichiro Mori. "Mathematical properties of pump-leak models of cell volume control and electrolyte balance". *Journal of Mathematical Biology* 65.5 (2012), pp. 875–918 (cit. on pp. 6, 9).

[Nader, 2021] Guilherme Pedreira de Freitas Nader, Sonia Agüera-Gonzalez, Fiona Routet, Matthieu Gratia, Mathieu Maurin, Valeria Cancila, et al. "Compromised nuclear envelope integrity drives TREX1-dependent DNA damage and tumor cell invasion". *Cell* 184.20 (2021), 5230–5246.e22 (cit. on pp. 85, 86).

[Nava, 2020] Michele M. Nava, Yekaterina A. Miroshnikova, Leah C. Biggs, Daniel B. Whitefield, Franziska Metge, Jorge Boucas, et al. "Heterochromatin-Driven Nuclear Softening Protects the Genome against Mechanical Stress-Induced Damage". *Cell* 181.4 (2020), 800–817.e22 (cit. on p. 48).

[Neumann, 2007] Frank R. Neumann and Paul Nurse. "Nuclear size control in fission yeast". *The Journal of Cell Biology* 179.4 (2007), pp. 593–600 (cit. on p. 20).

[Neurohr, 2020] Gabriel E. Neurohr and Angelika Amon. "Relevance and Regulation of Cell Density". *Trends in Cell Biology* 30.3 (2020), pp. 213–225 (cit. on pp. 5, 23).

[Neurohr, 2019] Gabriel E. Neurohr, Rachel L. Terry, Jette Lengefeld, Megan Bonney, Gregory P. Brittingham, Fabien Moretto, et al. "Excessive Cell Growth Causes Cytoplasm Dilution And Contributes to Senescence". *Cell* 176.5 (2019), 1083–1097.e18 (cit. on pp. vi, 5, 6, 12, 13, 23, 103).

[Park, 2016] Junyoung O. Park, Sara A. Rubin, Yi-Fan Xu, Daniel Amador-Noguez, Jing Fan, Tomer Shlomi, et al. "Metabolite concentrations, fluxes and free energies imply efficient enzyme usage". *Nature Chemical Biology* 12.7 (2016), pp. 482–489 (cit. on pp. 9, 12, 21, 24, 114, 115).

[Park, 2018] YongKeun Park, Christian Depeursinge, and Gabriel Popescu. "Quantitative phase imaging in biomedicine". *Nature Photonics* 12.10 (2018), pp. 578–589 (cit. on pp. 3, 5).

[Pegoraro, 2017] Adrian F. Pegoraro, Paul Janmey, and David A. Weitz. "Mechanical Properties of the Cytoskeleton and Cells". *Cold Spring Harbor Perspectives in Biology* 9.11 (2017), a022038 (cit. on p. 134).

[Pennacchio, 2022] Fabrizio A. Pennacchio, Alessandro Poli, Francesca Michela Pramotton, Stefania Lavore, Ilaria Rancati, Mario Cinquanta, et al. *Force-biased nuclear import sets nuclear-cytoplasmic volumetric coupling by osmosis*. 2022 (cit. on pp. 20, 39).

[Peters, 1986] A. Peters and S. J. Candau. "Kinetics of swelling of polyacrylamide gels". *Macromolecules* 19.7 (1986), pp. 1952–1955 (cit. on pp. 73, 82).

[Picas, 2012] Laura Picas, Felix Rico, and Simon Scheuring. "Direct Measurement of the Mechanical Properties of Lipid Phases in Supported Bilayers". *Biophysical Journal* 102.1 (2012), pp. L01–L03 (cit. on pp. 88, 93).

[Raab, 2016] Matthew Raab, Matteo Gentili, Henry de Belly, Hawa-Racine Thiam, Pablo Vargas, Ana Joaquina Jimenez, et al. "ESCRT III repairs nuclear envelope ruptures during cell migration to limit DNA damage and cell death". *Science* 352.6283 (2016), pp. 359–362 (cit. on p. 85).

[Renkawitz, 2019] Jörg Renkawitz, Aglaja Kopf, Julian Stopp, Ingrid de Vries, Meghan K. Driscoll, Jack Merrin, et al. "Nuclear positioning facilitates amoeboid migration along the path of least resistance". *Nature* 568.7753 (2019), pp. 546–550 (cit. on p. 40).

[Requião, 2017] Rodrigo D. Requião, Luiza Fernandes, Henrique José Araujo de Souza, Silvana Rossetto, Tatiana Domitrovic, and Fernando L. Palhano. "Protein charge distribution in proteomes and its impact on translation". *PLOS Computational Biology* 13.5 (2017), e1005549 (cit. on p. 115).

[Rizzotto, 2017] Andrea Rizzotto and Eric C. Schirmer. “Breaking the scale: how disrupting the karyoplasmic ratio gives cancer cells an advantage for metastatic invasion”. *Biochemical Society Transactions* 45.6 (2017), pp. 1333–1344 (cit. on p. 24).

[Rob Philipps, 2015] Ron Milo Rob Philipps. *Cell Biology by the numbers*. 2015 (cit. on pp. v, 3, 7, 10, 24, 40, 88, 103, 113, 114, 116, 134).

[Roffay, 2021] Chloé Roffay, Guillaume Molinard, Kyoohyun Kim, Marta Urbanska, Virginia Andrade, Victoria Barbarasa, et al. “Passive coupling of membrane tension and cell volume during active response of cells to osmosis”. *Proceedings of the National Academy of Sciences* 118.47 (2021), e2103228118 (cit. on p. 3).

[Rowat, 2006] A. C. Rowat, J. Lammerding, and J. H. Ipsen. “Mechanical properties of the cell nucleus and the effect of emerin deficiency”. *Biophysical Journal* 91.12 (2006), pp. 4649–4664 (cit. on p. 120).

[Roy, 2018] Bibhas Roy, Saradha Venkatachalapathy, Prasuna Ratna, Yejun Wang, Doorgesh Sharma Jokhun, Mallika Nagarajan, et al. “Laterally confined growth of cells induces nuclear reprogramming in the absence of exogenous biochemical factors”. *Proceedings of the National Academy of Sciences* 115.21 (2018) (cit. on p. 3).

[Sansom, 2002] Mark S. P. Sansom, Indira H. Shrivastava, Joanne N. Bright, John Tate, Charlotte E. Capener, and Philip C. Biggin. “Potassium channels: structures, models, simulations”. *Biochimica et Biophysica Acta (BBA) - Biomembranes*. Membrane Protein Structure 1565.2 (2002), pp. 294–307 (cit. on p. 40).

[Schiessel, 2014] Helmut Schiessel. *Biophysics for beginners: a journey through the cell nucleus*. Singapore: Pan Stanford Pub., 2014 (cit. on p. 119).

[Schmidt, 2012] Daniel Schmidt, Josefina del Mármol, and Roderick MacKinnon. “Mechanistic basis for low threshold mechanosensitivity in voltage-dependent K+ channels”. *Proceedings of the National Academy of Sciences* 109.26 (2012), pp. 10352–10357 (cit. on p. 40).

[Sender, 2021] Ron Sender and Ron Milo. “The distribution of cellular turnover in the human body”. *Nature Medicine* 27.1 (2021), pp. 45–48 (cit. on p. 2).

[Shah, 2021] Pragya Shah, Chad M. Hobson, Svea Cheng, Marshall J. Colville, Matthew J. Paszek, Richard Superfine, et al. “Nuclear Deformation Causes DNA Damage by Increasing Replication Stress”. *Current biology: CB* 31.4 (2021), 753–765.e6 (cit. on p. 29).

[Sinha, 2011] Bidisha Sinha, Darius Köster, Richard Ruez, Pauline Gonnord, Michele Bastiani, Daniel Abankwa, et al. “Cells Respond to Mechanical Stress by Rapid Disassembly of Caveolae”. *Cell* 144.3 (2011), pp. 402–413 (cit. on p. 100).

[Slater, 2005] D. N. Slater, S. Rice, R. Stewart, S. E. Melling, E. M. Hewer, and J. H. F. Smith. “Proposed Sheffield quantitative criteria in cervical cytology to assist the grading of squamous cell dyskaryosis, as the British Society for Clinical Cytology definitions require amendment”. *Cytopathology: Official Journal of the British Society for Clinical Cytology* 16.4 (2005), pp. 179–192 (cit. on p. 5).

[Smeets, 2019] Bart Smeets, Maxim Cuvelier, Jiri Pešek, and Herman Ramon. “The Effect of Cortical Elasticity and Active Tension on Cell Adhesion Mechanics”. *Biophysical Journal* 116.5 (2019), pp. 930–937 (cit. on p. 134).

[Son, 2015] Sungmin Son, Joon Ho Kang, Seungeun Oh, Marc W. Kirschner, T.J. Mitchison, and Scott Manalis. “Resonant microchannel volume and mass measurements show that suspended cells swell during mitosis”. *Journal of Cell Biology* 211.4 (2015), pp. 757–763 (cit. on pp. 14, 25).

[Srivastava, 2021] Nishit Srivastava, Guilherme Pedreira de Freitas Nader, Alice Williart, Romain Rollin, Damien Cuvelier, Alexis Lomakin, et al. “Nuclear fragility, blaming the blebs”. *Current Opinion in Cell Biology*. Cell Nucleus 70 (2021), pp. 100–108 (cit. on pp. 85, 100).

[Sten-Knudsen, 2002] Ove Sten-Knudsen. *Biological Membranes: Theory of Transport, Potentials and Electric Impulses*. Cambridge University Press, 2002 (cit. on pp. 6, 109, 110).

[Stephens, 2017] Andrew D. Stephens, Edward J. Banigan, Stephen A. Adam, Robert D. Goldman, and John F. Marko. “Chromatin and lamin A determine two different mechanical response regimes of the cell nucleus”. *Molecular Biology of the Cell* 28.14 (2017), pp. 1984–1996 (cit. on pp. 22, 30, 116).

[Swift, 2013] Joe Swift, Irena L Ivanovska, Amnon Buxboim, Takamasa Harada, P C Dave P Dingal, Joel Pinter, et al. “Nuclear lamin-A scales with tissue stiffness and enhances matrix-directed differentiation”. *Science (New York, N.Y.)* 341.6149 (2013), p. 1240104 (cit. on pp. 18, 116).

[Taimen, 2009] Pekka Taimen, Katrin Pfleghaar, Takeshi Shimi, Dorothee Möller, Kfir Ben-Harush, Michael R. Erdos, et al. “A progeria mutation reveals functions for lamin A in nuclear assembly, architecture, and chromosome organization”. *Proceedings of the National Academy of Sciences* 106.49 (2009), pp. 20788–20793 (cit. on p. 41).

[Tanaka, 1979] Toyoichi Tanaka and David J. Fillmore. “Kinetics of swelling of gels”. *The Journal of Chemical Physics* 70.3 (1979), pp. 1214–1218 (cit. on pp. viii, 65, 72, 73, 82, 105).

[Tatara, 1993] Yoichi Tatara. “Large Deformations of a Rubber Sphere under Diametral Compression : Part 1 : Theoretical Analysis of Press Approach, Contact Radius and Lateral Extension”. *JSME international journal. Ser. A, Mechanics and material engineering* 36.2 (1993), pp. 190–196 (cit. on pp. x, 83, 107).

[Thompson, 1912] D’Arcy Wentworth Thompson. *On Growth and Form*. Revised ed. édition. New York: Dover Publications Inc., 1912 (cit. on p. 2).

[Tinevez, 2009] Jean-Yves Tinevez, Ulrike Schulze, Guillaume Salbreux, Julia Roensch, Jean-François Joanny, and Ewa Paluch. “Role of cortical tension in bleb growth”. *Proceedings of the National Academy of Sciences* 106.44 (2009), pp. 18581–18586 (cit. on pp. 87, 100).

[Tosteson, 1960] D. C. Tosteson and J. F. Hoffman. “Regulation of Cell Volume by Active Cation Transport in High and Low Potassium Sheep Red Cells”. *Journal of General Physiology* 44.1 (1960), pp. 169–194 (cit. on pp. v, 7, 9, 103).

[Tse, 2010] Justin R. Tse and Adam J. Engler. “Preparation of Hydrogel Substrates with Tunable Mechanical Properties”. *Current Protocols in Cell Biology* 47.1 (2010), pp. 10.16.1–10.16.16 (cit. on p. 74).

[Turgay, 2017] Yagmur Turgay, Matthias Eibauer, Anne E. Goldman, Takeshi Shimi, Maayan Khayat, Kfir Ben-Harush, et al. “The molecular architecture of lamins in somatic cells”. *Nature* 543.7644 (2017), pp. 261–264 (cit. on p. 48).

[Venkova, 2022] Larisa Venkova, Amit Singh Vishen, Sergio Lembo, Nishit Srivastava, Baptiste Duchamp, Artur Ruppel, et al. “A mechano-osmotic feedback couples cell volume to the rate of cell deformation”. *eLife* 11 (2022). Ed. by Felix Campelo, e72381 (cit. on pp. 3, 5–7, 14, 35, 39, 57, 82, 100, 120).

[Venturini, 2020] Valeria Venturini, Fabio Pezzano, Frederic Català Castro, Hanna-Maria Häkkinen, Senda Jiménez-Delgado, Mariona Colomer-Rosell, et al. “The nucleus measures shape changes for cellular proprioception to control dynamic cell behavior”. *Science (New York, N.Y.)* 370.6514 (2020), eaba2644 (cit. on pp. vii, 41, 54, 105).

[Wang, 2021] Qirun Wang and Jie Lin. “Heterogeneous recruitment abilities to RNA polymerases generate nonlinear scaling of gene expression with cell volume”. *Nature Communications* 12.1 (2021), p. 6852 (cit. on p. 11).

[Webster, 2009] Micah Webster, Keren L. Witkin, and Orna Cohen-Fix. “Sizing up the nucleus: nuclear shape, size and nuclear-envelope assembly”. *Journal of Cell Science* 122.Pt 10 (2009), pp. 1477–1486 (cit. on pp. 5, 17, 23, 24).

[Weigelin, 2012] Bettina Weigelin, Gert-Jan Bakker, and Peter Friedl. “Intravital third harmonic generation microscopy of collective melanoma cell invasion”. *IntraVital* 1.1 (2012), pp. 32–43 (cit. on p. 53).

[West, 1997] Geoffrey B. West, James H. Brown, and Brian J. Enquist. “A General Model for the Origin of Allometric Scaling Laws in Biology”. *Science* 276.5309 (1997), pp. 122–126 (cit. on p. 2).

[Wilson, 1925] E.B. Wilson. *The karyoplasmic ratio. In The Cell in Development and Heredity (The MacMillan Company), pp. 727–733*. 1925 (cit. on p. 5).

[Wolpert, 1969] L. Wolpert. “Positional information and the spatial pattern of cellular differentiation”. *Journal of Theoretical Biology* 25.1 (1969), pp. 1–47 (cit. on p. 2).

[Wu, 2022] Yufei Wu, Adrian F. Pegoraro, David A. Weitz, Paul Janmey, and Sean X. Sun. “The correlation between cell and nucleus size is explained by an eukaryotic cell growth model”. *PLOS Computational Biology* 18.2 (2022), e1009400 (cit. on pp. 9, 20, 115).

[Yamaue, 2005] Tatsuya Yamaue, Hiroto Mukai, Kinji Asaka, and Masao Doi. “Electrostress Diffusion Coupling Model for Polyelectrolyte Gels”. *Macromolecules* 38.4 (2005), pp. 1349–1356 (cit. on pp. x, 83, 107).

[Zatulovskiy, 2020] Evgeny Zatulovskiy, Shuyuan Zhang, Daniel F. Berenson, Benjamin R. Topacio, and Jan M. Skotheim. “Cell growth dilutes the cell cycle inhibitor Rb to trigger cell division”. *Science* 369.6502 (2020), pp. 466–471 (cit. on pp. ix, 107).

[Zhiteneva, 2017] Alisa Zhiteneva, Juan Jose Bonfiglio, Alexandr Makarov, Thomas Colby, Paola Vagnarelli, Eric C. Schirmer, et al. “Mitotic post-translational modifications of histones promote chromatin compaction in vitro”. *Open Biology* 7.9 (2017), p. 170076 (cit. on p. 16).

[Zink, 2004] Daniele Zink, Andrew H. Fischer, and Jeffrey A. Nickerson. “Nuclear structure in cancer cells”. *Nature Reviews Cancer* 4.9 (2004), pp. 677–687 (cit. on p. 5).

[Zlotek-Zlotkiewicz, 2015] Ewa Zlotek-Zlotkiewicz, Sylvain Monnier, Giovanni Cappello, Mael Le Berre, and Matthieu Piel. “Optical volume and mass measurements show that mammalian cells swell during mitosis”. *Journal of Cell Biology* 211.4 (2015), pp. 765–774 (cit. on pp. 14, 18, 25, 113, 115).

RÉSUMÉ

Tout système vivant se développe grâce à la croissance et la division de ses cellules. Il est donc essentiel que ces cellules puissent réguler activement leur taille et leur densité. Ce contrôle précis s'incarne dans des lois d'échelle universelles qui relient linéairement la taille de la cellule à son contenu en protéines et à la taille de son noyau. Malgré l'accumulation de preuves expérimentales, l'origine de la régulation de ces quantités biologiques fondamentales est mal comprise. Dans cette thèse, nous étudions donc comment l'interaction entre les contraintes physiques et les processus biologiques conduisent à l'émergence de ces lois mais aussi à leurs dérèglements.

MOTS CLÉS

Lois d'échelle cellulaire, Volume cellulaire, Volume nucléaire, Densité cellulaire, Pump-leak model, Blebs nucléaires

ABSTRACT

All living systems develop from individual cell growth and division. It is thus crucial for cells to actively regulate their size and densities. This exquisite control is embodied in the robust scaling laws relating cell size, protein content, and nuclear size. Despite accumulating experimental evidence, the origin of the regulation of these key cellular quantities are poorly understood. Therefore, in this thesis, we study how the interplay between physical constraints and biological processes both leads to the emergence of these scaling laws but also to their disruptions in diseases or under specific perturbations.

KEYWORDS

Cell size scaling laws, Cell volume, Nucleus volume, Cell density regulation, Pump-leak model, Nuclear blebs